Ballistic Josephson junctions and vertical tunnelling transistors based on graphene heterostructures

A thesis submitted to the University of Manchester for the degree of
Doctor of Philosophy
in the Faculty of Sciences and Engineering

2016

Mengjian Zhu

School of Physics and Astronomy

Table of Contents

Word count: 50,402

List of Figures

List of Tables

Abstract

This thesis, submitted to The University of Manchester for the degree of Doctor of Philosophy, covers a range of topics related to the research in two-dimensional materials and van der Waals heterostructures under the title: ‘Ballistic Josephson junctions and vertical tunnelling transistors based on graphene heterostructures.’

In this thesis, we study the transport properties of two different types of graphene devices. The first one is ballistic graphene Josephson junction and the second one is graphene-hexagonal boron nitride-graphene vertical tunnelling transistor.

We report on ballistic graphene Josephson junctions with contacts made from type II superconductor, niobium. We observe pronounced Fabry-Pérot oscillations not only in the normal-state resistance but also in the critical current. The proximity effect is mostly suppressed in magnetic fields of $B<10$ mT, showing a conventional Fraunhofer pattern. However, some proximity superconductivity survives in fields higher than 1 T which corresponds to more than 1000 flux quanta threading into the junction. We attribute such high-field Josephson effect to individual Andreev bound states that persist near the graphene edges.

By studying the Fraunhofer pattern of graphene Josephson junctions, we reconstruct the spatial supercurrent distribution in graphene. The edge-dominated transport is observed only in the case of an energy gap opening in bilayer graphene and graphene/hexagonal boron nitride superlattices, which points to its non-trivial topological origin. Owing to the band structure topology of gapped graphene, the valley-polarized edge modes can extend above the disorders and propagate efficiently for micrometres.

By probing the density of states of graphene using graphene tunnelling transistors, we demonstrate a stacking transition in bilayer graphene from incommensurate twisted stacking state to a commensurate AB stacking state by a macroscopic graphene self-rotation. This structural transition is driven by van der Waals energy of two graphene layers and is thermally activated by unpinning the microscopic chemical adsorbents which are then removed by the self-cleaning of graphene.

We observe a series of sharp resonant features in the differential conductance of graphene-hexagonal boron nitride tunnelling transistors over a wide range of bias voltages. We attribute them to electron tunnelling assisted by the emission of phonons. The phonon energies corresponding to the resonances are compared with the lattice dispersion curves of graphene-hexagonal boron nitride heterostructure and are close to peaks in the single phonon density of states.

24 October 2016

Mengjian Zhu

Declaration

No portion of the work referred to in this thesis has been submitted in support of an application for another degree or qualification of this or any other university or other institute of learning.

Copyright statement

i. The author of this thesis (including any appendices and/or schedules to this thesis) owns certain copyright or related rights in it (the "Copyright") and s/he has given The University of Manchester certain rights to use such Copyright, including for administrative purposes.

ii. Copies of this thesis, either in full or in extracts and whether in hard or electronic copy, may be made only in accordance with the Copyright, Designs and Patents Act 1988 (as amended) and regulations issued under it or, where appropriate, in accordance with licensing agreements which the University has from time to time. This page must form part of any such copies made.

iii. The ownership of certain Copyright, patents, designs, trademarks and other intellectual property (the "Intellectual Property") and any reproductions of copyright works in the thesis, for example graphs and tables ("Reproductions"), which may be described in this thesis, may not be owned by the author and may be owned by third parties. Such Intellectual Property and Reproductions cannot and must not be made available for use without the prior written permission of the owner(s) of the relevant Intellectual Property and/or Reproductions.

iv. Further information on the conditions under which disclosure, publication and commercialisation of this thesis, the Copyright and any Intellectual Property and/or Reproductions described in it may take place is available in the University IP Policy (see http://documents.manchester.ac.uk/DocuInfo.aspx?DocID=487), in any relevant Thesis restriction declarations deposited in the University Library, The University Library's regulations (see http://www.manchester.ac.uk/library/aboutus/regulations) and in The University's policy on Presentation of Theses.

Acknowledgements

Even in my wildest dream, I never thought I would become a PhD student in physics and have an opportunity to work in a world-leading laboratory led by two Nobel Prize laureates. I started my PhD in September 2013 in Manchester Institute of Biotechnology supervised by Prof. Xuefeng Yuan with a project titled ‘the rheological properties of carbon-based polymer composites’. We spent nearly three months to set up the facilities until Prof. Yuan accepted an offer from China and decided to move back to China. Before Prof. Yuan left Manchester, he sent my CV to Prof. Andre Geim. After a short interview, I formally became a PhD student in condensed matter physics. I guess the main reason of Andre accept a young man with no knowledge in physics and graphene at all as his PhD student is that I was fully funded by the National University of Defense Technology (NUDT, China) oversea scholarship. I always appreciate the NUDT scholarship to cover my tuition fee and living expense in Manchester so that I can focus on my study and research.

I am very grateful to have had the opportunity to work under Andre’s supervision. He won the Noble Prize in physics and he is my superhero in science but he never gave me a snort of contempt when I made some naive mistakes or sent him an E-mail at middle night to discuss the experimental results. Andre has a great understanding and elegant taste in physics but not limited in physics. I have to confess that most of the time I cannot follow his idea until I had enough reference reading and discussion with other people. One thing I definitely can learn from Andre is his time management. He knows the work done by each student and post-doctoral; he analyses the data and writes the papers; he attends several conferences every year; he is always there when I want to show him new experimental data. Even though, he still has time to make new jokes! Above all, I am grateful to Andre for his supervision over the last three years.

As my advisor, Prof. Kostya Novoselov gave me many very warm-hearted help during my PhD not only in science but also in life. He is the greatest experimental physicist and the best teacher I have ever met. Kostya always encourage and sponsor me to participate in academic conferences to represent our latest results. I also enjoyed every football game we have played together in Wednesday nights.

It is impossible to finish this thesis without the enormous help from my co-supervisors, Dr Artem Mishchenko. From devices wire bonding to facility setting to LabVIEW program writing, I have learned so many things from him. Artem is a genius in experimental physics not only because of his great skills in experiments but also because of his strong ability to figure out and solve the problems. It is my luck to start my first year PhD under his guidance.

Dr. Moshe Ben Shalom has also been a significant mentor to me after I decided to switch my research from graphene tunnelling transistor to graphene Josephson junction. Moshe fabricated many high quality devices for me and we had a successful collaboration on proximity superconductivity in graphene. I was always inspired by his idea when sitting together with him analysing the data and discussing the results. Moshe has a very solid background in superconductivity and quantum transport and he always kindly shared his knowledge with me.

I am very grateful to Artem and Moshe for their leadership and for their role in training me to become a better PhD student in physics. Now, both of them have received decent offers to continue their works in science. I hope they can get bigger success in the future and enjoy their lives.

Many thanks go to the great theorists who have provided theoretical support for our experimental results. Especially Prof. Vladimir Fal’ko, without his beautiful theory, it would be much harder to complete our first paper on ballistic graphene Josephson junctions.

I also want to thank the group members in Manchester, who gave me so many help over the last three years, including Prof. Irina Grigorieva, Dr. Yang Su, Dr. Yang Cao, Dr. Kaige Zhou, Dr. Sheng Hu, Dr. Geliang Yu, Dr. Jhih-Sian Tu, Dr. Freddie Whithers, Dr. Roman Gorbachev, Dr. Andey Kretiny, Dr. Marcelo Lozada-Hidalgo, Dr. Colin Woods, Dr. James Chapman, Roshan Krishna Kumar, Denis Bandurin, Davit Ghazaryan, Katerina Khestanova, John Brickbeck, Renyan Zhang and Xianjun Huang. Many thanks go to our wonderful lab technicians: Stan Gillot, Mark Sellers and Paul Richardson. They fill cryostats; make inserts; fix broken stuffs and make nice coffee. I cannot imagine doing my research without their enormous help. I also thank our executive assistant Charlotte Hooson-Sykes for her hep about all the paper works. Special thanks go to my dear friend Roshan for his proof reading of this thesis.

I would also like to thank our collaborators Dr. Jonathan Prance and Dr. Michael Thompson in Lancaster University for their help in low-temperature measurements of our graphene Josephson junctions at 10mK.

Many thanks also go to two examiners for their reading and correcting of my PhD thesis.

I would like to thank my parents, thank them so much for bringing me up and supporting me all the time without any expectation of repayment from me. I also thank my dear three sisters and their family members as well. One of the happiest moments in my life is going back to home, sitting close to parents, embracing my sisters, enjoying the cooking and laughing like a child who never grows up.

亲爱的爸妈，谢谢你们抚养我长大，给予我如此多的爱和支持。亲爱的大姐、二姐和小妹，谢谢你们陪伴我长大，帮我照顾爸妈，祝你们的宝贝小孩们健康快乐，茁壮成长。

I am very grateful to my wife’s parents for their trusting and generousness to marry their only daughter to me, a poor student with no money and no job.

亲爱的爸妈，谢谢你们把宝贝女儿嫁给我。

Finally, I dedicate this thesis to my best friend and my wife Fay. She is an amazing girl of intelligence, integrity and independence. It is impossible to finish my PhD without her accompany, understanding and love.

List of Publications

1. M. J. Zhu, A. V. Kretinin, M. D. Thompson, D. A. Bandurin, S. Hu, A. Mishchenko, K. Watanabe, T. Taniguchi, M. Polini, J. R. Prance, K. S. Novoselov, A. K. Geim, M. B. Shalom. Edge currents shunt the insulating bulk in gapped graphene. *arXiv*: 1612.05902 (under review of *Nature Communications*).
2. M. J. Zhu, Davit Ghazaryan, Seok-Kyun Son, Collin R. Woods, Abhishek Misra, Lin He, Takashi Taniguchi, Kenji Watanabe, Kostya S. Novoselov, Yang Cao, Artem Mishchenko. Stacking transition in bilayer graphene caused by thermally activated rotation. *2D Materials* **4**, 01013 (2017).
3. M. J. Zhu, *et al*. Supercurrent in long ballistic graphene Josephson junctions. *In preparation.*
4. M. B. Shalom, M. J. Zhu, V. I. Fal'ko, A. Mishchenko, A. V. Kretinin, K. S. Novoselov, C. R. Woods, K. Watanabe, T, Taniguchi, A. K. Geim, J. R. Prance. Quantum Oscillation of the critical current and high field superconducting proximity in ballistic graphene. *Nature Physics* **12**, 318-322(2016).
5. C. R. Woods, F. Withers, M. J. Zhu, Y. Cao, G. Yu, A. Kozikov, M. B. Shalom, S. V. Morozov, M. Wijk, A. Fasolino, M. Katsnelson, K. Watanabe, T, Taniguchi, A. K. Geim, A. Mishchenko, K. S. Nocoselov. Macroscopic self-reorientation of interacting two-dimensional crystals. *Nature Communications* **7**, 10800(2016).
6. E. E. Vdovin, A. Mishchenko, M. T. Greenaway, M. J. Zhu, D. Ghazaryan, A. Misra, Y. Cao, S. V. Morozov, O. Makarovsky, A. Patanè, G. J. Slotman, M. I. Katsnelson, A. K. Geim, K.S. Novoselov, L. Eaves. *Physical Review Letters* **116**, 186603(2016).
7. X. Huang, T. Leng, M. J. Zhu, X. Zhang, J.-C. Chen, K.-H. Chang, M. Aqeeli, A. K. Geim, K. S. Novoselov, Z. Hu. Highly flexible and conductive printed graphene for wireless wearable communications applications. *Scientific Reports* **5**, 18298(2015).

8. M. T. Greenaway, E. E. Vdovin, A. Mishchenko, O. Makarovsky, A. Patanè, J. R. Wallbank, Y. Cao, A. V. Kretinin, M. J. Zhu, S. V. Morozov, V. I. Fal’ko, K. S. Novoselov, A. K. Geim, T. M. Fromhold, L. Eaves. Resonant tunnelling between the chiral Landau states of twisted graphene lattices. *Nature Physics* **11**, 1057-1062(2015).
9. A. Mishchenko, J. S. Tu, Y. Cao, R. V. Gorbachev, J. R. Wallbank, M. T. Greenaway, V. E. Morozov, S. V. Morozov, M. J. Zhu, S. L. Wong, F. Withers, C. R. Woods, Y. J. Kim, K. Watanabe, T. Taniguchi, E. E. Vdovin, O. Makarovsky, T. M. Fromhold, V. I. Fal'Ko, A. K. Geim, L. Eaves, K. S. Novoselov. Twist-controlled resonant tunnelling in graphene/boron nitride/graphene heterostructures. *Nature Nanotechnology* **9**, 808-813(2014).

Chapter 1

Introduction

Superconductivity is one of the most spectacular phenomena in condensed matter physics. The discovery of new materials is always accompanied by a profound question: is this material a superconductor and whether the superconductivity order could be of an unusual kind.

Since graphene was first exfoliated and characterized by Geim and Novoselov[1] in 2004 at the University of Manchester, the electronic properties of graphene have been extensively studied over the past ten years[2,3]. There have been a number of ground-breaking experimental observations such as massless Dirac fermions[4,5], half integral quantum Hall effect[4,5], Klein tunnelling[6-8], negative refractive index[9,10], fractional quantum Hall effect[11,12] and Hofstadter's butterfly[13-15]. However, graphene holds one important but not yet experimentally observed prediction: the intrinsic superconductivity[16,17], even at extremely high carrier densities[18].

Although not an intrinsic superconductor, graphene still can sustain superconductivity due to the proximity effect by bringing graphene into a contact with a superconductor. This is a direct result of the wave-like nature of the electrons. The wavefunction of Cooper pairs in the superconductor must be continuous even at the graphene-superconductor interface. Proximity induced superconductivity in graphene originates from a number of phase-coherent electron-hole states supported by a process called Andreev reflection[19]. When two superconducting electrodes are connected by a piece of graphene, a zero-voltage dissipationless supercurrent can flow through graphene, forming a superconductor-graphene-superconductor junction, namely a graphene Josephson junction. Since the first observation of bipolar supercurrents in graphene by Heersche[20] in 2007, the diffusive graphene Josephson junctions have been intensively investigated by experiments[21-31]. However, to date it is still quite challenging to fabricate high quality ballistic graphene Josephson junctions[32-37]. The low transmission probability and high disorder are believed to have prevented the emergence or observation of new physics. For instance, the chiral nature of the charge carriers (electrons and holes) in graphene is predicted to give rise to specular Andreev reflection[38,39], which is possible only if the superconducting energy gap (usually below a few meV for conventional superconducting metals or alloys) larger than the Fermi level in graphene. In addition, there is an interesting argument about injecting supercurrents into a quantum Hall regime[36,40-42]. To check this scenario, it requires graphene to enter the quantum Hall regime before the applied magnetic field breaks the superconductivity in the electrodes.

Here we demonstrate our advanced approach to ballistic graphene Josephson junctions by utilising superconducting edge contacts to high quality hexagonal boron nitride-graphene-hexagonal boron nitride heterostructures. We show that the propagation of charge carriers in the graphene Josephson junctions is ballistic. Furthermore, as niobium is a type-II superconductor with a relatively high critical field H_{c2} ~ 4T, it is possible to study the interplay between proximity induced superconductivity and the quantum Hall states in ballistic graphene.

The gapless nature in the band structure of monolayer graphene is protected by its crystal lattice symmetry[3,43]. An energy gap can be opened in graphene by breaking the lattice symmetry. In bilayer graphene, it is possible to open a gap up to 0.2 eV by applying an electric field between two graphene layers[44-46]. However, such gap rarely led to a highly insulating state as expected for same quality semiconductors even at low temperatures. We try to understand this long-standing puzzle by studying the spatial current flow in gapped graphene systems including bilayer graphene and graphene/hexagonal boron nitride superlattices.

Lacking of a band gap in monolayer graphene and intrinsic bilayer graphene results in low ON/OFF ratios of graphene based transistors, which limits their potential logical applications[47]. An energy gap can be opened in graphene by using graphene nanoribbons[48,49] or chemical derivatives[50]. However, it also has been proven difficult to achieve high ON/OFF ratios in graphene nanoribbons and chemical derivatives without degrading graphene’s electronic quality[51]. It is tempting to consider bilayer graphene with a tunable energy gap as a promising candidate for higher ON/OFF ratio transistors – but there is a long-standing argument about the topologically protected edge states in gapped bilayer graphene[52], which shunts the highly insulating bulk.

Recently, scientists at the University of Manchester have built an alternative device architecture to achieve high ON/OFF ratio in graphene – the field-effect tunnelling transistors based on quantum tunnelling from two graphene electrodes through a thin insulating barrier[51]. The use of hexagonal boron nitride as a tunnel barrier is particularly attractive owing to its large band gap (~6 eV), atomically flat surface and high breakdown field[53,54]. The tunnelling current is determined by the height and thickness of the potential barrier and the electronic density of states of graphene electrodes.

This thesis is organized as follows:

In Chapter 2, we give an overview of the background of this thesis. We start with a quick introduction of mesoscopic physics. Then we introduce the electronic properties of graphene including the band structures and principles of quantum Hall effect of monolayer and bilayer graphene, respectively. Hexagonal boron nitride is mentioned in this chapter as an excellent substrate for high quality graphene devices. We introduce the Josephson effect and Andreev reflection with a special focus on specular Andreev reflection in graphene. At last, we briefly describe the concept of quantum mechanical tunnelling.

In Chapter 3, we demonstrate our efforts to prepare high quality ballistic graphene Josephson junctions and graphene tunnelling transistors. We use the recently developed flake stacking technique, ‘dry’ transfer and van der Waals pick-up techniques, to obtain contamination-free graphene-hexagonal boron nitride heterostructures. Then we quickly describe the measurement set-up and device configuration for electrical transport measurements in graphene Josephson junctions and tunnelling transistors, respectively.

In Chapter 4, we present graphene Josephson junctions with a mean free path of several micrometers, low contact resistance and large supercurrents. Such devices exhibit pronounced Fabry-Pérot oscillations not only in the normal-state resistance but also in the critical current. The proximity effect is mostly suppressed in magnetic fields below 10 mT, showing a conventional Fraunhofer pattern. Unexpectedly, some proximity superconductivity survives even in fields higher than 1 T. Superconducting states randomly appear and disappear as a function of magnetic field and carrier concentration. We attribute the high-field Josephson effect to mesoscopic Andreev states that persist near the graphene edges.

In Chapter 5, we investigate the spatial distributions of Josephson supercurrents in gapped bilayer graphene and graphene/hexagonal boron nitride superlattices. We compare transport measurements between the Hall bar and the Corbino geometries in the normal-state of bilayer graphene. By gradually opening the gap in bilayer graphene, we find that the supercurrent at the charge neutrality point changes from uniform to such that it propagates along narrow stripes near the graphene edges. Similar stripes are found in graphene/hexagonal boron nitride superlattices. These observations are corroborated by using the 'edgeless' Corbino geometry in which case resistivity at the charge neutrality point increases exponentially with increasing the energy gap, as expected for a conventional semiconductor. This is in contrast to the Hall bar geometry where resistivity measured under similar conditions saturates to values of only about a few resistance quanta.

In Chapter 6, we demonstrate a stacking transition of bilayer graphene from an incommensurate twisted stacking state to a commensurate AB stacking state by a macroscopic graphene self-rotation. This structural transition is driven by van der Waals interaction energy of two graphene layers and is thermally activated by unpinning the chemical adsorbents which are then removed by the self-cleaning of graphene. The structural transition is detected by using graphene tunnelling transistors and Raman spectroscopy mapping of twisted bilayer graphene before and after thermal annealing.

In Chapter 7, we present our observation of a series of sharp resonant features in the differential conductance of graphene tunnelling transistors over a wide range of bias voltages between 10 and 200 mV. We attribute them to electron tunnelling assisted by the emission of phonons of well-defined energies. The phonon energies corresponding to the resonances are compared with the lattice dispersion curves of graphene-hexagonal boron nitride heterostructures and are close to peaks in the single phonon density of states.

In Chapter 8, we make a short summary based on our experimental results in this thesis. Then we speculate further works including supercurrents in the quantum Hall regime of graphene and using graphene-hexagonal boron nitride resonant tunnelling diodes as high-frequency oscillators.

Chapter 2

Overview

2.1 Mesoscopic physics

2.1.1 Characteristic length scales

Our typical graphene devices have dimensions from hundreds of nanometres to tens of micrometres. For systems of this size, quantum effects and fluctuations cannot be ignored and cannot be treated as classical conductors because the dimensionality of the devices are small enough to be comparable to or even less than the characteristic lengths such as phase coherence length and mean free path of the electrons. On the other hand, they are also too large for the full quantum mechanical treatment as they consist of thousands of carbon atoms. This intermediate size range between microscopic and macroscopic scale is called mesoscopic[55], where some classical laws can be applied safely and the quantum mechanics must be used as well. Mesoscopic systems demonstrate a number of intriguing physics. For instance, conductance quantization has been studied in quantum point contacts, whereas weak localization has been investigated in the diffusive transport regime.

The Fermi wavelength

$$\lambda_F = 2\pi/k_F \tag{2.1}$$

is nothing but the de Broglie wavelength of electrons near the Fermi level, where the Fermi wave vector k_F is related to the momentum by $p = \hbar k_F$. The Fermi energy is $E_F = \hbar^2 k_F^2/2m^*$ for massive non-relativistic particles and $E_F = \hbar k_F v_F$ for massless Dirac fermions in graphene, where $\hbar$ the reduced Planck constant, v_F the Fermi velocity and m^* the effective mass.

The mean free path l_m is the average length that an electron travels before being scattered by a scattering centre. Because only electrons near the Fermi level contribute to the electrical transport, we have

$$l_m = v_F \tau, \tag{2.2}$$

where τ is the relaxation time. In mesoscopic systems, if the size of the device L is larger than l_m the electrical transport is diffusive. If l_m is larger than L the transport is in the ballistic regime and the electrons experience zero or few scattering events inside of the conductor. For ballistic transport, the device boundary plays an important role for scattering instead of the impurities.

The phase coherence length l_φ is the length scale over which an electron can maintain its phase coherence. l_φ is bounded by for instance the inelastic scattering length. Elastic scattering does not modify the phase coherence so that quantum effects of electrons interference can be observed in both ballistic and diffusive systems. For the ballistic regime,

$$l_\varphi = v_F \tau_\varphi, \tag{2.3}$$

where τ_φ is the phase relaxation time.

For the diffusive regime,

$$l_\varphi = \sqrt{D\tau_\varphi}, \tag{2.4}$$

where D is the diffusion constant given by $D = v_F^2\tau/2 = v_F l_m/2$ for two-dimensional systems.

The coherence length l_φ defines the length scale of the interference of the wavefunction of a single electron state. At finite temperatures, thermal averaging occurs over an energy scale of k_BT. Electrons with an energy difference of k_BT will lose their phase coherence after a time interval of the order of $\hbar/k_BT$. This corresponds to a length scale of

$$l_T = \sqrt{D\hbar/k_BT}, \tag{2.5}$$

which is known as the thermal length or the Thouless length. For a system of finite size L, we can define an energy scale named the Thouless energy $E_{Th} = D\hbar/L^2$. Two electron states with close energies are correlated unless the energy difference is larger than E_{Th} and then they can be considered as two independent states. If $l_T > l_\varphi$, the dominant dephasing properties are defined by l_φ. On the other hand, if $l_\varphi > l_T$, the primary dephasing is due to thermal fluctuations.

2.1.2 Ballistic transport and Landauer formula

For an ideal conductor, there is no scattering inside the conductor and therefore the resistance should be zero. However, the resistance from the interface between the conductor and the conducting pads is non-zero due to the mismatch of modes of the conductor and the contact pads.

In a ballistic conductor, the electrons entering the conductor from one side will transport to the other side without any scattering. For each band, the net current from one side to the other side when one applies a voltage difference V across the conductor is

$$I = (2e/h)\int_{-\infty}^{\infty} dE[f(E - eV) - f(E)], \tag{2.6}$$

where $f(E) = 1/(e^{(E-\mu)/k_BT} + 1)$ is the Fermi-Dirac distribution function (here, μ is the chemical potential).

At zero temperature $T = 0$,

$$I = (2e^2/h)V. \tag{2.7}$$

Therefore, the conductance of a ballistic conductor that has M sub-bands (one-dimensional channels) at zero temperature is

$$G = I/V = M(2e^2/h), \tag{2.8}$$

which means the conductance will be a multiple of $2e^2/h$ and independent of the device length L.

In realistic experiments of systems with multiple sub-bands, there is a certain probability R that an electron entering the conductor will be reflected and a probability T that it will be transmitted. These two probabilities obey a simple relation that $R + T = 1$. Here, we assume the transmission probability is the same for all the sub-bands. Thus, the conductance of a ballistic system can be written as

$$G = MT(2e^2/h). \tag{2.9}$$

This formula is known as the two-terminal Landauer formula[56], which takes the transmission probability T at two contacts into account.

2.1.3 Conductance quantization

Two pieces of high mobility two-dimensional electron gas (2DEG) can be separated by a ballistic quantum point contact (QPC) which is a short and narrow constriction with a width W of the order of the Fermi wavelength but smaller than the electron mean free path: $W \sim \lambda_F < l_m$. This condition can be achieved by depleting the 2DEG using split-gates, as depicted in Fig. 2.1(a). Such a QPC constitutes a potential well for the electrons in the 2DEG, resulting in a one-dimensional (1D) system when only one sub-band of this potential well is filled. Such a sub-band is referred to as a mode. The number of modes for a square potential well is

$$N = int[2W/\lambda_F]. \tag{2.10}$$

The conductance through a QPC quantized in units of $2e^2/h \approx 13\mathrm{k}\Omega$ was observed by two independent groups in 1988[57,58], as shown in Fig. 2.1(b). The quantum conductance per transmission channel is e^2/h and the factor 2 comes from the spin degeneracy of the electron. Each mode therefore contributes $2e^2/h$ to the conductance so that the total conductance through a QPC is

$$G = N(2e^2/h). \tag{2.11}$$

The ballistic nature assures that backscattering processes do not affect the conductance through a QPC. With increasing width of the constriction, the energy separation between the modes becomes smaller and the quantum effect smears. In this case the conductance is referred as the Sharvin conductance limit[59] for a ballistic 2D conductor:

$$G = (2W/\lambda_F)(2e^2/h). \tag{2.12}$$

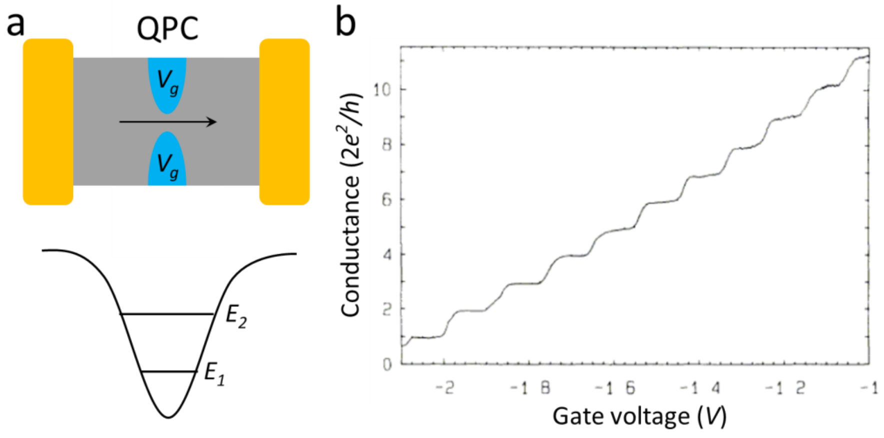

Fig. 2.1 Quantum point contact and conductance quantization

(a) Schematics of a QPC from a top view (top) and the sub-band energy spacing (bottom). Electrical contacts and the 2DEG are represented by yellow and grey areas, respectively. Two blue zones on top of the 2DEG demonstrate the split-gates. Black arrow shows only a single mode is allowed to propagate through the constriction. **(b)** Quantized conductance of $\boldsymbol{G = N(2e^2/h)}$ through a QPC. Fig. 2.1(b) is adapted from ref.[57].

2.1.4 Weak localization

In a diffusive regime with $l_m < L < l_\varphi$, an electron moving in a conductor experiences elastic scattering as $l_m < L$ but still maintains its phase coherence due to $L < l_\varphi$. There are many interesting phenomena in this regime. One important example is weak localization (WL). There are many paths for electrons to go between two positions r and r' within a conductor. In addition, there is possibility for an electron to return to the same position r, as depicted in Fig. 2.2(a). The probability of an electron propagating from position r to position r' during a time scale of t is

$$P(r,r',t) = \left|\sum_i A_i\right|^2 = \sum_i |A_i|^2 + \sum_{i\neq j} A_i A_j^*, \tag{2.13}$$

where A_i is the probability for each single trajectory i between r and r'. The first term corresponds to the classical diffusion probability, while the second term describes the quantum interference contribution. If positions r and r' are different, then the phase difference is irrelevant over all trajectories. However, if positions r and r' are the same, $P(r,r',t)$ will describe all closed loop trajectories. At zero magnetic field, the time-reversal invariance implies that A^+, A^- (for clockwise and counter clockwise propagating, respectively) are the same $A^{+} = A^{-} = A$. Thus, the probability of returning to position *r* during a time *t* is

$$P(r, r, t) = |A^{+} + A^{-}|^{2} = 4|A|^{2}. \tag{2.14}$$

The interference between these paths leads to enhanced resistance, which is known as weak localization.

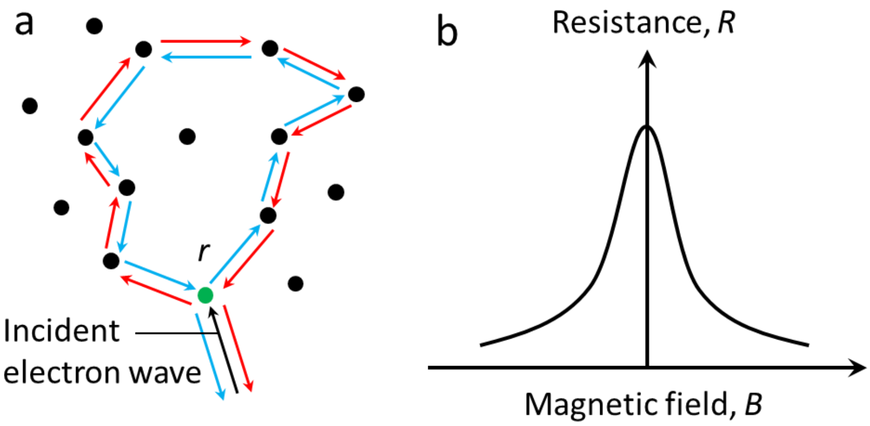

Fig. 2.2 Weak localization and negative magneto-resistance

(a) An electron travels from position r and returns to position r. For each path, there is a reverse path, as shown in blue and red arrows. **(b)** The weak localization effect is partially destroyed if a magnetic field is applied perpendicular to the 2DEG. As a result, a negative magneto-resistance appears with a peak centered at zero magnetic field.

WL can be supressed by applying a small perpendicular magnetic field *B*. A magnetic field breaks the time reversal symmetry of such paths $A^{+} \neq A^{-}$, and causes the two reverse paths to diverge, hence reducing the quantum interference. When a magnetic field is applied, the phase difference acquired between the clockwise and counter clockwise path is

$$\varphi = 2\pi\Phi/\Phi_0, \tag{2.15}$$

where Φ is the magnetic flux threading into the enclosed area and $\Phi_0 = h/2e$ the magnetic flux quantum. By estimating the magnetic field at which the WL is reduced by a factor of two: $B_c \sim h/(el_{\varphi}^{2})$, one can thus determine the phase coherence length l_{φ}. This can be done by measuring the amplitude of the WL correction and the critical magnetic field at which this correction has decayed by a factor of 2[60].

2.2 Electronic properties of graphene

2.2.1 Monolayer graphene

Monolayer graphene (MLG) consists of a single planar honeycomb net of carbon atoms. The hexagonal crystal lattice is schematically shown in Fig. 2.3(a), where each carbon atom has three nearest neighbours in the plane and four valence electrons. The Bravais lattice is triangular, with the lattice vectors:

$$\vec{a}_{1,2} = \left(3a/2,\ \pm\sqrt{3}a/2\right), \tag{2.16}$$

where $a \approx 1.42$ Å is the nearest-neighbour distance.

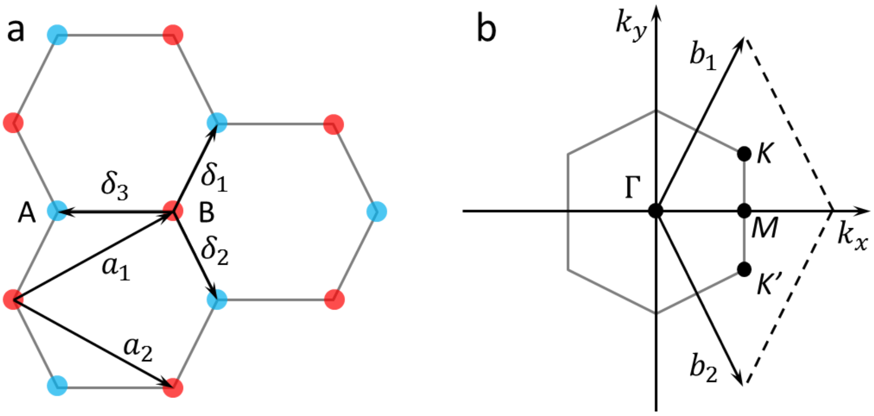

Fig. 2.3 Crystal lattice and reciprocal lattice of monolayer graphene

(a) Honeycomb lattice of MLG. Sublattice A and B are shown as blue and red, respectively. **(b)** Reciprocal lattice vectors and several special high-symmetry points in the first Brillouin zone of MLG.

The honeycomb lattice of graphene contains two atoms per elementary cell. They belong to two sublattices, A and B. The three nearest-neighbour vectors are

$$\vec{\delta}_{1,2} = \left(a/2,\ \pm\sqrt{3}a/2\right), \vec{\delta}_3 = (-a,\ \ 0). \tag{2.17}$$

The reciprocal lattice is also triangular, with the lattice vectors:

$$\vec{b}_{1,2} = \left(2\pi/3a,\ \pm 2\sqrt{3}\pi/3a\right). \tag{2.18}$$

Fig. 2.3(b) describes the first Brillouin zone and several special high-symmetry points, K, K' and M, with the wave vectors:

$$\vec{K} = \left(2\pi/3a, 2\pi/3\sqrt{3}a\right), \vec{K}' = \left(2\pi/3a, -2\pi/3\sqrt{3}a\right), \vec{M} = (2\pi/3a, 0). \quad (2.19)$$

The basic electronic structure of graphene was first calculated by Wallace[61] in 1947 based on the above honeycomb lattice. He pointed out that the spacing of the planes of graphite, 3.37 Å, is so large compared with the nearest-neighbour distance 1.42 Å so that useful calculations of graphite can neglect interaction between different planes. Wallace also pointed out that of the four valence electrons three are involved in the sp^2 trigonal bonding and played no role in the conduction bands of interest. One needs to consider only bands arising from one $2p_z$ electron per atom. Essentially, Wallace used the tight-binding theory to treat the band of energies formed by the $2p_z$ electrons of carbon in graphene. In the nearest-neighbour approximation, there are no hopping processes within the sublattice A and B; hopping occurs only between them. For arbitrary wave vector $\vec{k}$, from the tight-binding approximation we can get the energy dispersion of graphene:

$$E_{\pm}(\vec{k}) = \pm\gamma\sqrt{3 + 2\cos\left(\sqrt{3}k_y a\right) + 4\cos\left(\sqrt{3}k_y a/2\right)\cos(3k_x a/2)}, \quad (2.20)$$

where γ=2.8 eV is the nearest-neighbour hopping energy (hopping between different sublattices A and B).

After taking the next-nearest-neighbour hopping parameter γ' (hopping in the same sublattice), one can find the energies instead of Eq. (2.20),

$$E_{\pm}(\vec{k}) = \pm\gamma\sqrt{3 + 2\cos\left(\sqrt{3}k_y a\right) + 4\cos\left(\sqrt{3}k_y a/2\right)\cos(3k_x a/2)}$$

$$+\gamma'(2\cos\left(\sqrt{3}k_y a\right) + 4\cos\left(\sqrt{3}k_y a/2\right)\cos(3k_x a/2)). \quad (2.21)$$

It is clear from Eq. (2.21) that the energy spectrum is symmetric around the zero energy if $\gamma' = 0$. The finite γ' breaks the electron-hole symmetry, shifting the conical point from $E = 0$ to $E = -3\gamma'$ and hence the π and π^* bands become asymmetric. However, it will not change the behavior of the Hamiltonian near the conical points. Fig. 2.4 shows the full band structure of graphene with a zoomed in image of the band structure close to one of the conical points (the K or K' point in the Brillouin zone, as shown in Fig. 2.3(b)). This linear dispersion can be obtained by expanding the full energy band structure in Eq. (2.20) close to the conical points K (or K'):

$$E_{\pm}(q) = \pm v_F |q|, \tag{2.22}$$

where q is the momentum to the conical points and v_F is the Fermi velocity, with a value of $v_F \approx 1.0 \times 10^6$ m/s. The result was first obtained by Wallace[61].

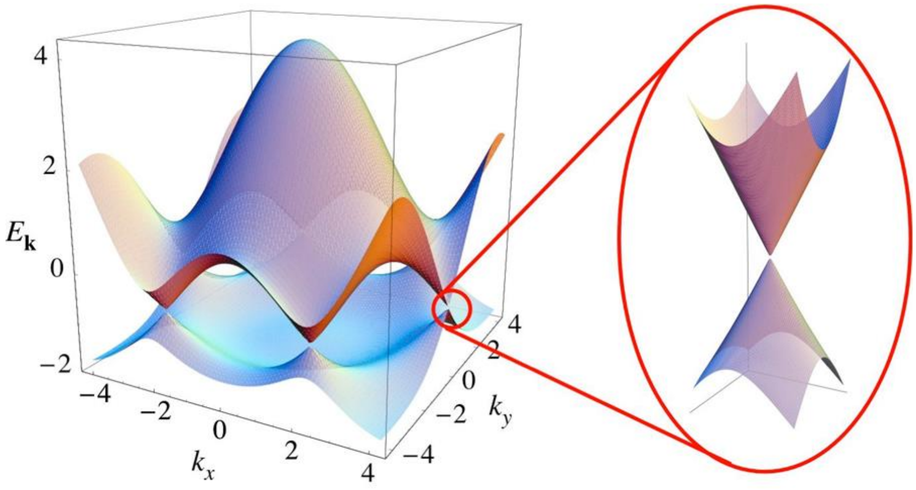

Fig. 2.4 The electronic energy spectrum of monolayer graphene

The calculated energy spectrum of MLG from the tight binding model, showing a linear dispersion at the low energy scale. Fig. 2.4 is adapted from ref.[3].

As shown in Fig. 2.4, graphene exhibits a linear low-energy dispersion with the conduction band and the valence band touching at the conical points. For undoped graphene, the valence band is completely filled and the conduction band is empty. These conical K and K' points are known as Dirac points. In the nearby energy regions the following linear dispersion relation for electron (e) and hole (h) states is found:

$$E_{e,h} = \pm \hbar v_F |k|, \tag{2.23}$$

where $\hbar$ the reduced Planck constant. It is very important to mention here that the gapless state with the Dirac point is symmetry protected[43]. The evidence is based on the consideration of two symmetry operations: time reversal symmetry and inversion symmetry. In principle, a perturbation that is invariant under time reversal and inversion symmetry can shift the Dirac point, but cannot open the band gap. If the sublattices A and B are no longer equivalent, then the inversion symmetry is broken, the mass term naturally appears, and the gap opens.

Because of its 2D nature, the carrier density n in graphene is relatively low and can be easily tuned by electrostatic gating[1,2]. We fabricate graphene field-effect devices on a silicon wafer with silicon oxide layer (SiO_2/Si). Applying a back gate voltage to the conducting Si substrate allows opposite charged carriers to accumulation at the graphene-SiO_2 interface. Thus, the Fermi level in graphene can be tuned into the conduction band (electron, n-type doping) or the valence band (hole, p-type doping). At the Dirac point, the carrier density in graphene is close to zero and the electronic density of states (DoS) almost vanishes, resulting in a large resistivity peak, as shown in Fig. 2.5(b). However, it is experimentally difficult to explore the physics in the vicinity of the Dirac point due to the existing electron-hole puddles, especially for low quality graphene on silicon wafers. By using commercial standard Si/SiO_2 wafers, the achievable carrier density in graphene is of the order of 10^{12} cm^{-2}, which corresponds to a change of the Fermi level $E_F = \pm\hbar v_F\sqrt{\pi|n|}$~±0.3 eV relative to the Dirac point.

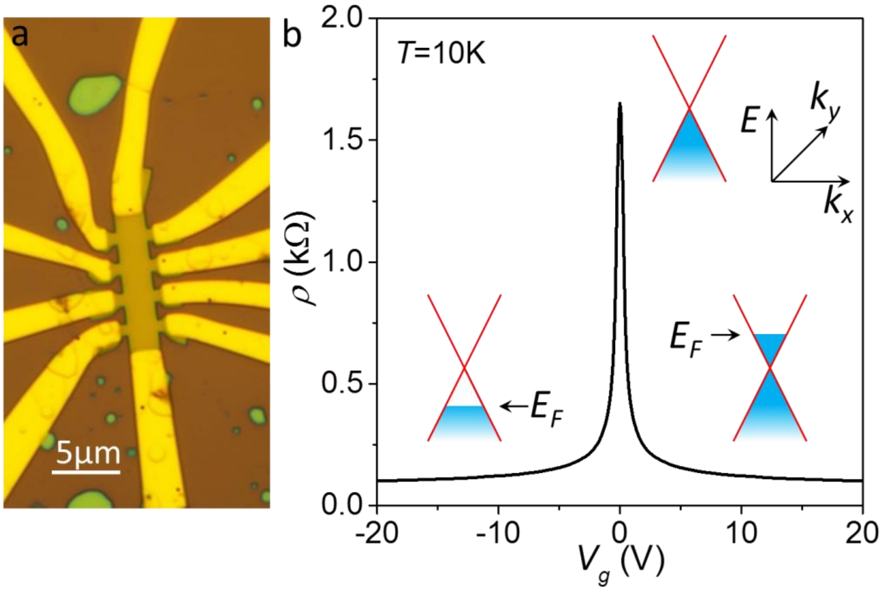

Fig. 2.5 Ambipolar electric field effect in monolayer graphene device

(a) Optical microscopy image of a graphene Hall bar device on top of a silicon wafer with 290nm SiO_2. **(b)** Measured resistivity of graphene as a function of applied gate voltage at 10K. The insets show the low-energy spectrum of holes (left), the Dirac point (middle), and electrons (right).

2.2.2 Bilayer graphene

Following the same mechanical exfoliation technique for producing MLG, one can also obtain different layers of graphene. Bilayer graphene (BLG) is especially interesting because the integral quantum Hall effect shows anomalies, different both from MLG and from conventional 2DEGs[62,63]. Furthermore, BLG exhibits a tunable gap up to a few hundred meV, which makes it potentially interesting for realistic applications[44-46].

The crystal lattice structure of BLG is schematically shown in Fig. 2.6(a). The same as for three-dimensional graphite, the second layer is rotated by 60° relative to the first layer, which is known as AB stacking or Bernal stacking. Thus, the sublattice A in one layer sits exactly on top of the other layer.

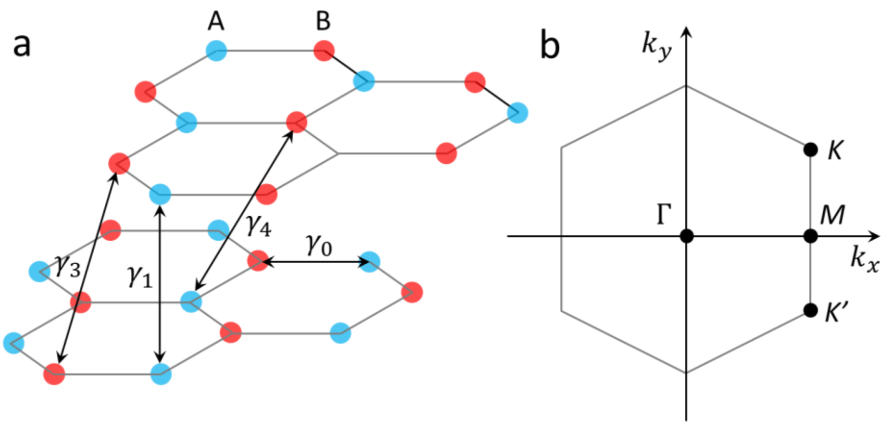

Fig. 2.6 Crystal lattice and reciprocal lattice of bilayer graphene

(a) The crystal structure of BLG with different hopping parameters. **(b)** The reciprocal lattice of BLG and several special high-symmetry points in the first Brillouin zone.

Apart from the nearest-neighbour hopping parameter $\gamma_0 = \gamma \approx$2.8eV in MLG, a substantial hopping between two sublattices A in two layers is expected as a result of the overlapping of the out-of-plane π orbitals, denoted by the hopping parameter $\gamma_1 \approx$0.4eV. The energy spectrum of BLG is shown in Fig. 2.7(a). The conduction and valence band touch at the point *K* and *K'*. Near these two points,

$$E_{1,2}(k) \approx \pm \hbar^2 k^2/(2m^*), \tag{2.24}$$

where $m^* = |\gamma_1|/(2v_F^2) \approx 0.03 m_e$ is the effective mass (m_e is the mass of a free electron)[64]. From the band structure, we can see that BLG is also a gapless semiconductor but with a parabolic-like band touching, which indicates the charge carriers near the Dirac point in BLG are massive Dirac fermions instead of massless in the monolayer case. Two other energy branches $E_{3,4}(k)$ are separated by a gap of $2\gamma_1 \approx 0.8$ eV, which are irrelevant for the low-energy physics of graphene we discuss in this thesis.

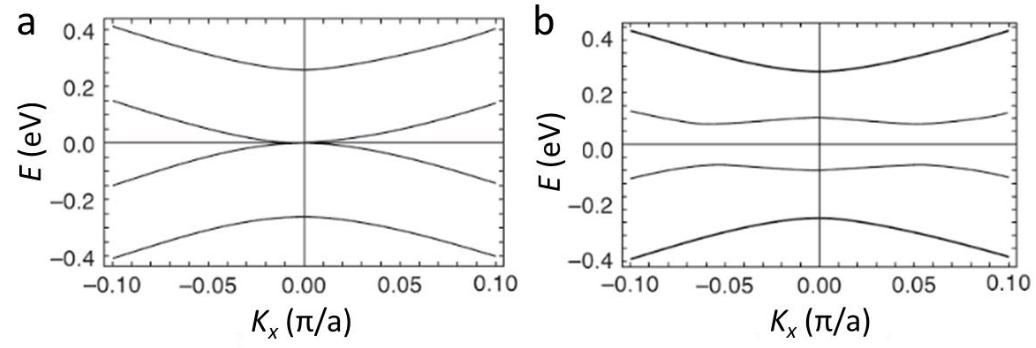

Fig. 2.7 Calculated band structure of bilayer graphene

(a) Without any bias the conduction and valence bands of BLG meet at the *K* points, similar to MLG but the dispersion relation in BLG is now parabolic instead of linear as in MLG. Two higher energy bands separated by an energy band gap of ~0.8eV are also shown. **(b)** A band gap is opened in BLG by applying a perpendicular bias to the two graphene layers. The 'Mexican hat' dispersion is also visible. Fig. 2.7 is adapted from ref.[43]

Note that the above discussions are based on an intrinsic bilayer system without any potential bias between the two graphene layers. The equivalence of two layers, namely the inversion symmetry of BLG, can be broken by applying a bias voltage V perpendicular to the graphene layers. The broken inversion symmetry gives rise to the band structure as shown in Fig. 2.7(b), and to the opening of a gap in the energy spectrum. For small momentum and $V \ll \gamma$, in the vicinity of K (or K') point , the energy spectrum has the so called 'Mexican hat' dispersion[43]:

$$E(k) = \pm(V/2 - V\hbar^2 v_F^2 k^2/\gamma_1^2 + \hbar^4 v_F^4 k^4/\gamma_1^2 V), \tag{2.25}$$

where we assume that $\hbar v_F k \ll V \ll \gamma_1$. Eq. (2.25) results in an energy maximum at k=0 and two energy minimum at $k = V/\sqrt{2}\hbar v_F$, as shown in Fig. 2.7(b). The band gap opening in BLG has been experimentally confirmed by electrical transport[45] and infrared microspectroscopy[46]. Furthermore, the size of gap in BLG is tunable by adjusting the amplitude of the bias between two graphene layers[46].

The opportunity to open a tunable gap makes BLG very interesting for potential applications, for example the realization of graphene based field-effect transistors (FET) with high ON/OFF ratios[47].

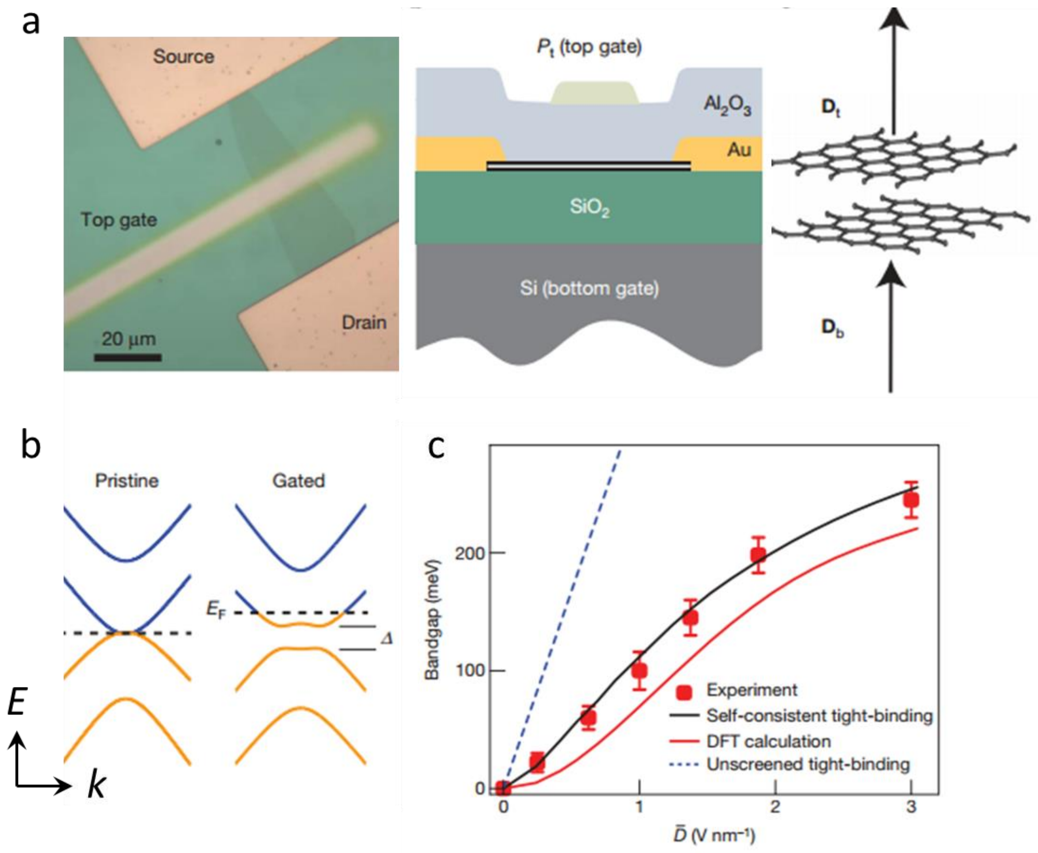

Fig. 2.8 Band gap opening in a dual-gated bilayer graphene device

(a) Optical micrograph of a BLG device (left). Schematics of the cross-sectional side view of BLG device (middle). Illustration showing gate voltage inducing top (D_t) and bottom (D_b) electrical displacement fields (right). **(b)** The band structure of pristine (left) and gated (right) BLG. In the latter case, a band gap Δ is opened in BLG. **(c)** Band gap dependence on the electrical displacement field. Fig. 2.8 is adapted from ref.[46].

2.2.3 Quantum Hall effect in graphene

The quantum Hall effect (QHE) is a fascinating quantum mechanical phenomenon that occurs in high mobility 2DEG systems. When the electrons in a 2DEG are subjected to strong perpendicular magnetic fields and low temperatures, its Hall conductance σ_{xy} undergoes certain transitions and becomes a quantized value:

$$\sigma_{xy} = \nu e^2/h, \tag{2.26}$$

where e the elementary charge and h the Planck's constant. The pre-factor ν is known as the filling factor, which can take on either integer (ν =1, 2, 3…) or fractional values (ν =1/3, 2/5, 3/7…). Depending on whether ν is an integer or a fraction, the QHE is referred to the integer QHE (IQHE) or fractional QHE (FQHE), respectively. In this section, we limit our discussion to the IQHE.

The QHE was first discovered by K. von Klitzing in the 1980s, working at the high magnetic field laboratory in Grenoble with silicon-based metal-oxide-semiconductor field-effect transistors (MOSFETs)[65]. After that, most QHE experiments were performed on high quality semiconductor heterostructures, particularly on gallium arsenide/aluminium gallium arsenide (GaAs/AlGaAs). Graphene is the first real 2D material whose electrons behave as massless Dirac fermions, as opposed to massive Schrödinger fermions in conventional semiconductors. Thus, the QHE in graphene has become one of the most intense research topics in the last ten years[4,5,11-15,62,66,67].

Let us consider a 2DEG under a perpendicular magnetic field *B*, as illustrated in Fig. 2.9(a). The energy spectrum:

$$E_n = \hbar\omega_c(n + 1/2), n = 0, 1, 2, 3 \ldots \tag{2.27}$$

describes the discrete energy levels of non-relativistic Schrödinger fermions in a magnetic field, where $\omega_c = eB/m^*$ is the cyclotron frequency determined by the field B and the effective mass m^*. Such discrete energy levels are known as Landau levels[68]. As shown by Eq. (2.27), for non-relativistic fermions the energy of Landau level is linear with magnetic field B and there is no zero energy state ($E_n = \frac{1}{2}\hbar\omega_c$ when n=0). However, these two properties of Landau levels are significantly different for massless Dirac fermions in MLG graphene, which will be shown in the following.

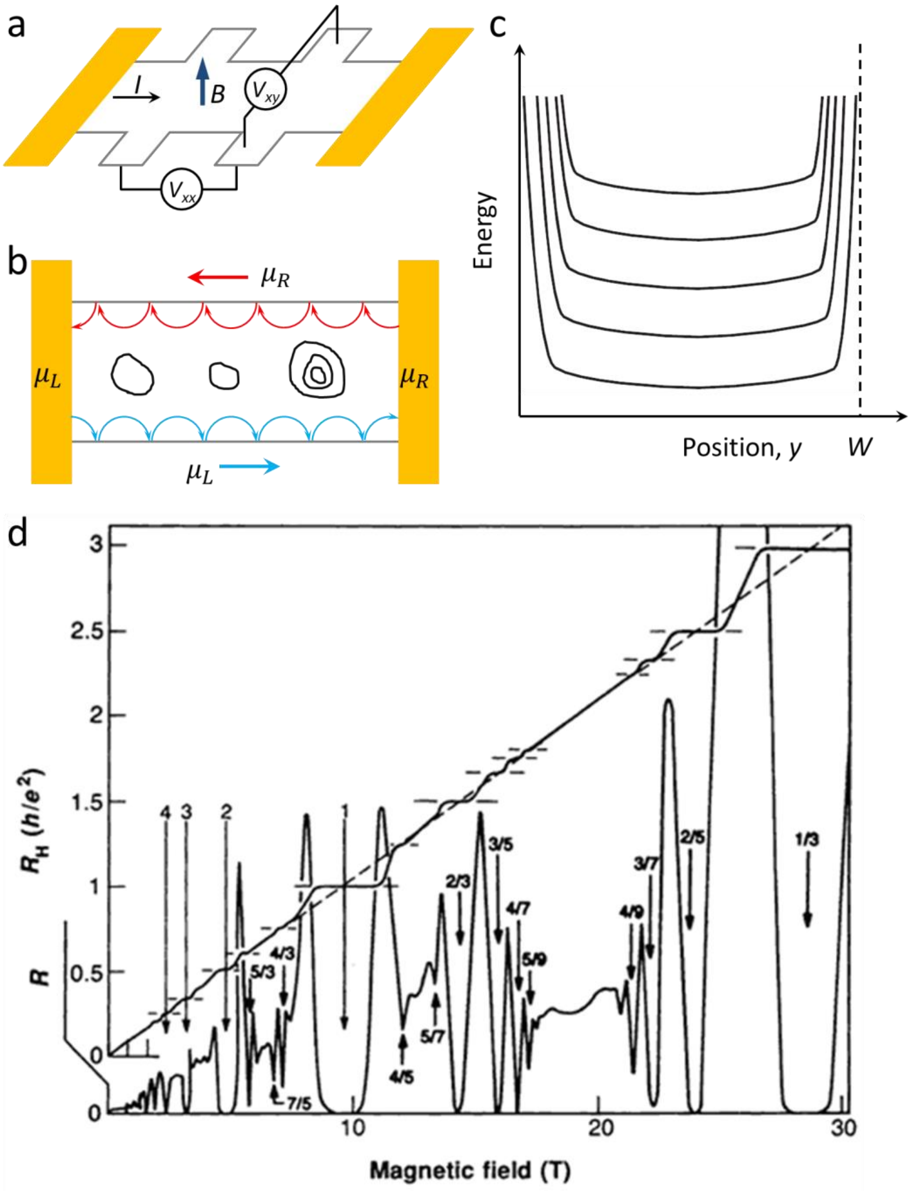

Fig. 2.9 Quantum Hall effect

(a) Schematics of a 2DEG device of Hall bar geometry with four-terminal measurement configuration under a perpendicular magnetic field *B*. **(b)** Conducting states along the edges and localized states in the bulk. **(c)** Landau levels as a function of distance along width direction from one edge to the other. The confining potential at the edges causes the Landau levels to rise up in energies. **(d)** Typical signatures of the QHE. Each plateau in the Hall resistance (R_H) is accompanied by a vanishing longitudinal resistance (R_{xx}). The dashed line indicates the classical Hall resistance, which is linear to increased magnetic field. The numbers label the plateaus. The integers denote the IQHE and fractions indicate the FQHE. Fig. 2.9(d) is adapted from ref.[69].

In a quantum Hall system there is an important property known as the degeneracy, which represents how many electrons can squeeze into a Landau level. If one takes spin and valley degeneracies of the electrons into account, the number of states that each Landau level can hold is $g_s g_v n_B$, where $n_B = eB/h$ implies the number of possible states for the momentum in the x-direction p_x. Another important index describing the number of filled Landau levels is called the filling factor, which is defined by a dimensionless quantity $\nu = n_e/n_B$ (n_e is the carrier concentration).

One assumption often made in the description of Landau levels is that the sample size is infinite. However, a real sample has finite size and, therefore, the electrons are subjected to a confining potential at the sample edges, which causes the energy of the Landau levels to rise, see in Fig. 2.9(c). Thus, we can divide a quantum hall system into two parts, one for the bulk and the other for the edge.

Due to existing of disorders in the bulk region which induces a spatially-vary potential, the states in a Landau level in the bulk are not completely degenerate, resulting in broadened Landau levels. If the Fermi level is much lower than a half-filled Landau level, the electrons in the bulk are localized and form islands across the device with a gapped region in between, as depicted in Fig. 2.9(b). As a result, the bulk becomes insulting since the localized electrons cannot propagate from one lead to the other. If the Fermi level is gradually increased to close to a half-filled Landau level, the formed islands becomes bigger and start to connect to others. As a result, the bulk becomes conductive since now there are conducting pathways for electrons to transport through the sample. The above processes occur repeatedly when the Fermi level is tuned form one Landau level to the next.

Under perpendicular B, the electrons along one edge propagate in a skipping orbit fashion, as shown in Fig. 2.9(b). This prevents electrons moving along the edge from back scattering if the Fermi level is much less than a half-filled Landau level. Therefore, the longitudinal resistance (R_{xx}) is zero because there is no voltage drop along the direction of applied current. As the Fermi level is increased to close to a half-filled Landau level, it is possible for electrons, propagating along one edge, to back scatter as they can now travel to the opposite side through the conductive bulk. As a result, R_{xx} becomes finite. The oscillation phenomenon in R_{xx} under magnetic field is known as the Shubnikov-de-Haas oscillations.

Now we turn to the behavior of R_{xy}. When the Fermi energy is tuned between two Landau levels, the bulk becomes insulating and electrons propagate only along the edge. Since the backscattering is supressed, electron entering edge states from the left contact and the right contact will maintain their electrochemical potential at μ_L and μ_R, respectively, as shown in Fig. 2.9(b). According to the Landauer-Buttiker formalism[56], electrons moving in a 1D edge channel will have a quantized conductance of $Mg_s g_v e^2/h$, where M is the number of the modes that equals to the number of Landau levels below the Fermi level. Hence, the net current from the left contact to the right contact is

$$I = Mg_s g_v (e^2/h)(\mu_L - \mu_R)/e = \nu(e^2/h)V_{xy} \qquad (2.28)$$

and the Hall conductance σ_{xy} now can be written as

$$\sigma_{xy} = I/V_{xy} = \nu e^2/h. \qquad (2.29)$$

The quantized plateaus in Hall conductance require the presence of disorder in the bulk. As the Fermi level is increased away from a completely filled Landau level, the injected electrons will enter the bulk and will be localized in the bulk. Therefore, they do not contribute to the conductance. As a result, the Hall conductance stays constant as the Fermi level is tuned between two fully occupied Landau levels and shows up as a plateau in the quantum Hall regime. As the Fermi level is further increased to reach the centre of the Landau level (half-filled Landau level), electrons in the bulk can now propagate across the sample and can be backscattered along the edges. As a result, the value of Hall conductance will increase and then approach a new plateau. Typical signatures of the QHE (including IQHE and FQHE) are represented in Fig. 2.9(d).

Due to the chiral and massless nature of carriers in MLG, the QHE in MLG is significantly different to non-relativistic electrons in the conventional 2DEG. The Landau levels energies of MLG can be written as[43]

$$E_n = \pm\hbar\omega_c\sqrt{n}, \qquad (2.30)$$

where $\omega_c = \sqrt{2\hbar v_F^2 |e| B}$ and $n = 0, 1, 2 \ldots.$

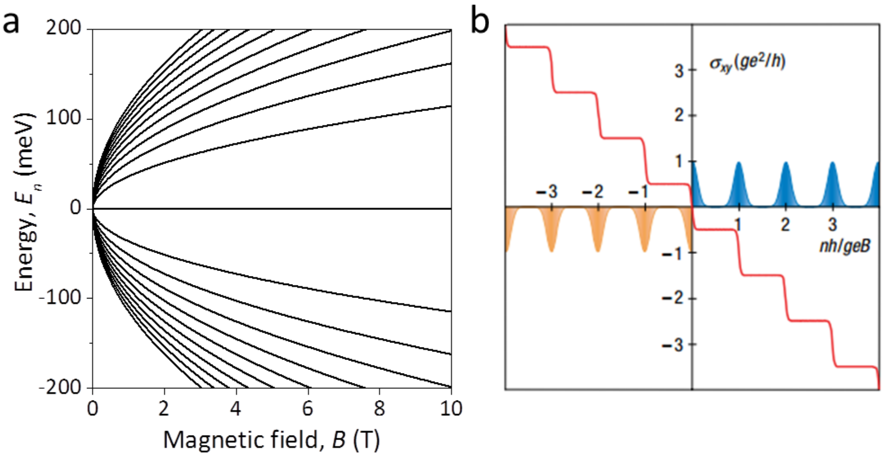

Fig. 2.10 Quantum Hall effect in monolayer graphene

(a) A graph depicting the Landau levels in MLG. Energy as a function of magnetic field, *B*. **(b)** Schematic demonstration of quantized Hall conductance in MLG. Blue (electrons) and orange (holes) shows the number of Landau levels as a function of carrier concentrations. Fig. 2.10(b) is adapted from ref.[62].

The differences between the Landau levels in MLG (as shown in Fig. 2.10) and non-relativistic electrons in a conventional 2DEG are significant. Firstly, the energy of Landau levels in MLG is proportional to $\sqrt{B}$ and $\sqrt{n}$ instead of B and n. Secondly, the Landau levels in MLG have both positive and negative energies depending on the carrier types. Most importantly, there exists the zero-energy Landau level, which results in a unique half-integer QHE phenomenon in MLG, as the consequence of the electron-hole symmetry in MLG. The total degeneracy of each Landau level is four, two from the spin degeneracy and two from the valley degeneracy. Thus, the quantized plateaus of Hall conductance in MLG occur at

$$\sigma_{xy} = 4(n + 1/2)(e^2/h), n \in Z. \tag{2.31}$$

Note that the filling factors $\nu = -2$ and $\nu = 2$ correspond to the emptying and filling of the zero-energy Landau level. Since the Landau levels of MLG are proportional to $\sqrt{n}$ and are unevenly spaced in energy, and according to the Fermi level of MLG $E_F = \pm\hbar v_F\sqrt{\pi|n_{e,h}|}$, the Landau levels are evenly spaced with varying carrier density $n_{e,h}$, as shown in Fig. 2.10(b).

The QHE in MLG was first predicted theoretically[70], and then observed experimentally by two research groups independently[4,5].

For the case of BLG, the Landau levels are[43]

$$E_n = \pm\hbar\omega_c\sqrt{n(n-1)}, \tag{2.32}$$

with $\omega_c = eB/m^*$. $E_n^+$and E_n^- are assigned to electron and hole states, respectively. Note that the energy of Landau levels in BLG depends linearly on magnetic field, which is the same as the non-relativistic case, as shown in Fig. 2.11.

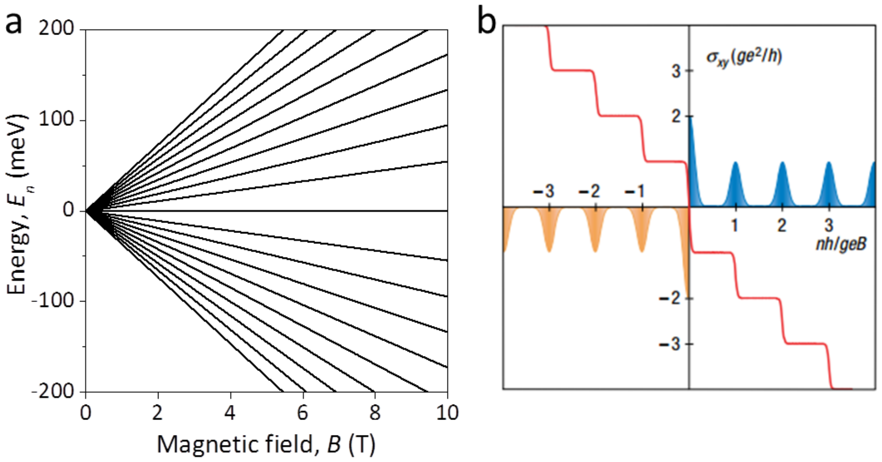

Fig. 2.11 Quantum Hall effect in bilayer graphene

(a) A graph depicting the Landau levels in BLG. Energy as a function of magnetic field, *B*. **(b)** Schematic demonstration of quantized Hall conductance in BLG for the case of $V = 0$. Blue (electrons) and orange (holes) shows the number of Landau levels as a function of carrier concentrations. Fig. 2.11(b) is adapted from ref.[62].

Similar to MLG, each non-zero Landau level contains four degenerate states, caused by the spin and pseudospin degeneracy, while for the E=0 state, the degeneracy doubles because of the orbital degeneracy n=0, or n=1. The zero-energy Landau level therefore contains an eight-fold degeneracy. Consequently, the quantum Hall plateaus occur at filling factors $\nu = 4n$ where n is non-zero integer:

$$\sigma_{xy} = 4n(e^2/h), n \in Z, n \neq 0. \tag{2.33}$$

The QHE in BLG was first predicted by theorists[63], and then observed experimentally by a research group at the University Manchester[62].

2.2.4 Graphene on hexagonal boron nitride

Hexagonal boron nitride (hBN) has a layered structure, as shown in Fig. 2.12, very similar to graphite. Within each layer, boron and nitrogen atoms are bounded by strong covalent bonds, whereas the layers are held together by weak van der Waals force.

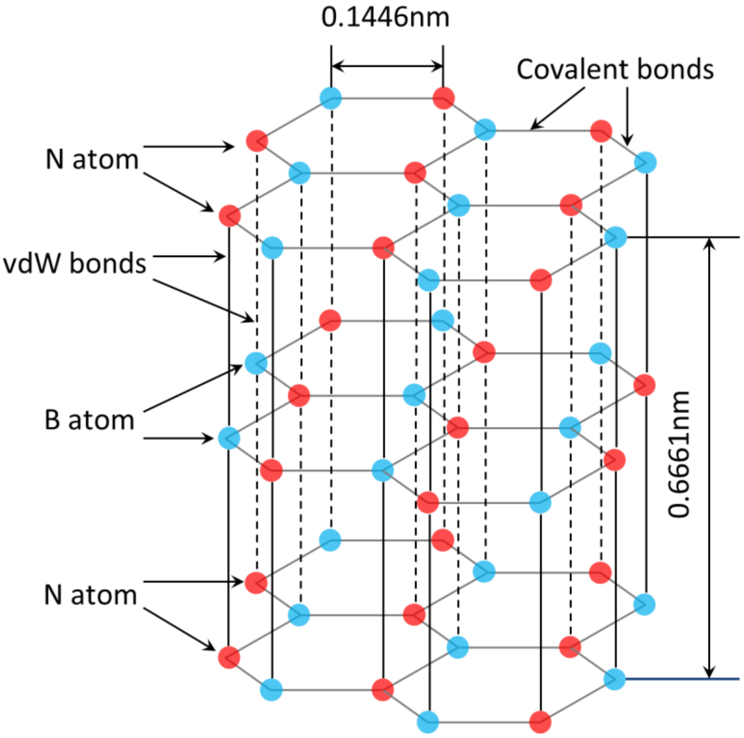

Fig. 2.12 The crystal structure of hexagonal boron nitride

The crystal lattice of hBN consists of hexagonal rings forming thin parallel planes. Atoms of boron (B) and nitrogen (N) are covalently bonded to other atoms in the plane with the angle 120^o between two bonds (each B atom is bonded to three N atoms and each N atom is bonded to three B atoms as well). The planes are bonded to each other by weak Van der Waals (vdW) forces.

One can obtain thin hBN flakes down to monolayer thickness by using the same exfoliation technique for graphene[71]. Since boron (atomic number 5) and nitrogen (atomic number 7) sit either side of carbon (atomic number 6) in the Periodic Table, the lattice mismatch between hBN and graphene is only ~1.8% (hBN the larger one)[72]. The difference in electronic properties between hBN and graphene arises from the fact that the two atoms in the unit cell are not equivalent, which makes hBN insulating with a large band gap of ~6 eV[73]. hBN is chemically inert and lacks surface traps and dangling bonds due to the strong in-plane bonding between boron and nitride atoms. In addition, the dielectric properties of hBN compare favourably with SiO_2. These properties make hBN an ideal substrate for graphene-based devices[53]. Experiments of scanning tunnel microscopy and spectroscopy (STM and STS) demonstrate that graphene devices on hBN substrate have reduced roughness, intrinsic doping and chemical reactivity, as shown in Fig. 2.13[74].

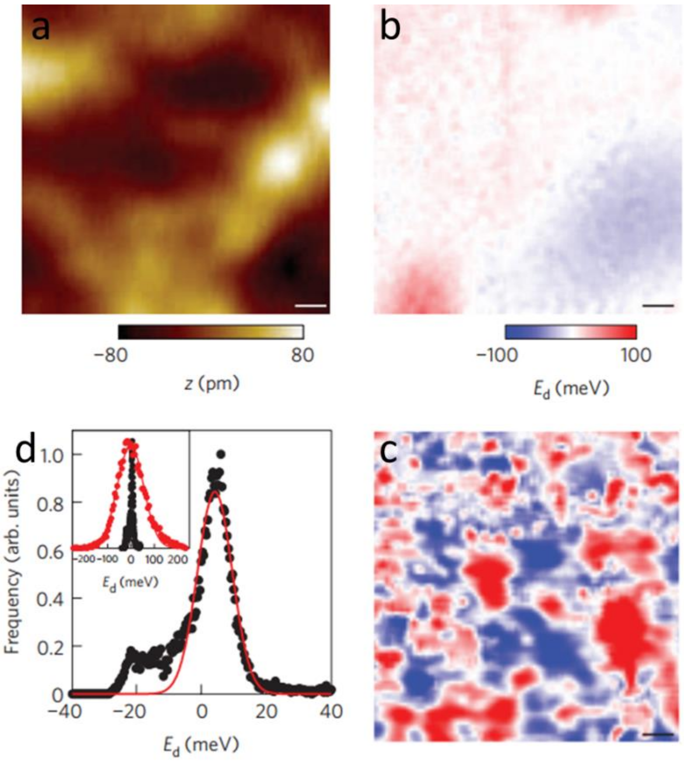

Fig. 2.13 Spatial maps of the density of states of graphene on hBN and SiO_2

(a) Topography of graphene on hBN. **(b)** Tip voltage at the Dirac point as a function of position for graphene on hBN. **(c)** Tip voltage at the Dirac point as a function of position for graphene on SiO_2. **(d)** Histogram of the energies of the Dirac point from (b). The inset shows the same data but also includes the histogram for graphene on SiO_2 (red). Fig. 2.13 is adapted from ref.[74].

Transport measurements of graphene on hBN devices show a significant improvement of charge carrier mobility by a factor of ~10-50 compared with the previous graphene on SiO_2[75]. By combining hBN encapsulation and novel 1D edge contacts to graphene, ultra-high mobility of graphene at both room temperature (~140,000 $cm^2V^{-1}s^{-1}$) and at cryogenic temperature (~1,000,000 $cm^2V^{-1}s^{-1}$) can be achieved in hBN/graphene/hBN van der Waals heterostructures[76].

In addition to being a superior substrate for high performance graphene-based devices, hBN can also alter the electronic spectrum of graphene[77]. For graphene placed on hBN, the moiré pattern induced by the similar honeycomb structures and tiny lattice mismatch (1.8%) between hBN and MLG creates a periodic perturbation, usually referred to as graphene/hBN superlattices, as shown in Fig. 2.14[78]. Graphene/hBN superlattices act on graphene's charge carriers and lead to multiple mini-bands and the generation of secondary Dirac-like spectra. The alignment of graphene and hBN leads to a number of fascinating phenomena, such as a gap opening in MLG[79], the Hofstadter butterfly[13-15] and topologically protected valley current[80].

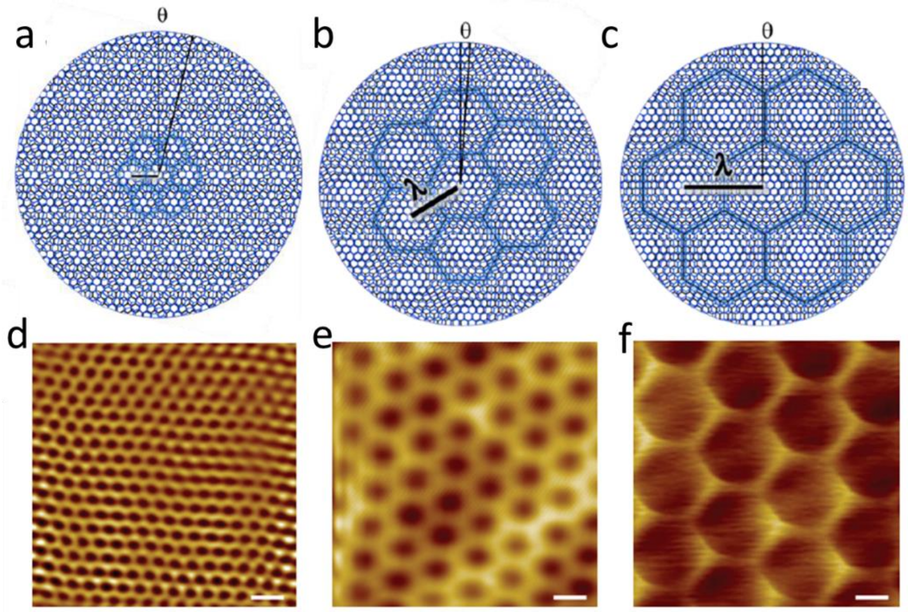

Fig. 2.14 Graphene/hBN superlattices with different periodicity

(a)-(c) The schematics of the alignment between graphene and hBN with alignment angle of 3° (a), 1° (b) and 0° (c); λ is the periodicity of the superlattices. **(d)-(f)** STM topography images showing 2.4 nm (d), 6 nm (e) and 11.5 nm (f) moiré patterns. Scale bar: 5 nm. Fig. 2.13 is adapted from ref.[78].

2.3 Josephson Junction

2.3.1 Superconductivity

Superconductivity, discovered in 1911 by Onnes[81], is a macroscopic quantum phenomenon that certain materials exhibit under particular magnetic fields and temperatures. All superconductors show a drop of resistance to zero, either gradually or suddenly, at critical temperatures, T_C. Another characteristic, later found by Meissner and Ochsenfeld in 1933[81], is that all superconductors are diamagnetic, known as the Meissner effect. In 1935, London brothers developed a phenomenological theory[82] to explain the Meissner effect. They derived an equation for the penetration depth of the superconductor, λ_L. The isotope effect discovered by Maxwell and Reynolds in the 1950s describes a decrease in T_C with an increase in isotopic mass[83,84]. A phenomenological model was built by Ginzburg and Landau in 1950, in which they introduced some important superconducting order parameters, such as the superconducting coherence length ξ [81]. In 1957, after 46 years of discovery of superconductivity, Bardeen, Cooper and Schrieffer proposed the first microscopic theory that describes the microscopic origins of superconductivity (BCS theory)[85,86]. They convincingly showed that superconductivity is caused by the condensation of electrons near the Fermi level into Cooper pairs through interaction between the electrons and the vibrations of crystal lattices (phonons). At low temperatures, the attractive force between electrons and phonons in a superconductor might be stronger than the Coulomb repulsion between the electrons. However, the attractive force is still a weak attraction and is not strong enough to bind the electrons. Cooper showed that a pair of electrons with opposite spins and momentum could experience the attractive force due to the polarization of the lattice (via electron-phonon interaction) so that this pair can have energy lower than the Fermi energy without using any of the states in the Fermi surface. Cooper pairs can be considered as bosons with total spin equals to zero. Therefore, many Cooper pairs are allowed to condense into a same quantum state that has the condensation wave function:

$$\Psi = |\Psi| e^{i\varphi}, \tag{2.34}$$

where φ the macroscopic quantum phase of a superconductor and $|\Psi|$ the measure of the Cooper pair density.

Owing to the conservation of momentum during the electron-phonon interaction, the system will tend towards a configuration, in which each Cooper pair has the same average momentum. Then, scattering a single electron or single Cooper pair to a new momentum would require overcoming the attractive force between that pair and every other Cooper pair. Since at low temperatures there is no energy fluctuation large enough to overcome this attraction, once the Cooper pairs as a group have a common momentum, they will keep this momentum permanently, which explains the zero resistance electrical state observed in superconductors.

One important prediction made in BCS theory is the superconducting energy gap Δ. The origin of Δ is electrons pairing and it is impossible to have an individual electron with an energy below one required to form a Cooper pair. The DoS in a superconductor, shown in Fig. 2.15, is:

$$N_S(|E-E_F|)/N(0) = \begin{cases} (|E-E_F|)/\sqrt{(E-E_F)^2-\Delta^2}, & |E-E_F| > \Delta \\ 0, & |E-E_F| < \Delta \end{cases}, \quad (2.35)$$

where $N(0)$ and $N_S(|E-E_F|)$ represent the DoS of a BCS superconductor in the normal state and in the superconducting state, respectively. The energy $|E-E_F|$ is counted from the Fermi level in the metal.

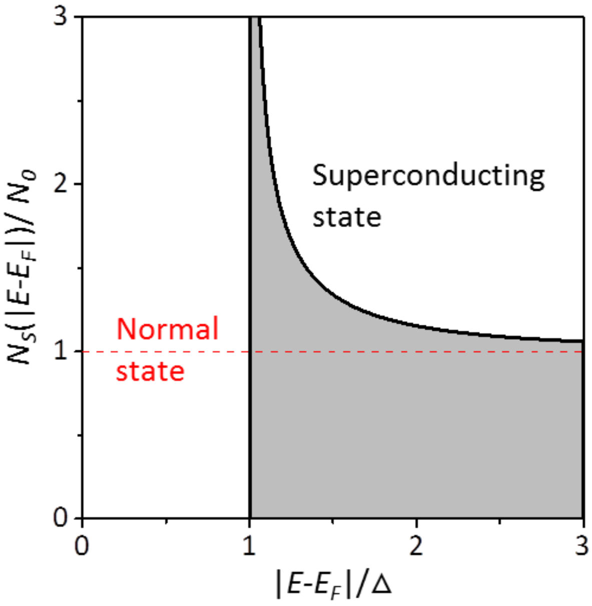

Fig. 2.15 The density of states of a BCS superconductor

The DoS in the superconducting state (black solid curve) and in the normal-state (red dashed line) of a BCS superconductor. No quasi-particle is allowed below the energy gap Δ.

2.3.2 Andreev reflection

When a normal metal (N) is contacted with a superconductor (S), an electron with energy E higher than Δ can enter the superconductor and the electron can be converted into a quasi-particle with the same energy. However, this does not work for an incident electron with E lower than Δ since there are no available states in the gap. As a result, the single-particle transmission from the normal metal into the superconductor is forbidden. The only way for an electron to enter the superconductor is by forming a Cooper pair. In order to do that, the electron in the normal metal must pair with another electron in the superconductor but with opposite spin and momentum. This process may proceed when an incident electron from the normal metal is reflected back as a hole at the N-S interface, as depicted in Fig. 2.16(a). While this process conserves energy, it does not conserve the charge in the normal metal. During this process, a total charge of $2e$ is transferred from the normal metal to the superconductor since the reflected hole has a charge e but with positive sign. The amplitude of the momentum of the reflected hole is almost equal to that of the incident electron because of $E < \Delta \ll E_F$ in the normal metal. This process works the same for an incident hole owing to the time reversal symmetry, in which the hole is reflected as an electron at the N-S interface. This process is known as Andreev reflection[19].

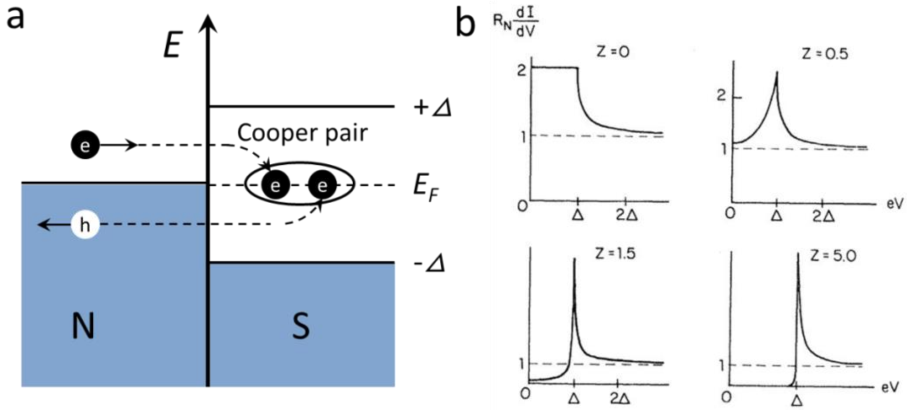

Fig. 2.16 Andreev reflection and the BTK model

(a) Schematics of Andreev reflection. An electron impinging onto the N-S interface picks up a second electron to form a Cooper pair and condense in the superconductor energy gap. The Andreev reflected hole travels backward. **(b)** Differential conductance dI/dV across the N-S junction as a function of the bias voltage for different values of the barrier intensity Z at $T = 0$. Fig. 2.16(b) is adapted from ref.[87].

However, Fig. 2.16(a) is a simplistic picture and we can use a slightly modified version of Schrödinger's equation to look at this problem in a more formal light. This work was first done by Blonder, Tinkham and Klapwijk in 1982, and is named as the BTK model after their work[87]. At the N-S interface, an incident electron can be either reflected as a hole by Andreev reflection with a probability *A* or reflected as an electron by the normal backscattering with a probability *B*. The BTK model defines a parameter Z to describe the transparency T_r of the N-S interface, $T_r = 1/(1+Z^2)$. For $Z = 0,\ A = 1$, hence only Andreev reflection can take place when the energy of incident electrons are below the superconducting gap. However, for $Z > 0,\ A$ is rapidly reduced and the normal reflection process become more probable. Thus, the $I - V_{NS}$ characteristics across the N-S junction can be written with the normal conductance G_0above T_C:

$$I(V_{NS}) = G_0/e \cdot \int_{-\infty}^{\infty} dE(f(E - eV_{NS}) - f(E))(1 + A(E) - B(E)) \qquad (2.36)$$

with the Fermi-Dirac distribution $f(E) = 1/(e^{(E-\mu)/k_BT} + 1)$ to account for temperature smearing of the Fermi energies.

We can now introduce the normalized differential conductance G_S/G_N since it is more relevant for the experimental measurements. Eq. (2.36) then can be written as

$$G_S/G_N(V_{NS}) = 1/G_0 \cdot dI/dV = (1 + A(eV_{NS}) - B(eV_{NS})). \qquad (2.37)$$

It is evident from Eq. (2.37) that *A* effectively enhances the differential conductance and *B* rapidly reduces it.

The BTK model gave the normalized differential conductance across an N-S interface as a function of the bias voltage by calculating the probability of each microscopic process and its individual contribution to the current, as shown in Fig. 2.16(b). In the case of $Z = 0$, there is no barrier between N and S and the probability of normal reflection is zero. Thus, Andreev reflection for electrons (or holes) with $E < \Delta$ is perfect. When $Z \gg 1$, there is a strong barrier at the N-S interface and the probability of Andreev reflection is strongly supressed while the normal reflection dominates the transport within the gap. The BTK model was later experimentally confirmed by the $I - V_{NS}$ characteristics of Cu-Nb point contacts[88].

2.3.3 Josephson effect

In 1962, Josephson predicted that a dissipationless supercurrent could flow between two superconductors separated by a thin insulating barrier without application of any voltage[89]:

$$I_S = I_C \, sin(\Delta\varphi), \tag{2.38}$$

where I_S the supercurrent and $\Delta\varphi$ the phase difference of two superconductors. I_C denotes to the maximum supercurrent that the junction can support. Josephson made a further prediction that the phase difference $\Delta\varphi$ can be modified by applying a constant voltage difference V across the junction:

$$d(\Delta\varphi)/dt = 2eV/\hbar. \tag{2.39}$$

By combing Eq. (2.39) and Eq. (2.38), one can obtain an alternating supercurrent with amplitude of I_C and frequency of $2eV/\hbar$. Eq. (2.38) and Eq.(2.39) are known as the dc and ac Josephson effect, respectively. Such a junction is called Josephson junction. Both the dc and ac Josephson effect have been fully confirmed by many experimental works and also have been implemented in a wide number of applications, such as superconducting quantum interference devices (SQUIDs) and qubits in superconducting quantum computing. In this thesis, we limit all discussions to the dc Josephson effect.

Although Josephson's original predictions were based on the tunnelling process of electrons from one superconductor to another through a thin insulating barrier, it is now clear that the effect are more general, and occurs whenever two superconductors are connected by a 'weak link'[81]. A 'weak link' can be established in several different ways. Instead of a thin insulating layer that was originally proposed by Josephson, other materials also could be used, for instance a normal metal layer. These two cases are usually referred to as SIS and SNS Josephson junctions, respectively. For SNS junctions, the thickness of the normal metal layer can be much larger than that in SIS junctions, since the normal metal connected to the superconductor is weakly superconducting due to the proximity effect.

In Fig. 2.17(a), a schematic demonstration is shown of two superconductors with a Ginzburg-Landau wavefunction $|\Psi_1|e^{i\varphi_1}$ and $|\Psi_2|e^{i\varphi_2}$ that are contacted to a graphene strip of size $L \times W$. The phase difference can be tuned by a small perpendicular magnetic flux, which would modify the supercurrents. The flux threading into the graphene strip is $\Phi = B \times L \times W$ and the corresponding phase addition across the width W as a function of position x is then

$$\varphi(x) = 2\pi BLy/\Phi_0, \tag{2.40}$$

where $\Phi_0 = h/2e = 2.068 \times 10^{-15}$ Wb is the flux quantum. Now the phase $\varphi(x)$ is position dependent. To obtain the total supercurrent flow through the junction, the supercurrent density has to be integrated over the width W, following the derivation:

$$I_C = I_{C0}|sin(\pi\Phi/\Phi_0)/(\pi\Phi/\Phi_0)|, \tag{2.41}$$

where I_{C0} denotes the maximum critical current at zero magnetic field. As plotted in Fig. 2.17(b), this periodic pattern is known as Fraunhofer interference pattern, analogous to optical diffraction when light pass through a single slit. In a SNS Josephson junction, when the total flux equals an integer number of flux quantum, $\Phi = N\Phi_0$, the sum of the phase across the junction is exactly zero and the supercurrent would disappear.

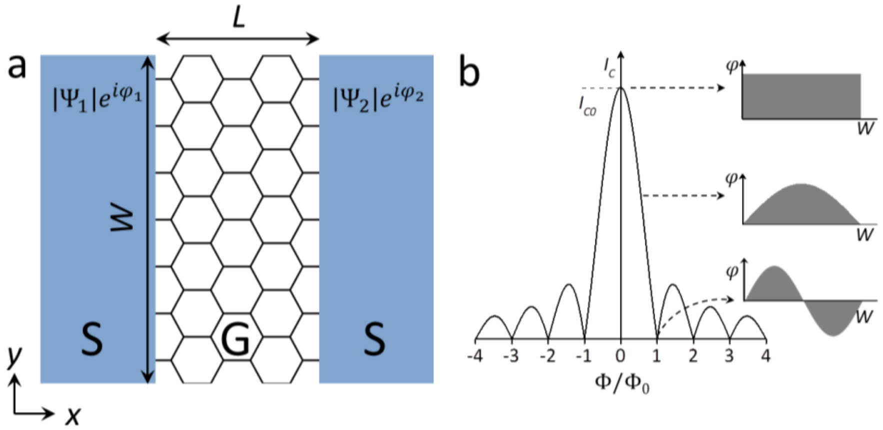

Fig. 2.17 Schematics of graphene Josephson junction and Fraunhofer interference pattern of the critical current in magnetic field

(a) Schematics of a graphene Josephson junction. Two superconductors are contacted by a graphene strip. **(b)** Fraunhofer interference pattern. The critical current of graphene Josephson junction periodically oscillates as a perpendicular magnetic field is increased. The insets demonstrate three examples of the position dependent phase cross the Josephson junction. When the total flux equals an integer number of flux quantum, $\Phi = N\Phi_0$, the sum of the phase across the junction is exactly zero and the supercurrent disappears.

We described the general mechanism of Andreev reflection at the N-S interface in section 2.3.2. The treatment of Andreev reflection processes can be well extended to SNS junctions. In a graphene (G) Josephson junction depicted in Fig. 2.18(a), graphene plays a role as the normal metal part. Andreev reflection occurs at both left and right G-S interfaces. An incident electron coming from graphene is Andreev reflected into a hole at the right G-S interface travelling to the left. At the left G-S interface, the hole is Andreev reflected into an electron travelling to the right. When a bias voltage V_b is applied to the junction, electrons and holes, moving in opposite direction, are both accelerated by V_b. An electron in graphene can be reflected back and forth several times between two G-S interfaces, gaining energy eV_beach time when it traverses across the junction, until it accumulates enough high energy to escape graphene into the superconducting electrode as a quasiparticle. A total charge of $2e$ is transferred from graphene to the superconductor after each Andreev reflection, which modifies the differential resistance (dV/dI) of the junction depending on the number of Andreev reflections that occur in the junction. This causes a feature in the dV/dI characteristics at each bias $V_b = 2\Delta/ne$, where n is an integer number[87,88]. An example of multiple Andreev reflections (MAR) in graphene Josephson junction is shown in Fig. 2.18(b).

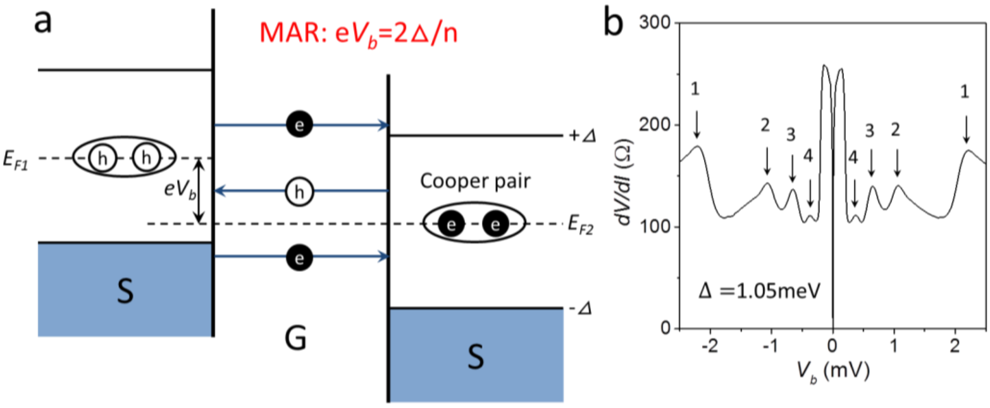

Fig. 2.18 Multiple Andreev reflections in a graphene Josephson junction

(a) Schematic representation of MAR between two identical superconductors with an energy gap Δ. The electron is retro-reflected as a positive charged hole, creating a Cooper pair in the superconductor; conversely, retro-reflection of a hole annihilates a Cooper pair. Electrons and holes, moving in opposite directions, are both accelerated by the applied bias voltage V_b. **(b)** Measured dV/dI of a typical graphene Josephson junction as a function of applied bias. A series of sub-harmonic peaks in dV/dI represent the MAR phenomenon.

At vanishing temperature $T = 0$, the critical current in a SIS Josephson junction is related to the superconducting energy gap Δ as

$$eI_C R_N(T = 0) = \pi\Delta/2, \tag{2.42}$$

where R_N is the normal-state resistance of the junction[90]. This is also the case for short SNS Josephson junctions operating in the ballistic regime[91]. However, it has been found that for the case of diffusive SNS Josephson junctions, Δ is no longer the dominant parameter. Instead, the critical current is related to the Thouless energy E_{Th} as[92]

$$eI_C R_N(T = 0) = 10.82E_{th}. \tag{2.43}$$

In the diffusive regime, Thouless energy $E_{Th} = \hbar D/L^2$ is the characteristic energy scale determined by the diffusive constant D and junction length L. The numerical results for $eI_C R_N(T = 0)$ as a function of the Thouless energy E_{Th} are presented in Fig. 2.19(a). It demonstrates that it is the minimum of the superconducting gap Δ and the Thouless energy E_{Th} that limits the critical current in the diffusive SNS Josephson junctions[92]. At temperatures close to T_C the critical current through a SNS junction is suppressed since the density of Cooper pairs inside a normal metal decays exponentially with the distance away from the contact to the superconductor. Therefore, the critical current is supressed as $I_C \propto exp(-L/L_T)$, where $L_T = \sqrt{\hbar D/k_B T}$ is the characteristic thermal length. At moderate temperature $E_{th} < k_B T < k_B T_C$ the temperature dependence of $eI_C R_N$ in units of E_{th} has been numerically analyzed, as shown in Fig. 2.19 (b). For $k_B T > 5E_{th}$ and in the limit of $\Delta/E_{th} \to \infty$, the critical current through a long SNS Josephson junction can be expressed analytically as[92]

$$eI_C R_N = (32/(3 + 2\sqrt{2}))E_{th}(L/L_T)^3 e^{(-L/L_T)}. \tag{2.44}$$

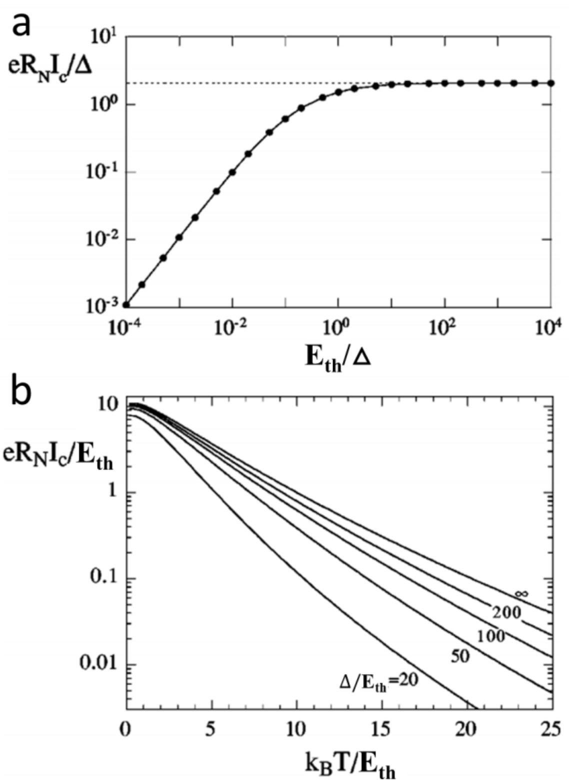

Fig. 2.19 Calculated eI_CR_N in long SNS Josephson junctions

(a) Calculated energy dependence of the zero-temperature eI_CR_N in units of Δ as a function of the ratio Δ/E_{th}. The long junction regime is on the left part where $E_{th} < \Delta$, the short junction regime is on the right part where $E_{th} > \Delta$. The dashed line corresponds to the eI_CR_N only depending on the superconducting energy gap Δ when the junction is in the short ballistic regime. (b) Calculated temperature dependence of the eI_CR_N. The different curves correspond to various values of the ratio Δ/E_{th} in the long junction regime. The curve for $\Delta/E_{th} \rightarrow \infty$ is universal in the sense it does not depend on Δ. Fig. 2.19 is adapted from ref.[92].

2.3.4 Graphene Josephson junction

In 2007, Graphene Josephson junctions were first experimentally demonstrated by Heersche in aluminium-graphene-aluminium hybrid systems, which were characterized at milikelvin temperatures[20]. The results showed that graphene performs extremely well as the N-member of a SNS Josephson junction. Over the past ten years, a number of experimental works have proven that graphene is a promising material for building superconducting devices[21-37,93-95]. Graphene exhibits a linear dispersion and vanishing DoS at the Dirac point. The quasiparticles in graphene are massless Dirac fermions that differ from other materials. The unique electronic properties of graphene suggest new physics to be found in proximity superconductivity and the Josephson effect. The transport properties of graphene Josephson junctions near the Dirac point are particularly intriguing. Specular Andreev reflection[38] and supercurrents supported by evanescent modes[96,97] have been theoretically predicted. In addition, both the sign and density of charge carriers in graphene can be tuned by applying an electric field to graphene, providing an excellent platform for studying the energy dependence of superconducting properties of Josephson junctions. From the view of device fabrication, it is relatively easy to obtain transparent G-S interfaces because graphene is inert in ambient atmosphere which prevents oxidation on its surface.

Specular Andreev reflection is a remarkable phenomenon that occurs in graphene-superconductor hybrid junctions. An incident electron from a normal metal with energy lower than the gap can be reflected into a hole at the N-S interface, creating a Cooper pair in the superconductor, known as Andreev reflection[19]. For most normal metals, the Fermi energy is much greater than the superconducting gap[17], $E_F \gg \Delta$. Thus, the reflected hole will remain in the same conduction band and has an opposite sign mass compared with the incident electron. The momentum of the electron is almost conserved before and after Andreev reflection by neglecting the term Δ/E_F. For electrons in the conduction band, the velocity is parallel to its momentum, while the velocity of a hole in the same conduction band has direction opposite to its momentum. As a result, the hole is retro-reflected, as shown in Fig. 2.20(a) and (b). However, a completely different type of Andreev reflection will occur if the Fermi energy can be tuned small enough such that $E_F < \Delta$. In this case, the energy difference between the incident electron and the reflected hole, $2E$, can result in the reflected hole appearing in the valence band of graphene rather than the conduction band. The reflected hole now has the same mass sign as the incident electron. According to momentum conservation, the reflected hole will move in the same direction as the incident electron along the G-S interface. Therefore, the hole is not retro-reflected but specular-reflected instead. This new type of reflection process is called specular Andreev reflection[38], as shown in Fig. 2.20(c) and (d).

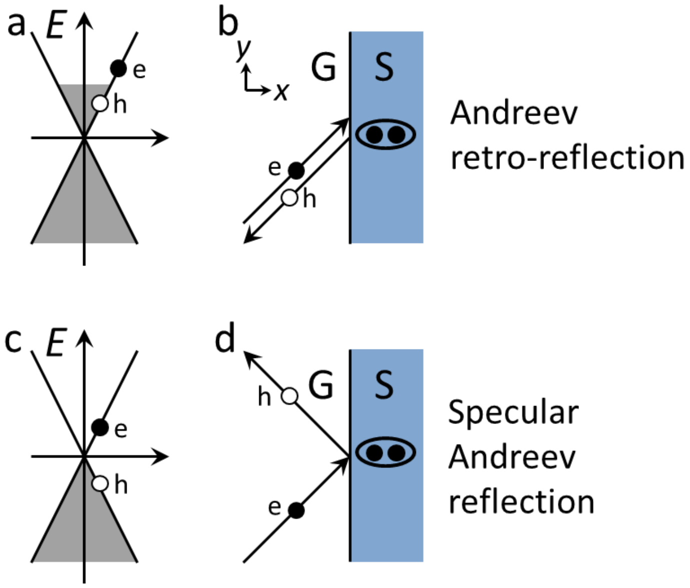

Fig. 2.20 Schematics of different types of Andreev reflection at graphene-superconductor interface

The linear band dispersion of graphene at high carrier density **(a)** and at near zero carrier density **(c)**. **(b)** Andreev retro-reflection occurs in the highly doped $E_F \gg \Delta$ regime. A conduction band electron is reflected into a hole in the conduction band with approximately the same momentum. The velocity of a conduction band hole is opposite to its wave vector and the hole is therefore retro-reflected. **(d)** Specular Andreev reflection occurs in the undoped regime with $E_F < \Delta$. A conduction band electron is reflected into a valance band hole. A valance band hole moves in the same direction of its wave vector. Hence, v_x changes sign whereas v_y remains unchanged and namely the electron is specular reflected into a hole.

There are two major approaches for fabricating high quality graphene devices: by suspending graphene, and by sandwiching graphene between two hBN crystals. Compared with the suspended devices[98], hBN encapsulated graphene are more robust[75]. Furthermore, it is possible to combine hBN-graphene-hBN heterostructures with the 1D edge contacts[76] which further improve the quality of graphene devices.

In addition to a number of fascinating physical phenomena, the gate tunability and large magnitude of the supercurrents in graphene Josephson junctions suggest many promising applications for the graphene based superconducting devices, such as SQUIDs[23] and single-photon detectors [99].

2.4 Quantum mechanical tunnelling

2.4.1 Tunnel barrier

The vertical graphene-hBN tunnelling transistors considered in this thesis can be formed by sandwiching a thin hBN (2 to 5 layers) between two graphene layers, where the two graphene layers work as top (Gr_T) and bottom (Gr_B) electrodes and hBN acts as a thin tunnel barrier. There are several advantages of using hBN as the tunnel barrier, such as a large bandgap (~6 eV) and high breakdown field strength (~1 V/nm)[54]. In addition, the atomically flat surface of hBN with no dangling bonds considerably maintains the high quality of graphene and well defines the clean interfaces between hBN and graphene due to the van der Waals interactions[100,101]. After assembling, the graphene-hBN-graphene heterostructure is placed on hBN/SiO_2/Si substrate with an additional top protection from hBN, as depicted in Fig. 2.21.

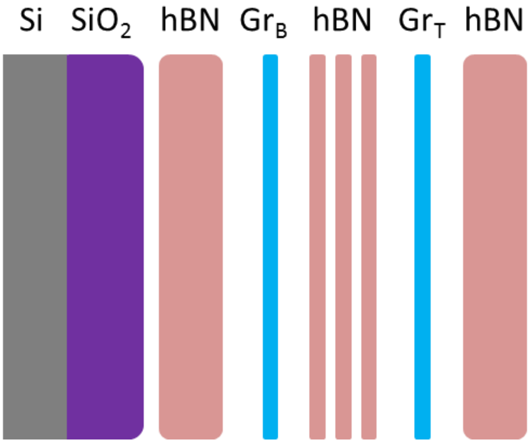

Fig. 2.21 Schematics of the structure of graphene-hBN tunnelling transistor
Two graphene electrodes (blue) are separated by a few-layer hBN (red), forming a graphene-hBN-graphene heterostructure. This heterostructure is encapsulated by two thick hBN, and then is placed on the SiO_2/Si substrate.

In the classical case, if an electron is incident onto a potential barrier with energy E higher than the barrier height U_0 ($E > U_0$), the electron then will pass over the barrier, resulting a current. If $E < U_0$, the electron cannot pass the barrier and is thus reflected. Quantum mechanically, the result of $E < U_0$ is similar to the classical case for a thick potential barrier, since the wavefunction of the incident electron will exponentially decay to zero before the electron passes through the barrier and thus there is almost no probability for quantum mechanical tunnelling. However, if the barrier is thin enough (~nm), it is quite possible that an incident electron with energy $E < U_0$ can tunnel through the barrier. Both classical and quantum mechanical cases are schematically demonstrated in Fig. 2.22. Quantum tunnelling is a direct result of the wave-like nature of the electrons, as the wavefunction of the electrons must be continuous at the barrier boundaries. Therefore, there is a finite probability of finding the electrons on either side of the barrier. Such a potential barrier, in this thesis, can be formed by sandwiching a thin hBN between two graphene layers.

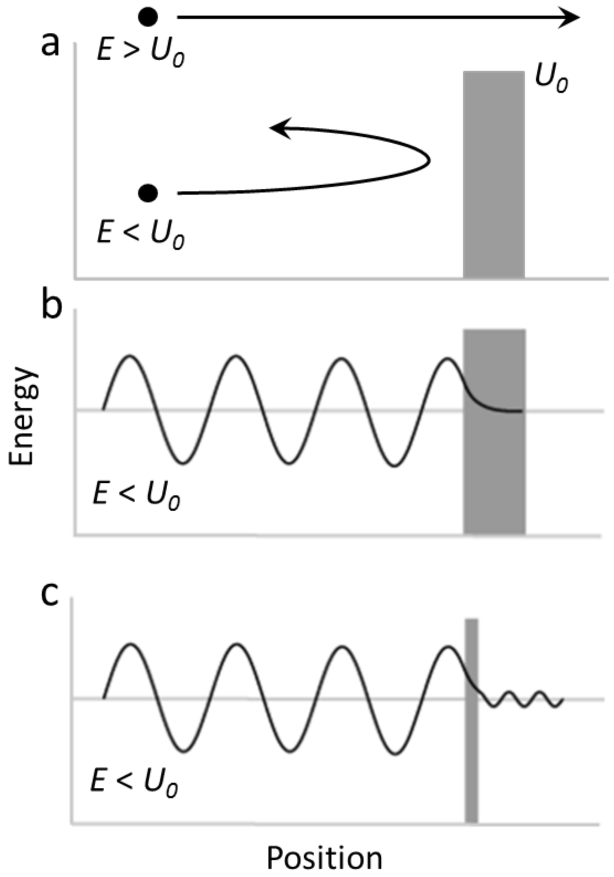

Fig. 2.22 An electron incident to a potential barrier

(a) Classically, electrons with energy $E > U_0$ can pass over a potential barrier while electrons with energy $E < U_0$ cannot pass and they will be reflected. **(b)** and **(c)** Quantum mechanically, for electrons with energy $E < U_0$ the wavefunction of the electrons doesn't abruptly end, but decays exponentially in the barrier. For a thick barrier **(b)** the electrons cannot pass through the barrier before the wavefunction decays to zero. However, if the barrier is thin enough **(c)**, there is a finite probability of electrons undergo quantum tunnelling through the barrier.

2.4.2 Resonant tunnelling

In this section, we start with a simple discussion of resonant tunnelling through the double-barrier heterostructure. Typically, a resonant tunnelling diode (RTD) consists of an undoped quantum well layer with a small band gap sandwiched between undoped barrier layers with a larger band gap and where the emitter and collector contact regions are heavily doped. The most common double-barrier system is based on the $Al_xGa_{1-x}As$ (barrier)/GaAs(well)/$Al_xGa_{1-x}As$ (barrier) heterostructures[102]. The conduction band diagrams for a RTD under four different bias voltages are shown in Fig. 2.23.

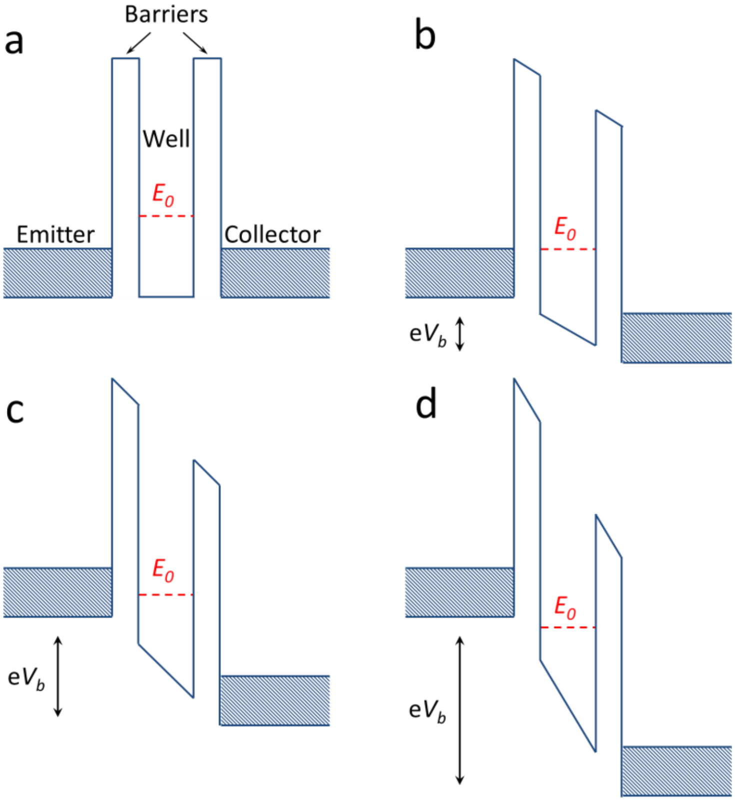

Fig. 2.23 Conduction band diagrams of a double-barrier structure RTD at four different bias voltages

(a) Zero bias. **(b)** Threshold bias. **(c)** Resonance. **(d)** Off-resonance. Left and right patterned regions are the Fermi sea in the emitter and collector contacts, respectively. Dashed red lines represent the resonant states E_0 in the quantum well confined by the two barriers. Black arrows in (b)-(d) indicate the applied bias energies.

In a RTD shown in Fig. 2.23, the resonant tunnelling occurs when the energy of the electrons flowing from the emitter coincides with the energy of resonant states E_0 in the quantum well confined by the two barriers. The alignment between the Fermi level of the emitter and the resonant states can be adjusted by applying an external bias V_b. When V_b is applied across the RTD, the Fermi level shifts in both emitter and collector, and increases the number of electrons contained in the quantum well. A resonant tunnelling current starts to flow when the Fermi level of the emitter reaches E_0 (threshold state, Fig. 2.23(b)). At the threshold state, the transmission of the incident electrons is close to unity, that is, an electron with the resonant energy can cross the double-barrier without being reflected. This resonance phenomenon is similar to that taking place in the optical Fabry-Pérot resonators. The tunnelling current reaches its maximum when the Fermi sea of the emitter passes through E_0 (resonant state, Fig. 2.23(c)) and exhibits a negative differential conductance (NDC) at V_b just beyond the resonant bias where the current peak occurs. Further increasing V_b will decrease the tunnelling current when the conduction band edge is above E_0 (off-resonant state, Fig. 2.23(d)), as shown in Fig. 2. 24.

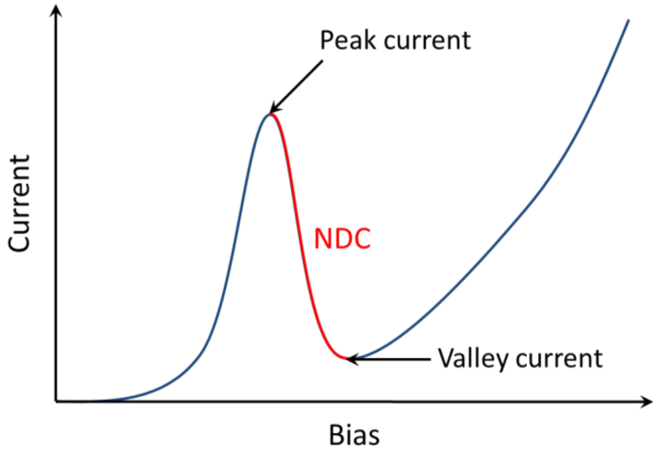

Fig. 2.24 An example of *I-V* characteristic of a RTD

A typical *I-V* curve of a RTD device. The peak and valley currents are pointed out by the black arrows. The NDC region is highlighted by the red curve.

In addition to double-barrier structures we discussed above, RTDs can also be formed by graphene-hBN-graphene tunnelling transistors[103,104]. The resonant tunnelling and NDC are achieved by carefully controlling the twist angle between two graphene layers separated by a thin hBN. The operation is simple and based on the conservation of both energy and momentum[104]. The peak-to valley ratios (peak current/valley current, PVR) of graphene-based RTDs approaching ~2 have already been achieved at room temperature.

2.4.3 Scattering-assisted resonant tunnelling

Our discussion of resonant tunnelling in section 2.4.2 neglected the scattering processes, which is known as direct tunnelling where both energy and momentum are conserved. However, in real devices there always are some imperfections in the crystals, such as impurities, defects and vibrations of the lattice. Thus, the effects of electron scattering on resonant tunnelling are inevitable in real systems operating at room temperature. There are two types of scattering, elastic and inelastic. Elastic scattering usually occurs when an incident electron collides with an impurity or a defect in a lattice, which conserves the energy, but does not conserve the momentum. During inelastic scattering, neither the energy nor the momentum of the electron is conserved[102]. For resonant tunnelling, most of the inelastic scattering processes arise from the electron-phonon interactions, such as emission (if the bias voltage is high enough), or absorption (if the temperature is high enough) of a phonon, as shown in Fig. 2.25. Both elastic and inelastic scattering processes are of great interest not only from a fundamental point of view, but also because of the possibility of controlling and even engineering these interactions in nanostructure semiconductor devices[105]. We will later describe the phonon-assisted resonant tunnelling in graphene-hBN tunnelling transistor in Chapter 7.

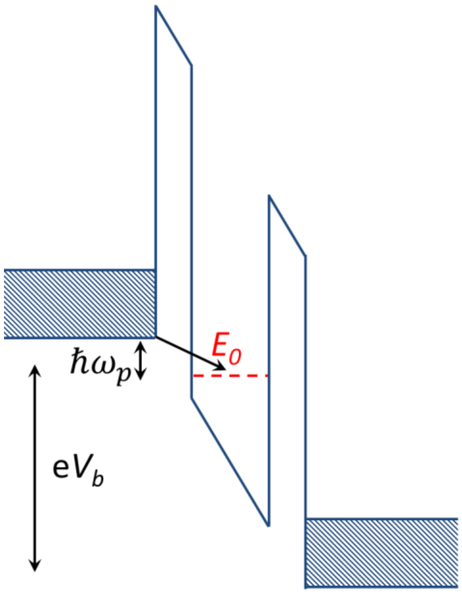

Fig. 2.25 Schematics of phonon-assisted resonant tunnelling

Conduction band diagram of phonon-emission-assisted resonant tunnelling process in a double-barrier structure tunnelling diode.

Chapter 3

Experimental methods

3.1 Device fabrication

3.1.1 Mechanical exfoliation

In order to obtain high quality graphene-based devices, all graphene and hBN flakes with different thickness in this thesis are prepared by mechanical exfoliation[1,71].

We start with a natural graphite crystal and a piece of adhesive tape. We gently press the graphite onto the tape, leaving an impression of broken graphite crystals on the tape. We repeat this procedure several times to produce numerous thin graphite flakes. Then we press the tape, which is now covered with many thin graphite flakes, onto a freshly cleaned substrate such as a silicon wafer. During this procedure, we apply some pressure on the tape to enhance the adhesion between the flakes and the substrate. After that, we carefully peel off the tape, leaving thin graphite flakes with varying thickness down to the monolayer (MLG) on the substrate. Graphene of different layers on specific substrates can be identified by optical contrast even in white light without any filters, as shown in Fig. 3.1.

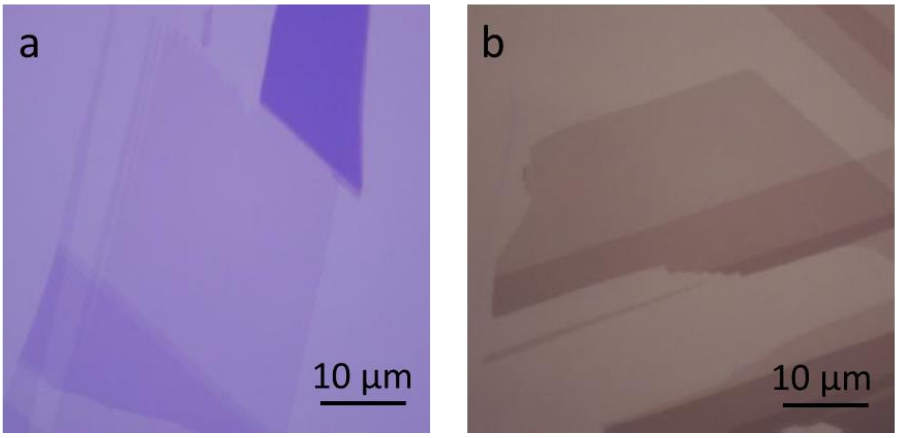

Fig. 3.1 Optical images of mechanically exfoliated graphene flakes on SiO_2/Si substrates

(a) Graphene flakes on 290 nm SiO_2/Si wafer. **(b)** Graphene flakes on 90nm SiO_2/Si wafer. Both images are taken under white light.

For the substrate, oxidized silicon wafer (SiO_2/Si) or bilayer polymer poly-methyl-methacrylate and poly-methyl-glutarimide (PMMA/PMGI) are most commonly used in our lab. SiO_2/Si substrate provides better optical contrast of the flakes. PMMA/PMGI substrate is more convenient for advanced flake transfer techniques, such as ‘dry’ transfer and van der Waals pick up. In this thesis, we employ a combination of the two different substrates to prepare our devices. For the SiO_2/Si substrate, the SiO_2 layer usually has two different thicknesses: 290nm and 90nm.

We can find the position of graphene flakes on different substrates and estimate the number of layers just by using optical microscopy. However, for the conclusive evidence, the number of graphene layers is confirmed by either atomic force microscopy (AFM) or Raman spectroscopy. Fig. 3.2 shows the AFM images of mechanically exfoliated graphene flakes on 290 nm SiO_2/Si substrate.

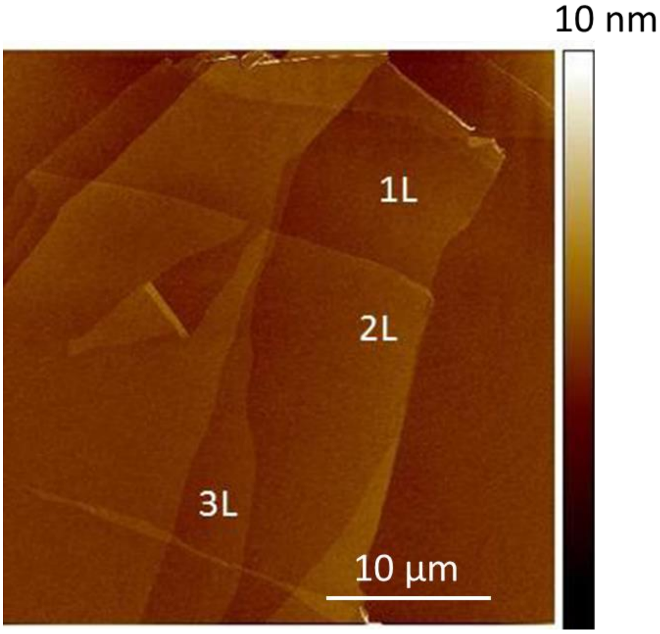

Fig. 3.2 AFM images of mechanically exfoliated graphene flakes on 290 nm SiO_2/Si substrate

AFM images of the graphene flakes with different thickness. Monolayer, bilayer and trilayer graphene regions are labelled by 1L, 2L and 3L, respectively.

The Raman spectroscopy of MLG shows distinct features that can be used to differentiate MLG from few-layer graphene and graphite[106]. Fig. 3.3 shows the Raman spectroscopy of MLG, few-layer graphene and graphite.

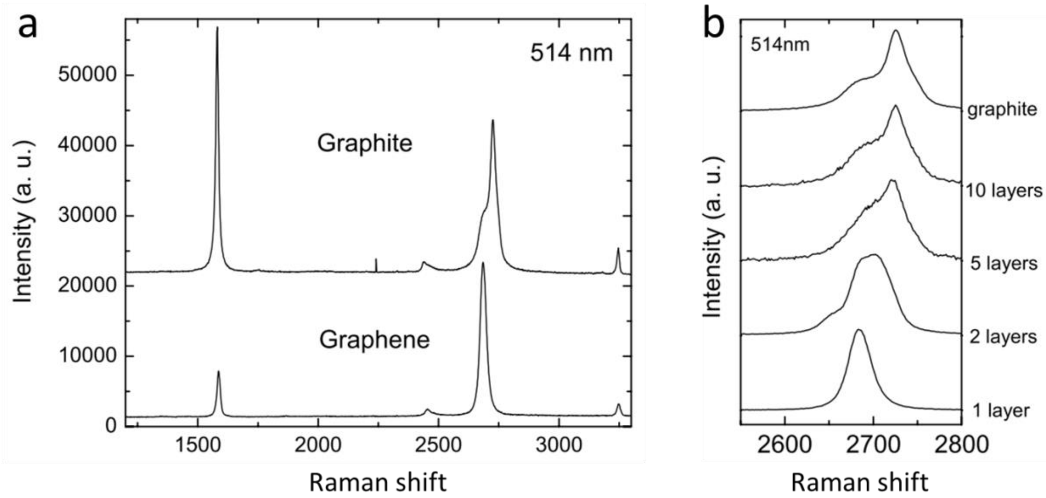

Fig. 3.3 Raman spectroscopy of graphene and graphite

(a) The Raman spectroscopy of graphene and graphite, showing the G peak at 1580 cm^{-1} and the 2D peak at 2700 cm^{-1}. **(b)** The evolution of the 2D peak from MLG to few-layer graphene to graphite. Raman spectroscopy was taken using 514nm wavelength excitation source. Fig. 3.3 is adapted from ref.[106].

The main peaks in the Raman spectroscopy of MLG and graphite are found at 1580 cm^{-1} and 2700 cm^{-1} (see Fig. 3.3(a)), which refers to the G peak and the 2D peak, respectively. The G peak intensity of MLG and graphite are similar (Fig. 3.3(a) is rescaled to get the similar height of the 2D peaks). There is a significantly difference in the 2D peaks between MLG and graphite. The 2D peak of MLG is a single sharp peak with intensity much higher than the G peak. However, the 2D peak of graphite splits into two components and has a height of intensity less than its G peak. Thus, we can use the 2D peak as the main feature to distinguish MLG from graphite. The 2D peak can further tell the difference between MLG and few-layer graphene, as shown in Fig. 3.3(b). A single Lorentzian line can fit the single sharp 2D peak in MLG, which originates from only one scattering process in MLG. However, in BLG for example, the number of allowed scattering processes is four-fold due to its special band structure and each of them has slightly different energies, resulting in a more complicated line shape of the 2D peak[106]. Fig. 3.3(b) also shows the evolution of the 2D peaks from MLG to other few-layer graphene. Thus, Raman spectroscopy provides an easy and reliable way to confirm the number of graphene layers.

We prepare thin hBN flakes from bulk hBN crystals using the standard mechanical cleave technique as used for the exfoliation of graphene from graphite. In this thesis, hBN have three main applications: as substrate for high quality graphene device, as dielectric layer between graphene and top gate electrodes, and as tunnel barrier for graphene-hBN-graphene transistors. For substrate and dielectric layer, we search for large size hBN with clean and flat surface and there is no strict requirement of the thickness. Usually, we choose the hBN with thickness between 20 nm to 80 nm, as show in Fig. 3.4(a). For graphene-hBN tunnelling transistors, the use of larger size thin hBN is one of the most important factors that affect performance of the transistors. The tunnelling resistance per area of thin hBN exponentially increases with increasing thickness, as we expect for quantum tunnelling. Thin hBN between 2-layers and 5-layers are the best choice for tunnel barrier, as shown in Fig. 3.4(b). The number of layers and the thickness of hBN can be subsequently confirmed by AFM measurement[54,107] and Raman spectroscopy[107].

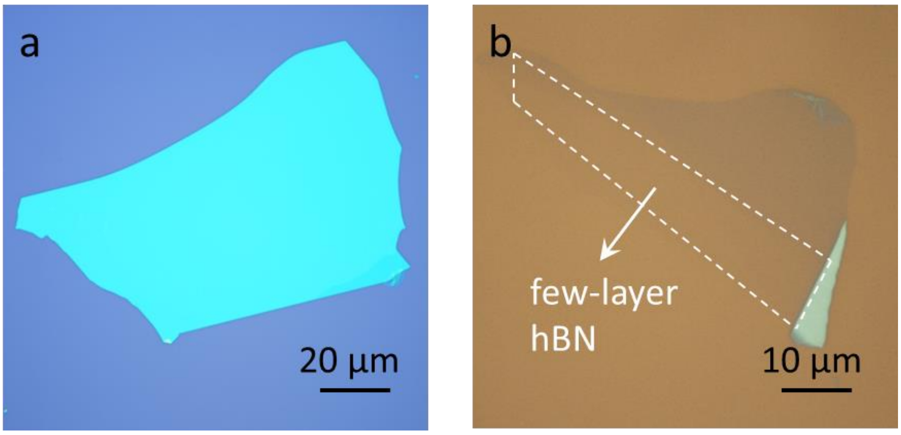

Fig. 3.4 Optical images of mechanically exfoliated hBN flakes on SiO_2/Si substrates

(a) hBN flake with thickness about 60 nm on top of 290 nm SiO_2/Si substrate. This hBN can be used as substrate or top gate dielectric layer for graphene-based devices. **(b)** Few-layer hBN flake (highlighted by white dash outline) on top of 90 nm SiO_2/Si substrate. This hBN is a good choice as tunnel barrier in graphene-hBN tunnelling devices after etching away the thick part. Both images are taken under white light.

3.1.2 van der Waals heterostructures

Recent progresses in 2D materials and van der Waals heterostructures have enabled creating artificial materials with tailorable properties for a range of different applications[108,109].

In this thesis, in order to obtain high quality graphene devices, we use hBN as a substrate and for encapsulation to protect graphene from the roughness of oxidized silicon surface and other contaminations. An electric field bias between two graphene layers is essential for opening a tunable band gap in BLG. hBN is a perfect choice as a dielectric layer between the top gate electrode and BLG. The alignment between graphene and hBN is the key point to build graphene/hBN superlattices. In addition, few-layer hBN, as the tunnel barrier, is one of the key factors affecting the performance of graphene-hBN tunnelling transistors. Unlike the molecular beam epitaxial (MBE) technique used in growing high quality GaAs/AlGaAs heterostructures, van der Waals heterostructures are achieved by stacking one flake on top of another. In order to get atomically clean interface between different flakes, it is very important to reduce the contaminations as much as possible during the flake transfer. Several transfer techniques are used in our group depending on the design of the device. Here, we introduce three different transfer techniques which are most commonly applied in preparation of the graphene-hBN van der Waals heterostructures in this thesis.

'Wet' transfer

The very first flake transfer technique is called 'wet' transfer. This is because graphene has to be immersed in some solvents and unavoidably contaminated by the solvent during the transfer from one silicon substrate to another. We first exfoliate graphene and hBN on separate silicon substrates and then spin coat a polymer layer (usually PMMA) on top of the silicon covering the graphene. A tape with a window is attached to a PMMA layer where a graphene flake sits in the middle of the window. After that, we use 3% KOH solvent to dissolve the SiO_2 layer of silicon substrate, leaving the PMMA with graphene floating in KOH solvent. Then we pick up the PMMA membrane and transfer it to deionized (DI) water to remove the residual KOH solvent. Now, the graphene attached to PMMA is ready to be transferred onto top of the hBN that is sitting on another silicon substrate.

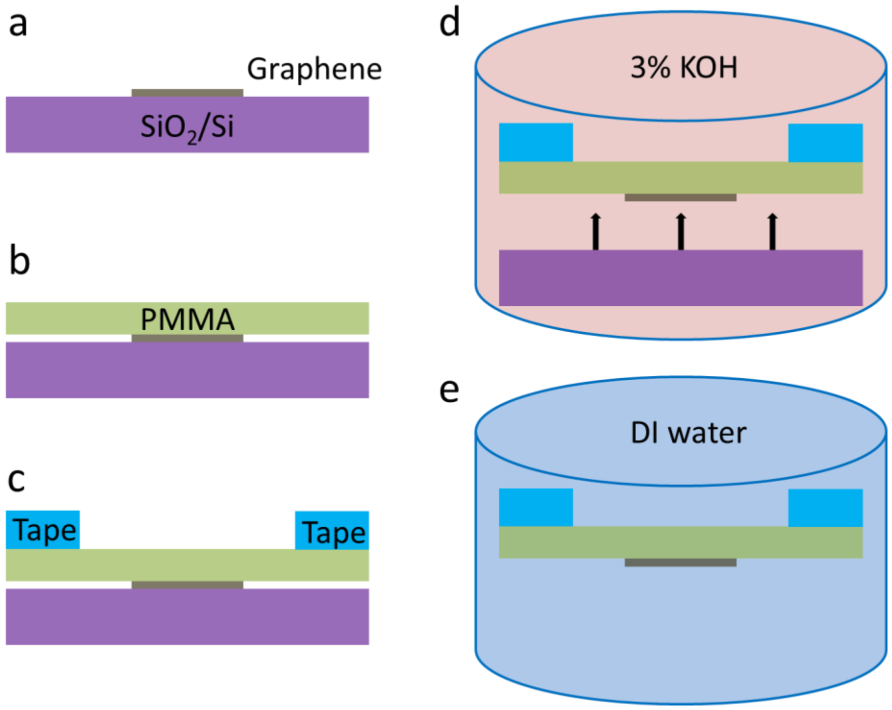

Fig. 3.5 Schematics of 'wet' transfer procedures

(a) Exfoliate graphene flake on SiO_2/Si surface. **(b)** Spin coat a layer of PMMA resist on SiO_2/Si substrate and bake it at 130 ^{o}C for 5 minutes. **(c)** Place a tape window (a piece of tape with a 1 mm×1 mm hole in the middle) on PMMA aiming the centre of the hole to the graphene flake ready for transfer. **(d)** Dive the whole substrate into 3% KOH solvent for 6 hours at room temperature for etching away the SiO_2 layer. **(e)** Leave the rest tape window/PMMA/graphene into fresh DI water for 2 hours for cleaning residual KOH.

'Dry' transfer

To improve the interface between two different flakes, researchers have developed a 'dry' transfer technique. We exfoliate hBN flake onto silicon substrate, same as 'wet' transfer. However, the graphene flake is exfoliated onto a double-layer polymer PMMA/PMGI that has been spun onto a silicon wafer. The bottom PGMI layer then can be dissolved by injecting MF-319 solvent, leaving the PMMA with graphene floating on top of the solvent. This technique has the drawback that in general the flakes obtained are smaller due to the weaker adhesion between graphene and the polymer. It is also harder to identify the graphene flakes by optical contrast due to the changes in the interference conditions of the substrate. However, the major advantage of 'dry' transfer technique is that the bottom layer polymer can be selectively dissolved by specific solvents without graphene touching the solvent. The

PMMA membrane then can be picked up, inverted, and carefully transferred onto top of the hBN. The remaining PMMA can be either dissolved or peeled off. As the last step, we anneal the graphene/hBN heterostructure at 200 ^{o}C in mixed H_2/Ar atmosphere to remove the residual contaminations on the top surface of graphene. Since there is no or very little contamination trapped in the interface between two flakes, it is possible to obtain high quality graphene devices with clean graphene-hBN interfaces using this 'dry' transfer technique.

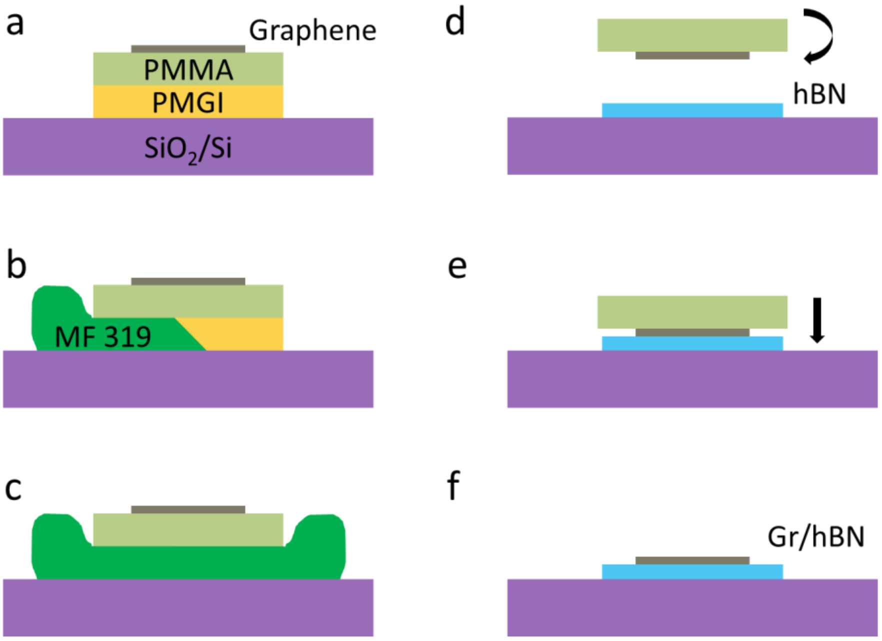

Fig. 3.6 Schematics of 'dry' transfer procedures

(a) Exfoliate graphene flake on PMMA/PMGI bilayer on top of SiO_2/Si substrate. **(b)** Carefully inject MF 319 droplets at the edge of PMMA/PMGI. The bottom PGMI layer can be dissolved by the MF-319 solvent **(c)** PMGI layer is fully dissolved by MF 319, leaving the graphene flake on top of PMMA layer floating. **(d), (e)** Pick up the PMMA membrane with graphene on top and transfer it to the target hBN flake. **(f)** The remaining PMMA can be either dissolved or peeled off, leaving graphene/hBN heterostructures on SiO_2/Si substrate.

Van der Waals pick-up

Even for the 'dry' transfer process, the residual polymer and other contaminations to graphene are still unavoidable. Now, we introduce a recently developed van der Waals pick-up transfer technique, otherwise known as the 'stamp' transfer method. Graphene and bottom hBN are exfoliated onto separate SiO_2/Si substrates. The top hBN is prepared onto PMMA/PMGI coated transparent substrate (usually a microscope glass slide). We use the top hBN as an adhesive layer to pick up the graphene due to a strong van der Waals interaction between hBN and graphene. The top hBN/graphene is then transferred onto the bottom hBN. During the entire assembling process, graphene is always protected by hBN without touching any solvents and polymers. Thus, we can get ultra-high quality graphene devices by employing this method. Notably, the van der Waals pick-up method is not limited to graphene and hBN, it is possible to build different van der Waals heterostructures by stacking other 2D crystals.

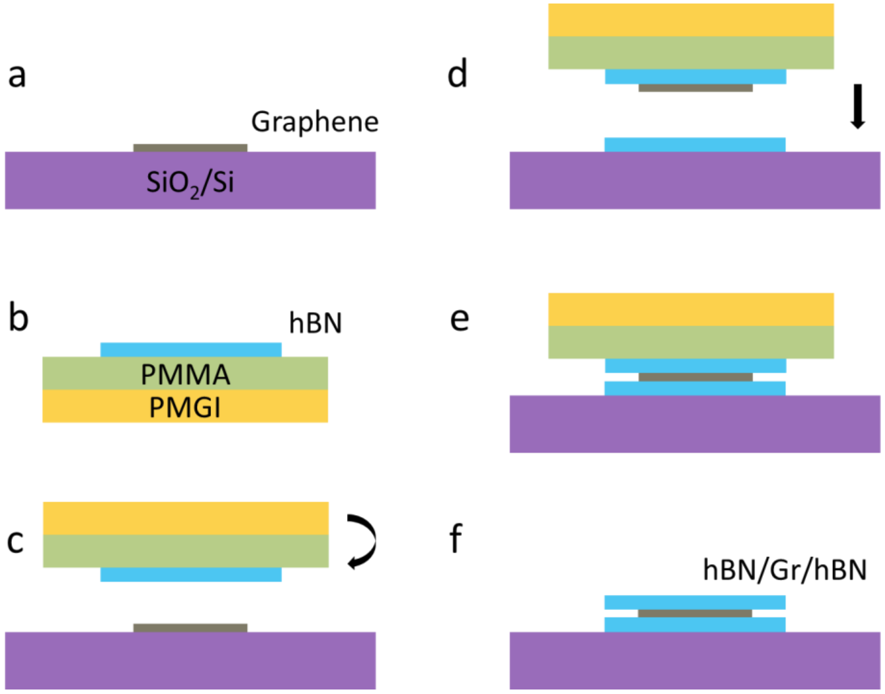

Fig. 3.7 Schematics of van der Waals pick-up transfer procedures

(a) Prepare exfoliated graphene flake on SiO_2/Si substrate. **(b)** Prepare exfoliated hBN flake on PMMA/PMGI substrate. **(c)** Invert PMMA/PMGI membrane with hBN flake on top of a target flake (graphene in here) and then carefully pick up the graphene flake. **(d), (e)** Transfer hBN/graphene to another hBN flake which is prepared on SiO_2/Si substrate. **(f)** The remaining PMMA/PMGI layer can be either dissolved or peeled off, leaving hBN/graphene/hBN heterostructures on SiO_2/Si substrate.

After the graphene-hBN heterostructures are prepared, we apply a series of standard electron-beam (e-beam) lithography, metal deposition (e-beam evaporation or magnetic controlled sputtering), flake etching (oxygen plasma or chemical gas) and lift-off procedures to fabricate the graphene devices studied in this thesis.

3.1.3 Edge contacts to graphene

A well-defined interface between the superconductor and graphene (G-S) is crucial for approaching high quality ballistic graphene Josephson junctions, where the transparency of the G-S interface directly affects the Andreev reflection. All previous reports on graphene Josephson junctions to date have involved superconducting contacts directly deposited onto the graphene surface, which results in diffusive transport through the junctions. In addition to the modest electronic quality of such devices, the use of surface contacts leaves ambiguity, that is, it is not clear how far electrons travel beneath the contact before entering the superconductor. Thanks to the recent development in fabrication techniques of graphene device, now we can make a one-dimensional (1D) electrical contact to graphene by choosing proper metals deposited along the exposed graphene edges.

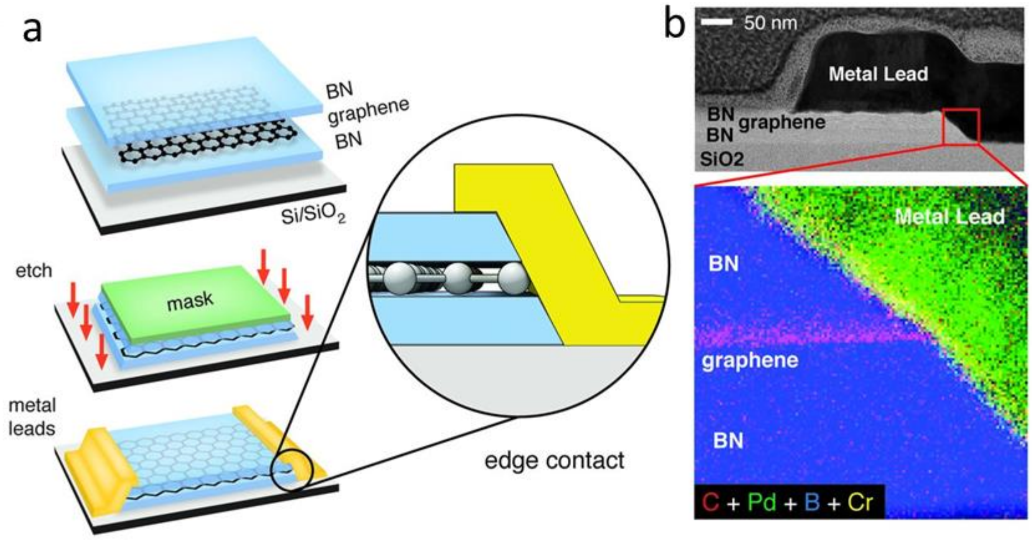

Fig. 3.8 One-dimensional edge contact to graphene

(a) Schematics of edge contact fabrication. **(b)** High-resolution bright-field STEM image showing details of the edge contact geometry. Fig. 3.8 is adapted from ref.[76]

To realize high quality ballistic graphene Josephson junctions we encapsulate graphene flakes between two hBN crystals using van der Waals pick-up method, which guarantees that the graphene is never in contact with any polymer during the assembling and thereafter. Electrical contact is made by metal deposition onto areas where the hBN/graphene/hBN van der Waals heterostructure has been etched through. Unlike earlier works, where metal deposition was carried out in a separate lithographic step, we begin by etching only the region to be contacted, followed immediately by metal deposition to avoid contamination and then to minimalize the contact resistance along the G-S interface, which is necessary to achieve a transparent contact. Instead of normal metal contacts, we sputter a superconductor Nb as contact to graphene, which has relatively higher critical temperature (T_C~8 K) and upper critical field (H_{C2}~4 T). We use 50nm thick film of Nb with an adhesion sublayer of 5 nm Ta. In addition, a 5 nm layer of Ta was put on top of Nb film to protect it from oxidation. The trilayer thin film was then deposited along the graphene edge by radio-frequency sputtering at a rate of 5 nm/min and a base pressure of ~10^{-9} Torr.

3.1.4 Graphene Josephson junction

After deposition of the superconducting contacts, the van der Waals heterostructure is etched into the desired geometries. For typical graphene Josephson junctions, the separation between two Nb contacts (junction length, L) varies from 100 nm to 2 µm and the junction width (W) ranges from 3 µm to 8 µm. In this thesis, we have investigated more than twenty ballistic graphene Josephson junctions. The schematic drawing and scanning electron microscopy image of one typical graphene Josephson junctions are shown in Fig. 3.9.

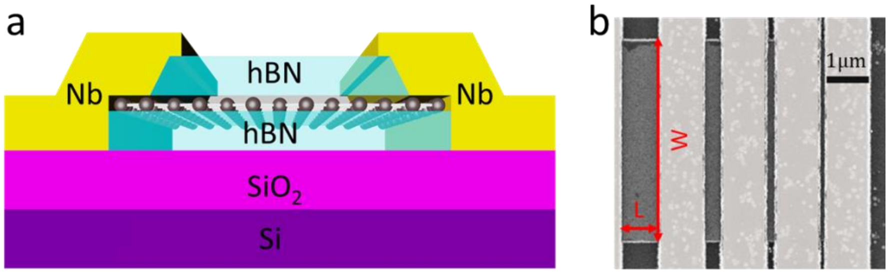

Fig. 3.9 Graphene Josephson junctions

(a) Schematics of graphene Josephson junction. Graphene sheet (grey atom array) is encapsulated by two hBN and placed on SiO_2/Si substrate. Superconducting Nb contacts are deposited along the exposed edges of graphene. **(b)** Scanning electron microscopy (SEM) image of one of our graphene Josephson junctions.

3.1.5 Graphene tunnelling transistor

We fabricated graphene-hBN tunnelling transistors using a sequence of mechanical exfoliation and dry transfer procedures. We first prepare a relatively thick (20-30 nm) hBN on top of oxidised silicon wafer which acted as a back gate. This thick hBN serves as a high-quality atomically flat substrate. We then transfer a first graphene on top of the selected thick hBN. A few-layer hBN is transferred on top of the first graphene flake by repeating the same procedure. This thin hBN serves as the tunnel barrier. The above processes are repeated again to complete the stack with the second graphene electrode. After depositing of 5 nm Ti / 50 nm Au metallic contacts, the structure is annealed at 200 °C in Ar/H_2 gas. One of our graphene tunnelling devices is shown in Fig. 3.10.

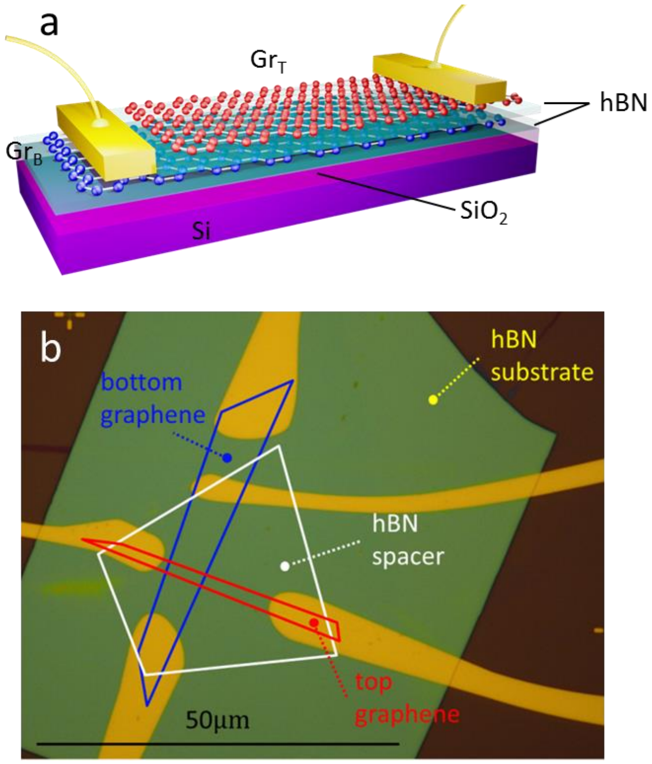

Fig. 3.10 Graphene tunnelling transistor

(a) Schematics of the tunnelling device. Bottom graphene (Gr_B) and top graphene (Gr_T) layers are separated by a thin hBN. The Gr_B-hBN-Gr_T heterostructure is placed on hBN-SiO_2/Si substrate. **(b)** Optical micrograph of one of our tunnelling devices. Two graphene sheets are separated by a trilayer hBN tunnel barrier (white outline). The overlap between Gr_B (blue outline) and Gr_T (red outline) corresponds to an active tunnelling area $A \approx 10\ \mu m^2$.

3.2 Electrical Measurement

3.2.1 Measurement set-up

Transport properties of graphene Josephson junctions and graphene tunnelling transistors in this thesis are measured in a liquid Helium cryostat with a base temperature of 4.2 K. Further cooling down to 0.3 K can be achieved by using a Helium 3 insert (Heliox VL, Oxford instruments, as shown in Fig. 3.11(a).) through pumping and adjusting the needle valve. For high temperature measurement, it is possible to achieve temperatures up to 300 K by controlling the heater near the sample. For magnetic fields below 6 T, a small magnet is mounted on to the IVC tube and provides magnet operation in persistent mode in a transport dewar, as shown in Fig. 3.11(d).

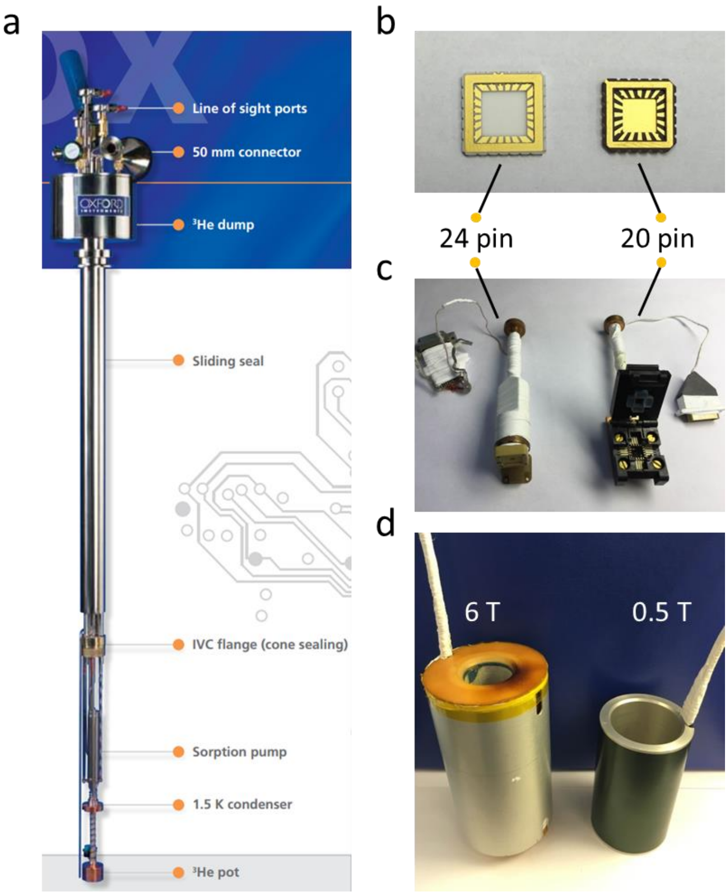

Fig. 3.11 Set-up for electrical transport measurements

(a) Heliox VL Helium 3 insert (Oxford Instruments). **(b)** 24 pin and 20 pin Chip carriers. **(c)** 24 pin and 20 pin sample holders. **(d)** 6 T and 0.5 T superconducting solenoids.

For the measurement of quantum interference (Fraunhofer pattern) of critical currents, the applied magnetic field is usually below 10 mT with a resolution up to 0.01 mT. Such requirement is satisfied by using a current source meter (Keithley 2614B) instead of the magnet power supplies (IPS 120, Oxford Instruments) to control the output current and determine the small magnetic field.

3.2.2 Resistance measurement

In this thesis, we carry out all the resistance measurements by standard low-frequency lock-in techniques using SR830 lock-in amplifiers (Stanford Research Systems). Typical values of resistances we measure range from a few tens of Ohms up to a few hundreds of kilo-Ohms. Thus, it is possible to connect a series resistor of 10 MΩ in the measurement circuit to provide a nearly constant ac current, measure the voltage drop across the device, and eventually determine the resistance. According to the designed geometry of graphene Josephson junctions, we use the four-probe configuration to measure the resistance, as schematically shown in Fig. 3.12(a).

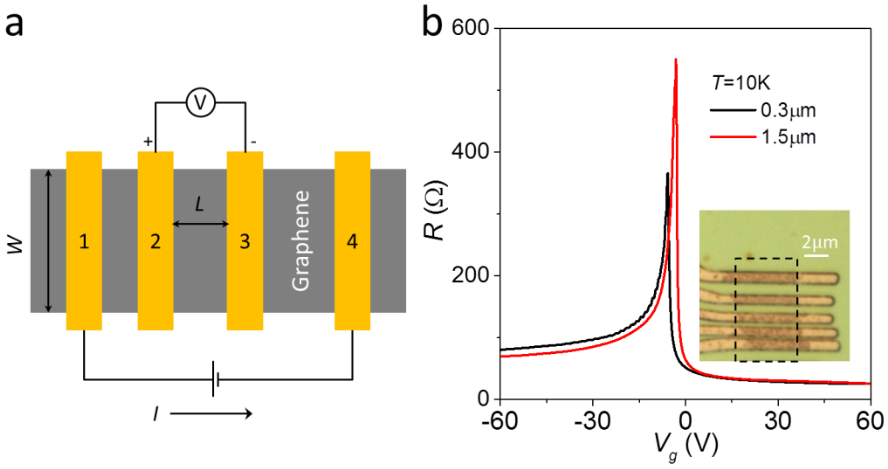

Fig. 3.12 Four-probe resistance measurement

(a) Schematics of four-probe measurements. A current I is driven from probe 1 to probe 4 while a voltage drop V is detected between probe 2 (high) and probe 3 (low). The grey area represents the graphene sheet and the golden areas indicate 4 superconducting Nb contacts. The silicon back gate and hBN are not shown in here. **(b)** The resistance of graphene Josephson junctions with same width W but difference L at T=10 K ($T > T_C$). The inset shows an optical micrograph of graphene Josephson junction. Graphene sheet is marked by the dashed area.

Fig. 3.12(b) shows the resistance of graphene Josephson junctions with same W but different L at T=10 K ($T > T_C$). One can tune the charge carrier density in graphene from electrons to holes by applying a back gate voltage (V_g) between the graphene and the highly doped Silicon substrate. The gate voltage induces a surface charge density in graphene via a two-plate capacitance, $n = \varepsilon\varepsilon_0 V_g/(ed)$, where ε_0 is the vacuum permittivity and ε the dielectric constant of SiO_2, e is the elementary charge and d the thickness of SiO_2. Due to the change of carrier density, the Fermi level (E_F) in graphene accordingly shifts to conduction (electron) band or valence (hole) band. Typically, the carrier density in MLG can be tuned from 10^{10} cm^{-2} to 10^{12} cm^{-2} by applying a gate voltage, which corresponds to E_F from a few meV to a few hundred meV, respectively.

From the resistance measurements, one can obtain important information of the graphene Josephson junctions, such as resistivity ($\rho = RW/L$), conductivity ($\sigma = 1/\rho$), inhomogeneity, mobility (μ) and contact resistance (R_C). Carrier mobility is one of the most important parameters for modern semiconductor materials, which represents how fast the charge carriers can move under an electric field and determines the conductivity of the semiconductor. As shown in Fig. 3.12(b), the resistance of graphene rapidly increases as we reduce the carrier density by gating, reaching its maximum value at the Dirac point. One can extract the carrier mobility $\mu = 1/en\rho$. The typical mobility of graphene in our graphene Josephson junction devices varies from 100,000 cm^{2}V^{-1}s^{-1} to 500, 000 cm^{2}V^{-1}s^{-1} at T=10 K.

3.2.3 Superconductivity measurement

Once we have cooled our sample down to 0.3 K, we can carry out the superconducting measurement of our graphene Josephson junctions. For current-voltage characteristics (I-V), the configuration is the same as in the normal-state resistance measurement, as shown in Fig. 3.13(a). We pass a dc current I_{dc} through probe 1 to Probe 4 and measure the voltage drop between probe 2 and probe 3. A typical I-V curve of one of our junctions is shown in Fig. 3.13(a). There is no voltage drop across the junction when the applied dc current is below the critical current I_C, indicating the sample is in a superconducting state. Further increasing the current will break the superconducting state. The critical current strongly depends on the sample geometry, junction quality and graphene doping level. I_C varies from 10 nA at the charge neutrality point (CNP) to 15 μA at high n-type doping in our graphene Josephson junctions.

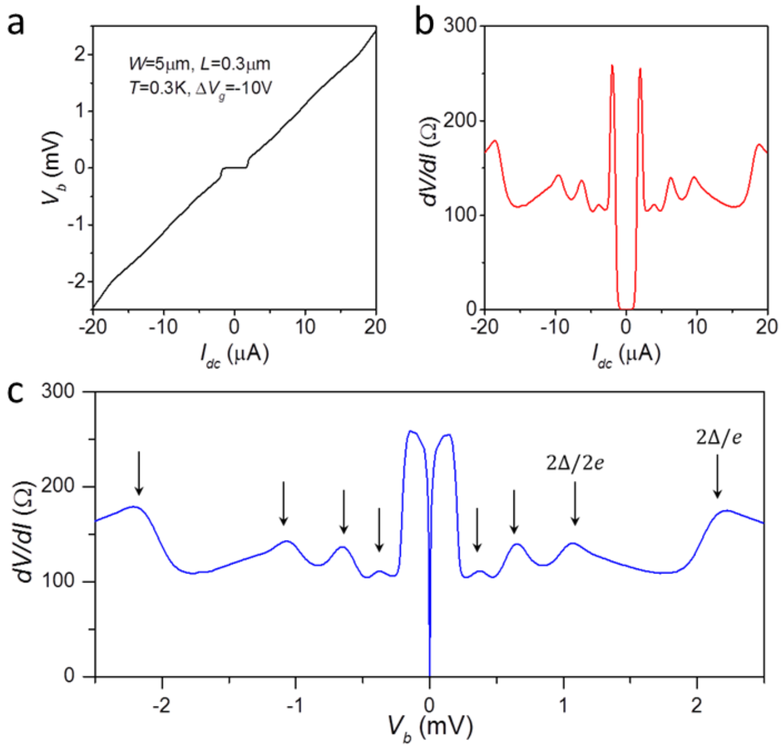

Fig. 3.13 Supercurrent and multiple Andreev reflections in graphene

(a) *I*-*V* characteristics. The zero voltage drop indicates the superconducting state. **(b)** Differential resistance *dV*/*dI* as a function of I_{dc}. **(c)** *dV*/*dI* as a function of applied bias V_b. A series of sub-harmonic peaks in *dV*/*dI* represent the multiple Andreev reflections in graphene Josephson junctions. The first and second order MAR are labelled by black arrows at $V_b = 2\Delta/e$ and $V_b = 2\Delta/2e$, respectively.

In order to measure the differential resistance *dV*/*dI* simultaneously, we mix a small ac current (I_{ac}=2 nA for example) with I_{dc} and then detect the ac voltage drop between two probes. Such an ac voltage drop can be very small (below 1 μV) and therefore a voltage amplifier (SR560, Stanford Research Systems) is always used here prior to the lock-in amplifier to magnify the ac voltage signal. A typical *dV*/*dI*-I_{dc} curve of one of our junctions is shown in Fig. 3.13(b). In graphene Josephson junctions, an electron in graphene can be reflected back and forth several times between the two S/G interfaces, gaining energy eV_b each time when it transverse the junction until it accumulates sufficient energy to enter the superconductor as a quasiparticle. The quantum mechanical description of this physical picture is so called multiple Andreev reflections (MAR). To observe MAR in our graphene

Josephson junctions, we measure the dV/dI of our device as a function of the bias voltage across the junction, as shown in Fig. 3.13(c). At zero bias, there is a giant dip indicating the proximity superconductivity. The peaks at $V_b = \pm 2.2$ meV mark the onset of first order MAR and corresponds to 2Δ, where Δ is the superconductor energy gap. Below 2Δ, there are a series of dV/dI peaks when $V_b = \pm 2\Delta/ne$, where n is an integer and e the elementary charge. Those sub-harmonic features arise from the MAR. As taken from Fig. 3.13(c), the sub-harmonic features occur at V_b = 1.1, 0.72, and 0.5 meV, corresponding to n = 2, 3 and 4 respectively. The observation of MAR indicates well defined G-S interfaces in our ballistic graphene Josephson junctions.

3.2.4 Tunnelling measurement

In our graphene-hBN tunnelling devices, the tunnelling current I is measured as a function of applied bias voltage V_b between the bottom and top graphene electrodes and the back gate voltage V_g applied between bottom graphene and highly doped silicon gate electrode. In order to measure the differential tunnelling conductance dI/dV, we mixed small low-frequency ac voltage to a dc bias V_b and measured the current with a lock-in amplifier. Typical I-V and dI/dV characteristics for different V_g measured at temperature of T=1.6 K are shown in the Fig. 3.14(a) and (b), respectively.

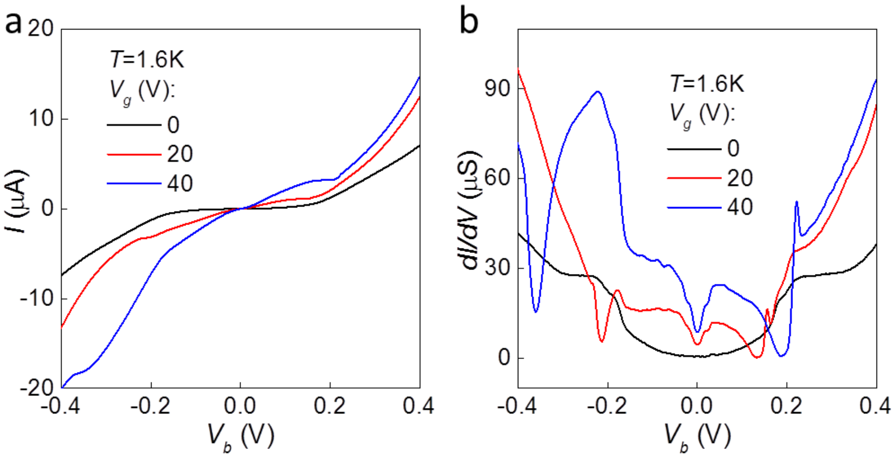

Fig. 3.14 Tunnelling characteristics of graphene-hBN tunnelling transistor

Measured tunnelling current I **(a)** and differential tunnelling conductance dI/dV **(b)** as a function of V_b for three different V_g at 1.6 K.

Chapter 4

Quantum oscillations of the critical current and high field superconducting proximity in ballistic graphene

The results demonstrated in chapter 4 are from the publication: “Quantum oscillations of the critical current and high field superconducting proximity in ballistic graphene” *Nature Physics* **12**, 318-322 (2016).

Due to the unique linear dispersion of graphene and its gate tunability, graphene provides an ideal platform to study the proximity superconductivity and the Josephson effect. However, previous reported graphene Josephson junctions are mostly limited into the diffusive transport regime, ballistic graphene Josephson junctions remain little studied.

Here, we demonstrate ballistic graphene Josephson junctions with micron scale mean free path and transparent interface. Due to the ballistic nature of the electrons propagating in the junction, pronounced Fabry-Pérot oscillations are observed in the normal-state resistance and the critical current. At low magnetic field, the critical current decays exponentially, showing a conventional Fraunhofer interference pattern. However, at higher magnetic field up to 1T, which corresponds to more than 1000 flux quanta, the proximity superconductivity still survives in the ballistic junctions. We attribute such high-field Josephson effect in ballistic graphene to the mesoscopic Andreev bound states that persist near the edges of graphene.

My personal contribution to this work is: I carried out the electrical transport measurements, analysed the data, and prepared all the figures for the main text and supplementary information.

The acknowledgements for the paper are: A.K.G., A.V.K. and M.B.S. designed the experiment. M.B.S. and A.V.K. fabricated the devices. M.J.Z. and J.R.P. carried out the measurements. M.B.S., M.J.Z., V.I.F., A.K.G. and J.R.P. analysed and interpreted the data. V.I.F. provided theory support. K.W. and T.T. supplied hBN crystals. A.M. and C.R.W. helped with experiments. M.B.S., J.P.R., V.I.F. and A.K.G. wrote the manuscript with input from all the authors.

Quantum oscillations of the critical current and high field superconducting proximity in ballistic graphene

M. Ben Shalom[1], M. J. Zhu[1], V. I. Fal'ko[2], A. Mishchenko[1], A. V. Kretinin[1], K. S. Novoselov[1], C. R. Woods[1], K. Watanabe[3], T. Taniguchi[3], A. K. Geim[1], J. R. Prance[2]

[1]*School of Physics & Astronomy, University of Manchester, Oxford Road, M13 9PL Manchester, UK*

[2]*Department of Physics, University of Lancaster, Lancaster, UK*

[3]*National Institute for Materials Science, 1-1 Namiki, Tsukuba, 305-0044 Japan*

Graphene-based Josephson junctions have attracted significant interest as a novel system to study the proximity effect[1-3] due to graphene's unique electronic spectrum and the possibility to tune junction properties by gate voltage[4-16]. Here we describe graphene junctions with the mean free path of several micrometers, low contact resistance and large supercurrents. Such devices exhibit pronounced Fabry-Pérot oscillations not only in the normal-state resistance but also in the critical current. The proximity effect is mostly suppressed in magnetic fields of <10 mT, showing the conventional Fraunhofer pattern. Unexpectedly, some proximity survives even in fields higher than 1 T. Superconducting states randomly appear and disappear as a function of field and carrier concentration, and each of them exhibits a supercurrent carrying capacity close to the universal limit[17,18] of $e\Delta/h$ where Δ is the superconducting gap, e the electron charge and h Planck's constant. We attribute the high-field Josephson effect to mesoscopic Andreev states that persist near graphene edges. Our work reveals new proximity regimes that can be controlled by quantum confinement and cyclotron motion.

The superconducting proximity effect relies on penetration of Cooper pairs from a superconductor (S) into a normal metal (N) and is most pronounced in systems with transparent SN interfaces and weak scattering so that superconducting correlations penetrate deep inside the normal metal. Despite being one atom thick and having a low density of states, which vanishes at the Dirac point, graphene (G) can exhibit low contact resistance and ballistic transport on a micrometer scale[19,20] exceeding a distance between superconducting leads by an order of magnitude. These properties combined with the possibility to electrostatically control the carrier density n offer tunable Josephson junctions in a regime that can be referred to as ballistic proximity superconductivity[21]. Despite intense interest in SGS devices[3-16] that can show features qualitatively different from the conventional SNS behavior[2,3], ballistic graphene Josephson junctions[15,16] remain little studied.

Our SGS devices are schematically shown in Fig. 4.1 and described in further detail in Supplementary Section 1. The essential technological difference from the previously studied SGS junctions[4-14] is the use of graphene encapsulated between boron-nitride crystals[19,20] as well as a new nanostrip geometry of the contacts. This allows high carrier mobility, low charge inhomogeneity and low contact resistance. More than twenty SGS junctions with the width W between 3 and 8 μm and the length L between 0.15 and 2.5 μm were studied, all exhibiting a finite supercurrent at low temperatures (T), reproducible behavior and consistent changes with L and W. First, we characterize the devices above the transition temperature $T_C \approx 7$ K of our superconducting contacts. Fig. 4.1b shows examples of the normal-state resistance R_n as a function of back gate voltage V_g that changes n in graphene. The neutrality point (NP) was found shifted to negative V_g by a few V, with the shift being consistently larger for shorter devices (Supplementary Information). This is due to electron doping induced by our Nb contacts. For ballistic graphene, such doping is uniform away from the metal interface[22]. The observed smearing of $R_n(V_g)$ curves near the NP allows an estimate for charge inhomogeneity in the graphene bulk as $\approx 2\times10^{10}$ cm^{-2}. For consistency, data for devices with different L are presented as a function of ΔV_g, the gate voltage counted from the NP.

For positive ΔV_g (electron doping) and $n > 10^{11}$ cm^{-2}, SGS junctions made from the same graphene crystal and having the same W exhibit the same $R_n(\Delta V_g)$ dependence, independently of L (Fig. 4.1b). This shows that mean free path is larger than the contact separation and yields carrier mobility > 300,000 cm^2 V^{-1} s^{-1}, in agreement with the quality measured for similarly made Hall bar devices. The dashed curve in Fig. 4.1b indicates the behavior expected in the quantum ballistic limit, $R_Q = (h/e^2)/4N$ where $N = \mathrm{int}(2W/\lambda_F)$ is the number of propagating electron modes, λ_F the Fermi wavelength that depends on $n(\Delta V_g)$ and the factor 4 corresponds to graphene's degeneracy. The difference between R_Q and the experimental curves yields a record low contact resistivity, ≈ 35 Ohm μm. This value corresponds to an angle-averaged transmission probability $T_r \approx 0.8$ (Supplementary Section 2).

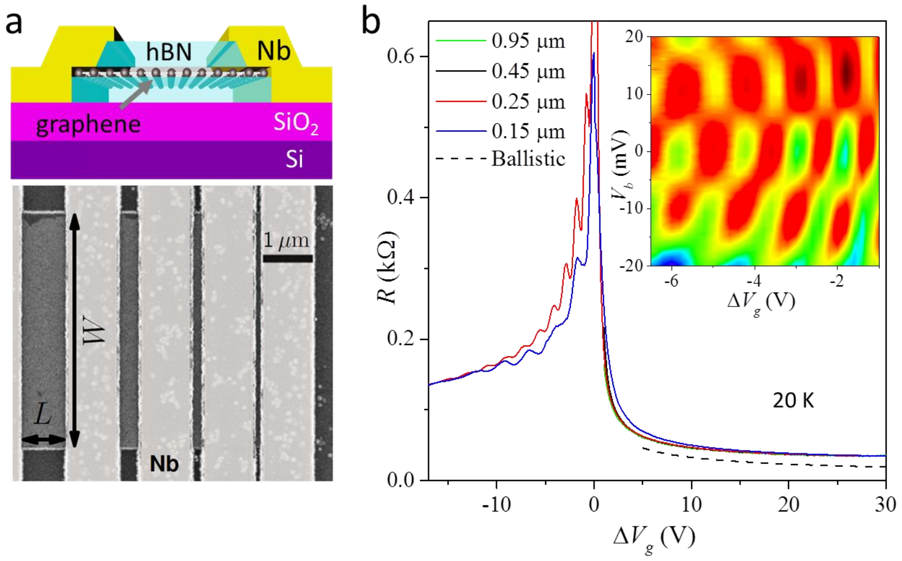

Fig. 4.1 Ballistic SGS junctions

a, Top: Junctions' schematics. Bottom: Electron micrograph of a set of four junctions with different L. A few nm-wide graphene ledge (top drawing) is referred to as a nanostrip contact. **b**, Typical behavior for SGS junctions with different L but for the same set of junctions with W = 5 μm. To avoid an obscuring overlap between four oscillating curves, we plot R_n at negative ΔV_g only for the two shortest junctions. For positive $\Delta V_g > 5$ V, the four curves overlap within the line width. The dashed curve shows calculated $R_Q(n)$. Inset: Changes in the differential conductance dI/dV; L =0.25 μm. Color scale: -1 to 1 mS.

For hole doping, R_n becomes significantly higher indicating smaller Tr. This is because pn junctions appear at the Nb contacts and lead to partial reflection of electron waves, which effectively creates a Fabry-Pérot (FP) cavity[5,23]. The standing waves lead to pronounced oscillations in R_n as a function of both V_g and applied bias

V_b (Fig. 4.1b). The oscillatory behavior indicates that charge carriers can cross the graphene strip several times preserving their monochromaticity and coherence. Some FP oscillations could also be discerned for positive ΔV_g but they were much weaker because of higher *Tr*. The observed FP behavior in the normal-state agrees with the earlier reports[5,23]. Its details can be modelled accurately if we take into account that the position of pn junctions varies with V_g so that the effective length of the FP interferometer becomes notably shorter than L at low hole doping (Supplementary Section 3).

After characterizing our SGS devices at $T > T_C$, we turn to their superconducting behavior. All of the junctions (including $L = 2.5$ µm) exhibited the fully developed proximity effect. Fig. 4.2a,b show that the critical current I_c remained finite at the NP and rapidly increased with $|\Delta V_g|$, reaching densities > 5 µA/µm for high electron doping and short L, notably larger than I_c previously reported[4-16]. Such high I_c are due to ballistic transport and low contact resistance. Indeed, I_c can theoretically reach a value[2,24]

$$I_c = \alpha\Delta/eR_n \tag{1}$$

with $\alpha \approx 2.1$. Because in our devices $R_n \approx R_Q = h/4Ne^2$, the equation implies that we approach the quantum limit $I_c \approx (e\Delta/h)4N$ where the supercurrent is determined solely by the number of propagating electronic modes that transfer Cooper pairs between superconducting contacts, and each of the modes has the supercurrent carrying capacity[3,17] $I_Q \approx e\Delta/h$.

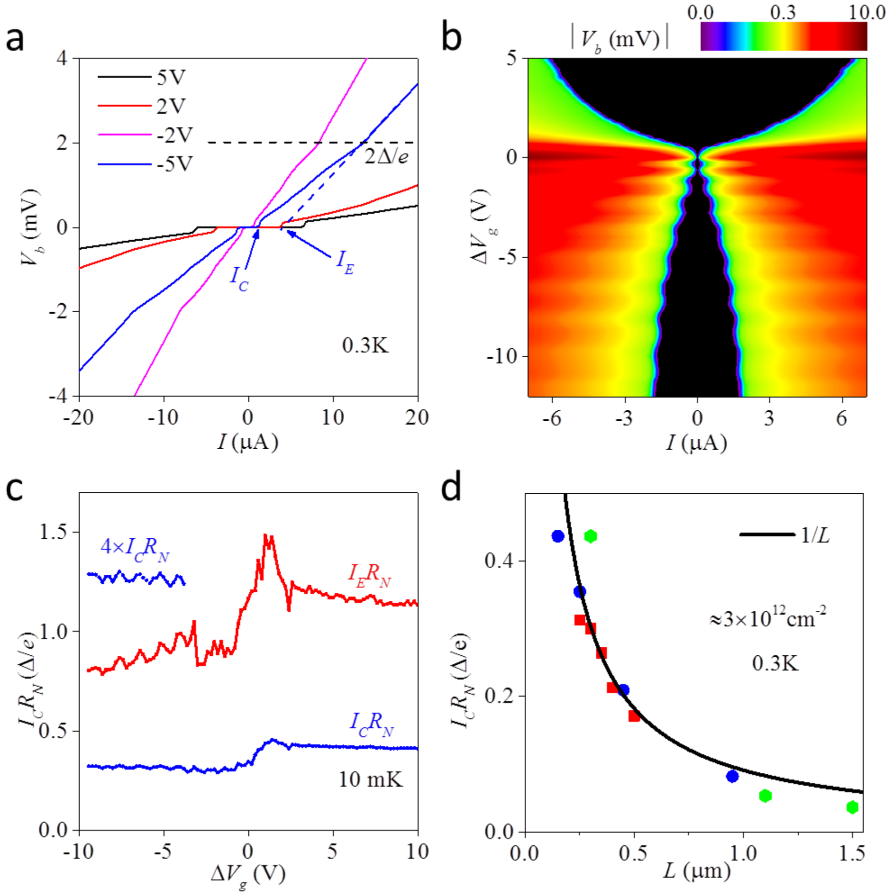

Fig. 4.2 Quantum oscillations in supercurrent

a, Examples of *I*-*V* characteristics for ballistic SGS junctions in the superconducting state. The data are for the device in Fig. 4.1 with L = 0.25 μm. The arrows explain notions I_c and I_e. **b**, Absolute voltage drop $|V_b|$ across the SGS junction in (a) for a wide range of doping. The black region corresponds to the zero-resistance state, and its edge exhibits clear FP oscillations. **c**, I_cR_n and I_eR_n for a device with L = 0.3 μm, W = 6.5 μm and $\Delta \approx 0.8$ meV estimated from its T_C. Each data point is extracted from a trace such as in (a). Inset: Oscillatory part of I_cR_n is magnified. Similar behavior was observed for other devices. **d**, Effect of the junction length on supercurrent for 12 devices with different W. Red symbols - W = 3 μm; blue - 5 μm; green - 6.5 μm. For each data set, I_c follows the same dependence as I_cR_n because R_n were practically independent of L for the same W. For the two longest devices in (d), the critical current falls below the plotted 1/L dependence, probably because of thermal fluctuations (Supplementary Section 4).

Eq. (1) suggests that I_cR_n should be a constant. This holds well in our SGS devices away from the NP (Fig. 4.2c) and indicates that, at low T, external noise, fluctuations and other mechanisms[4-16] which are dependent on n or R_n do not limit I_c. However,

Fig. 4.2c yields α that is notably smaller than the expected constant in eq. (1). For hole doping, this can be attributed to the presence of pn junctions at the superconducting interfaces but even for electron doping and high Tr we find $\alpha \approx 0.4$ (Fig. 4.2c). Furthermore, we measured the excess current $I_e > I_c$ as shown in Fig. 4.2a and found that, in the case of I_e, α also does not reach a value close to 2.1 (Fig. 4.2c). This corresponds to the fact that all our devices were in the limit of long $L > hv_F/\Delta$ (v_F is the Femi velocity), as also follows from the $1/L$ dependence found for I_cR_n (Fig. 4.2d). In this long-junction regime, the critical current is given by $I_c \approx E_{Th}/eR_n$ being determined by the Thouless energy E_{Th} rather than the superconducting gap[2,17,24]. For a ballistic system, E_{Th} depends on time charge carriers spent inside the FP cavity and can be estimated[25] as $\sim hv_F/L$. This yields $I_c \propto 1/L$ and $I_cR_n \propto 1/L$ because R_n is independent of ballistic device's length. Our detailed studies of I_c as a function of T and L show that all data for I_cR_n/E_{Th} collapse on a universal curve $f(T/E_{Th})$ with $E_{Th} \sim hv_F/L$, which again agrees well with expectations for the long-junction limit (Supplementary Section 4). We estimate that to reach the transition regime $E_{Th}/\Delta \sim 1$ for our SGS junctions would require $L < 100$ nm. Let us also mention that no definitive signs of specular Andreev reflection[3,17] were found in our devices (Supplementary Section 4).

As a consequence of FP resonances in the normal-state (Fig. 4.1), the supercurrent also exhibits quantum oscillations that are clearly seen in Fig. 4.2b for hole doping. Eq. (1) implies that such oscillations in I_c should occur simply because R_n oscillates. Indeed, R_n and I_c are found to oscillate in antiphase, compensating each other in the final products eI_cR_n. However, we find that oscillations in the critical current are approximately 3 times stronger than those in R_n. This observation is consistent with the fact that I_c is not only inverse proportional to R_n but also depends on the Thouless energy as discussed above whereas the latter is expected to oscillate because of the oscillating transparency of FP resonators (Supplementary Section 4). We note in passing that R_n and its FP oscillations exhibit little temperature dependence below 20K, which justifies the use of R_n measured above T_C in the above analysis of the superconducting behavior.

In magnetic field B, our ballistic junctions exhibit further striking departures from the conventional behavior (Fig. 4.3). In small B such that a few flux quanta $\phi_0 = h/2e$ enter an SGS junction, we observe the standard Fraunhofer dependence[2]

$$I_c = I_c(B = 0)|\sin(\pi\Phi/\phi_0)/(\pi\Phi/\phi_0)| \qquad (2)$$

where $\Phi = L \times W \times B$ is the flux through the junction area. Marked deviations from eq. (2) occur in $B > 5$ mT (Fig. 4.3a). Figs. 4.3b-e show that, in this regime, the supercurrent no longer follows the oscillatory Fraunhofer pattern but pockets of proximity superconductivity can randomly appear as a function of n and B. At low doping, the pockets can be separated by extended regions of the normal-state where no supercurrent could be detected with accuracy of a few nA << I_Q (Figs. 4.3c,e). Within each pocket, I-V characteristics exhibit a gapped behavior (inset of Fig. 4.3d) with $I_c \sim I_Q \approx 40$ nA, although the exact value depends on doping and I_c falls down to ≈ 10 nA close to the NP, possibly due to rising contributions of electrical noise and thermal fluctuations that suppress apparent I_c (Fig. 4.3c). These proximity states persist until B as large as ≈1 T ($\Phi/\phi_0 \sim 10^3$) and are highly reproducible, although occasional flux jumps in Nb contacts can reset the proximity pattern (Supplementary Section 5). Correlation analysis presented in Supplementary Section 6 yields that, to suppress such superconducting states, it requires changes in Φ of $\approx \phi_0$ and changes in the Fermi energy of ≈ 1 meV.

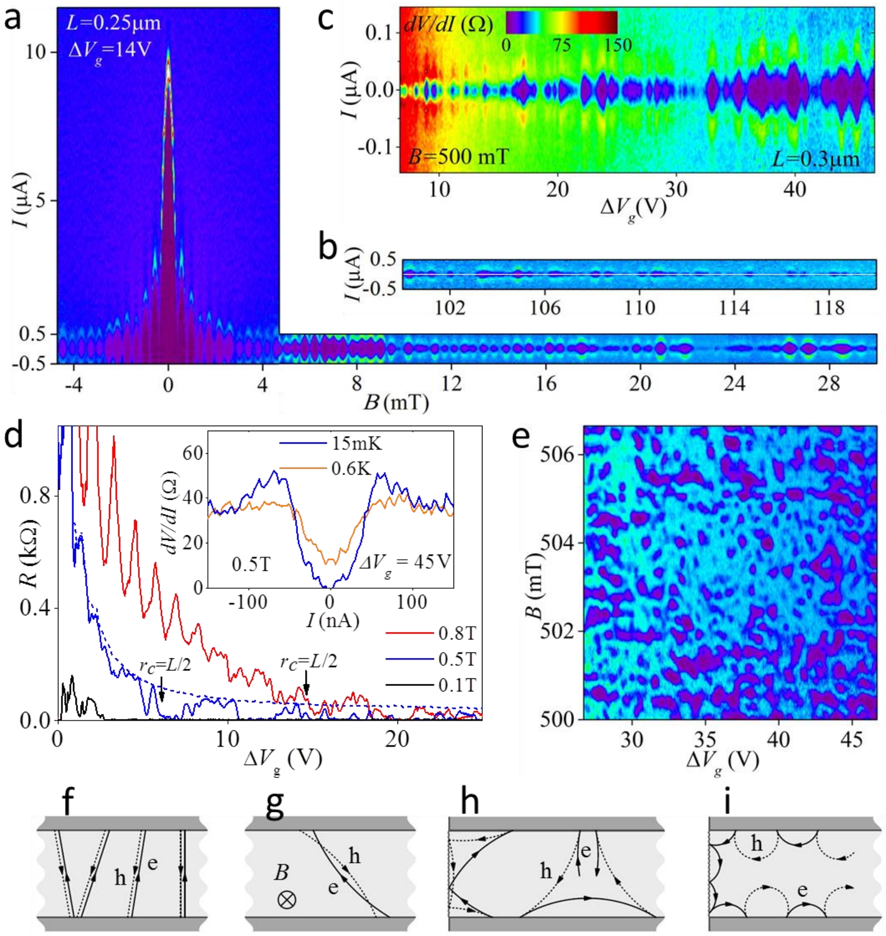

Fig. 4.3 Fluctuating proximity superconductivity

a, Example of *dV*/*dI* as a function of applied current *I* and *B*. The purple regions correspond to the zero-resistance state and their edges mark I_c (see Supplementary Section 10). The map is symmetric in both *I* and *B*. The white curve is given by eq. (2). The low-*B* periodicity is ≈ 0.4 mT, smaller than expected from the device's area, which is attributed to the Meissner screening that focuses the field into the junction[30]. **b**, Continuation of the map from (a) above 0.1 T. Intervals with finite I_c continue randomly appear, despite the Fraunhofer curve is indistinguishable from zero. **c**, Another high-*B* example but as a function of ΔV_g in 0.5 T. **d**, Examples of low-current resistance (I = 2 nA) in different *B*. The dashed curve for 0.5 T shows that current I = 150 nA > I_Q completely suppresses superconductivity. The arrows mark the expected onset of edge state transport. **e**, Local map of fluctuating superconductivity. T ≈10 mK; all color scales are as in (c). Inset in (d): Typical *I-V* characteristics for high-*B* superconducting states. **f-i**, Electron-hole paths responsible for Andreev states in ballistic junctions in zero (f), intermediate (g,h) and high *B* (i). In (h), the cyclotron bending suppresses the transfer of Cooper pairs in the middle of the graphene strip but Andreev states can persist near the edges.

The semiclassical description[2,24-27] of the superconducting proximity relates the Cooper pair transfer between the leads to electrons and Andreev-reflected holes, which travel along same trajectories but in opposite directions (Fig. 4.3f). In low B, interference between many Andreev states traversing the graphene strip results in the Fraunhofer-type oscillatory suppression of I_c described by eq. (2) (see Fig. 4.3a). Although not reported before, the Fraunhofer pattern in ballistic devices can be expected to break down in relatively small B because the cyclotron motion deflects electrons and holes in opposite directions so that they can no longer retrace each other (Fig. 4.3g). We have estimated the field required to suppress Andreev states in the bulk as $B^* \sim \Delta/eLv_F$ (Supplementary Section 7). For the devices in Fig. 4.3, this yields $B^* \approx 5$ mT, in agreement with the field where strong deviations from the Fraunhofer curve are observed.

As for the random pockets of superconductivity at $B >> B^*$ which exhibit I_c much higher than that expected from eq. (2), we invoke the previously noticed analogy[18] between mesoscopic fluctuations in the normal-state conductance[28], $<\delta G^2>$ and in the supercurrent[17,18], $<\delta I_c^2>$. Both types of fluctuations are due to interference of electron waves propagating along different paths but start and finish together. In contrast to the case of B =0, for which semiclassical phases of counter-propagating electrons and holes near the Fermi level cancel each other because of time-reversal symmetry (Fig. 4.3f), electrons and holes propagating along non-retracing trajectories in a finite B acquire large and random phase differences (Figs. 4.3g,h). Averaging over all imaginable geometrical paths would lead to complete suppression of the supercurrent[18]. However, for each given realisation of either diffusive or chaotic ballistic SNS junction, the characteristic values of fluctuations are set[17,18,28-30] at $<\delta G^2>^{1/2} \sim e^2/h$ and $<\delta I_c^2>^{1/2} \sim e\Delta/h$. In the case of $B >> B^*$, non-retracing paths that can transfer Cooper pairs between superconducting contacts can occur only near graphene edges (see Fig. 4.3h and Supplementary Section 7). In a way, a combination of cyclotron motion and edge scattering provides a chaotic ballistic billiard near each graphene edge, and this leads to random pockets of superconductivity with $I_c = <\delta I_c^2>^{1/2} \sim I_Q$. Moreover, the analogy with chaotic billiards allows us to estimate the change in the Fermi energy, which is needed to change a realization of the mesoscopic system and, therefore, suppress an existing pocket of superconductivity. The required change is again given by the Thouless energy $E_{Th} \sim hv_F/\Lambda$ where Λ is the typical length of Andreev paths in a strong magnetic field (Fig. 4.3h). At high B, we estimate Λ as $\approx(r_cL)^{1/2}$ where r_c is the cyclotron radius. This yields $E_{Th} \leq 1$ meV, in agreement with the observed changes in doping which are required to suppress the pockets of superconducting proximity (Supplementary Section 6). An interference pattern in mesoscopic systems is also known[18,28-30] to change upon changing the flux Φ through the system by $\approx\phi_0$. This scale agrees well with that observed experimentally (Fig. 4.S8).

Finally, the discussed mesoscopic proximity effect can be expected to disappear if r_c becomes shorter than $L/2$ (Fig. 4.3i). This condition is marked in Fig. 4.3d and seen more clearly in the data of Supplementary Section 8. It is also worth noting that that the near-edge superconductivity was not observed for hole doping, which we attribute to the fact that Klein tunneling in graphene collimates trajectories perpendicular to the pn interface[23], making it essentially impossible to form closed-loop Andreev states shown in Fig. 4.3h (Supplementary Section 7). In principle, the effect of near-edge Andreev states could be further enhanced by presence of extended electronic states at graphene edges[16] but, based on our experimental data, no evidence for this or other spatial inhomogeneity was found in the studied samples (Supplementary Section 9).

Methods

The measurements were carried out in a helium-3 cryostat for T down to 0.3 K and in a dilution refrigerator, for lower T. All electrical connections to the sample passed through cold RC filters (Aivon Therma) and additional ac filters were on the top of the cryostats. The differential resistance was measured in the quasi-four-terminal geometry (using 4 superconducting leads to an SGS junction) and in the current-driven configuration using an Aivon preamplifier and a lock-in amplifier. To probe the superconducting proximity, we used an excitation current of 2 nA.

References

[1] H. Meissner. Range of order of superconducting electrons. *Phys. Rev. Lett.* **2**, 458-459 (1959).

[2] M. Tinkham, *Introduction to superconductivity*. Courier Dover Publications, 2012.

[3] C. W. J. Beenakker. Colloquium: Andreev reflection and Klein tunneling in graphene. *Rev. Mod. Phys.* **80**, 1337-1354 (2008).

[4] H. B. Heersche, P. Jarillo-Herrero, J. B. Oostinga, L. M. K. Vandersypen, A. F. Morpurgo. Bipolar supercurrent in graphene. *Nature* **446**, 56-59 (2007).

[5] F. Miao, S. Wijeratne, Y. Zhang, U. C. Coskun, W. Bao, C. N. Lau. Phase-coherent transport in graphene quantum billiards. *Science* **317**, 1530-1533 (2007).

[6] X. Du, I. Skachko, E. Andrei. Josephson current and multiple Andreev reflections in graphene SNS junctions. *Phys. Rev. B* **77**, 184507 (2008).

[7] C. Ojeda-Aristizabal, M. Ferrier, S. Guéron, H. Bouchiat. Tuning the proximity effect in a superconductor-graphene-superconductor junction. *Phys. Rev. B* **79**, 165436 (2009).

[8] C. Girit *et al*. Tunable graphene dc superconducting quantum interference device. *Nano Lett.* **9**, 198–199 (2009).

[9] I. V. Borzenets, U. C. Coskun, S. J. Jones, G. Finkelstein. Phase diffusion in graphene-based Josephson junctions. *Phys. Rev. Lett.* **107**, 137005 (2011).

[10] K. Komatsu, C. Li, S. Autier-Laurent, H. Bouchiat, S. Gueron. Superconducting proximity effect through graphene from zero field to the quantum Hall regime. *Phys. Rev. B* **86**, 115412 (2012).

[11] U. C. Coskun, M. Brenner, T. Hymel, V. Vakaryuk, A. Levchenko, A. Bezryadin. Distribution of supercurrent switching in graphene under proximity effect. *Phys. Rev. Lett.* **108**, 097003 (2012).

[12] N. Mizuno, B. Nielsen, X. Du. Ballistic-like supercurrent in suspended graphene Josephson weak links. *Nature Commun.* **4**, 3716 (2013).

[13] J. H. Choi *et al*. Complete gate control of supercurrent in graphene pn junctions. *Nature Commun.* **4**, 3525 (2013).

[14] F. Deon, S. Šopić, A. F. Morpurgo. Tuning the influence of microscopic decoherence on the superconducting proximity effect in a graphene Andreev interferometer. *Phys. Rev. Lett.* **112**, 126803 (2014).

[15] V. E. Calado *et al*. Ballistic Josephson junctions in edge-contacted graphene. arXiv:1501.06817.

[16] M. T. Allen *et al*. Spatially resolved edge currents and guided-wave electronic states in graphene. arXiv:1504.07630.

[17] C. W. J. Beenakker. Universal limit of critical-current fluctuations in mesoscopic Josephson junctions. *Phys. Rev. Lett.* **67**, 3836-3839 (1991).

[18] B. L. Altshuler, B. Z. Spivak. Mesoscopic fluctuations in a superconductor-normal metal-superconductor junction. *Sov. Phys. JETP* **65**, 343-347 (1987).

[19] A. S. Mayorov *et al*. Micrometer-scale ballistic transport in encapsulated graphene at room temperature. *Nano Lett.* **11**, 2396-2399 (2011).

[20] L. Wang *et al*. One-dimensional electrical contact to a two-dimensional material. *Science* **342**, 614-617 (2013).

[21] I. P. Krylov, Y. V. Sharvin. Radio-frequency size effect in a layer of normal metal bounded by its superconducting phase. *Sov. Phys. JETP* **37**, 481-486 (1973).

[22] P. Blake *et al*. Influence of metal contacts and charge inhomogeneity on transport properties of graphene near the neutrality point. *Solid State Commun.* **149**, 1068-1071 (2009).

[23] P. Rickhaus *et al*. Ballistic interferences in suspended graphene. *Nature Commun.* **4**, 2342 (2013).

[24] P. Dubos, H. Courtois, B. Pannetier, F. K. Wilhelm, A. D. Zaikin, G. Schön. Josephson critical current in a long mesoscopic SNS junction. *Phys. Rev. B* **63**, 064502 (2001).

[25] C. Ishii. Josephson currents through junctions with normal metal barriers. *Prog. Theor. Phys.* **44**, 1525-1547 (1970).

[26] A. F. Andreev. The thermal conductivity of the intermediate state in superconductors. *Sov. Phys. JETP* **19**, 1228-1231 (1964).

[27] T. M. Klapwijk. Proximity effect from an Andreev perspective. *J. Superconductivity* **17**, 593-611 (2004).

[28] R. A. Jalabert, H. U. Baranger, A. D. Stone. Conductance fluctuations in the ballistic regime: A probe of quantum chaos? *Phys. Rev. Lett.* **65**, 2442-2445 (1990).

[29] H. Takayanagi, J. B. Hansen, J. Nitta. Mesoscopic fluctuations of the critical current in a superconductor—normal-conductor—superconductor. *Phys. Rev. Lett.* **74**, 166-169 (1995).

[30] J. P. Heida, B. J. van Wees, T. M. Klapwijk, G. Borghs. Nonlocal supercurrent in mesoscopic Josephson junctions. *Phys. Rev. B* **57**, 5618-5621 (1998).

Acknowledgements

This work was supported by the European Research Council, the EU Graphene Flagship Program, the Royal Society, the Air Force Office of Scientific Research, the Office of Naval Research and ERC Synergy Grant Hetero2D. We thank C. Barton, G.

H. Auton, R.V. Gorbachev and F. Guinea for helpful discussions. M.J.Z. acknowledges the National University of Defense Technology (China) overseas PhD scholarship. J.R.P. acknowledges support of the Marie Curie People Program.

Contributions

A.K.G., A.V.K. and M.B.S. designed the experiment. M.B.S. and A.V.K. fabricated the devices. M.J.Z and J.R.P. carried out the measurements. M.B.S., M.J.Z, V.I.F, A.K.G. and J.R.P. analyzed and interpreted the data. V.I.F provided theory support. K.W. and T.T. supplied hBN crystals. A.M. and C.R.W. helped with experiments. M.B.S., J.P.R, V.I.F and A.K.G wrote the manuscript with input from all the authors.

Additional information

Correspondence and requests for materials should be addressed to A.K.G or V.I.F. geim@man.ac.uk and v.falko@lancaster.ac.uk

Quantum oscillations of the critical current and high field superconducting proximity in ballistic graphene

Supplementary Information

M. Ben Shalom *et al*

1. Device fabrication

Monolayer graphene was encapsulated between two relatively thick (typically, >30 nm) crystals of hexagonal boron nitride (hBN) by using the dry-peel transfer technique as detailed previously[S1]. The hBN-graphene-hBN stack was assembled on an oxidized Si wafer (300 nm of SiO_2) and then annealed at 300 °C in a forming gas (Ar-H_2 mixture) for 3 hours. As the next step we used the standard electron-beam lithography to make a PMMA mask that would define contact regions. Reactive ion etching (Oxford Plasma Lab 100) was employed to make trenches in the heterostructure through the mask. The etching process was optimized to achieve high etching rates for hBN with respect to both PMMA and graphene. We used a mixture of CHF_3 and O_2 which allowed rates of 300, 60 and 3 nm per min for hBN, PMMA and graphene, respectively. Importantly, the PMMA mask was not cross-linked during the etching and allowed easy liftoff so that metal contacts could be deposited directly after plasma etching. This procedure allowed us to avoid additional processing and, accordingly, contamination of the exposed graphene edges. The same etching recipe was later used to define the device geometry. We chose that all Josephson junctions made on the same graphene crystal would have the same width W.

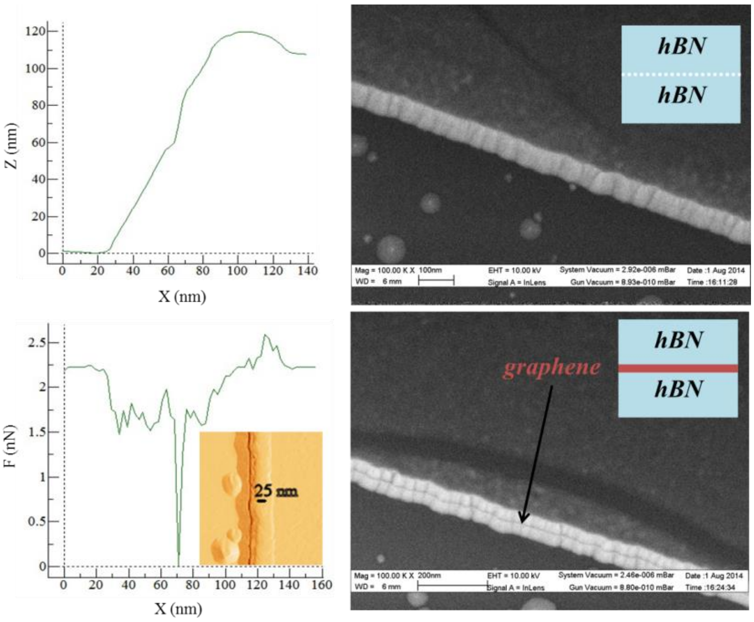

Fig. 4.S1 Nanostrip contacts to encapsulated graphene

Left column: Atomic force microscopy of a plasma-etched edge of an hBN-graphene-hBN stack. Top: Typical topography line scan across the step. Bottom: Typical adhesion scan. Inset: Imaging in the adhesion mode (color scale: 0 to 2.5 nN). A narrow graphene ledge appears in the middle due to the large difference in etching rates between graphene and hBN. The right column shows scanning electron microscopy images of etched edges for hBN-hBN and hBN-graphene-hBN stacks. The narrow step is clearly visible in the bottom image.

Due to the large difference in the etching rates of graphene and hBN, the resulting edge profile was found to exhibit a step of, typically, 5 nm in width as depicted schematically in Fig. 4.1a of the main text and shown in micrographs of Fig. 4.S1. This step developed because graphene effectively served as a mask during etching of the bottom hBN, leading to a gradual exposure of graphene buried under the top hBN. In comparison with contacts prepared in the same manner but without the highly selective etching, the graphene nanostrip provided a notably lower contact resistance (see below).

2. Superconducting contacts to graphene

As superconducting contacts, we used 50 nm thick films of Nb with an adhesion sublayer of Ta (5nm). Also, a few nm of Ta were put on top to protect Nb from oxidation. The trilayer film was deposited by radio-frequency sputtering at a rate of 5 nm per min and a base pressure of $\approx 10^{-9}$ Torr. The resulting films exhibited a sharp superconducting transition as shown in Fig. 4.S2a. Here T_C =7.2 K and the second critical field H_{C2} ≈3.5 T, which yields the superconducting gap $\Delta = 1.76T_C \approx 12$K and the coherence length $\xi = (\phi_0/2\pi H_{C2})^{1/2} \approx 10$ nm. The data are for the same set of SGS devices as in Fig. 4.1 of the main text. Variations in superconducting characteristics between different sets of SGS junctions did not exceed 10%.

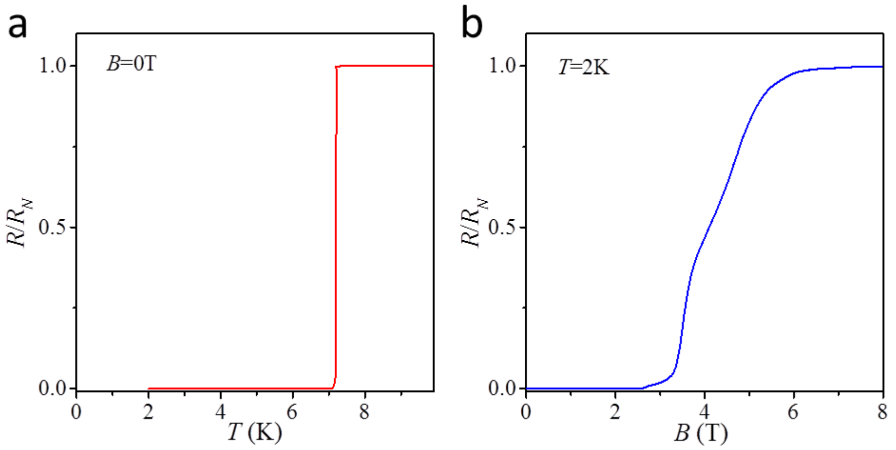

Fig. 4.S2 Characterization of Nb contacts

Resistive measurements of their critical temperature (**a**) and critical field (**b**). R_n is the normal-state resistance of our Nb/Ta films above T_C.

For a ballistic device with superconducting (zero-resistance) leads, the measured resistance is given by $R_n = R_Q + 2R_C$ where R_Q is the quantum ballistic resistance determined in the main text and R_C is the contact resistance per interface. Fig. 4.1b of the main text plots R_Q using the Fermi wavelength λ_F that was calculated from carrier density n induced by gate voltage, using the standard equation $\lambda_F = 2\sqrt{\pi/C_g\Delta V_g}$ where the capacitance C_g (typically, $\approx 5\times10^{10}$ cm^{-2}/V) was determined experimentally from the frequency of Shubnikov-Haas oscillations at high n. One can see that, independently of L, all the devices in Fig. 4.1b exhibited the same shift in R_n upwards with respect to R_Q, which indicates a constant resistance contribution, $2R_C$. For electron doping of graphene with $\Delta V_g \sim 10$ V, which corresponds to $n \approx 5\times10^{11}$ cm^{-2}, $R_Q \approx 32$ Ohm for devices with $W = 5$ μm whereas we measured $R \approx 46$ Ohm. This yields $R_C \approx 7$ Ohm and contact resistivity of 35 Ohm μm. We find the same R_C for all $\Delta V_g > 10$ V. The quality of our graphene-superconductor interface can also be characterized by their average transmission probability T_r given by[S2] $Tr = R_Q/(R_Q + R_C)$. For $\Delta V_g \approx 10$ V, we calculate $T_r \approx 0.82$, that is, we have a highly transparent GS interface. As discussed below, this estimate is also supported by analysis of differential *I-V* characteristics in the superconducting state.

The low contact resistivity and high transmission probability of our nanostrip contacts were found to be highly reproducible for different devices, even though the etching and metal deposition required transfer between different equipment and, consequently, exposure of the interfaces to air. The nanostrip contacts' quality can be attributed to the finite width of the graphene-metal contact area (compared to one-dimensional contacts[20] without a ledge) and an extensive damage of the exposed graphene by oxygen plasma, which is known to improve contact quality[S3]. A good match between the work functions of Ta and damaged graphene[S3] is probably a contributing factor, too. For hole doping (ΔV_g <-10 V), the contact resistance is much larger (≈70 Ohm), yielding $T_r \approx 0.3$. This additional resistivity is due to reflection of charge carriers at pn junctions formed near the superconducting contacts.

3. Fabry-Pérot oscillations in the normal-state

The term Fabry-Pérot (FP) interferometer refers to a cavity defined by two parallel semitransparent mirrors, in which monochromatic waves bouncing back and forth between the mirrors lead to interference and, therefore, resonances in transmission. The pronounced oscillations observed in resistance of our devices (Fig. 4.1b of the main text) are due to interference of electron waves partially reflected by the pn junctions formed near the nanostrip contacts[S4,23].

For a pn junction with a smooth potential profile only incident waves almost perpendicular to the junction have a non-vanishing transmission probability[S5]. This determines the relative size, δG, of the peaks in R_n which appear under the resonance condition, $2L^*/\lambda_F = N$ where N is integer, corresponding to the formation of standing waves in a cavity of length L^*. Using the dispersion relation $\varepsilon_F = hv_F/\lambda_F$ (ε_F and v_F are the Fermi energy and velocity, respectively) the period of the standing-wave resonances on the energy scale ε is expected to be $\varepsilon_0 = hv_F/2L^*$. Taking into account the energy-dependent contributions to the conductivity, $G(\varepsilon) = G_0 + \delta G \sin\frac{2\pi\varepsilon}{\varepsilon_0}$, the current I flowing through the FP cavity is given by $I = \frac{1}{e}\int_{\varepsilon_F - eV_b/2}^{\varepsilon_F + eV_b/2} G(\varepsilon)d\varepsilon$, which yields oscillations in I and the differential conductance dI/dV_b in the form

$$I = G_0 V_b + \frac{\varepsilon_0}{\pi e}\delta G \sin\frac{2\pi\varepsilon_F}{\varepsilon_0}\sin\frac{\pi e V_b}{\varepsilon_0} \qquad \frac{dI}{dV_b} = G_0 - \delta G \sin\frac{2\pi\varepsilon_F}{\varepsilon_0}\cos\frac{\pi e V_b}{\varepsilon_0}. \qquad \text{(S1).}$$

The latter expression describes FB oscillations as a function of both $\varepsilon_F \propto n^{1/2} \propto |\Delta V_g|^{1/2}$ and V_b. Qualitatively, this is the behavior observed experimentally and shown in Fig. 4.1b of the main text.

Despite the overall agreement, the experiment shows notable deviations from the exact periodicity expected in eq. (S1). They are not important in the context of this report but probably worth of pointing out. The observed deviations are due to changes in the effective position of pn junctions with varying graphene's doping. Indeed, one can see in the inset of Fig. 4.1b (also, Fig. 4.S3b below) that the chequered pattern becomes stretched along the y-axis with approaching the NP. This indicates that ε_0 becomes progressively larger closer to the NP, which means that the effective length L^* of our FP cavity becomes shorter with decreasing hole doping. Fig. 4.S3a plots the inferred values of L^* for different ΔV_g, which shows that the length of the FP cavity changes as much as by a factor of 2. This behavior is not unexpected. Indeed, graphene is electron doped by the contact with Nb/Ta and, as we increase $|\Delta V_g|$ and induce hole doping in graphene, the pn junctions are expected to become sharper and shift closer to the nanostrip contacts, approaching the limit $L^* = L$ at high doping. For completeness, we have also modelled changes in R_n using eq. (S1) and the inferred changes in L^*. The results are plotted in Fig. 4.S3b that shows good agreement with the detailed behavior observed experimentally in Fig. 4.1b of the main text.

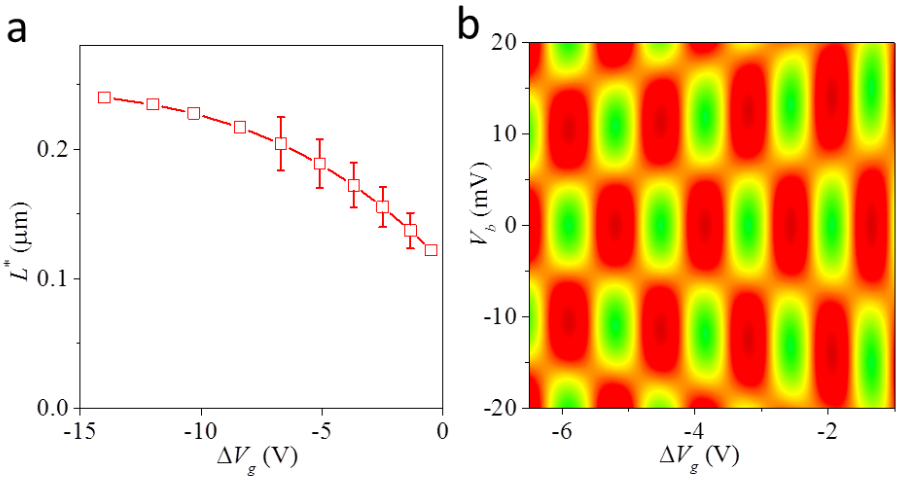

Fig. 4.S3 Changing length of graphene FP resonators

(**a**) The effective length of the FP cavity as found from the periodicity of the resistance oscillations along the V_b axis. The data points with error bars are from the plot shown in the inset of Fig. 4.1a of the main text. At low doping, the cavity is significantly shorter than the lithographically-defined distance between Nb contacts, $L \approx 0.25$ μm. (**b**) Modelling the chequered pattern found experimentally (Fig. 4.1b of the main text). In the calculations we used the cavity length found in (a) and a constant C_g to the back gate. The latter is $\approx 5\times10^{10}$ cm^{-2} per V as found from Shubnikov-de Haas oscillations.

4. Proximity superconductivity in the ballistic regime

In our SGS devices the critical current at low T increased with decreasing L down to our shortest junctions (Fig. 4.2d of the main text). This implies that our experiments were not in the limit of short L, in which case I_c should be independent of L. In the limit of long diffusive junctions, it is known[2,24] that Δ in eq. (1) of the main text should be substituted with the Thouless energy $E_{Th} \approx hD/L^2$, determined by the diffusion time across a Josephson junction (D is the diffusion coefficient). In the case of ballistic SNS junctions, we estimate a characteristic time of crossing such junctions as $\sim L/v_F$ and, accordingly, the Thouless energy E_{Th} can be written as $\sim hv_F/L$. Such scaling with the distance between superconducting contacts is characteristic for SNS junctions made from any ballistic metal[25,S6]. At the same time, the normal-state resistance of wide ballistic devices does not depend on their length (it is determined only by cross-sectional width and the Fermi wavelength). Therefore, we expect $I_cR_n \propto 1/L$ for long ballistic junctions, in agreement with the behavior reported in Fig. 4.2d.

To substantiate further the above conclusion about the long-L limit for our SGS junctions, we studied temperature dependence of their supercurrent. Fig. 4.S4 shows measurements for a set of five SGS junctions made from the same graphene crystal and having the same W but different L. The figure shows their resistance in the normal-state (Fig. 4.S4a), temperature dependence of the critical current (Fig. 4.S4b) and the product I_cR_n as a function of graphene doping (Fig. 4.S4c). One can see that R_n away from the NP is practically the same for all the junctions, independent of L (Fig. 4.S4a). Similar to the device in Fig. 4.2c of the main text, I_cR_n in Fig. 4.S4 varies little at high doping and, again, yields a relatively small ratio of $eI_cR_n/\Delta < 1$. Furthermore, Fig. 4.S4b shows that at high electron doping I_c rapidly increases with decreasing T, even for the shortest junction with $L = 0.25$ μm. This behavior again indicates that we are not in the short-L limit described by eq. (1) of the main text, where temperature should play little role, except for reducing the superconducting gap at k_BT comparable to Δ where k_B is the Boltzmann constant. As discussed above, for long devices with $E_{Th}/\Delta < 1$, the critical current I_c is limited by E_{Th} rather than Δ and, using the scaling arguments that are also valid for long diffusive junctions[24], we can write

$$eI_cR_n \sim E_{Th} f\left(\frac{E_{Th}}{k_BT}\right) \tag{S2}$$

In our case, $E_{Th} \approx hv_F/L$, and eq. (S2) yields $I_cR_n \propto 1/L$ at low T as expected. We also examined the validity of eq. (S2) at finite T by plotting I_cR_n/E_{Th} as a function of E_{Th}/k_BT (Fig. 4.S4d). One can see that the data for all L and T collapse on a single curve. Although the function $f(x)$ remains to be determined theoretically, which would require taking into account angle-dependent contributions of different trajectories responsible for Andreev bound states and including the effect of Klein tunneling[S4,S5,S7,23], the universal behavior in Fig. 4.S4d leaves little doubt that the observed critical current is determined by the Thouless energy, hv_F/L.

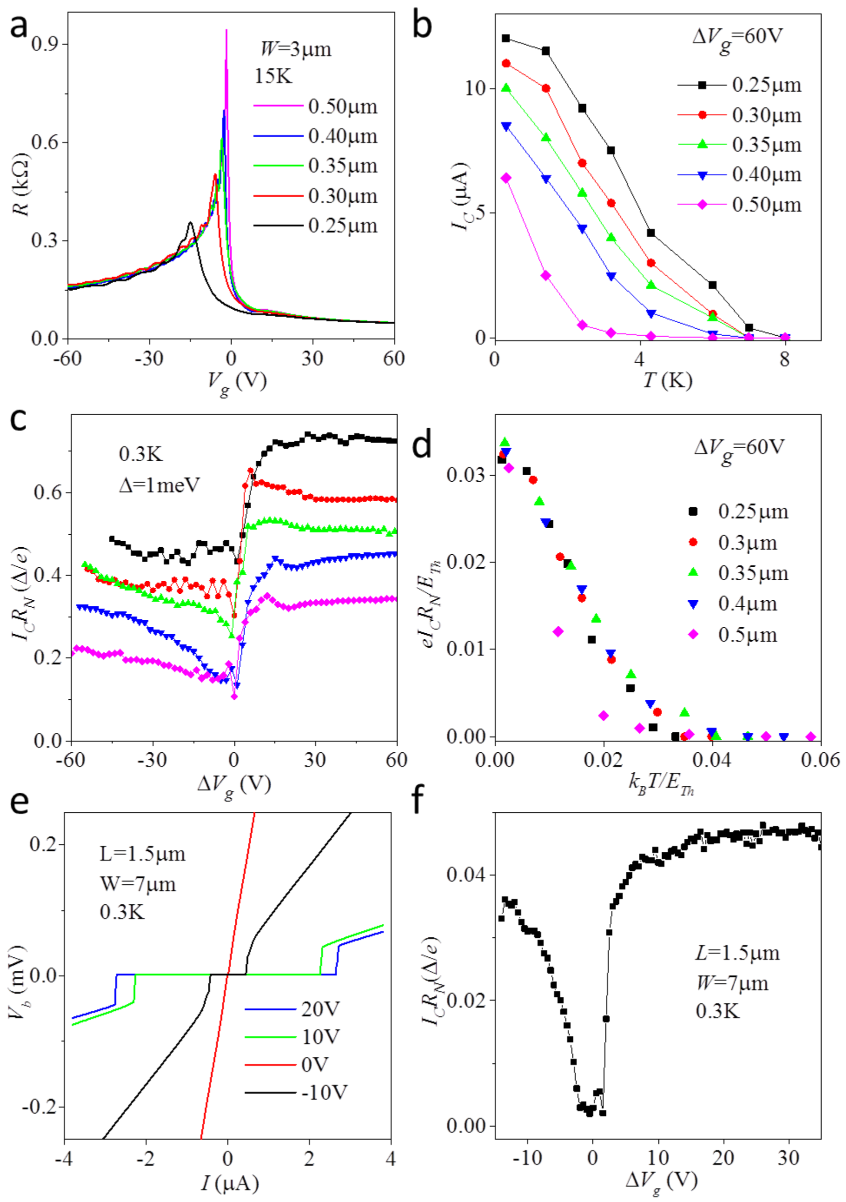

Fig. 4.S4 Effect of length, doping and temperature on the critical supercurrent

(**a**) Normal-state resistance of 5 adjacent junctions fabricated on the same graphene crystal. The NP shifts to increasingly negative values for shorter junctions because of doping induced by the Nb/Ta contacts. Note that R_n can be determined by measuring at temperatures $T > T_C$ or currents $I > I_c$. In both cases, we find the same amplitude of oscillations in R_n. (**b**) Temperature dependence of I_c at high electron doping. (**c**) Low-temperature $R_n I_c$ as a function of gate voltage. (**d**) Scaling dependence of eq. (S2) holds accurately for all the junctions, except for the longest one among them (L = 0.5 μm) which shows stronger T dependence. For such long junctions, *I*-*V* curves are found more “rounded” near the superconducting-normal transition. This probably indicates that the supercurrent is suppressed by thermal fluctuations. (**e**) Examples of *I*-*V* curves and the $I_c R_n$ product (**f**) for such SGS devices (L = 1.5 μm).

Note that in contrast to Fig. 4.2c of the main text, I_cR_n in Fig. 4.S4c shows a pronounced minimum rather than maximum at the NP. In principle, such a minimum can indicate specular Andreev reflection. Unfortunately, we find that different devices exhibit qualitatively different behavior of I_cR_n at the NP as illustrated by Fig. 4.S4c and Fig. 4.2c. Moreover, although our devices had very low charge inhomogeneity at the NP, it is still $\approx 10^{10}$ cm^{-2}, which translates into smearing of the Dirac point by ≈10 meV, an order of magnitude larger than Δ. Specular Andreev reflection is predicted for the opposite inequality[3]. This fact combined with poor reproducibility for different devices does not allow us to make conclusions about the nature of Andreev bound states at the neutrality point.

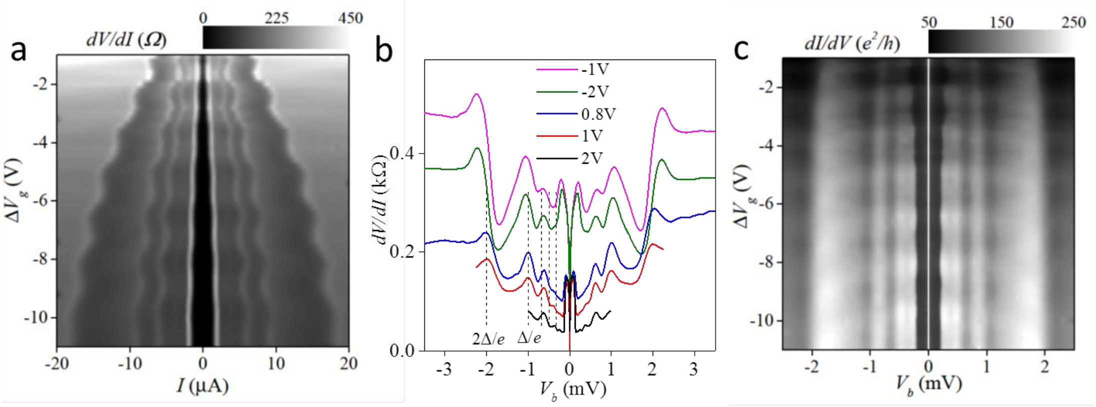

Fig. 4.S5 Sub-gap multiple Andreev reflection in a FP cavity

(**a**) Differential resistance for hole doping of the device in Figs. 4.2a,b of the main text. Larger currents I are used here. Different resistance is calculated using I-V curves such as in Fig. 4.2a. (**b**) Differential resistance as a function of bias V_b rather than current. (**c**) The same characteristics as in (a) but plotted as a function of V_b rather than I.

Figs. 4.2 of the main text showed pronounced Fabry-Pérot oscillations in the critical current $I_{c,e}$. As discussed in the main text, these oscillations cannot be explained simply by FP oscillations in R_n and require a more fundamental mechanism. We have argued in the main text that the oscillations arise due to changes in E_{Th} that depends on the effective length of Andreev bound states and, therefore, also changes with changing T_r. This mechanism is straightforward and should be expected to play a certain role in any SNS junction with FP oscillations. In principle, one can try an alternative explanation and attribute the oscillatory behavior to FP oscillations in the gap Δ itself. We confirmed experimentally that this was not the case. Indeed, Fig. 4.S5 shows how features in the differential I-V characteristics of our SGS devices evolve as a function of doping, current and bias. Again, the FP transmission resonances result in a pronounced oscillatory pattern in the critical current (Fig. 4.S5a). For $I > I_c$, the FB oscillations are mirrored in by oscillation multiple Andreev reflections (MAR)[2,26]. Fig. 4.S5b,c show the same differential I-V characteristics but as a function of applied bias V_b rather than I. The peaks due to MAR occur at $V_b \approx 2\Delta/N$ (Fig. 4.S5b), and their positions do not exhibit any discernable FP oscillations that would indicate oscillations in Δ. The somewhat wavy pattern in Fig. 4.S5c appears only due to oscillatory broadening of MAR peaks.

The observed MAR also allow an alternative estimate[S8] for the transmission coefficient T_r using the differential resistance at biases below Δ. In the case of a single NS interface, it is known that the sub-gap resistance is half the R_n value if $T_r = 1$ (perfect normal-electron transmission and only Andreev reflections at the interface). When a finite barrier strength Z is introduced, sub-gap dV/dI increases and can be calculated using this parameter[2] all the way up to the tunnel limit ($T_r = 0$). In the case of SNS junctions, calculations are more complicated and sensitive to employed models[S8]. This is particularly valid for wide ballistic junctions where gap-less Andreev spectrum has been predicted[S9]. It is nevertheless instructive to compare the observed MAR behavior with the simplest model[S8]. To this end, we focus on the sub-gap differential resistance at $V_b < 0.5$ mV, significantly below Δ/e, where individual Andreev resonances are no longer resolved. Fig. 4.S5b yields $dV/dI \approx 0.5R_n$ for positive V_g (3 bottom curves), and $dV/dI \approx 0.8R_n$ for negative V_g, (here R_n is determined as dV/dI at large biases $V_b > 2\Delta/e$, where its value reaches close to the normal-state resistance measured above T_C). Repeating the previous analysis[S8], we find $Z \approx 0.5$ and 0.75, which corresponds to $T_r = \frac{1}{1+Z^2} \approx 0.6$ and 0.8 for electron and hole doping, respectively. This is in good agreement with $T_r \approx 0.8$ found from the normal-state contact resistance for electron doping. As for hole doping, the MAR analysis suggests twice higher transmission compared with the normal-state analysis, which can be attributed to pn junctions and Klein tunneling, the effects not currently included in theory. Finally, we note that theory predicts[S8] a minimum rather than a peak for our MAR curves at $V_b = 2\Delta/e$. However, it was shown experimentally[S10] that minima usually appear for superconductors with long coherence lengths (e.g., aluminum) whereas MAR spectroscopy for Nb junctions previously reported peaks, similar to our results.

5. Reproducibility of proximity patterns in high magnetic fields

In the high-flux regime, the supercurrent randomly changed with varying *B* and ΔV_g. Fluctuating patterns such as the one shown in Fig. 4.3e of the main text were found to be stable over a period of several hours and reproducible if *B* was swept up and down (Fig. 4.S6). This proves that the observed fluctuations are not caused by flux creep in the adjacent superconducting contacts. Such creep can indeed appear due to movements of pinned vortices and is an irreversible process. Flux jumps could be observed over longer time scales and with varying *B* over intervals larger than several mT. The flux instability is easily distinguishable leading to abrupt changes in proximity patterns as illustrated in Fig. 4.S7.

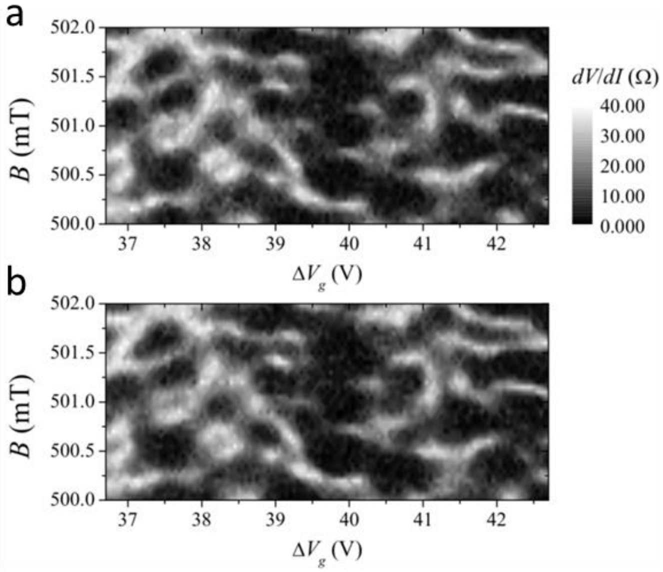

Fig. 4.S6 Reproducibility

Differential resistance maps measured by sweeping V_g and gradually increasing (**a**) and decreasing (**b**) *B* in steps of 0.1 mT. Time elapsed between the shown maps was 12 h.

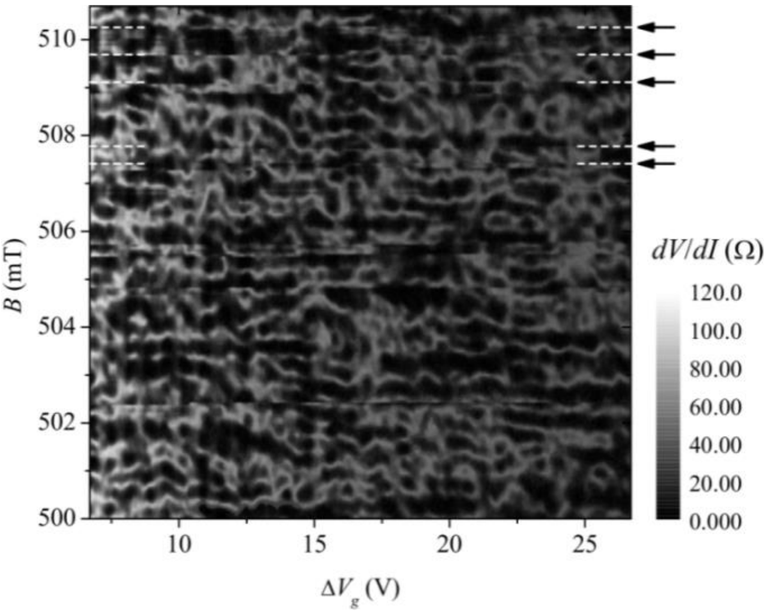

Fig. 4.S7 Abrupt changes in a proximity pattern caused by flux creep

The map was acquired over a period of 3.8 days. The arrows indicate some of the discontinuities caused by flux jumps between consecutive sweeps of V_g.

6. Correlation scales

Characteristic scales for the observed fluctuations in I_c were calculated as follows. For a given set of N resistance values R_i measured at magnetic fields $B_i = B_0 + i\Delta B$ where $0 \le i < N$ is an integer and ΔB is the spacing in B between consecutive sweeps, the autocorrelation $K_n^{(B)}$at a scale $\delta B = n\Delta B$ ($0 \le n < N$ is an integer) is given by

$$K_n^{(B)} = \left[\sum_i \frac{(R_i)^2}{N}\right]^{-1} \sum_i \frac{R_i R_{i+n}}{N-n}.$$

Similarly, given a discrete set of N resistances R_j measured at Fermi energies $\varepsilon_j = \varepsilon_0 + j\Delta\varepsilon$ (where j is an integer and $\Delta\varepsilon$ is the spacing of energies) the autocorrelation $K_n^{(\varepsilon)}$ for an energy scale $\delta\varepsilon = n\Delta\varepsilon$ is given by

$$K_n^{(\varepsilon)} = \left[\sum_j \frac{(R_j)^2}{N}\right]^{-1} \sum_j \frac{R_j R_{j+n}}{N-n}.$$

Fig. 4.3e of the main text and Fig. 4.S8a show two maps of the fluctuating proximity effect. For each of them, the found autocorrelations $K_n^{(B)}$ are averaged over all ε_F to find $\langle K_n^{(B)} \rangle$, and the autocorrelations $K_n^{(\varepsilon)}$ are averaged over all B to find $\langle K_n^{(\varepsilon)} \rangle$. The averaged autocorrelations are shown in Figs 4.S8b,c. The plots yield a characteristic scale for suppression of I_c with changing B as ≈0.5 mT (Fig. 4.S8b). It requires changes in ε_F by ≈ 1.7 meV at low n whereas somewhat smaller changes of ≈1 meV are required at high n (Fig. 4.S8c). The latter can be understood by longer effective lengths at higher doping, which should lead to smaller E_{Th}, as discussed in the main text.

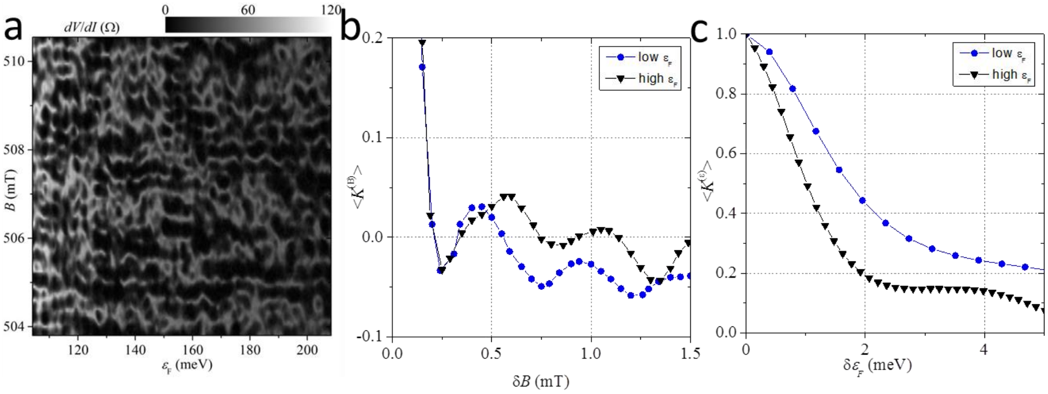

Fig. 4.S8 Characteristic scales for high-field Andreev bound states

(**a**) Another example of *dV*/*dI* maps, covering a different range of doping with respect to the map in Fig. 4.3e of the main text. (**b**) and (**c**) are autocorrelation functions $\langle K^{(B)}\rangle$ and $\langle K^{(\varepsilon)}\rangle$, respectively, for maps in (a) and of Fig. 4.3e, which are labelled as low and high ε_F, respectively. The large peak at zero δB arises due to a finite interval (0.1 mT) between consecutive sweeps.

7. Andreev bound states at zero and finite magnetic fields

The supercurrent through a normal metal placed between two superconductors is mediated by a process known as Andreev reflection[26]. In this process (Fig. 4.S9a), an electron arriving at the NS interface forms a Cooper pair with another electron found near the Fermi energy ε_F, and this sends a hole back into the Fermi sea of the normal metal. The transfer of a Cooper pair through an SNS junction requires two such reflections at the opposite NS interfaces ('double' Andreev process, in which the involved electrons (*e*) and holes (*h*) retrace each other's trajectories). This leads to the formation of so called Andreev bound states.

If *e* and *h* forming Andreev states have exactly opposite momenta ($\boldsymbol{p} = -\boldsymbol{p}'$), their phases acquired along trajectories inside the normal metal cancel exactly. Andreev bound states can also be formed by *e* and *h* with slightly different momenta, provided the carriers reside within the superconducting gap Δ (that is, $|p - p'|v_F < \Delta$) and the phase shift acquired along the retracing *e-h* trajectories, $\delta = |p - p'|\Lambda/\hbar$, is small. This leads to the known constraint, $\Delta < hv_F/\Lambda = E_{Th}$ where Λ is the effective length determined by the time charge carriers spend in graphene. This length is larger than *L* because of a finite probability of reflection at contacts and different reflection angles with respect to the GS interface. Andreev-type trajectories with longer effective length Λ do not contribute to the transfer of Cooper pairs.

Following a consideration similar to the above, one can find that *e* and *h* involved in the formation of Andreev bound states do not have to retrace each other exactly and may have slightly misaligned trajectories as illustrated in the top part of Fig. 4.S9a. The conversion of two electrons from a 2D metal into a Cooper pair necessitates the condition $p_y = -p'_y$ (indices x and y refer to the directions perpendicular and parallel to the GS interface, respectively). On the other hand, restrictions on the *x*-components of the momenta $[p_x = (\varepsilon/v)\cos\theta$ and $p'_x = (\varepsilon'/v)\cos\theta']$ are set by the requirement $\left|v_F\sqrt{p_x^2 + p_y^2} - \varepsilon_\mathrm{F}\right| < \Delta$, which means that energies of the charge carriers involved in Andreev bound states should reside within the gap. This sets the following constraint,

$$\cot\theta' - \cot\theta \approx \frac{\theta' - \theta}{\sin^2\theta} < \frac{\Delta/(v_F\cos\theta)}{p\sin\theta},$$

on the misalignment angle, $\delta\theta = \theta - \theta'$, between ballistic *e* and *h* trajectories forming Andreev bound states (Fig. 4.S9a). The above expression can be simplified as

$$\delta\theta < \frac{\Delta}{\varepsilon_\mathrm{F}}\tan\theta \qquad \text{(S3).}$$

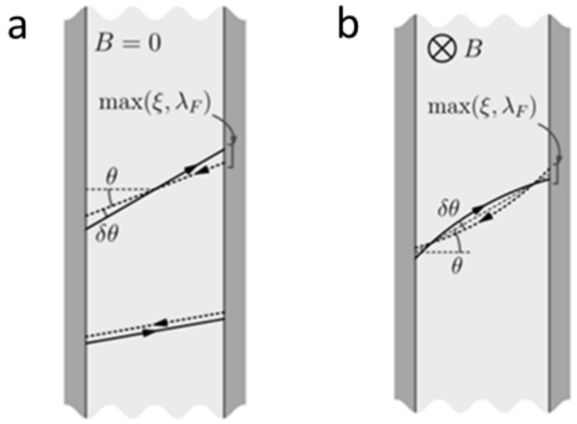

Fig. 4.S9 Andreev bound states and allowed misalignment of contributing trajectories

(**a**) The bottom set of *e-h* trajectories illustrates the standard double Andreev process. Top: Slightly misaligned *e-h* trajectories can also form Andreev bound states if their positions at the two NS interfaces are spatially close. The constraints are given by equations (S3) and (S4). (**b**) Similarly, slightly curved cyclotron trajectories ($r_c >> L$) can form Andreev bound states with constraints set by eq. (S4).

Another important requirement is that the ends of *e-h* trajectories should not be farther away from each other than max [ξ, λ_F] (see Fig. 4.9a). Otherwise, two electrons cannot form a Cooper pair inside a superconductor, where its size is given by the coherence length ξ. On the other hand, positions of two electrons within a normal metal are indistinguishable if they are separated by less than λ_F. For all carrier densities in our experiments, $\xi < \lambda_F$, which results in the following condition, $\frac{L\delta\theta}{\cos^2\theta} < \lambda_F$. Finally, one more limitation is set by the requirement that the phase shift between an electron and Andreev-reflected hole should be small, which leads to $(\sec\theta' - \sec\theta)L/\lambda_F \approx \frac{L\delta\theta\sin\theta}{\lambda_F\cos^2\theta} < 1$. The latter two constraints are nearly identical and require

$$\delta\theta < \frac{\lambda_F}{L}\cos^2\theta. \tag{S4}$$

If $\Delta \sim E_{Th} = hv_F/L$ (see the main text), constraints (S3) and (S4) have similar strengths. Note that eq. (S3) discriminates against Cooper pairs transferred perpendicular to the NS interface, whereas eq. (S4) against those at shallow angles.

For our devices, we estimate that Andreev bound states with θ ~1 and δθ less than a couple of degrees should dominate Cooper-pair transport.

The supercurrent provided by Andreev bound states is suppressed by magnetic field. In low B, the dominant effect is interference between Cooper pairs that cross the normal metal along different paths. If $BS \sim \phi_0$, Cooper pairs acquire broadly distributed phase shifts, and this leads to the oscillatory suppression of the supercurrent as described by eq. (2) of the main text.

In ballistic devices with large L, magnetic field curves *e-h* trajectories, leading to their misalignment such that Andreev-reflected electrons and holes can no longer retrace each other exactly[21,S11]. The effect is rather similar to the zero-B misalignment described above but is caused by a finite cyclotron radius, $r_c = p_F/eB = \hbar\sqrt{\pi n}/eB$ (Fig. 4.S9b). For *e-h* trajectories leaving a superconducting contact at an angle θ (Fig. 4.S9b), the cyclotron curvature leads to misalignment

$$\delta\theta \sim \frac{L}{r_c \cos\theta} \qquad \text{(S5).}$$

Combined with the constraint set by (S3), eq. (S5) yields $r_c > \frac{\varepsilon_F}{\Delta} L$, in order to support Andreev bound states at finite B. This condition is satisfied if $B < B^*$ where

$$B^* \sim \frac{\Delta}{eLv_F} \qquad \text{(S6).}$$

For our ballistic SGS devices with submicron L, B^* is a few mT. For $B > B^*$, it becomes impossible for Andreev-reflected electrons and holes to form closed loops that are necessary to transfer Cooper pairs. Accordingly, the supercurrent in the graphene bulk is suppressed.

One may wonder whether Andreev bound states can be formed for $B \gg B^*$ by a fortuitous combination of a number of segments of cyclotron orbits as charge carriers bounce between two superconducting contacts. The answer is No. As shown in Fig. 4.S10, the condition $B \gg B^*$ results in long open trajectories. Indeed, each Andreev reflection process involves two segments of the full cyclotron orbit, one for an electron and the other for a hole (Fig. 4.S10b). Each consecutive reflection increases the deflection angle by $\delta\theta \sim L/r_c$, until the final segment (#1 and 6 in Fig. 4.S10) brings the quasiparticle back to the same NS interface where the last Andreev reflection took place. After this step, a reversed sequence of Andreev reflections follows, transferring the charge in the opposite direction. This results in an infinite path containing periodic sets of star-shaped e-h orbits bouncing between the superconducting leads. As shown in Fig. 4.S10b, the number N of Andreev processes linking sets of (N +1)-pointed stars is determined simply by int[$2r_c/L$]. The shape of such open trajectories is quite generic: they describe the electron drift along a graphene strip. It is also worth of mentioning that, depending on partition of the cyclotron orbit in Fig. 4.S10b, such drifts can be in both ‘up’ and ‘down’ directions in Fig. 4.S10a. Among such star-shaped orbits, there is a special one that has a zero drift velocity and, hence, it is closed. Nonetheless, even the special orbit cannot support an Andreev bound state, because half such an orbit provides the electron (hole) transfer from one S contact to the other whereas the other half brings it back.

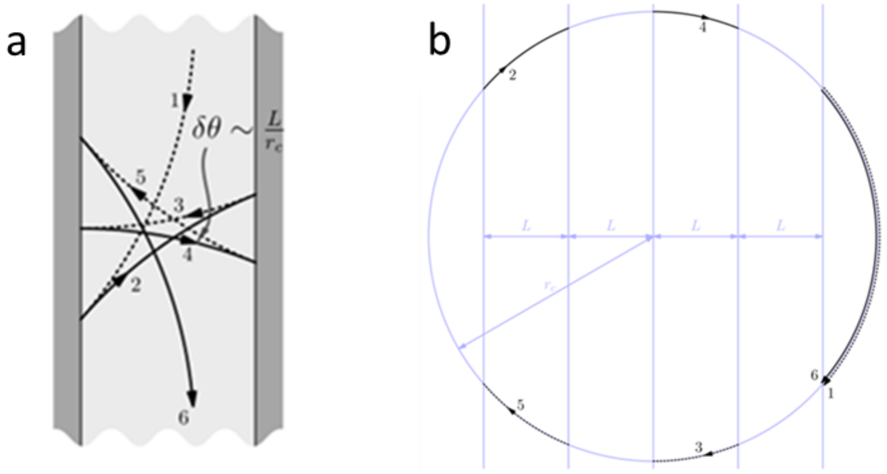

Fig. 4.S10 No Andreev bound states for strongly curved trajectories

(**a**) Typical trajectory formed by Andreev-reflected electrons and holes for $B > B^*$. (**b**) Ballistic orbits in (a) correspond to well-defined sectors of the full cyclotron orbit. Labelling of the segments is the same in both plots.

Although closed Andreev trajectories are forbidden in the ballistic bulk for $B >> B^*$, they are still allowed near graphene edges. Two examples of such orbits are shown in Fig. 4.S11, and many others can be drawn depending on scattering details and B. These near-edge orbits have closed ends at both NS interfaces. This means that, despite different lengths of e and h parts (solid and dashed curves in Fig. 4.S11), the e-h trajectories transfer Cooper pairs between the superconducting contacts. In a way, a combination of cyclotron motion and scattering from graphene edges creates a ‘chaotic ballistic billiard’ near SGS junction’s edges. For each Andreev state, its current carrying capacity I_Q is $\approx e\Delta/h$ as discussed in the main text.

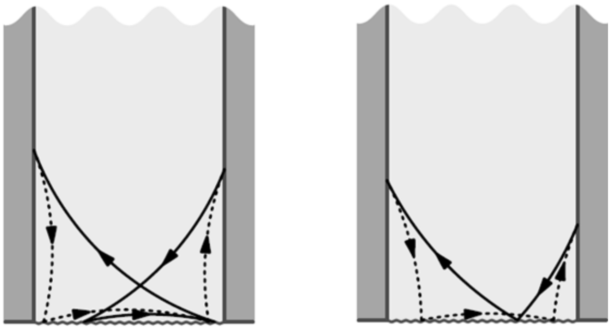

Fig. 4.S11 Andreev bound states near graphene edges

Examples of closed Andreev trajectories due to diffusive scattering at graphene edges.

In contrast to the retracing *e*-*h* paths at B =0, for which semiclassical phases of propagating electrons and holes near the Fermi level almost cancel each other, phase differences acquired along non-retracing paths in large B are large and random. If we average over all imaginable geometrical paths, the supercurrent would be zero. However, for each realisation of a disordered SNS device, the characteristic values of mesoscopic fluctuations are known[18,28-30] to be given by $\sqrt{\langle \delta G^2 \rangle} \sim \frac{e^2}{h}$ and $I_c = \sqrt{\langle \delta I_c^2 \rangle} \sim I_Q = \frac{e\Delta}{h}$. The same fluctuations are expected for the case of chaotic ballistic conductors. The latter statement is based on the analogy between mesoscopic fluctuations in conductance[18,28] and supercurrent[17,18,29,30]: both originate from interference of electron waves propagating along different paths. This mesoscopic effect provides a supercurrent with a random phase, different at the opposite graphene edges. These two edge contributions results in Aharonov-Bohm-type oscillations in the total supercurrent as a function of the magnetic flux Φ through the junction, which have a characteristic periodicity of about the flux quantum, ϕ_0. The analogy with chaotic billiards enables us to estimate the change in the Fermi energy needed to change the sample realization as the Thouless correlation energy $E_{Th} \sim hv_F/\Lambda$ determined by the typical length Λ of Andreev *e*-*h*-*e* path (see the main text). For the case of a finite magnetic field (Fig. 4.3h), $\Lambda \sim \sqrt{Lr_c}$ for $r_c >> L$ and $\Lambda \sim L$ for $L/2 < r_c < L$, which yields $E_{Th} \leq$ 1meV, the scale at which the interference pattern should change with changing gate voltage.

Finally, the situation changes again if $r_c < L/2$, that is, if the cyclotron orbit becomes small enough to fit within the graphene strip without touching the NS interfaces. In this case, which takes place in $B > \frac{2\hbar}{eL}\sqrt{\pi n(V_g)}$, charge carriers can be transferred between the contacts only by skipping orbits and only in one direction at each of the two graphene edges (Fig. 4.3i of the main text). As a result, the transfer of Cooper pairs is no longer possible anywhere, either along graphene edges or in the bulk.

8. High-field cutoff in the proximity effect

It was argued above and indicated in the main text (Fig. 4.3d) that random Andreev-bound states could survive in high B only until cyclotron orbits start fit between superconducting contacts. To further substantiate this experimentally, Fig. 4.S12 shows the differential resistance R measured over a large range of B and V_g. Three different regions can clearly be distinguished for the case of positive ΔV_g (electron doping; no pn junctions at the Nb contacts). One of the regions corresponds to the conventional Josephson effect and is found in a narrow interval of small B (black stripe in Fig. 4.S12a). Here the cyclotron radius $r_c >> L$, and the proximity is mediated by practically straight Andreev bound states, that is, $B < B^*$ (Fig. 4.S12b). In high B, our ballistic devices enter the opposite regime, $r_c << L$ (Fig. 4.S12d), which results in skipping trajectories and Shubnikov-de Haas oscillations, characteristic of the quantum Hall regime in the two-terminal geometry. In high B, clear quantum Hall plateaus develop (Fig. 4.S12e). In between the two extremes lies a wide range of B and ΔV_g in which pockets of the proximity superconductivity were observed (blue region). Boundaries between the three regimes are clearly seen due to changes in color in Fig. 4.S12a. From the high-B side, the boundary is well described by the condition $2r_c = L$ which is shown by the black curve. In the blue region, the proximity effect randomly occurs all the way up to the high-B boundary (see Fig. 4.3d of the main text). A finite resistance that appears in the blue region of Fig. 4.S12a is due to sampling and averaging over relatively large intervals of B. On this scale (>> 1mT), individual superconducting states such as in Figs. 4.3e and 4.S8a cannot be resolved but their occurrence frequency is reflected in different shades of blue.

Note that high-B pockets of the superconducting proximity could not be observed for hole doping. Instead clear quantum oscillations cover nearly the entire interval of B

and n (Fig. 4.S12a). The latter oscillations continue first as an extension of FP oscillations in low B (see Fig. 4.2b of the main text) but then they exhibit a phase shift and start bending. This behavior is attributed[S4,23] to Klein tunneling through the hole-doped graphene strip between n-doped contact regions. It is important to note that Klein tunneling collimates electron and hole trajectories perpendicular to pn interfaces[S5]. To form near-edge Andreev states shown in Fig. 4.S11, it requires cyclotron trajectories tilted towards the NS interface and, therefore, the Klein-tunneling collimation is expected to strongly suppress such Andreev states. This is likely to be the reason that no high-B proximity states could be observed in this hole-doping regime.

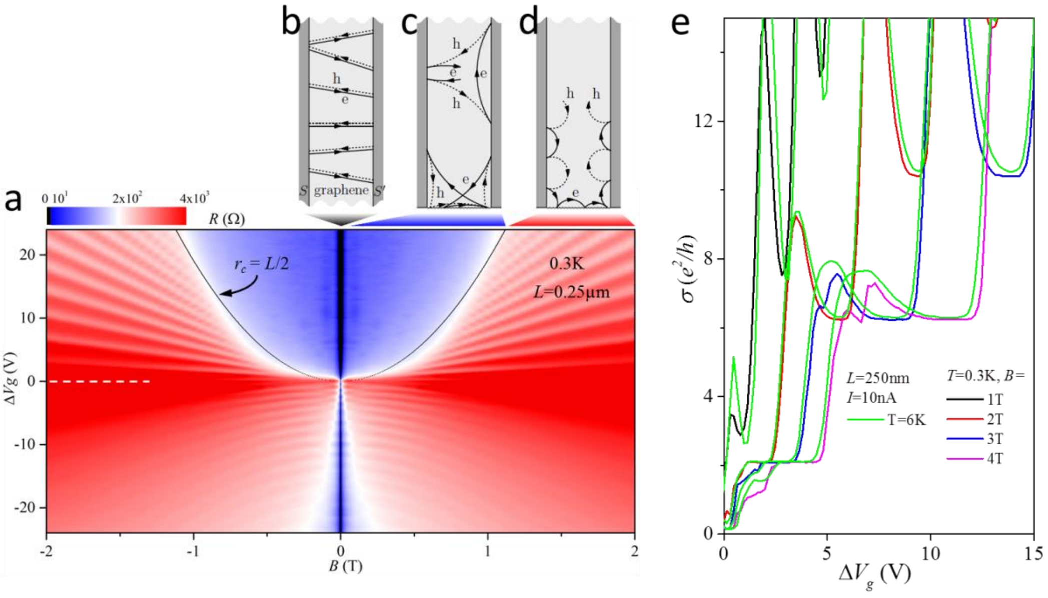

Fig. 4.S12 Characteristic regimes in ballistic Josephson junctions

(**a**) Resistance map obtained using the probing current of 2 nA. The Josephson effect mediated by the conventional Andreev bound states shows up in black. Blue: Pockets of proximity superconductivity are observed for electron doping. (**b-d**) Sketches of electron and Andreev-reflected hole trajectories in graphene in low (b), intermediate (c) and high B (d). In (b), graphene can support large supercurrents. In (c), the supercurrent is suppressed because the cyclotron motion prevents e and h trajectories from retracing each other. In this case, the proximity can still be mediated by Cooper pairs that cross the junction near graphene edges. In the high-B regime (d), no Andreev states are possible. (**e**) Quantum Hall plateaus observed in high B. Our Nb contacts remain superconducting at $B \leq 3$ T. No sign of superconductivity mediated by edge states could be observed, which is not surprising because such states are unidirectional along each edge and, therefore, cannot mediate the transfer of Cooper pairs across graphene.

9. Spatial distribution of supercurrents

A non-uniform distribution of supercurrent through an SNS junction can appear due to fluctuations in its length, charge inhomogeneity in graphene, or a non-uniform Nb-graphene contact resistance. It has also been shown in literature that zigzag segments at graphene edges may lead to enhanced conductance, even for strongly disordered, non-crystallographic egdes[S12,S13]. Furthermore, in the strip geometry, an extended back gate can causes inhomogeneous doping for purely electrostatic reasons[S14]. Therefore, it is reasonable to ask whether the observed high-B Andreev states could also be enhanced by such mechanisms that influence local or near-edge conductance.

First of all, a clear indication of high homogeneity of our devices comes from the pronounced FP oscillations that would be smeared if the Fermi wavelength λ_F would noticeably change across the graphene junctions (in the W direction). Second, change inhomogeneity in our devices is estimated to be only $\approx 10^{10}\text{cm}^{-2}$ (see the main text) whereas L is lithographically defined with accuracy better than ~10%; see Fig. 4.1a and Fig. 4.S1). Third, all the studied junctions exhibited similar behavior consistent with the explanation provided in Section 8. Nonetheless, to address the issue of supercurrent uniformity further, we have calculated the inverse Fourier transform for the observed Fraunhofer patterns in low B (see Fig. 4.3a of the main text). The Fourier transform yields directly the spatial distribution of supercurrents across the junction[2,S15]. An example of our analysis is shown Figs. 4.S13a,b, which confirms a fairly uniform supercurrent distribution along the junction. One can see in Fig. 4.S13b that I_c varies by approximately ±10% but this is probably an overestimate because the Fourier transform's accuracy was limited by the finite B window for the Fraunhofer pattern that has to be analyzed for $B < B^*$. We emphasize that distribution patterns similar to the one in Fig. 4.S13b were obtained for many doping levels and many devices.

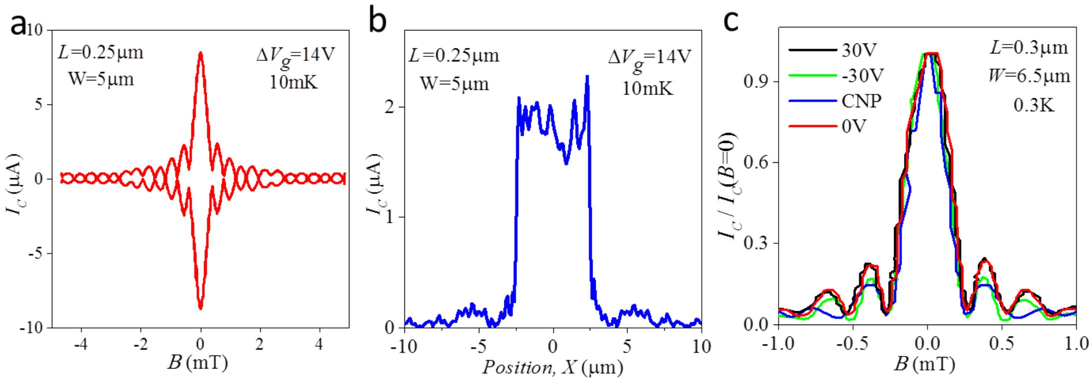

Fig. 4.S13 Uniform supercurrent distribution in low magnetic fields

(**a**) Another example of the observed Fraunhofer patterns. (**b**) Supercurrent distribution along *W*, which was calculated as the inverse Fourier transform of the data in (a) following the procedures described in refs 16 and S15. (**c**) Diffraction patterns measured for several representative gate voltages. The central peak is twice wider than the other peaks, which is a clear signature that, in $B < B^*$, no significant portion of supercurrent flows along graphene edges, in contrast to the observations of ref.[S16].

A particularly important case is the edge inhomogeneity[S12-S14] such that the supercurrent can predominantly flow along more conductive graphene edges[16]. This is clearly not the case of our SGS devices. Indeed, edge inhomogeneity leads to easily distinguishable signatures in the Fraunhofer pattern. For weak inhomogeneity, the central peak in the Fraunhofer pattern first narrows and, if the near-edge supercurrent becomes significant, the peak splits into two[2,16]. As shown in Fig. 4.S13c, no narrowing of the central Fraunhofer peak could be detected at any doping including the NP, indicating that in low *B* the supercurrent flows uniformly through the graphene bulk.

As for structural non-uniformities in graphene or at its interface, they can also lead to a finite localized supercurrent surviving even in high *B*, similar to the case of inhomogeneous tunnel junctions[S17]. However, in this case the envelope for the maxima in Fraunhofer oscillations should tend to a finite I_c value[S17] rather than to zero as in Figs 4.3a and 4.S13a. Furthermore, in the presence of several superconducting shorts, they should smear out the Fraunhofer pattern above a few flux quanta[S17], in contrast to the behavior observed in our SGS devices.

10. Measuring small critical currents for individual Andreev bound states

I_c is usually defined as the current at which the voltage measured across the junction is indistinguishable from background noise. This condition is easy to achieve for large Josephson junctions and even in our case of low-B measurements where the supercurrent flows uniformly and the Josephson energy eI_cR_n is higher than thermal one. However, in a magnetic field, we encounter the case of individual superconducting states with small critical currents and I_cR_n as small as 2 μV (see the inset in Fig. 4.3d), which translates into thermal energy of 20 mK. In this case, voltage fluctuations smear the standard Josephson I-V characteristics and it is difficult to observe a clearly-defined zero resistance state. Whereas the superconductivity can still be verified for individual measurements such as in the inset of Fig. 4.3d by using long averaging times, it is impractical to use such time consuming measurements when dealing with a large parameter space such as, e.g., in Figs 4.3a-c of the main text. In the latter measurements, we have used a quicker and more convenient way to determine the critical current as explained by Fig. 4.S14. To this end, we have used the half width at half height on differential resistance curves to estimate I_c. This estimate is rather insensitive to noise and fluctuations as Fig. 4.S14 shows.

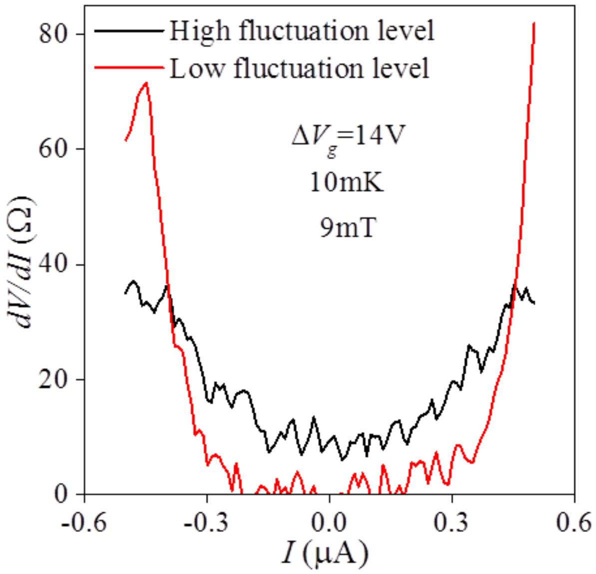

Fig. 4.S14 Defining small critical currents

Typical differential resistance measurements of the same SGS junction but at different levels of external noise. The critical current is clearly defined as ≈300 nA in the case of low noise (red curve). If one of the filters in our measurement system was removed, this resulted in a higher noise level and smearing of the *I-V* characteristics (black curve). Nevertheless, the notion of half width at half height yields the same value of I_c for the black curve as for the red one.

Supplementary references

[S1] A. V. Kretinin *et al.* Electronic properties of graphene encapsulated with different 2D atomic crystals. *Nano Lett.* **14**, 3270-3276 (2014).

[S2] M. Octavio *et al*. Subharmonic energy-gap structure in superconducting constrictions. *Phys. Rev. B* **27**, 6739 (1983).

[S3] J. A. Robinson *et al*. Contacting graphene. *Appl. Phys. Lett.* **98**, 053103 (2011).

[S4] A. F. Young, P. Kim. Quantum interference and Klein tunnelling in graphene heterojunctions. *Nature Phys.* **5,** 222-226 (2009).

[S5] V. Cheianov, V. I. Fal'ko. Selective transmission of Dirac electrons and ballistic magnetoresistance of n-p junctions in graphene. *Phys. Rev. B* **74**, 041403 (2006).

[S6] A. V. Svidzinsky, T. N. Antsygina, E. N. Bratus. Concerning the theory of the Josephson effect in pure SNS junctions. *J. Low Temp. Phys.* **10**, 131-136 (1973).

[S7] M. I. Katsnelson, K. S. Novoselov, A. K. Geim. Chiral tunnelling and the Klein paradox in graphene. *Nature Phys.* **2**, 620-625 (2006).

[S8] K. Flensberg, B. Hansen, M. Octavio. Subharmonic energy-gap structure in superconducting weak links. *Phys. Rev. B* **38**, 8707-8711 (1988).

[S9] A. Lodder, Y. V. Nazarov. Density of states and the energy gap in Andreev billiards. *Phys. Rev. B* **58**, 5783-5788 (1998).

[S10] H. Y. Gunel *et al*. Crossover from josephson effect to single interface Andreev reflection in asymmetric superconductor/nanowire junctions. *Nano Lett.* **14**, 4977-4981 (2014).

[S11] F. Giazotto, M. Governale, U. Zulicke, F. Beltram. Andreev reflection and cyclotron motion at superconductor-normal-metal interfaces. Phys. Rev. B 72, 054518 (2005).

[S12] A. Rycerz, J. Tworzydlo, C. W. J. Beenakker. Valley filter and valley valve in graphene. *Nature Phys.* **3**, 172–175 (2007).

[S13] J. Li, I. Martin, M. Buttiker, A. F. Morpurgo. Topological origin of subgap conductance in insulating bilayer graphene. *Nature Phys.* **7**, 38-42 (2011).

[S14] E. J. H. Lee *et al*. Contact and edge effects in graphene devices. *Nature Nano* **3**, 486-490 (2008).

[S15] S. Hart *et al*. Induced superconductivity in the quantum spin Hall edge. *Nature Phys.* **10**, 638-643 (2014).

[S16] A. Barone & G. Paterno. *Physics and Applications of the Josephson Effect*. Wiley & Sons, New York, 1982.

[S17] I. K. Yanson. Effect of fluctuations on the dependence of the Josephson current on a magnetic field. *JETP* **31**, 800-807 (1970).

Chapter 5

Edge currents shunt the insulating bulk in gapped graphene

The results demonstrated in chapter 5 are from the publication: 'Edge currents shunt the insulating bulk in gapped graphene' *arXiv:*1612.05902 (under review of *Nature communications*).

The gapless nature of graphene is protected by its crystal symmetry. An energy gap can be opened in bilayer graphene by applying a bias between two graphene layers. However, such energy gap up to few hundred meV in bilayer graphene rarely leads to an ON/OFF ratio above 100 in realistic devices.

We try to answer this puzzle by studying the spatial supercurrent flow in graphene Josephson junctions. While we gradually open a gap in bilayer graphene, the uniform supercurrent flow switches to an edge-dominated distribution. Similar phenomenon occurs in graphene/hBN superlattices. We carry out transport measurements in bilayer graphene Hall bar and Corbino devices. For Hall bar geometry, the resistance saturates to few resistance quanta at finite gap. In contrast, the resistance in 'edgeless' Corbino devices keep increasing. Our results show that due to the topology of gapped graphene systems the insulating bulk is shunted by the edge channels.

My personal contribution to this work is: I generated the idea of using Josephson junctions to detect the edge currents. I carried out the electrical transport measurements, analysed the data, prepared all the figures for main text and supplementary information, and participated to writing the manuscript.

The acknowledgements for the paper are: A.K.G., M.B.S. and M.J.Z. designed the experiment. M.B.S., A.V.K. and S.H. fabricated the devices. M.J.Z., M.D.T., J.R.P., D.B. and G.L.Y. carried out the transport measurements. M.J.Z., M.D.T., J.R.P., A.K.G. and M.B.S. analysed and interpreted the data. M.P. provided theory support. K.W. and T.T. supplied hBN crystals. A.M. and I.J.V.-M. helped with experiment and simulation. M.B.S., M.J.Z., J.P.R. and A.K.G. wrote the manuscript with input from all the authors.

Edge currents shunt the insulating bulk in gapped graphene

M. J. Zhu[1], A. V. Kretinin[2,3], M. D. Thompson[4], D. A. Bandurin[1], S. Hu[1], G. L. Yu[1], A. Mishchenko[1], I. J. Vera-Marun[1], K. Watanabe[5], T. Taniguchi[5], M. Polini[6], J. R. Prance[4], K. S. Novoselov[1,2], A. K. Geim[1,2*], M. Ben Shalom[1,2*]

[1]*School of Physics and Astronomy, The University of Manchester, Manchester M13 9PL, UK*

[2]*National Graphene Institute, The University of Manchester, Booth St. E, Manchester M13 9PL, UK*

[3]*School of Materials, The University of Manchester, Manchester M13 9PL, UK*

[4]*Department of Physics, University of Lancaster, Lancaster LA1 4YW, UK*

[5]*National Institute for Materials Science, 1-1 Namiki, Tsukuba 305-0044, Japan*

[6]*Istituto Italiano di Tecnologia, Graphene labs, Via Morego 30I-16163, Italy*

An energy gap can be opened in the electronic spectrum of graphene by lifting its sublattice symmetry[1-4]. In bilayers, it is possible to open gaps as large as 0.2 eV. However, these gaps have rarely led to a highly insulating state expected for such semiconductors at low temperatures[5-11]. This long-standing puzzle is usually explained by charge inhomogeneity[6-10]. Here we investigate spatial distributions of proximity-induced superconducting currents in gapped graphene and, also, compare measurements in the Hall bar and Corbino geometries in the normal-state. By gradually opening the gap in bilayer graphene, we find that the supercurrent at the charge neutrality point changes from uniform to such that it propagates along narrow stripes near graphene edges. Similar stripes are found in gapped monolayers. These observations are corroborated by using the 'edgeless' Corbino geometry in which case resistivity at the neutrality point increases exponentially with increasing the gap, as expected for an ordinary semiconductor. This is in contrast to the Hall bar geometry where resistivity measured under similar conditions saturates to values of only about a few resistance quanta. Our results demonstrate an edge-dominated current flow inherently related to the gapped graphene spectra[12-14].

The gapless spectra of mono- and bi- layer graphene (MLG and BLG, respectively) are protected by symmetry of their crystal lattices. If the symmetry is broken by interaction with a substrate[3,4] or by applying an electric field[1,2], an energy gap opens in the spectrum. In BLG, its size E_{gap} can be controlled by the displacement field D applied between the two graphene layers. Large gaps were found using optical methods[5] and extracted from temperature (T) dependences of resistivity ρ at sufficiently high T[6-10]. Their values are in good agreement with theory. On the other hand, at low T (typically, below 50 K), ρ at the charge neutrality point (CNP) in gapped graphene is found to saturate to relatively low values that are incompatible with large E_{gap}[6-11]. This disagreement is attributed to remnant charge inhomogeneity[6,8,10] that results in hopping conductivity and, therefore, weakens T dependences. Alternative models to explain the subgap conductivity were proposed, too. They rely on the nontrivial topology of Dirac bands in gapped MLG and BLG[12-15], which gives rise to valley-polarized currents[13-15]. Large nonlocal resistances were reported for both graphene systems at the CNP and explained by valley currents propagating through the charge-neutral bulk[16-18]. Graphene edges[12,15], p-n junctions[14,19] and stacking boundaries[20] can also support topological currents. These conductive channels were suggested to shunt the insulating bulk, leading to a finite ρ. Experimentally, the situation is even more complicated because additional conductivity may appear for trivial reasons such as charge inhomogeneity induced by chemical or electrostatic doping[21-23]. Here we show that there are intrinsic conductive channels near edges of charge-neutral graphene, which emerge if an energy gap is opened in its spectrum. In contrast to the naive expectation, at low disorder levels the gap is efficiently shunted, suggesting a significant role of the localization length at the device edge. We tentatively attribute the edge channels to the presence of unavoidable defects such as, e.g., short zigzag-edge segments[12]. Their wavefunctions extend deep into the insulating bulk where they sufficiently overlap to create a quasi-one-dimensional impurity band with little intervalley scattering and high conductivity.

We start with discussing behavior observed for superconductor-graphene-superconductor (SGS) Josephson junctions. Our devices were short and wide graphene crystals that connected superconducting Nb electrodes[24] (Fig. 5.1). Each device contained several such SGS junctions with the length L varying from 300 to

500 nm and the width W from 3 to 5 μm. To ensure highest possible quality[24], graphene was encapsulated between hexagonal boron nitride (hBN) crystals with the upper hBN serving as a top-gate dielectric and the Si/SiO$_2$ substrate as a bottom gate (Fig. 5.1b). For details of device fabrication and characterization we refer to Methods and Supplementary Information (SI). By measuring the critical current I_c as a function of perpendicular magnetic field B, the local density $J_s(x)$ in the x direction perpendicular to the super-current flow can be deduced[25], as illustrated in Fig. 5.1c,d. This technique is well established and was previously used to examine, for example, edge states in topological insulators[26] and wave-guided states in graphene[22]. In our report, we exploit the electrostatic control of the BLG spectrum to examine how $J_s(x)$ changes with opening the gap.

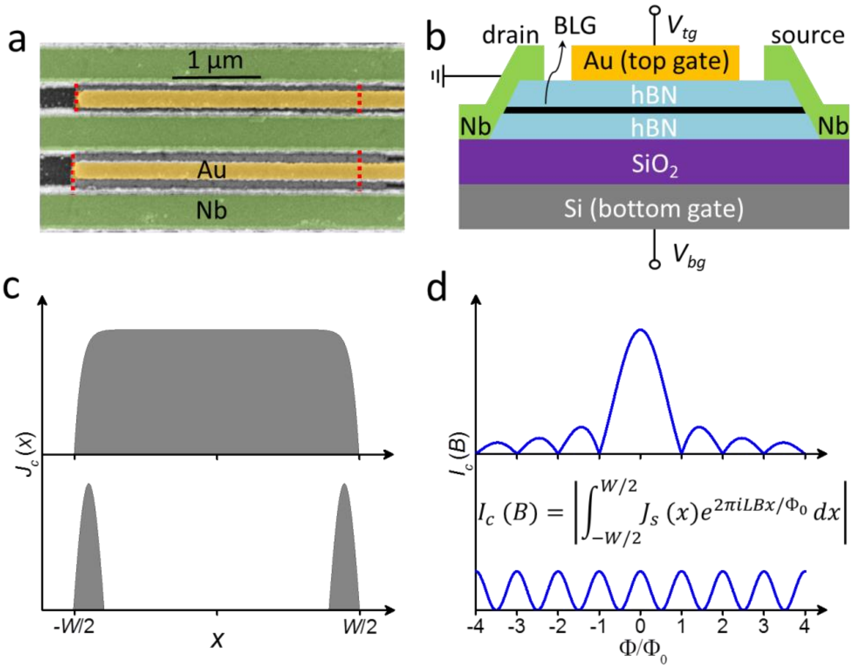

Fig. 5.1 Gated Josephson junctions and spatial distribution of supercurrents

a, Electron micrograph of our typical device (in false color). Nb leads (green) are connected to BLG (its edges are indicated by red dashes). The top gate is shown in yellow. **b,** Schematics of such junctions. **c,** Illustration of uniform and edge-dominated current flow through Josephson junctions (top and bottom panels, respectively). **d,** The corresponding behavior of the critical current I_c as a function of B. I_c is related to $J_s(x)$ by the equation shown in **d**. For a uniform current flow, I_c should exhibit a Fraunhofer-like pattern (top panel) such that the supercurrent goes to zero each time an integer number N of magnetic flux quanta Φ_0 thread through the junction. Maxima in I_c between zeros also become smaller with increasing N. For the flow along edges (bottom panel), I_c is minimal for half-integer flux values $\Phi = (N+1/2)\Phi_0$, and maxima in I_c are independent of B. The spatial distribution $J_s(x)$ can be found[24,25] from $I_c(B)$ using the inverse FFT. Due to a finite interval of Φ over which the interference pattern is usually observed experimentally, $J_s(x)$ obtained from the FFT analysis are usually smeared over the x-axis as shown schematically in **c**.

By varying the top and bottom gate voltages (V_{tg} and V_{bg}, respectively), it is possible to keep BLG charge neutral while doping the two graphene layers with carriers of the opposite sign (see Fig. 5.2a). This results in the displacement field $D(V_{tg},V_{bg})$ that translates directly into the spectral gap[1,2,5,6]. Its size $E_{gap}(D)$ can be deduced not only theoretically but also measured experimentally, as discussed in section 1 of SI. To quantify proximity superconductivity in our devices, we define their critical current I_c as the current at which the differential resistance dV/dI deviates from zero above our noise level[24]. With reference to Fig. 5.2b, I_c corresponds to the edge of the black area outlined by bright contours. At high doping (Fermi energy > E_{gap}) and low T, I_c is found to depend weakly on D, reaching values of a few µA/µm, in agreement with the previous reports[22,24,27]. The supercurrent generally decreases with increasing junction's resistance and becomes small at the CNP. Its value depends on E_{gap} (Fig. 5.2b). Accordingly, the largest I_c in the neutral state is found for zero D (no gap) reaching ≈300 nA for the junction shown in Fig. 5.2. The value drops to 2 nA at $D = \pm0.07$ V/nm, which corresponds to $E_{gap} \approx 7$ meV. For larger gaps, I_c becomes smaller than 1 nA and could no longer be resolved because of a finite temperature (down to 10 mK) and background noise[24].

We analyze changes in the interference pattern, $I_c(B)$, with increasing D (that is, E_{gap}). At zero D, we observe the standard Fraunhofer pattern at the CNP, which is basically similar to that measured at high doping (cf. two top panels of Fig. 5.2c). Only absolute values of I_c are different because of different ρ, as expected[24]. The Fraunhofer pattern corresponds to a uniform current flow (Fig. 5.1c,d). In contrast, the interference pattern measured at the CNP for a finite gap is qualitatively different (Fig. 5.2c; $D = 0.055$ V/nm). The phase of the oscillations changes by 90° and the central lobe becomes twice narrower. In addition, the side lobes no longer decay with increasing B but exhibit nearly the same amplitude. Such a pattern resembles the one shown schematically in Fig. 5.1d for the case of the supercurrent flowing along edges. The only difference with Fig. 5.1d is that in our case the central lobe remains higher than the others. For quantitative analysis, we calculated the inverse fast Fourier transform (FFT) of $I_c(B)$, which yielded[26] the current distributions $J_s(x)$ shown in Fig. 5.2d. The supercurrent is progressively pushed towards device edges with increasing the gap. This is already visible for D = 0.025 V/nm but further increase in D suppresses the bulk current to practically zero, within the experimental accuracy of our FFT analysis (Fig. 5.2d). The accuracy is limited by a finite range of B in which the interference pattern could be detected (section 2 of SI).

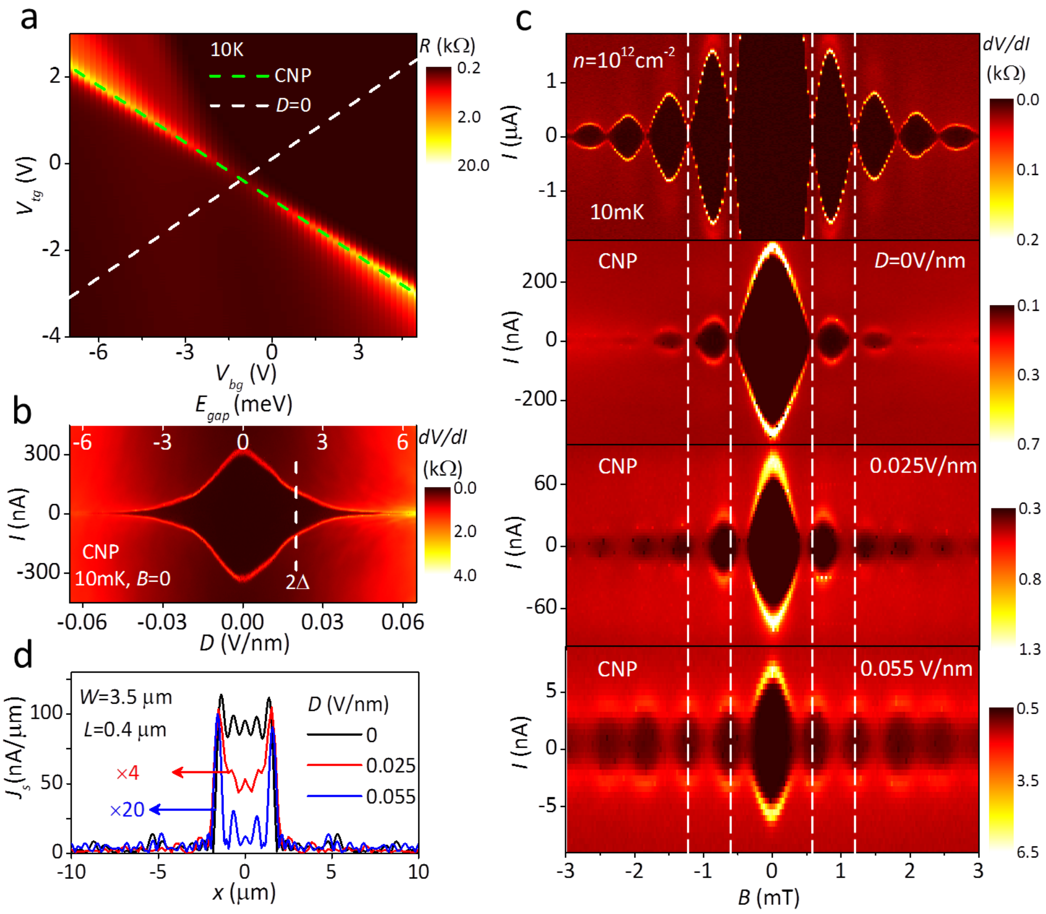

Fig. 5.2 Redistribution of supercurrent as the gap opens in bilayer graphene

a, Resistance R of one of our Josephson junctions (3.5 µm wide and 0.4 µm long) above the critical T as a function of top and bottom gate voltages. The dashed white line indicates equal doping of the two graphene layers with carriers of the same sign. The dashed green line marks the CNP (maximum R) and indicates equal doping with opposite-sign carriers. **b,** Differential resistance dV/dI measured along the green line in **a** at low T and in zero B. Transition from the dissipationless regime to a finite voltage drop shows up as a bright curve indicating I_c. The vertical line marks the superconducting gap of our Nb films. **c,** Interference patterns in small B. The top panel is for the case of high doping [$I_c(B=0) \approx 10$ µA] and indistinguishable from the standard Fraunhofer-like behavior illustrated in Fig. 5.1d. The patterns below correspond to progressively larger E_{gap}. Changes in the phase of Fraunhofer oscillations are highlighted by the vertical dashed white lines. **d,** Extracted spatial profiles of the supercurrent density at the CNP for the three values of D in **c**.

For completeness, we have also studied SGS junctions that were fabricated using monolayer graphene placed on top of hBN and aligned along its crystallographic axes. Such alignment (within 1-2°) results in opening of a gap of ≈30 meV at the main CNP[3,4], and secondary CNPs appear for high electron and hole doping[3,4,16]. Unlike for the case of BLG, E_{gap} cannot be changed in situ in MLG devices, but one can still compare interference patterns for neutral and doped states of the same SGS junction and, also, use nonaligned junctions as a reference. Fig. 5.3a,b show typical behavior of I_c as a function of carrier concentration n for SGS devices made from gapped (aligned) and gapless (nonaligned) MLG. In the gapped device, the supercurrent is suppressed not only at the main CNP but also at secondary CNPs. For all electron and hole concentrations away from the CNPs, both devices exhibit the standard Fraunhofer pattern indicating a uniform supercurrent flow (cf. top panels of Fig. 5.3c,d). The same is valid at the CNP in gapless graphene (Fig. 5.3d,f). In contrast, for gapped MLG, the interference pattern at the main CNP undergoes significant changes such that the phase and period of oscillations in I_c change (Fig. 5.3c; bottom panel), somewhat similar to the behavior of gapped BLG at the CNP. Quantitative analysis using FFT again shows that, in gapped MLG, the supercurrent flows predominantly along graphene edges for $n < \pm 5 \cdot 10^{10}$ cm^{-2} (Fig. 5.3e). The figure seems to suggest a shift of conductive channels from edges into the interior. This shift originates from the increase in the Fraunhofer period at the CNP in Fig. 5.3c and corresponds to a decrease in the junction's effective area. However, we believe that this shift arises from non-uniform doping along the current direction. Our MLG devices do not have a top gate and this allows doping by metal contacts to extend significantly (tens of nm) inside the graphene channel[28] which reduces the effective length of the junction.

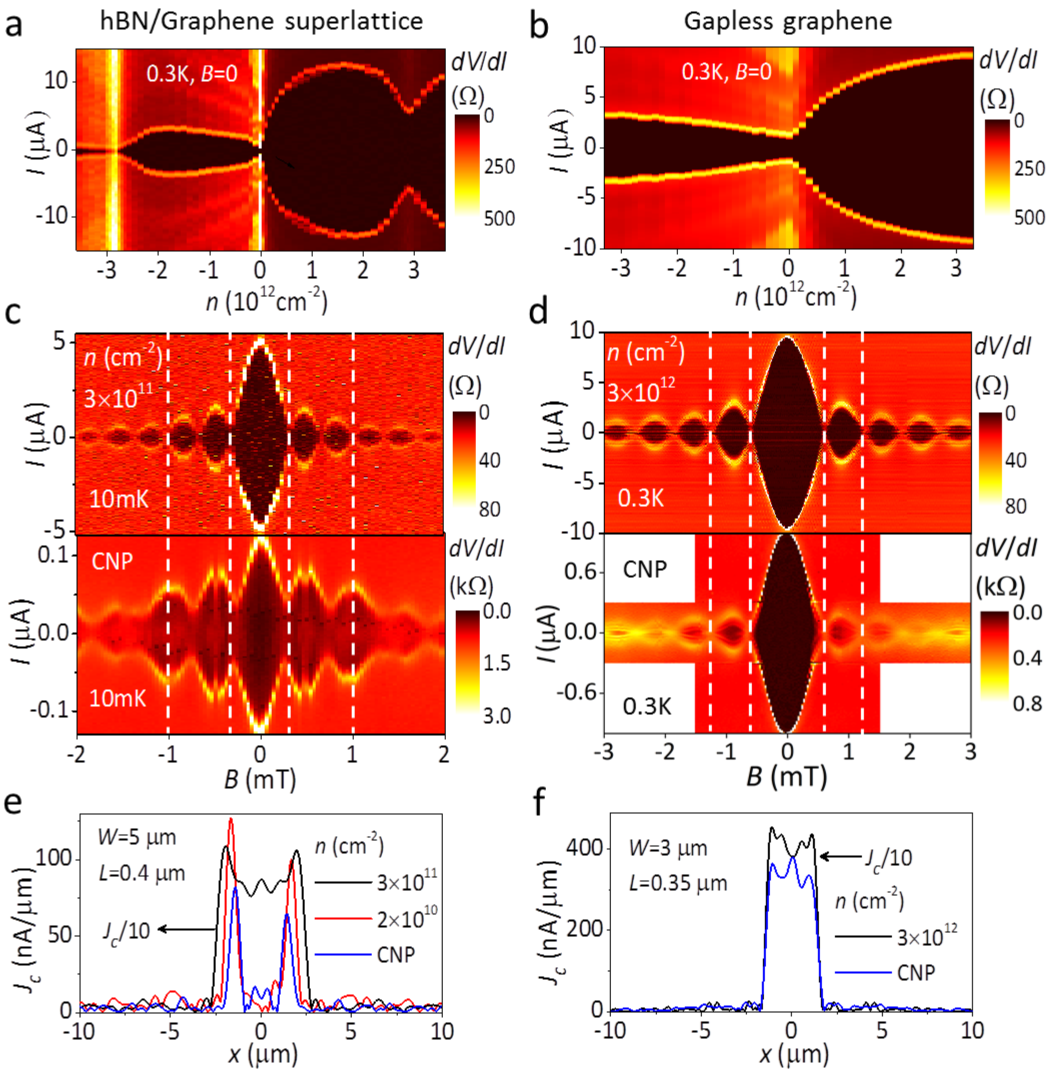

Fig. 5.3 Interference patterns and supercurrent flow in gapped and non-gapped MLG

a, Differential resistance as a function of carrier concentration *n* and applied current *I* for a Nb-MLG-Nb junction (5 μm wide and 0.4 μm long). The gap is induced by alignment with the bottom hBN crystal. **b,** Same for encapsulated but nonaligned monolayer graphene (the junction is 3 μm wide and 0.35 μm long). **c,** Interference patterns for gapped MLG at relatively high doping (top panel) and at the CNP. **d**, Same for non-gapped graphene. **e,f,** Corresponding spatial profiles of the current flow. They were calculated using experimental patterns such as shown in **c** and **d**. Note that graphene edges in **e** support fairly high supercurrent at the CNP whereas there is no indication of any enhanced current density along edges for the non-gapped case in **f**.

We emphasize that the observed redistribution of supercurrents towards edges is an extremely robust effect observed for all 8 gapped-graphene junctions we studied and in none without a gap (more than 10)[24]. In principle, one can imagine additional electrostatic and/or chemical doping near graphene edges[21-23], which would enhance their conductivity and, hence, favor local paths for supercurrent. The electrostatic doping is ruled out by the fact that edge supercurrents appeared independently of the CNP position as a function of gate voltage (residual doping in our devices varied from practically zero to $< 10^{11}$ cm^{-2}) and were observed for devices with the top gate being only a few nm away from the graphene plane, which ensured a uniform electric field. Chemical doping at graphene edges was previously reported in non-encapsulated[21] and, also, encapsulated but not annealed devices[23]. All our devices were encapsulated and thoroughly annealed, and some of them had edges that were fully covered by top hBN rather than exposed to air (section 4 of SI). We note that the Josephson interference experiment, which confirms an even supercurrent density at the two BLG edges, are independent of their profile. Importantly, we have found no evidence for enhanced transport along edges of similar but gapless-graphene devices. To this end, we refer, for example, to Fig. 5.3 e,f. In the gapped MLG device, near-edge J_s reaches ≈ 100nA/µm. Such supercurrents would certainly be visible in the distribution profile of the non-gapped graphene at the CNP in Fig. 5.3f. All the above observations point at a critical role of the gap presence in creating local edge currents.

While providing important insights about the current flow, Josephson interference experiments are limited to small E_{gap} such that junction's resistance remains well below 1 MOhm allowing superconducting proximity. To address the situation for the larger gaps accessible in BLG devices, we compare their normal transport characteristics in the Corbino and Hall bar geometries. Because the Corbino geometry does not involve edges, such a comparison has previously been exploited to investigate the role of edge transport (for example, in the quantum Hall effect[29]). A number of dual-gated BLG devices such as shown in Fig. 5.4a were fabricated and examined over a wide range of D and T. Our experiments revealed a striking difference between ρ measured in the two geometries. In the Corbino geometry, ρ at the CNP rises exponentially with D and its value is limited only by a finite dielectric strength of ≈0.7 V/nm achievable for our hBN (Fig. 5.4b) and, at low T, by leakage currents. In contrast, in the Hall bar geometry, ρ at the CNP saturates already at low $D < 0.2$ V/nm and reaches only to a few tens of kOhms for all our T (Fig. 5.4c). Importantly, this behavior is seen under the same measurement conditions and despite the same or higher homogeneity attained for the Hall bar devices. The profound difference unambiguously points at a finite conductivity caused by the presence of graphene edges, in agreement with the conclusions achieved from our Josephson experiments.

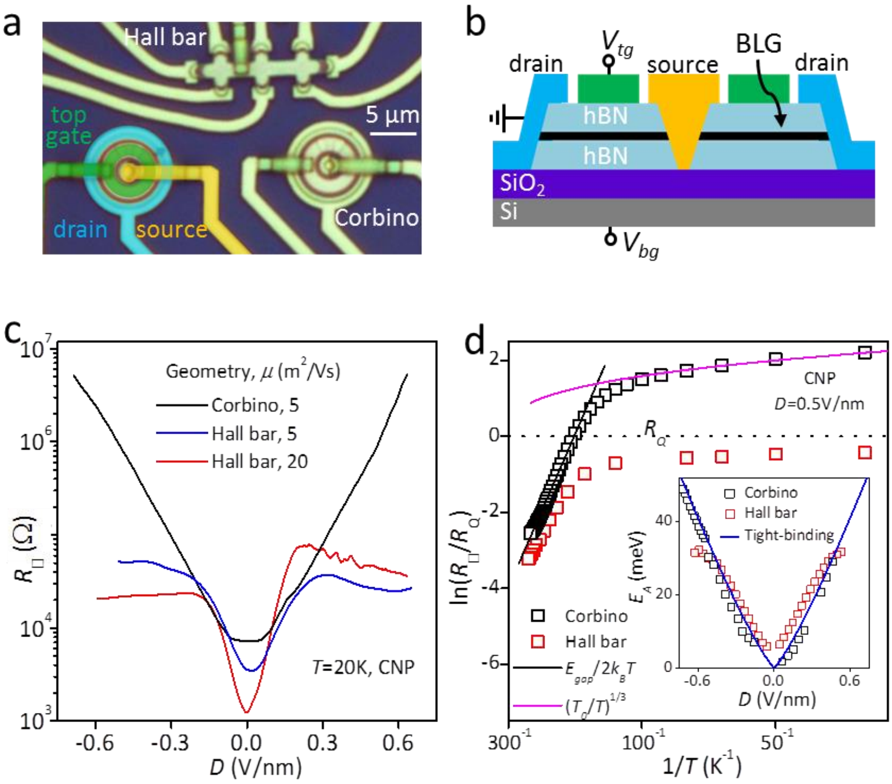

Fig. 5.4 Resistivity of charge-neutral bilayer graphene in Corbino and Hall bar geometries

a, Optical image of one of our devices with a Hall bar and two Corbino disks. The left disk is colored to indicate source, drain and top gate electrodes. **b,** Cross-sectional schematics of our double-gated Corbino devices. **c,** Resistivity ρ at the CNP for Corbino and Hall bar geometries as a function of D. For the Corbino device, ρ changes exponentially over 3 orders of magnitude. The Hall bars exhibit saturation to a few R_Q. **d,** Arrhenius plot for $\rho(T)$. The energy gap E_{gap} is calculated from the linear slopes at $T > 100$ K, which are similar for both Corbino and Hall bar geometries. Below 50 K, the Hall bar device exhibits little T dependence. Inset: E_{gap} found for various D (symbols). The blue curve is tight-binding calculations for the BLG gap from ref.[1].

Another noteworthy distinction between the two geometries is their temperature dependences at the CNP. For T above 100 K, both Corbino and Hall bar devices exhibited the same activation behavior $\rho \propto \exp(E_{gap}/2k_BT)$ as expected for a semiconductor with the gap E_{gap} (Fig. 5.4d). Our measurements over a wide range of D yielded E_{gap}[meV] ≈ 100×D[V/nm], in quantitative agreement with theory and previous reports[5] (inset of Fig. 5.4d). At lower T, resistivity of the Corbino devices continued growing and is well described by hopping conductivity that may involve both nearest-neighbor and variable range hopping[6,8-10] (Fig. 5.4d). On the other hand, ρ (T) found using the Hall bars rapidly saturated below 100 K to values of a few resistance quantum $R_Q=h/e^2$ and changed little (by <30%) with decreasing T down 2 K. The saturation behavior is similar to that observed for conductance along the line junction of oppositely biased BLG[19], and along walls separating BLG domains with AB and BA stacking[20].

Two possible scenarios for shunting the insulating state of gapped graphene have previously been put forward. Both rely on nontrivial topology of the gapped Dirac spectrum. One of them considers electronic states due to short zigzag segments[15] that may be present even at relatively random edges[12]. Although these states decay exponentially into the gapped bulk, their penetration length ξ is very long with respect to the lattice constant a. For MLG and BLG, ξ can be estimated as $\approx \hbar v/E_{gap}$ and $\hbar/\sqrt{mE_{gap}}$, respectively, where $\hbar$ is the reduced Planck constant, v the Fermi velocity in MLG and m the effective mass in BLG. For our typical gaps, ξ is about 10–20 nm, much larger than a. This suggests that wavefunctions of isolated zigzag states should strongly overlap inside the bulk creating a quasi-one-dimensional (1D) band. Moreover, because $\xi/a >> 1$, the wavefunctions mostly reside in the bulk where there are little defects, which ensures that impurity bands are effectively protected against backscattering. The situation resembles the modulation doping used to achieve high carrier mobilities in semiconductor quantum wells. The observed saturation of ρ to ~ R_Q and the long-range nonlocal resistance reported previously[16-18] imply that the mean free path along the quasi-1D channels can reach a micrometer scale for high-mobility graphene. Although numerical simulations[12] yielded zero-T localization lengths at least an order of magnitude shorter than this scale, localization in the edge channels may be suppressed by a finite T and electron-electron interactions that are prominent especially in low-dimensional conductors. Such delocalization effects have so far not been investigated theoretically. The invoked edge channels would explain our experimental observations. In addition, there is a complementary scenario that also relies on the nontrivial topology of the gapped Dirac spectra but may not require zigzag segments. The valley Hall effect is inherent to gapped graphene and generates valley currents that flow perpendicular to applied electric field[13,16]. If injected from electric contacts into the gapped bulk, they are expected to become squeezed towards weakly-conductive edges, similar to what is known for the case of the quantum Hall effect and in agreement with recent simulations for gapped MLG[14].

To conclude, our results show that the insulating state of gapped graphene is electrically shorted by narrow edge channels exhibiting high conductivity. This can explain low apparent resistivity often observed for charge-neural gapped graphene at low temperatures, especially in devices made from high quality graphene in which the bulk is expected to contribute little to either hopping conductivity or backscattering of edge modes[5-11,19]. Further experiments and theory are needed to distinguish between the described scenarios and elucidate the nature of the reported edge conductance.

Methods

Device fabrication. Mono- or bi-layer graphene crystals were encapsulated between hBN crystals (typically, ≈30 nm thick) using the dry transfer technique as detailed previously[31]. The hBN-graphene-hBN stack was assembled on top of an oxidized Si wafer (300 or 90 nm of SiO_2) and then annealed at 300 °C in a forming gas (Ar-H_2 mixture) for 3 hours. As the next step we used the standard electron-beam lithography to create a PMMA mask that defined contact regions. Reactive ion etching (Oxford Plasma Lab 100) was employed to make trenches in the heterostructure through the mask. We used a mixture of CHF_3 and O_2, which provided easy lift-off of PMMA, so that metal contacts could be deposited directly after plasma etching. This also allowed us to minimize contamination of the exposed graphene edges[24]. After this, for BLG devices, another metal film (typically, Au/Cr) was deposited on top of the heterostructure to serve as the top gate. In order to avoid the edges of graphene extending out of the metal gate, the latter is used as a part of the final etch-mask; the uncovered graphene between the contacts and the gate is protected by a second PMMA mask, allowing the metal gate to extend slightly at the crucial edge locations. For the Hall bar geometry, we often used an additional hBN crystal to cover the hBN-graphene-hBN stack after plasma etching, which allowed the metal film for the top gate to go over exposed graphene edges without touching them. To provide the central contact in Corbino devices, we used air bridges[32]. In some of our Josephson devices, graphene was not etched but made directly from cleaved crystals selected to have a strip-like shape. In this case, graphene edges were not exposed but fully encapsulated in hBN. Similar transport and Josephson behavior was found in all cases, independent of the variations in fabrication procedures.

Transport experiments. All electrical measurements were carried out in a He3 cryostat (Oxford Instruments) for T down to 0.3 K and, for lower T, in a dilution refrigerator with the base temperature of 10 mK (BlueFors Cryogenics). The differential resistance was measured in a quasi-four-terminal configuration (two superconducting leads for driving the current and the other two for measuring voltage) using a low-frequency lock-in technique. All electrical connections to our devices passed through a cold RC filter (Aivon Therma) placed close to the sample and additional AC filters were used outside the cryostats. At large displacement fields, our Corbino devices exhibited high resistivity such that the lock-in technique became inappropriate. In this case, we used dc measurements.

References

[1] McCann, E. Asymmetry gap in the electronic band structure of bilayer graphene. *Physical Review B* **74**, 161403 (2006).

[2] Ohta, T., Bostwick, A., Seyller, T., Horn, K. & Rotenberg, E. Controlling the electronic structure of bilayer graphene. *Science* **313**, 951-954 (2006).

[3] Hunt, B. *et al.* Massive Dirac Fermions and Hofstadter Butterfly in a van der Waals Heterostructure. *Science* **340**, 1427-1430 (2013).

[4] Woods, C. R. *et al.* Commensurate-incommensurate transition in graphene on hexagonal boron nitride. *Nature Physics* **10**, 451-456 (2014).

[5] Zhang, Y. *et al.* Direct observation of a widely tunable bandgap in bilayer graphene. *Nature* **459**, 820-823 (2009).

[6] Oostinga, J. B., Heersche, H. B., Liu, X. L., Morpurgo, A. F. & Vandersypen, L. M. K. Gate induced insulating state in bilayer graphene devices. *Nature Materials* **7**, 151-157 (2008).

[7] Xia, F., Farmer, D. B., Lin, Y. M. & Avouris, P. Graphene field-effect transistors with high on/off current ratio and large transport band gap at room temperature. *Nano letters* **10**, 715-718 (2010).

[8] Zou, K. & Zhu, J. Transport in gapped bilayer graphene: The role of potential fluctuations. *Physical Review B* **82,** 081407 (2010).

[9] Taychatanapat, T. & Jarillo-Herrero, P. Electronic Transport in Dual-Gated Bilayer Graphene at Large Displacement Fields. *Physical Review Letters* **105**, 166601 (2010).

[10] Yan, J. & Fuhrer, M. S. Charge transport in dual gated bilayer graphene with Corbino geometry. *Nano letters* **10**, 4521-4525 (2010).

[11] Weitz, R. T., Allen, M. T., Feldman, B. E., Martin, J. & Yacoby, A. Broken-Symmetry States in Doubly Gated Suspended Bilayer Graphene. *Science* **330**, 812-816 (2010).

[12] Li, J. A., Martin, I., Buttiker, M. & Morpurgo, A. F. Topological origin of subgap conductance in insulating bilayer graphene. *Nature Physics* **7**, 38-42 (2011).

[13] Lensky, Y. D., Song, J. C. W., Samutpraphoot, P. & Levitov, L. S. Topological Valley Currents in Gapped Dirac Materials. *Physical Review Letters* **114**, 256601 (2015).

[14] Kirczenow, G. Valley currents and nonlocal resistances of graphene nanostructures with broken inversion symmetry from the perspective of scattering theory. *Physical Review B* **92**, 125425 (2015).

[15] Castro, E. V., Peres, N. M. R., dos Santos, J. M. B. L., Castro, A. H. & Guinea, F. Localized states at zigzag edges of bilayer graphene. *Physical Review letters* **100**, 026802 (2008).

[16] Gorbachev, R. V. *et al.* Detecting topological currents in graphene superlattices. *Science* **346**,448-451 (2014).

[17] Sui, M. *et al.* Gate-tunable topological valley transport in bilayer graphene. *Nature Physics* **11,** 1027-1031 (2015).

[18] Shimazaki, Y. *et al.* Generation and detection of pure valley current by electrically induced Berry curvature in bilayer graphene. *Nature Physics* **11,** 1032-1036 (2015).

[19] Li, J. *et al.*Gate-controlled topological conducting channels in bilayer graphene. *Nature Nanotechnology* **11**, 1060-1065 (2016).

[20] Ju, L. *et al.* Topological valley transport at bilayer graphene domain walls. *Nature* **520**, 650- 655 (2015).

[21] Chae, J. *et al.* Enhanced carrier transport along edges of graphene devices. *Nano letters* **12**, 1839-1844, (2012).

[22] Allen, M. T. *et al.* Spatially resolved edge currents and guided-wave electronic states in graphene. *Nature Physics* **12,** 128-133 (2016).

[23] Woessner, A. *et al.* Near-field photocurrent nanoscopy on bare and encapsulated graphene. *Nature communications* **7**, 10783 (2016).

[24] Ben Shalom, M. *et al.* Quantum oscillations of the critical current and high-field superconducting proximity in ballistic graphene. *Nature Physics* **12,** 318-322 (2016).

[25] Dynes, R. C. & Fulton, T. A. Supercurrent Density Distribution in Josephson Junctions. *Physical Review B* **3**, 3015-3023 (1971).

[26] Hart, S. *et al.* Induced superconductivity in the quantum spin Hall edge. *Nature Physics* **10**, 638-643 (2014).

[27] Calado, V. E. *et al.* Ballistic Josephson junctions in edge-contacted graphene. *Nature Nanotechnology* **10**, 761-764 (2015).

[28] Blake, P. *et al.* Influence of metal contacts and charge inhomogeneity on transport properties of graphene near the neutrality point. *Solid State Communications* **149**, 1068-1071 (2009).

[29] Dolgopolov, V. T., Shashkin, A. A., Zhitenev, N. B., Dorozhkin, S. I. & von Klitzing, K. Quantum Hall effect in the absence of edge currents. *Physical Review B* **46**, 12560-12567 (1992).

[30] Ikushima, K., Sakuma, H., Komiyama, S. & Hirakawa, K. Visualization of quantum Hall edge channels through imaging of terahertz emission. *Physical Review B* **76**, 165323 (2007).

[31] Kretinin, A. V. *et al.* Electronic Properties of Graphene Encapsulated with Different Two-Dimensional Atomic Crystals. *Nano letters* **14**, 3270-3276 (2014).

[32] Borzenko, T., Gould, C., Schmidt, G. & Molenkamp, L. W. Metallic air-bridges fabricated by multiple acceleration voltage electron beam lithography. *Microelectronic Engineering* **75**, 210-215 (2004).

Edge currents shunt the insulating bulk in gapped graphene

Supplementary Information

M. J. Zhu *et al*

1. Characterization of double-gated bi-layer graphene

By implementing top and bottom gate electrodes in the studied devices, it is possible control the charge carrier density *n* and the electric displacement field *D* between the two layers independently[S1]. Below, the calibration procedure of $n(V_{\mathrm{tg}},V_{\mathrm{bg}})$ and $D(V_{\mathrm{tg}},V_{\mathrm{bg}})$ (V_{tg} and V_{bg} are the top and bottom gate voltages respectively). Examples of such measurements for Hall bar, Josephson junction, and Corbino device geometries are presented in Fig. 5.S1.

At first, the resistance *R* is plotted as a function of the two gates (Fig. 5.S1a,c,d). The sharp peak in *R* determines the position of the charge neutrality point (CNP), Fig. 5.S1b. The axis parallel to the charge neutrality line is determined (see black arrows, Fig. 5.S1a), and its slope: $\Delta V_{bg}/\Delta V_{tg}\approx 2$ is equal to the capacitance ratio of the two gates C_{tg}/C_{bg}. Smaller C_{bg} is expected for the thicker SiO_2 dielectric at the bottom, and requires separate characterization for each device due to the different thickness of hBN which we place on top of SiO_2. The negative slope ($\Delta V_{bg}/\Delta V_{tg}\approx -2$, marked by white line on Fig. 5.S1a), corresponds to adding the same charge to both layers and changing the total *n* while keeping a fixed *D*. In order to accurately measure *n* we analyze the quantum oscillations in *R* at high magnetic fields and away from CNP. From this, the capacitance (per unit of area) for each gate is extracted using: $ne = C_{tg}\Delta V_{tg} + C_{bg}\Delta V_{bg}$, and the displacement field is calculated to be: $D = (C_{tg}\Delta V_{tg} - C_{bg}\Delta V_{bg})/2\varepsilon_0$.

The energy gap E_{gap} is measured independently from the Arrhenius-like activation of *R* at high temperatures as shown in the main text, Fig. 5.4d. When measured at different *D*, we find E_{gap}[meV]≈100×*D*[V/nm] to hold for all our BLG devices (see inset to Fig. 5.4d), in agreement with previous reports[S2] and calculations[S3].

The devices presented here also show saturation of the sub-gap *R* with increasing *D* in the Hall bar and Josephson geometry, and exponentially increasing *R* in the Corbino geometry (Fig. 5.S1b,d). For the latter, an additional increase in *R* is observed at a fixed value of the bottom gate V_{bg}≈-3V (Fig. 5.S1c). It corresponds to the CNP of the BLG at the locations in the device not covered by the top gate (see image in Fig. 5.4a). This spatial separation of the top gate from the metal-graphene interface guarantees a negligibly-low contact resistance at high *D* for the two-probe measurement in this geometry.

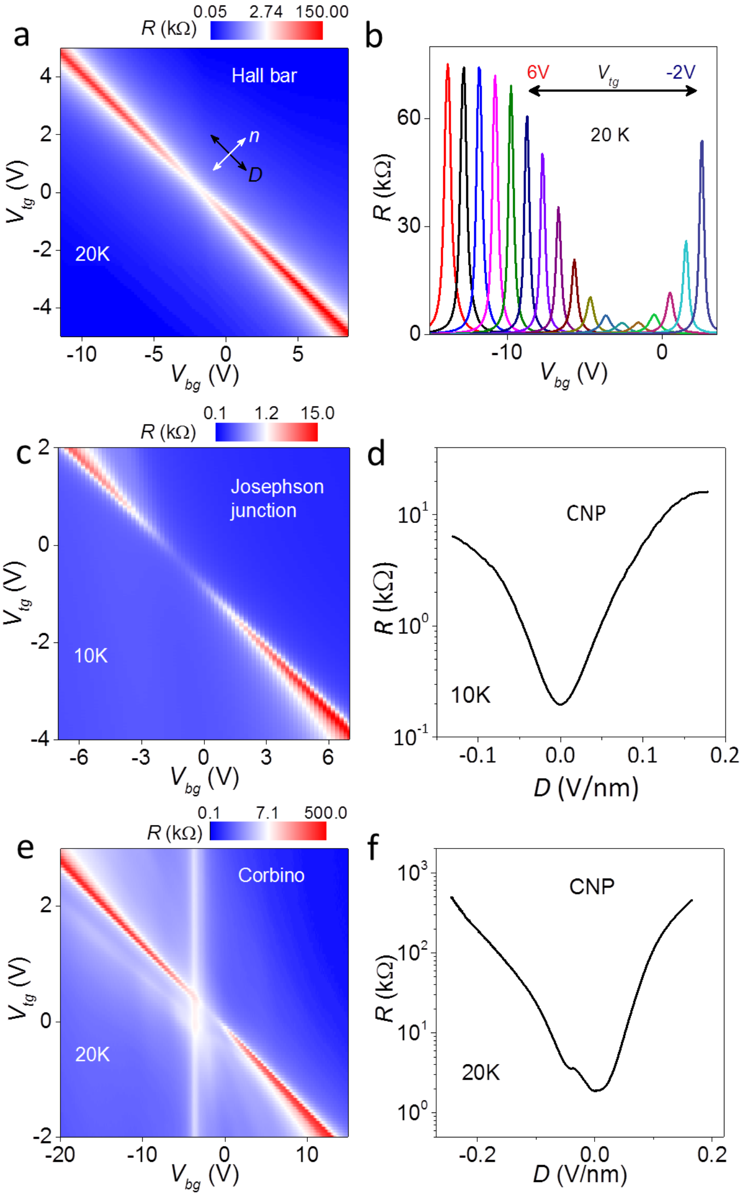

Fig. 5.S1 Characterization of double-gated bilayer graphene

a, Color-plots of the resistance *R* (in log-scale) as a function of the top and bottom gate voltages, for the Hall bar geometry (the measured section is 2.3 μm wide and 6.6 μm long). **b,** Bottom gate scans from the map in (a) at different fixed values of the top gate. At the charge neutrality point (CNP) *R* is saturated for V_{tg}>5V corresponding to *D* ≈-0.2V/nm as shown in the main text (Fig. 5.4c). **c,** Color-plots of the resistance *R* (in log-scale) as a function of the top and bottom gate voltages for the Josephson junction studied in the main text Figs. 5.2. **d,** Resistance at CNP extracted from the map in (c). The increase in R is saturated for displacement field $D\approx0.15$V/nm. **e,** Color-plots of the resistance R (in log-scale) as a function of the top and bottom gate voltages for a Corbino "edge-less" device. Here the top gate is 10 µm wide and 1 µm long, and it is separated by 1 µm from the inner and outer contacts. The vertical white line at $V_{bg}\approx$-3V corresponds to the charge neutrality point in the part of the device which is not covered by the top gate. **f,** Resistance at CNP extracted from the map in (c). The increase in R is exponential with the displacement field D.

2. Example of additional BLG Josephson junction

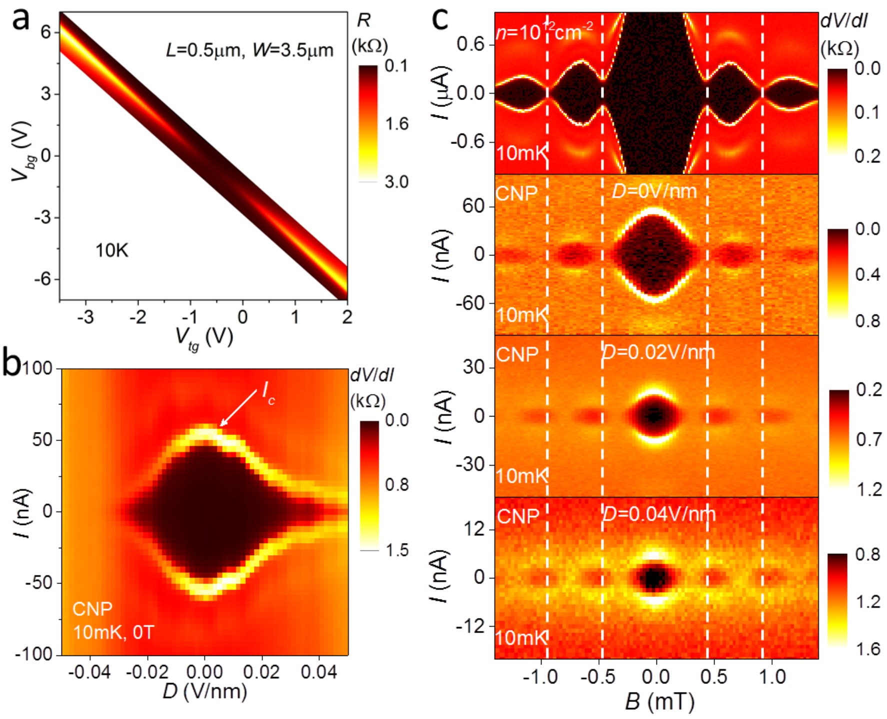

Fig. 5.S2 Redistribution of supercurrent as the gap opens in bilayer graphene **a,** Resistance R of a Josephson junctions (3.5 µm wide and 0.5 µm long) above the critical T as a function of top and bottom gate voltages. **b,** Differential resistance dV/dI measured along the CNP line in **a** at low T and in zero B. Transition from the dissipationless regime to a finite voltage drop shows up as a bright curve indicating I_c. **c,** Interference patterns in small B. The top panel is for the case of high doping [$I_c(B=0)\approx2$ µA] and indistinguishable from the standard Fraunhofer-like behavior illustrated in Fig. 5.1d. The patterns below correspond to progressively larger E_{gap}. Changes in the phase of Fraunhofer oscillations, consistent with the formation of edge modes, are highlighted by the vertical dashed white lines.

3. Bulk versus edge distribution of the supercurrent in bi-layer graphene

In this section we further analyze the interference patterns of the supercurrent $I_c(B)$ at CNP for different values of D. The inverse FFT is calculated to extract the local current distribution $J_s(\mathrm{x})$ (see Fig. 5.S3b and Fig. 5.2d of the main text). Then the current density at the edges is compared to the one at the center of the junction. We find that the transition from uniform current distribution to the edge-dominated flow is rather sharp and occupies the range in the displacement $0.015<D<0.03$ V/nm (see Fig. 5.S3b). The bulk component of J_s is dramatically reduced above $D\approx0.03$ V/nm and the supercurrent becomes restricted to the edge channels. To this end we note that the supercurrent in the graphene is carried by Andreev pairs coupled by the superconductor gap Δ. At zero temperature and for entirely gaped graphene, finite I_c is not expected for $E_{gap} > 2\Delta$ because tunneling processes are improbable across this 400nm long barrier (the length of the graphene channel). The analysis of $J_s(\mathrm{x},D)$ below suggest that the cut-off for the bulk contribution is indeed happening at $E_{gap} \approx 2\Delta$ (=2meV in the case of these Nb contacts[S4]). Thus the finite I_c at the edges persisting to large gaps indicates that the edges are less gapped than the bulk, or not gapped at all.

The inverse FFT shown in Fig. 5.S3b and Fig. 5.2d can be fitted by Gaussians in order to estimate the width w to which the edge mode extend into the bulk (taken as the width of the peak at half maximum). Yet a limit on the spatial resolution of $J_s(\mathrm{x})$ arise, which can be defined by the largest number of the magnetic flux in which the interference pattern $I_c(B)$ still can be detected (additional limitation of the calculation is the assumption of a sinusoidal current-phase relation, which is not accurate in these long and ballistic Josephson junctions). We can reliably extract the interference over ≈10 periods (flux quanta) before the noise level or other ballistic effects[S4] alter its pattern. This number correspond to a spatial resolution limit of $\approx W/10=350$ nm for the studied junctions of the width W. The calculated w from the FFT is 650nm and 450nm at D=0.025 V/nm and 0.055 V/nm respectively and should be regarded as an upper limit of the width of the edge channels.

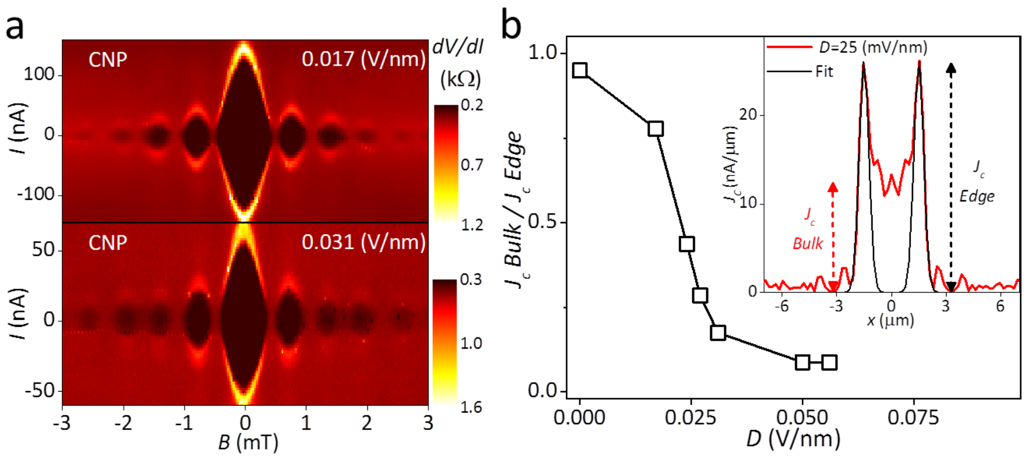

Fig. 5.S3 Supercurrent distribution as a function of the displacement field *D*

a, Examples of interference patterns measured at two different *D*. **b,** The supercurrent density at the bulk and at the edges is extracted from inverse FFTs of the $I_c(B)$ patterns (as shown in Fig. 5.2d). The transition from bulk dominant to edge current is sharp, in the range *D*≈0.015 to 0.03 V/nm. Inset, Gaussian fit to the edge current distribution.

4. Chemical and electrostatic variations at the edge

The effect of external doping at the edges of graphene, which may be different than the bulk doping, offers a trivial explanation for edge-transport when the bulk is gaped. In the following we consider three different doping scenarios, how to minimize their presence, and how to test their effect on the experiments. The three doping scenarios are: i) Chemical variations at the edge, which may depend significantly on the fabrication process[S5]; to minimize this effect we anneal all samples as part of the procedure. ii) Electrostatic doping arising from the finite separation between the gate electrodes and graphene[S6]; the spatial range of this stray doping is determined by the proximity of the top and bottom metal gates, which are fabricated very close to the graphene (≈30nm, 120nm away respectively). iii) Non-uniform termination of the two layers in the BLG; this is avoided by dry etching the two layers simultaneously using a highly anisotropic process.

To evaluate the effect of external doping, we measured devices in which the two edge-profiles of the Josephson junction are different (see Fig. 5.1a, Fig. 5.S4). One edge of the BLG is encapsulated by hBN and overlaid by the top gate, while at the other edge the top gate terminates and the BLG edge is uncovered. In principle, the different profiles should result in different chemical and electrostatic doping.

Calculations of the electrostatic doping profiles are shown for the two edge configurations (Fig. 5.S4). When the top gate terminates above the graphene edge, the charge density accumulation is diverging on approaching it, with a lateral scale of the dielectric spacer thickness as expected. At 100 nm away from the edge the carrier density is ≈5x10^{9} cm^{-2} for 1V / 0.24V on the bottom / top gate respectively (corresponding to CNP and D≈0.03V/nm). In contrast, the configuration of extended gate and hBN show negligible electrostatic doping as expected. The effect of electrostatic or chemical doping, if significant, should clearly favor edge conductance along one of the edges only.

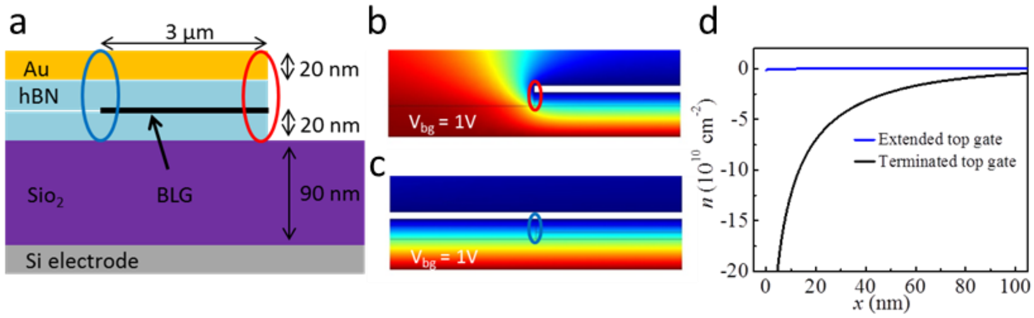

Fig. 5.S4 Electrostatic modelling of edge doping

a, Schematic cross-section of a Josephson junction with different edge profiles (the other cross-section and top view are shown in Figs. 5.1a,b main text). **b, c,** Finite element calculation of the electrostatic potential distribution for the two edge configurations. The bottom gate is fixed at 1 Volt while the top gate is tuned to fix a zero potential at the bulk of the BLG (colored circles mark the two edge configurations) **d,** Calculated carrier density accumulation as function of the distance from the edge for the extended (Blue curve) and edge-terminated (red) profiles. For the former, charge accumulation is negligible.

Here we point out the high sensitivity of the supercurrent interference patterns to asymmetric supercurrent density distribution. Conceptually this sensitivity can be described as follow: if the maximum supercurrent density in the two edges is precisely equal, flux penetration can force it in opposite directions for each edge, such that a zero net supercurrent can be driven across the junction (the measured I_c). On the other hand, uneven critical current density will preserve a finite “net” supercurrent in the better conducting edge, even when the flux-driven supercurrent at the less conducting edge is maximal. This will result in a non-zero net supercurrent flowing across the junction, at all values of magnetic flux. In the interference pattern, it will show up as a lifting of the minimum I_c[S7,S8]. Furthermore, in the case of supercurrent flowing only in one of the edges the period of the oscillations will increase significantly, reflecting the confined width of the supercurrent and the small effective area of flux penetration.

The fact that the interference of the BLG junctions drops to zero at half integer values of flux (see Fig. 5.2c, Fig. 5.S2c), indicates that the conductance at the two edges is very similar, and that the gate electrode profile does not have a significant effect on the edge modes observed.

To test the electrostatic doping scenario in the Hall bar devices, we compared top gates terminated at the edge of bilayer graphene (see Fig. 5.4a), or extend far beyond the bilayer (see Fig. 5.S5a). For both types of devices the sub-gap resistance at high D was measured and similar saturation of R was observed (Fig. 5.S5b). It indicates again that the edge profile and the resulting external doping is not significant in these devices.

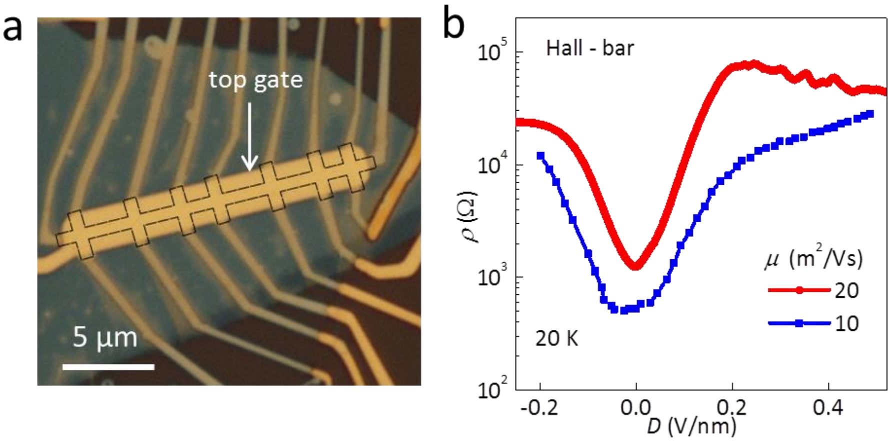

Fig. 5.S5 Sub-gap resistivity of bilayer graphene Hall bar device with the top gate extending above the edges

a, Optical image of the device. Additional hBN cover-layer was placed, enabling the extension of the top gate away from the BLG edges (marked by dashed black line). **b,** Resistivity ρ as a function of the displacement field measured at neutrality point for the device shown in **a** (blue curve). The exponential increase in resistivity is dumped above $D \approx 0.2$ V/nm, where ρ becomes comparable to the quantum of resistance. Devices with gate electrode terminated at the edge (red curve) show a more pronounced saturation, presumably owing to the higher mobility achieved.

We also point to the experiments on the gapped monolayer graphene discussed in the main text. There we compare Josephson junctions made using the same fabrication procedures and geometries (including the thickness of the dielectric materials) but for non-aligned (non-gapped) and aligned (gapped) devices. Any inhomogeneity in the external doping should be essentially the same for the two cases. After testing more than 10 non-gapped monolayers[S4] and 4 gaped (hBN-aligned) junctions we note that no edge current enhancement was observed in any of the former, while clear edge-dominated currents where observed in all the latter. Here, to avoid the case of the edge-modes being masked by the bulk currents, we examined different aspect-ratios of un-gapped junction with different normal-state resistance above the Nb transition temperature or at currents above I_c (see Fig. 5.3d,f). We note that no sign of edge currents was found even when the normal-state resistance exceeds the resistance where edge-dominated transport was observed in the gapped graphene. It points again to the crucial role of the gap in supporting the enhanced edge conductivity rather than external doping mechanism.

5. On-off ratio in gapped bi-layer graphene

Achieving high on-off ratio in gapped graphene devices is a focus of intense research driven by the practical requirements of electronic applications like field effect transistors (FET)[S9]. Owing to the ballistic transport over micron length scales in pristine graphene and BLG at room temperature, the “on” state resistance is mostly determined by the metal-graphene interface resistance, which can be as low as 35 Ohm×µm[S4].

The “off” state resistance is usually determined by the size of the gap and the device inhomogeneities. As has been discussed in the main text, for sufficiently clean bilayer graphene devices the edge conductance limits the sub-gap R to the order of the quantum resistance. In the Josephson junction FET geometry for example, the on-off ratio is limited to 10^2 at D=0.2V/nm and saturates for higher displacement fields. In contrast, for the edgeless Corbino geometry the highly resistive “off” state is recovered. Here we demonstrate on-off ratio $\approx 10^4$ (at 20K), achieved already at D=0.2V/nm owing to the high device homogeneity. Importantly the “off” resistance is limited only by the device quality and the achievable D.

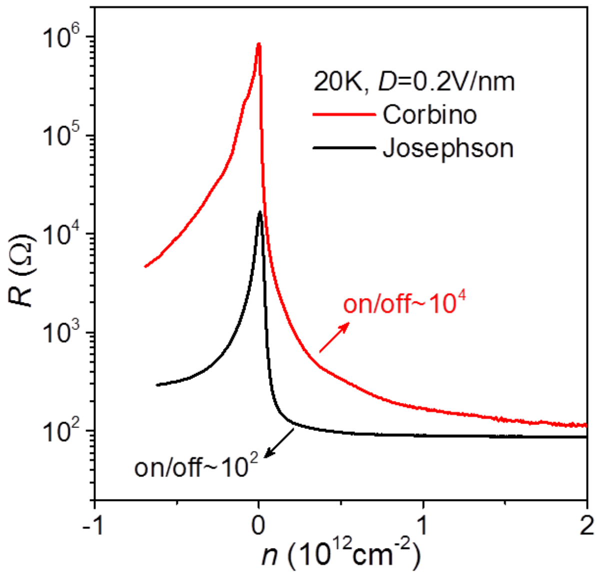

Fig. 5.S6 On-off ratios of bilayer graphene devices in Corbino and in field effect transistor (FET) geometry

The resistance of the device in the FET geometry (3.5μm wide, 0.4μm long) changes by only 2 orders of magnitude, due to the edge-conductance at the charge neutrality point. In the case of the "edge-less" Corbino geometry, R changes by over 4 orders of magnitude already at *D*=0.2 V/nm.

Supplementary references

[S1] Oostinga, J. B., Heersche, H. B., Liu, X. L., Morpurgo, A. F. & Vandersypen, L. M. K. Gate-induced insulating state in bilayer graphene devices. *Nature Materials* **7**, 151-157 (2008).

[S2] Zhang, Y. *et al.* Direct observation of a widely tunable bandgap in bilayer graphene. *Nature* **459**, 820-823 (2009).

[S3] McCann, E. Asymmetry gap in the electronic band structure of bilayer graphene. *Physical Review B* **74**, 161403 (2016).

[S4] Ben Shalom, M. *et al.* Quantum oscillations of the critical current and high-field superconducting proximity in ballistic graphene. *Nature Physics* **12**, 318-322 (2016).

[S5] Woessner, A. *et al.* Near-field photocurrent nanoscopy on bare and encapsulated graphene. *Nature communications* **7**, 10783 (2016).

[S6] Silvestrov, P. G. & Efetov, K. B. Charge accumulation at the boundaries of a graphene strip induced by a gate voltage: Electrostatic approach. *Physical Review B* **77**, 155436 (2008)

[S7] Dynes, R. C. & Fulton, T. A. Supercurrent Density Distribution in Josephson Junctions. *Physical Review B* **3**, 3015-3023 (1971).

[S8] Hart, S. *et al.* Induced superconductivity in the quantum spin Hall edge. *Nature Physics* **10**, 638-643 (2014).

[S9] Schwierz, F. Graphene transistors. *Nature Nanotechnology* **5**, 487-496 (2010).

Chapter 6

Stacking transition in bilayer graphene caused by thermally activated rotation

The results demonstrated in chapter 6 are from the publication: 'Stacking transition in bilayer graphene caused by thermally activated rotation' *2D Materials* **4**, 01013 (2017).

Here, we provide the first experimental evidence of thermally activated structural transition in bilayer graphene from twisted stacking state to AB stacking state. By using tunnelling spectroscopy, we directly probe the difference of the electronic density of states and the dispersion relation between twisted bilayer graphene and AB stacking bilayer graphene. We further confirm our observations by employing Raman spectroscopy mapping. We demonstrate that twisted bilayer graphene undergoes a macroscopic rotation and reaches an energetically favourable state – the AB stacking bilayer graphene. Such structural transition is also accompanied by a topological transition in the reciprocal space and by a pseudospin texturing.

My personal contribution to this work is: I generated the idea of employing graphene tunnelling transistors to detect the structural transition from twisted bilayer graphene to AB stacking bilayer graphene. I carried out the transport measurements, analysed the data and wrote the manuscript.

The acknowledgements for the paper are: M.J.Z., A.M. and K.S.N. designed the experiment. Y.C. and A.Misra fabricated the devices. M.J.Z., D.G. and A.M. carried out the transport measurements. S.-K.S. carried out Raman spectroscopy measurements. M.J.Z. and A.M. analysed and interpreted the data. L.H. did the calculation. K.W. and T.T. supplied hBN crystals. M.J.Z. and A.M. wrote the manuscript with input from all the authors.

Stacking transition in bilayer graphene caused by thermally activated rotation

M. J. Zhu[1,†], D. Ghazaryan[1,†], S.-K. Son[2,†], C. R. Woods[1], A. Misra[1,2], L. He[3], T. Taniguchi[4], K. Watanabe[4], K. S. Novoselov[1,2], Y. Cao[1,2,‡], A. Mishchenko[1,2,‡]

[1]School of Physics and Astronomy, University of Manchester, Oxford Road, Manchester, M13 9PL, UK

[2]National Graphene Institute, University of Manchester, Booth St. E, Manchester, M13 9PL, UK

[3]Department of Physics, Beijing Normal University, Beijing, 100875, China

[4]National Institute for Materials Science, 1-1 Namiki, Tsukuba, 305-0044, Japan

[†]These authors contributed equally

[‡]Corresponding authors, e-mail:

yang.cao@manchester.ac.uk, artem.mishchenko@gmail.com

Crystallographic alignment between two-dimensional crystals in van der Waals heterostructures brought a number of profound physical phenomena, including observation of Hofstadter butterfly and topological currents, and promising novel applications, such as resonant tunnelling transistors. Here, by probing the electronic density of states in graphene using graphene-hexagonal boron nitride tunnelling transistors, we demonstrate a structural transition of bilayer graphene from incommensurate twisted stacking state into a commensurate AB stacking due to a macroscopic graphene self-rotation. This structural transition is accompanied by a topological transition in the reciprocal space and by pseudospin texturing. The stacking transition is driven by van der Waals interaction energy of the two graphene layers and is thermally activated by unpinning the microscopic chemical adsorbents which are then removed by the self-cleaning of graphene.

1. Introduction

The recent progress in two-dimensional materials and van der Waals heterostructures enabled creating artificial materials with tailorable properties for a range of different applications [1]. Although it is desirable in many cases, in van der Waals heterostructures it is currently hard to achieve the perfect crystallographic alignment of individual layers during stacking procedure [2]. On the contrary, in the parent-layered crystals the constituent layers are in a commensurate registry with each other as this minimises the interlayer van der Waals energy of the crystal. For instance, in exfoliated bilayer graphene the individual graphene layers are in a commensurate AB (or Bernal) stacking, which minimises the van der Waals energy due to a maximal overlap of electronic orbitals in two graphene layers. This overlap leads to a strong interlayer coherence of electrons in the two graphene layers and the interlayer electron hopping dramatically modifies graphene band structure [3].

When bilayer graphene is prepared by mechanically transferring two graphene layers on top of each other, there exists another degree of freedom – a twist angle between graphene crystallographic directions. This rotational misalignment provides a tuning knob for the electronic spectrum of graphene bilayer. Twisting the two graphene crystals with respect to each other introduces a momentum mismatch between the two Dirac cones, which hinders the interlayer electronic coherence and preserves the linear energy dispersion [4].

When one MLG is strongly crystallographically misaligned with another MLG, the friction between two graphene layers can vanish, leading to a superlubric motion of the top layer [5-7]. Eventually, the van der Waals interaction energy will drive the system to the most energetically favourable commensurate state, the AB stacking bilayer graphene (BLG) [8,9]. Similar phenomena (though driven by maximization of the overlapping area) indeed have been observed at the micron scale for self-retraction of three-dimensional graphite mesa structures [9,10], and, more recently, for thermally induced self-alignment in MLG-hBN heterostructures[11,12]. The reason why thermal activation is often necessary for macroscopic self-alignment is the presence of chemical adsorbents between the atomic layers, acting as nanoscale ‘glue’ and preventing the superlubric motion [13]. Such pinning effect may stabilise the crystals in a thermodynamically unstable configuration, such as twisted bilayer graphene (tBLG).

In the following, we demonstrate that, despite the strong pinning effect due to chemical contaminations between two graphene layers, tBLG can rotate towards stable BLG state after a long-time thermal annealing. In order to probe the transition from tBLG to BLG precisely, we employ the tunnelling spectroscopy technique using graphene-hBN tunnelling transistors, which are known for their high sensitivity to the DoS of graphene [14].

2. Results and discussions

We fabricated graphene tunnelling transistors using a sequence of mechanical exfoliation and dry transfer procedures, similar to those described in previous works [14,15]. We first used the standard micromechanical cleavage technique to prepare relatively thick (20–30 nm) hBN crystal on top of oxidised (290 nm SiO_2) silicon wafer which acted as a back gate. The hBN crystals served as a high-quality atomically flat substrate. We then transferred a first MLG flake on top of the selected hBN crystal using dry transfer procedure. A trilayer (3L) hBN was identified and transferred on top of the first MLG by repeating the same procedure. This thin hBN layer served as the tunnel barrier. The above whole processes were repeated again to complete the stack with the second MLG. After depositing of 5 nm Ti / 50 nm Au metallic contacts, the structure was annealed at 200 ºC in Ar/H_2 gas. The device schematics and micrograph are shown in Fig. 6.1(a).

In our graphene tunnelling devices, the tunnelling current I was measured as a function of applied bias voltage V_b between the bottom and top graphene electrodes and the back gate voltage V_g applied between bottom graphene and highly doped silicon gate electrode. In order to measure the differential tunnelling conductance dI/dV, we mixed small low-frequency ac voltage to a dc bias V_b and measured the current with a lock-in amplifier.

Typical I-V and dI/dV characteristics for different V_g measured at a base temperature of T=1.6 K are shown in the Fig. 6.1(c).

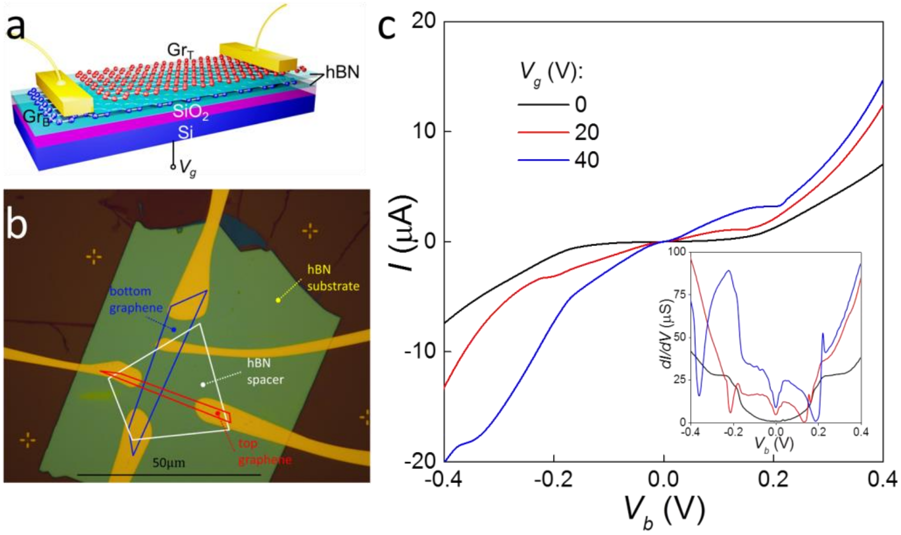

Fig. 6.1 Graphene-hBN-graphene field-effect tunnelling transistor

(a) Schematics of the device. **(b)** Optical micrograph of one of our devices. Two MLG sheets are separated by a 3L hBN tunnel barrier (white outline). The overlap between top layer graphene (red outline) and bottom layer graphene (blue outline) corresponds to an active tunnelling area $A \approx 10\mu\text{m}^2$. **(c)** Tunnelling current I as a function of V_b at T=1.6 K for different gate voltages. Inset shows the differential tunnelling conductance dI/dV.

It is more informative to plot a contour map of measured dI/dV map as a function of V_b and V_g, as shown in Fig. 6.2(b). Here, the X-shaped white feature is a low tunnelling conductance, which we attribute to the passing of the chemical potential μ_i through the CNP of each graphene layer. The dI/dV is suppressed in this region due to the vanishing DoS.

We analysed the electrostatic properties of our tunnel transistors using parallel-plate capacitor model [14, 16]. In addition, we took into account that the electric field generated by the charge on the gate electrode is only partially screened by the bottom graphene layer, due to graphene low DoS. Based on this model we have derived the following pair of simultaneous equations:

$$\begin{cases} eV_b = \mu_B - \mu_T - \Delta\varphi \\ eV_g = \mu_B + e^2 D(n_B + n_T)/\varepsilon\varepsilon_0 \end{cases}. \tag{1}$$

Here, e is the elementary charge and μ_i and n_i the chemical potentials and carrier densities of the bottom and top graphene, respectively. In the case of MLG, $\mu_i = \pm\hbar v_F\sqrt{\pi|n_i|}$. D is the total thickness of SiO$_x$ and hBN substrate, d is the thickness of hBN tunnel barrier, ε_0 is the vacuum permittivity and ε is the medium permittivity (3.2 for hBN and 3.9 for SiO_2). Additionally, the band offset between the top and bottom graphene layers is obtained using $\Delta\varphi = e^2 d n_T / \varepsilon\varepsilon_0$.

We then fitted the experimental data with this model and determined the conditions for the intersection of the chemical potentials with the CNP for each graphene layer. The fits are shown as dashed blue and red lines for top and bottom graphene layers, respectively (Fig. 6.2(b)). Note that Fermi velocity v_F=1.05×10^6 m/s extracted from our electrostatic model is in a good agreement with the literature [17].

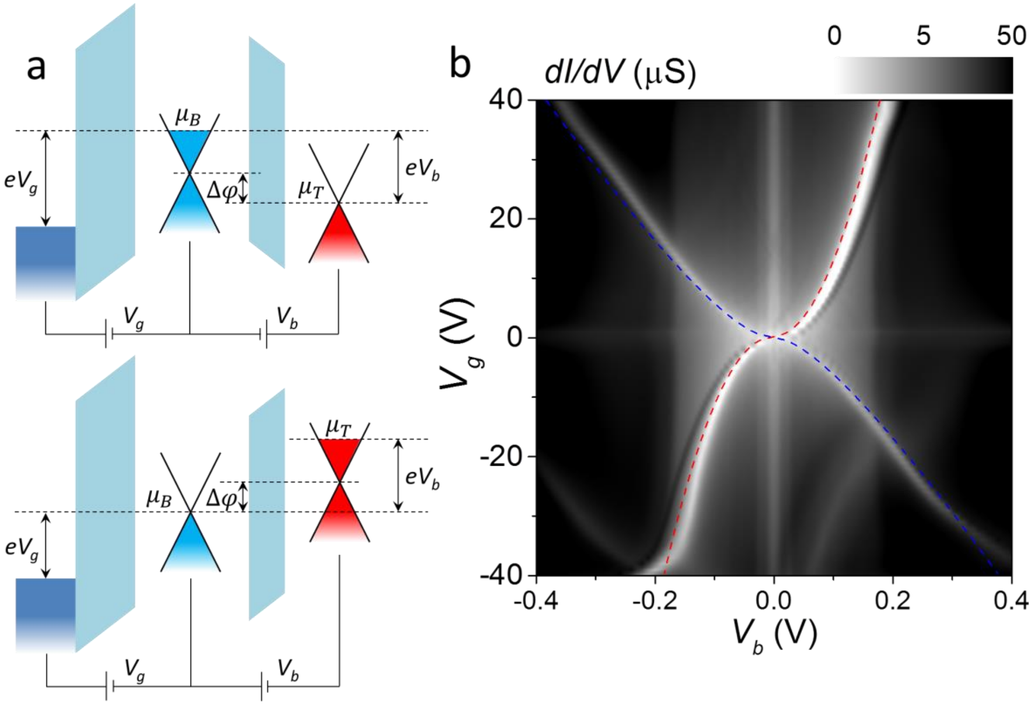

Fig. 6.2 Differential conductance of monolayer graphene-hBN-monolayer graphene tunnelling transistor

(a) Schematics of energy band diagrams of the MLG tunnelling transistor when the chemical potential in one graphene layer passing through its CNP. **(b)** Measured dI/dV map as a function of V_b and V_g. Blue and red dashed lines represent the electrostatic calculations with vanishing DoS in the bottom and top graphene, respectively.

Apart from CNP-related low DoS features, there are other regions with suppressed electronic DoS and we can clearly distinguish them from a darker background as sharp vertical (independent of V_g) lines at V_b≈12, 20, 170 and 200 mV. We attribute those features to phonon-assisted tunnelling process, where conductance increases as a series of steps every time V_b is large enough to excite a phonon $eV_b = \hbar\omega_{ph}$, where $\hbar$ the reduced Planck constant and ω_{ph} the phonon frequency [18,19].

Having characterised our tunnelling transistor we then carefully transferred another, smaller, MLG flake on top of the device using the same dry transfer method. During the transfer, we intended to align the graphene flake within 5° with the top graphene layer to obtain tBLG as the top electrode.

Rotational misalignment between two MLG crystals leads to a moiré pattern,, as depicted in Fig. 6.3(a). The superlattice period is determined by the twist angle θ. In addition to the structural modification, such rotation causes a shift between the Dirac points in the reciprocal space by $|\Delta K| = 2|K|sin(\theta/2)$, leading to a significantly different spectrum from both MLG and BLG, as demonstrated in Fig. 6.3(b). If there is a finite interlayer coupling between the two MLG layers, two saddle points will appear at the intersection of the two cones resulting in two van Hove singularities (VHS) in the DoS (Fig. 6.3(c)) at energies of $E_{VHS}^{\pm} = \pm(\hbar v_F \Delta K/2 - \tau_\theta)$, where v_F the Fermi velocity of MLG and τ_θ the interlayer hopping parameter [4,20-22].

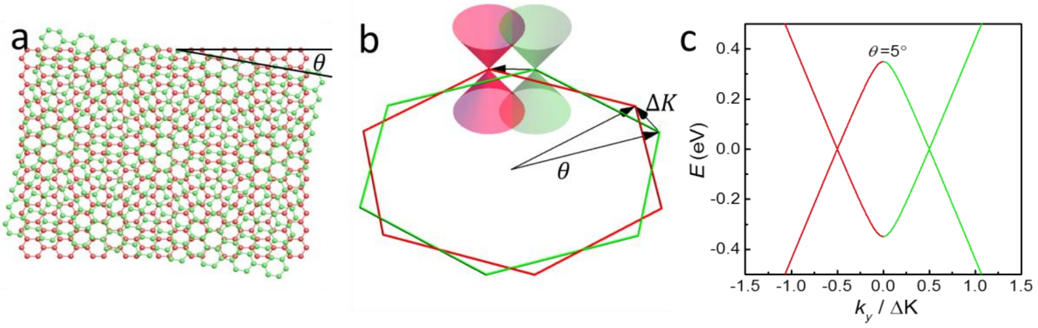

Fig. 6.3 Structure and electronic dispersion of twisted bilayer graphene
(a) Schematics of the structural model of two misoriented honeycomb lattice with a twist angle θ. **(b)** Shcmeatic Dirac cones of the two graphene layers in the reciprocal space at K point. **(c)** Electronic band structure of tBLG along a line joining the two Dirac points In the calculation, θ=5° and τ_θ=110 meV are used in here.

After transfer, we carried out the same tunnelling spectroscopy measurements, see Fig. 6.4(e). Noticeably, CNP of the top tBLG graphene electrode shifted from 0 V to 10 V after transfer. This is a strong evidence of the presence of adsorbents and chemical residues left after device fabrication in-between top graphene electrode and recently added graphene flake. This ‘glue’ prevents the superlubric motion and rotation of the top MLG flake immediately after the transfer and stabilises twisted bilayer configuration.

Crystallographic orientations of the flakes and corresponding tunnelling spectroscopy maps are shown in Fig. 6.4(b) and (e), where for consistency we used ΔV_g instead of V_g to characterise the carrier density in graphene electrodes. The *dI/dV* map of tBLG-MLG (Fig. 6.4(e)) compares well with MLG-MLG tunnelling device (Fig. 6.4(d)). That is, the X-shaped feature is also present in Fig. 6.4(e) indicating a low energy linear dispersion in tBLG, which is qualitatively similar with the MLG case. Quantitatively, there is a significant difference between of tBLG and MLG tunnelling devices when the chemical potential of bottom MLG sits at zero $\mu_B = 0$. We attribute the shrinked X-shaped feature in tBLG tunnelling device to the reduced chemical potential in tBLG electrode. At low energy, there are two Dirac cones at *K* (or *K*') point in the reciprocal space of tBLG instead of single Dirac cone for the MLG case. In this simple assumation we ignored the Fermi velocity renormalization in tBLG due to a relatively large twist angle (θ ~ 5^{o}) and the unknown interlayer coupling strength [23,24]. The calculation agrees well with our experimental data for tBLG tunelling devcie (dashed green line in Fig. 6.4(e)) after we sligtly modify the electrostatic model by adding an additional equation to Eq. (1) to describe the complementary MLG layer (T$_1$) shorted with the initial top MLG layer (T$_1$):

$$\begin{cases} eV_b = \mu_B - \mu_{T1} - \Delta\varphi_1 \\ eV_g = \mu_B + e^2 D(n_B + n_{T1})/\varepsilon\varepsilon_0 \ . \\ \mu_{T1} = \mu_{T2} + \Delta\varphi_2 \end{cases} \tag{2}$$

Here $\Delta\varphi_1 = e^2 d(n_{T1} + n_{T2})/\varepsilon\varepsilon_0$ is the band offset between bottom MLG and top tBLG electrodes separated by hBN and $\Delta\varphi_2 = e^2 d n_{T2}/\varepsilon_0$ is the band offset between T$_1$ and T$_2$ where d'=0.35 nm is the separation by vacuum. The relation between chemical potential and carrier density in tBLG is still defined as $\mu_i = \pm\hbar v_F\sqrt{\pi|n_i|}$. Worth to mention that we did not obeserve any singnatures of VHS in tBLG tunnelling device. We attribute this to a large twist angle (>5°) which shifts VHS to the high energy $|E_{VHS}| >$0.4 eV, higher than the chemial potential (~0.2 eV) in tBLG we can reach by applying gate and bias voltages.

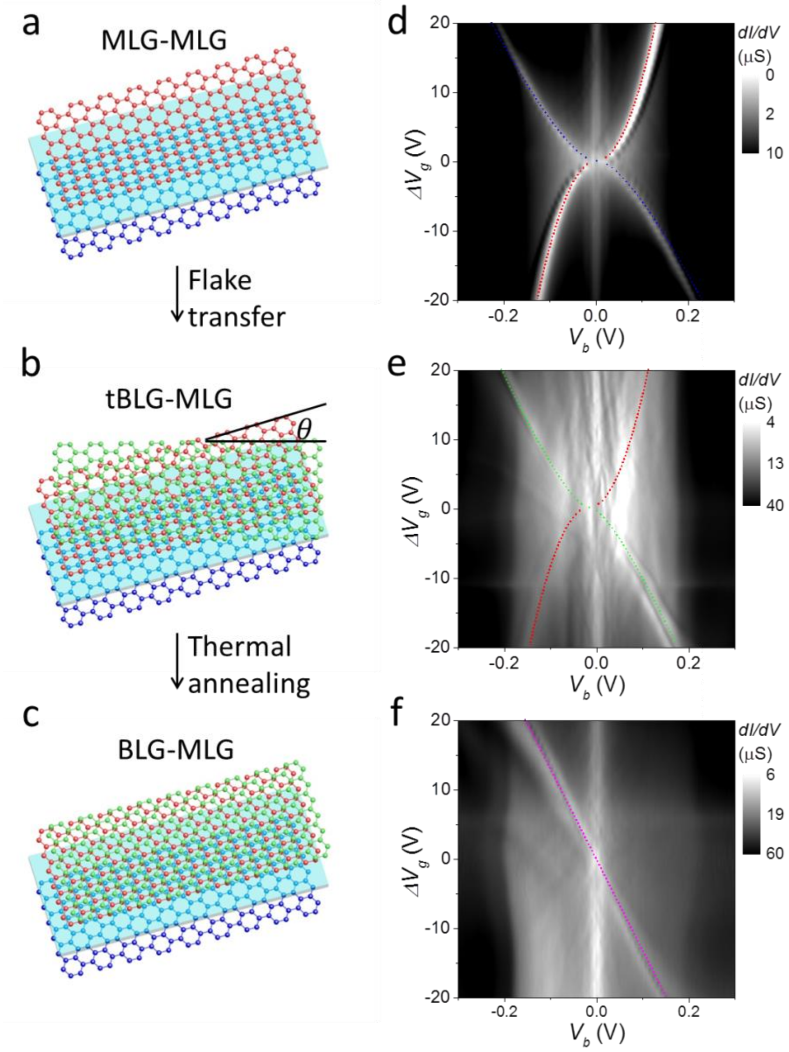

Fig. 6.4 Differential conductance of graphene-hBN tunnelling transistors with different top graphene electrodes

(a)-(c): Schematics of different graphene-hBN tunnelling transistors (only graphene-hBN-graphene heterostructures are shown in here). **(d)-(f):** measured *dI/dV* contour maps as a function of V_b and V_g for MLG-MLG, tBLG-MLG and BLG-MLG tunnelling devices. Dashed lines are the calculations of electrostatic models in Eq. (1).

Finally, we annealed the device at 200ºC for 12 hours under Ar/H_2 and then carried out the same tunnelling spectroscopy measurements again. The CNP of the top graphene layer shifts from 10 to 3 V, which implies that chemical adsorbents were partially removed by thermal annealing. Measured *dI/dV* map (Fig. 6.4(f)) clearly shows two differences in comparison with tBLG case (Fig. 6.4(e)). First of all, one of the lines of the X-shaped region ascribed to zero DoS in bottom graphene assumes linear rather than square root dependence (in contrast to both MLG-MLG and tBLG-

MLG cases). Secondly, the other line of the X-shaped region corresponding zero DoS in top graphene disappears.

To explain these findings we fit the linear low-DoS line (see Fig. 6.4(f)) with modified electrostatic model considering AB stacked bilayer graphene as a top electrode [25]:

$$\begin{cases} eV_b = \mu_B - \mu_T - e^2 d n_T/\varepsilon\varepsilon_0 \\ eV_g = \mu_B + e^2 D(n_B + n_T)/\varepsilon\varepsilon_0, \\ \Delta = e^2 d'(n_B + n_T'')/\varepsilon\varepsilon_0 \end{cases} \tag{3}$$

where the relation between carrier density and chemical potential is given by $n_T(\mu_T, \Delta) = \frac{m}{\pi} Re\sqrt{(2\mu_T)^2 - \Delta^2}$, here m is the effective carrier mass, Δ the tunable bandgap, $n_T'' = n_T - n_T'$ the carrier density on one particular layer in AB stacked bilayer.

To further confirm observed tBLG-to-BLG transition we performed another annealing experiment using Raman spectroscopy (Renishaw Raman spectrometer, excitation line of 514 nm, and incident power of 2 mW) as an independent tool to identify a twist angle between the top and bottom MLG flakes. The full width at half maximum (FWHM) of a 2D peak (~2690 cm^{-1}) of tBLG is sensitive to the twist angle, increasing from ~20 cm^{-1} for θ>15° up to ~50 cm^{-1} for θ=0° (BLG) [26]. We fabricated tBLG sample on hBN substrate (Fig. 6.5(a)) and measured its Raman maps of FWHM of 2D peak before and after annealing (Fig. 6.5(b)-(c)). Maps clearly show a difference in θ before and after annealing: the average FWHM was 45.3±0.9 cm^{-1}, which corresponds to ~4-5° twist, while after annealing FWHM increased to 50.0±0.9 cm^{-1} – a value typical for BLG. Interestingly, a small part of a top MLG has rotated in the opposite direction after annealing (FWHM 33.8±1.7 cm^{-1} corresponding to ~9-10° twist), probably to compensate for a strain due to the presence of two large bubbles in that region of the tBLG.

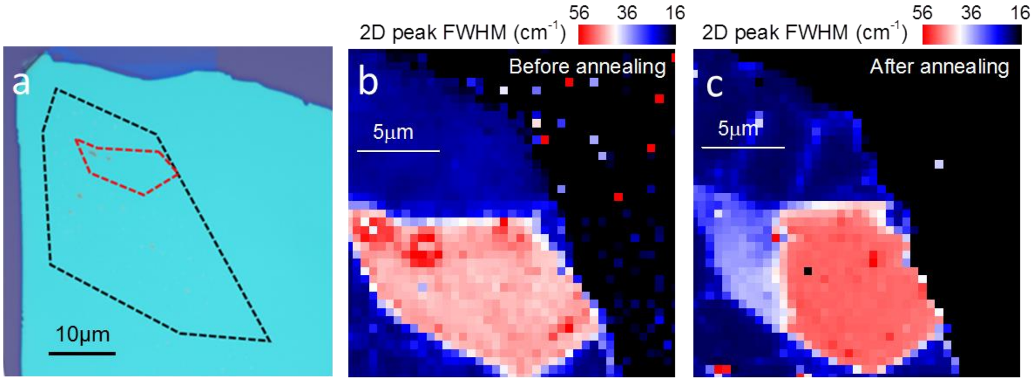

Fig. 6.5 Raman spectroscopy map of twisted bilayer graphene before and after thermal annealing

(a) Optical micrograph of tBLG on hBN heterostructure. The red and black dashed lines indicate the edges of top and bottom MLG flakes, respectively. **(b)** and **(c)** Raman maps of FWHM of 2Dpeak before (b) and after (c) annealing.

Van der Waals energy between graphene layers strongly depends on the misalignment – the minimum energy corresponds to the AB stacking at every 60° rotations [27, 28]. The energy difference (van der Waals energy) between the AB stacking and a fully misaligned (θ=30°) conformation is ~0.13 meV/atom [29]. This energy difference is sufficient to drive a transition from an incommensurate stacking state to a commensurate AB stacking since they are separated by a small barrier <0.02 meV/atom [29]. The reason why the transition doesn't happen before the thermal annealing is most likely the pinning effect due to the chemical adsorbents between the graphene layers [30]. Indeed, it was recently confirmed that the dissipative energy, related to irreversible removal of contaminants from the graphite-graphite interface, decreases rapidly with increasing temperature [31]. During the long-time thermal annealing, those contaminants become mobile and then are segregated to localised pockets by the self-cleaning driven by van der Waals force between two graphene layers [11,32]. Remarkably, the observed tBLG to BLG transition implies that the top 5 μm size MLG has rotated by at least 500 nm [11], which can find its applications in nanoelectromechanical systems (NEMS).

The observed incommensurate-commensurate transition between tBLG and BLG was predicted to occur under certain conditions, such as strain in one of the layers [34,35]. In our work, we present an alternative route to achieve this structural transition by graphene self-rotation, see Fig. 6.6. The tBLG behaves as two decoupled MLG when the twist angle is large enough and the interlayer interaction can be neglected (Fig. 6.6(a)). During annealing the top MLG rotates driven by van der Waals energy. As a result, θ decreases and two saddle points apear at the intersection of the two Dirac cones resulting in two VHS in DoS (Fig. 6.6(b), (c)). Finally, graphene reaches the BLG structure, forming a parabolic low-energy dispersion (Fig. 6.6(d)).

This structural transition is also accompanied by the topological transition in the reciprocal space - the twist dependent Lifshitz transition, where the rotation modifies the Fermi surface topology of the system: two independent Fermi surfaces merge into one after the rotation, Fig. 6.6(e)-(h). Analogous topological transitions were observed in tBLG and BLG in high magnetic fields [36,37], while in our case it is driven by a mechanical rotation of the two graphene crystals. In addition to topology, a pseudospin texture is also affected by the structural transition. The electron wave function in graphene consists of two components, which represent the probability of finding an electron on the two sublattices of the honeycomb lattice. The pseudospin is the phase shift between those components, which, for MLG is locked to the direction of the electron's motion. The tBLG with large twist angle (θ>5°) can be treated as two decoupled MLG layers with the same pseudospin texture, as shown in Fig. 6.6(e). For smaller-θ tBLG, due to the interlayer interaction, the pseudospin vectors rotate to lower the symmetry of tBLG, which merges the two Fermi surfaces above the VHS (Fig. 6.6(f), (g)) [33,38]. Finally, the tBLG system reaches its commensurate state when θ=0º and two MLG aligns with each other within a AB stacking, where the Fermi surfaces completely merge to single one and the pseudospin texture assumes the BLG case (Fig. 6.6(h)). This evolution of pseudospin texture also implies a continuous Berry phase transition from π for large-θ tBLG to 2π for BLG through a small-θ tBLG state [36,37].

Our results (as shown in Figs. 6.4 and 6.6) provide the first experimental evidence of a thermally activated stacking transition in bilayer graphene driven by the self-rotation, which paves the way to nanomechanical band structure engineering.

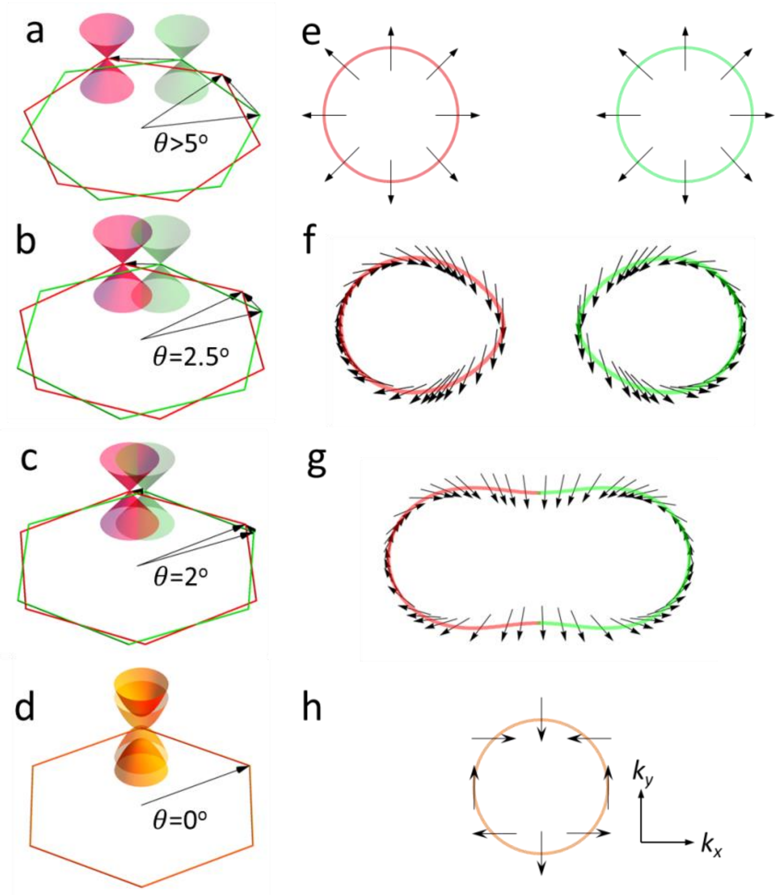

Fig. 6.6 Structural transition in bilayer graphene

(a)-(c) Schematics of the evolution of Brillouin zone from the large-θ tBLG to small-θ tBLG to BLG **(d)**. Low energy dispersions (Dirac cones) are shown only for one corner of the Brillouin zone for top (red) and bottom (green) graphene layers, Twist angles θ are exaggerated. **(e)-(h)** Low-energy (E=60 meV) Fermi surfaces and pseudospin texture *vs.* twist angle θ for K valley, calculated as described in ref. [33]. The interlayer hopping τ_θ=110 meV was used. Enclosed curves indicate the Fermi surface topology and black arrows represent the pseudospin angle.

3. Conclusions

To summarise, we demonstrated a structural transition from twisted bilayer graphene to AB stacking bilayer graphene using the highly sensitive technique of tunnelling spectroscopy. We also showed that thermal annealing unpins the graphene allowing its macroscopic self-rotation driven by van der Waals energy. We believe this technique will be useful to study similar structural transitions in nanoelectromechanical systems, clearing the way to mechanically driven band structure engineering.

Acknowledgments

This work was supported by the European Research Council, the EU Graphene Flagship Program, the Royal Society, the Air Force Office of Scientific Research, the Office of Naval Research and ERC Synergy Grant Hetero2D. Mengjian Zhu acknowledges the National University of Defence Technology (China) overseas PhD scholarship. Colin Woods acknowledges the support of the EPSRC (UK). Artem Mishchenko acknowledges the support of EPSRC (UK) Early Career Fellowship EP/N007131/1.

References

[1] Geim A K and Grigorieva I V 2013 Van der Waals heterostructures *Nature* **499** 419-25

[2] Novoselov K S, Mishchenko A, Carvalho A and Castro Neto A H 2016 2D materials and van der Waals heterostructures *Science* **353**

[3] McCann E and Koshino M 2013 The electronic properties of bilayer graphene *Rep Prog Phys* **76** 056503

[4] Lopes Dos Santos J M, Peres N M and Castro Neto A H 2007 Graphene bilayer with a twist: electronic structure *Phys Rev Lett* **99** 256802

[5] Dienwiebel M, Verhoeven G S, Pradeep N, Frenken J W, Heimberg J A and Zandbergen H W 2004 Superlubricity of graphite *Phys Rev Lett* **92** 126101

[6] Zheng Q, Jiang B, Liu S, Weng Y, Lu L, Xue Q, Zhu J, Jiang Q, Wang S and Peng L 2008 Selfretracting motion of graphite microflakes *Phys Rev Lett* **100** 067205

[7] Filippov A E, Dienwiebel M, Frenken J W, Klafter J and Urbakh M 2008 Torque and twist against superlubricity *Phys Rev Lett* **100** 046102

[8] Woods C R, Britnell L, Eckmann A, Ma R S, Lu J C, Guo H M, Lin X, Yu G L, Cao Y, Gorbachev R V, Kretinin A V, Park J, Ponomarenko L A, Katsnelson M I, Gornostyrev Y N, Watanabe K, Taniguchi T, Casiraghi C, Gao H J, Geim A K and Novoselov K S 2014 Commensurate-incommensurate transition in graphene on hexagonal boron nitride *Nature Physics* **10** 451-6

[9] Yang J, Liu Z, Grey F, Xu Z, Li X, Liu Y, Urbakh M, Cheng Y and Zheng Q 2013 Observation of high-speed microscale superlubricity in graphite *Phys Rev Lett* **110** 255504

[10] Liu Z, Yang J, Grey F, Liu J Z, Liu Y, Wang Y, Yang Y, Cheng Y and Zheng Q 2012 Observation of microscale superlubricity in graphite *Phys Rev Lett* **108** 205503

[11] Woods C R, Withers F, Zhu M J, Cao Y, Yu G, Kozikov A, Ben Shalom M, Morozov S V, van Wijk M M, Fasolino A, Katsnelson M I, Watanabe K, Taniguchi T, Geim A K, Mishchenko A and Novoselov K S 2016 Macroscopic self-reorientation of interacting two-dimensional crystals *Nature Communications* **7** 10800

[12] Wang D, Chen G, Li C, Cheng M, Yang W, Wu S, Xie G, Zhang J, Zhao J, Lu X, Chen P, Wang G, Meng J, Tang J, Yang R, He C, Liu D, Shi D, Watanabe K, Taniguchi T, Feng J, Zhang Y and Zhang G 2016 Thermally Induced Graphene Rotation on Hexagonal Boron Nitride *Phys Rev Lett* **116** 126101

[13] He G, Muser M H and Robbins M O 1999 Adsorbed layers and the origin of static friction *Science* **284** 1650-2

[14] Britnell L, Gorbachev R V, Jalil R, Belle B D, Schedin F, Mishchenko A, Georgiou T, Katsnelson M I, Eaves L, Morozov S V, Peres N M, Leist J, Geim A K, Novoselov K S and Ponomarenko L A 2012 Field-effect tunneling transistor based on vertical graphene heterostructures *Science* **335** 947-50

[15] Mishchenko A, Tu J S, Cao Y, Gorbachev R V, Wallbank J R, Greenaway M T, Morozov V E, Morozov S V, Zhu M J, Wong S L, Withers F, Woods C R, Kim Y J, Watanabe K, Taniguchi T, Vdovin E E, Makarovsky O, Fromhold T M, Fal'ko V I, Geim A K, Eaves L and Novoselov K S 2014 Twist-controlled resonant tunnelling in graphene/boron nitride/graphene heterostructures *Nature Nanotechnology* **9** 808-13

[16] Britnell L, Gorbachev R V, Geim A K, Ponomarenko L A, Mishchenko A, Greenaway M T, Fromhold T M, Novoselov K S and Eaves L 2013 Resonant tunnelling and negative differential conductance in graphene transistors *Nature Communications* **4** 1794

[17] Castro Neto A H, Guinea F, Peres N M R, Novoselov K S and Geim A K 2009 The electronic properties of graphene *Rev Mod Phys* **81** 109-62

[18] Vdovin E E, Mishchenko A, Greenaway M T, Zhu M J, Ghazaryan D, Misra A, Cao Y, Morozov S V, Makarovsky O, Fromhold T M, Patane A, Slotman G J, Katsnelson M I, Geim A K, Novoselov K S and Eaves L 2016 Phonon-Assisted Resonant Tunneling of Electrons in Graphene-Boron Nitride Transistors *Phys Rev Lett* **116** 186603

[19] Jung S, Park M, Park J, Jeong T Y, Kim H J, Watanabe K, Taniguchi T, Ha D H, Hwang C and Kim Y S 2015 Vibrational Properties of h-BN and h-BN-Graphene Heterostructures Probed by Inelastic Electron Tunneling Spectroscopy *Scientific Reports* **5** 16642

[20] Shallcross S, Sharma S and Pankratov O A 2008 Quantum interference at the twist boundary in graphene *Phys Rev Lett* **101** 056803

[21] Li G, Luican a, Santos J M B L D, Neto a H C, Reina a, Kong J and Andrei E Y 2009 Observation of Van Hove singularities in twisted graphene layers *Nature Physics* **6** 21

[22] Yan W, Liu M, Dou R F, Meng L, Feng L, Chu Z D, Zhang Y, Liu Z, Nie J C and He L 2012 Angle-dependent van Hove singularities in a slightly twisted graphene bilayer *Phys Rev Lett* **109** 126801

[23] Luican A, Li G, Reina A, Kong J, Nair R R, Novoselov K S, Geim A K and Andrei E Y 2011 Single-layer behavior and its breakdown in twisted graphene layers *Phys Rev Lett* **106** 126802

[24] Yin L-J, Qiao J-B, Wang W-X, Zuo W-J, Yan W, Xu R, Dou R-F, Nie J-C and He L 2015 Landau quantization and Fermi velocity renormalization in twisted graphene bilayers *Physical Review B* **92**

[25] Lane T L M, Wallbank J R and Fal'ko V I 2015 Twist-controlled resonant tunnelling between monolayer and bilayer graphene *Applied Physics Letters* **107** 203506

[26] Kim K, Coh S, Tan L Z, Regan W, Yuk J M, Chatterjee E, Crommie M F, Cohen M L, Louie S G and Zettl A 2012 Raman spectroscopy study of rotated double-layer graphene: misorientation angle dependence of electronic structure *Phys Rev Lett* **108** 246103

[27] Feng X, Kwon S, Park J Y and Salmeron M 2013 Superlubric sliding of graphene nanoflakes on graphene *ACS Nano* **7** 1718-24

[28] Hod O 2012 Interlayer commensurability and superlubricity in rigid layered materials *Phys. Review B* **86** 075444

[29] Shibuta Y and Elliott J A 2011 Interaction between two graphene sheets with a turbostratic orientational relationship *Chem Phys Lett.* **512** 146-50

[30] Muser M H, Wenning L and Robbins M O 2001 Simple microscopic theory of Amontons's laws for static friction *Phys Rev Lett* **86** 1295-8

[31] Wang W, Dai S, Li X, Yang J, Srolovitz D J and Zheng Q 2015 Measurement of the cleavage energy of graphite *Nature Communications* **6** 7853

[32] Kretinin A V, Cao Y, Tu J S, Yu G L, Jalil R, Novoselov K S, Haigh S J, Gholinia A, Mishchenko A, Lozada M, Georgiou T, Woods C R, Withers F, Blake P, Eda G, Wirsig A, Hucho C, Watanabe K, Taniguchi T, Geim A K and Gorbachev R V 2014 Electronic properties of graphene encapsulated with different two-dimensional atomic crystals *Nano Letters* **14** 3270-6

[33] He W Y, Chu Z D and He L 2013 Chiral tunneling in a twisted graphene bilayer *Phys Rev Lett* **111** 066803

[34] Popov A M, Lebedeva I V, Knizhnik A A, Lozovik Y E and Potapkin B V 2011 Commensurateincommensurate phase transition in bilayer graphene *Physical Review B* **84**

[35] Lebedeva I V, Lebedev A V, Popov A M and Knizhnik A A 2016 Dislocations in stacking and commensurate-incommensurate phase transition in bilayer graphene and hexagonal boron nitride *Physical Review B* **93**

[36] Varlet A, Bischoff D, Simonet P, Watanabe K, Taniguchi T, Ihn T, Ensslin K, Mucha-Kruczynski M and Fal'ko V I 2014 Anomalous sequence of quantum Hall

liquids revealing a tunable Lifshitz transition in bilayer graphene *Phys Rev Lett* **113** 116602

[37] Rode J C, Smirnov D, Schmidt H and Haug R J 2016 Berry phase transition in twisted bilayer graphene *2D Materials* **3** 035005

[38] Mele E J 2010 Commensuration and interlayer coherence in twisted bilayer graphene *Physical Review B* **81**

Chapter 7

Phonon-assisted resonant tunnelling of electrons in graphene–boron nitride transistors

The results demonstrated in chapter 7 are from the publication: ‘Phonon-assisted resonant tunnelling of electrons in graphene–boron nitride transistors’ *Physics Review Letters* **116**, 186603 (2016).

Understanding the process and mechanism of phonon-assisted resonant tunnelling is of great importance not only from a fundamental point of view, but also because of the possibility of controlling and engineering advanced tunnelling devices.

Here, we demonstrate a phonon-assisted resonant tunnelling phenomenon in graphene-hBN-graphene tunnelling transistors. We observe a series of sharp enhancement in the differential conductance at bias voltages between 10mV and 200mV. The positions of bias voltage corresponding to the resonant states are independent to the applied gate voltage. Therefore, we can safely exclude the contribution of plasmonic effect. We compare the energies of resonance with the phonon dispersion of graphene and graphene-hBN heterostructure and then attribute the resonant features in our devices to the electron tunnelling assisted by the emission of phonons of well-defined energies.

My personal contribution to this work is: I measured the tunnelling characteristics of graphene-hBN transistors at room temperature and participated in the data analysis and discussion.

The acknowledgements for the paper are: E.E.V., A.M., M.T.G., A.K.G., K.S.N. and L.E. designed the experiment. A.Misra and Y.C. fabricated the devices. E.E.V., A.M., M.J.Z., D.G. and S.V.M. carried out the measurements. O.M., T.M.F., A.P., G.J.S. and M.I.K. provided theoretical supports. K.W. and T.T. supplied hBN crystals. M.T.G. and L.E. wrote the manuscript with input from all the authors.

Phonon-assisted resonant tunnelling of electrons in graphene–boron nitride transistors

E. E. Vdovin,[1,5,6] A. Mishchenko,[2] M. T. Greenaway,[1,*] M. J. Zhu,[2] D. Ghazaryan,[2] A. Misra,[3] Y. Cao,[4] S. V. Morozov,[5,6] O. Makarovsky,[1] T. M. Fromhold,[1] A. Patanè,[1] G. J. Slotman,[7] M. I. Katsnelson,[7] A. K. Geim,[2,4] K. S. Novoselov,[2,3] and L. Eaves[1,2]

[1]*School of Physics and Astronomy, University of Nottingham, Nottingham NG7 2RD, United Kingdom*

[2]*School of Physics and Astronomy, University of Manchester, Manchester M13 9PL, United Kingdom*

[3]*National Graphene Institute, University of Manchester, Manchester M13 9PL, United Kingdom*

[4]*Centre for Mesoscience and Nanotechnology, University of Manchester, Manchester M13 9PL, United Kingdom*

[5]*Institute of Microelectronics Technology and High Purity Materials, RAS, Chernogolovka 142432, Russia*

[6]*National University of Science and Technology "MISiS," 119049 Leninsky Prospect 4, Moscow, Russia*

[7]*Radboud University, Institute for Molecules and Materials, Heyendaalseweg 135, 6525 AJ Nijmegen, The Netherlands*

We observe a series of sharp resonant features in the differential conductance of graphene-hBN tunnelling transistors over a wide range of bias voltages between 10 and 200 mV. We attribute them to electron tunnelling assisted by the emission of phonons of well-defined energy. The bias voltages at which they occur are insensitive to the applied gate voltage and hence independent of the carrier densities in the graphene electrodes, so plasmonic effects can be ruled out. The phonon energies corresponding to the resonances are compared with the lattice dispersion curves of graphene–boron nitride heterostructures and are close to peaks in the single phonon density of states.

The discovery of the remarkable electronic properties of graphene [1,2] has been followed by an upsurge of interest in other layered materials such as hBN, the transition metal dichalcogenides, and the III-VI family of layered semiconductors. These anisotropic layered materials have strong in-plane bonds of covalent character, whereas the interlayer bonding arises from weaker van der Waals like forces, so crystalline flakes, one or a few atomic layers thick, can be exfoliated mechanically from bulk crystals. These developments have led to the realization of a new class of materials, van der Waals heterostructures, in which nanoflakes of different materials are stacked together in an ordered way [3-5]. These heterostructures possess unique properties that can be exploited for novel device applications. An example is a tunnel transistor in which a barrier is sandwiched between two graphene layers and mounted on the oxidized surface layer of a doped Si substrate [6,7]. The tunnel current flowing between the two graphene layers can be controlled by applying a gate voltage to the doped Si layer and arises predominantly from resonant processes in which the energy, in-plane momentum, and chirality of the tunnelling electron are conserved [8-10].

Previous investigations of electron tunnelling in a variety of metal-insulator diodes [11] and conventional semiconductor heterostructures [12] have demonstrated that electrons can tunnel inelastically, with the emission of one or multiple phonons. Atomically resolved scanning tunnelling spectroscopy measurements on mechanically cleaved graphene flakes with a tunable back gate have revealed the presence of phonon-assisted tunnelling [13-16]. The multicomponent nature of our van der Waals heterostructure gives rise to a more complex set of lattice dispersion curves than for graphene [17-21] and to phonon-assisted tunnelling, as shown recently for a graphite-hBN-graphene transistor [22]. The study of electron-phonon interactions is relevant to interlayer conduction in twisted graphene bilayers [23] and, more generally, to the recent discovery of superconductivity in graphene-based van der Waals heterostructures [24-27].

Here we investigate tunnel transistors in which a ~ 1 nm layer of hBN is sandwiched between MLG electrodes. Unlike the devices reported in refs. [9,10], which have a similar composition, the crystalline lattices of the component layers in the two devices investigated here are not intentionally aligned. We estimate the lattice misalignment of the two graphene electrodes to be at least 3°. This gives rise to a misalignment in k space of the Dirac cones at the corners of the hexagonal Brillouin zones of the two electrodes, so the momentum-conserving elastic transitions cannot occur over the bias voltage range over which the device characteristics are measured. Under these conditions interlayer conductance is dominated by phonon-assisted tunnelling processes that relax the momentum conservation rule [23].

We observe a series of sharp resonant steps in the electrical conductance over a wide range of bias voltage, gate voltage, and temperature. This spectrum can be understood in terms of inelastic transitions whereby electrons tunnelling through the hBN barrier emit phonons of different and well-defined energies between ~ 12 and 200 meV, covering the range of lattice phonon energies in these heterostructures. The resonances correspond closely to van Hove-like peaks in the single phonon density of states of the heterostructure, with the strongest peaks arising from the emission of low- and high-energy optical mode phonons.

A schematic energy band diagram of our devices and circuit is shown in the inset of Fig. 7.1(a). The bottom graphene layer is mounted on an atomically flat hBN layer, placed above the silicon oxide substrate, and the active region of the device is capped with a hBN protective top layer. The tunnel current I was measured as a function of the bias voltage V_b applied between the two graphene electrodes and the gate voltage V_g applied across the bottom graphene electrode and the doped Si gate electrode. Fig. 7.1(a) shows plots of differential tunnel conductance, $G(V_b) = dI/dV_b$, measured at a temperature of T=4 K. The form of the $G(V_b)$ curves is strongly dependent on V_g. Close to $V_b = 0$, $G \approx 0$ at all gate voltages. With increasing $|V_b|$, the conductance increases in a series of well-defined steps, indicated by vertical arrows. We attribute each step to inelastic phonon-assisted tunnelling in which an electron emits a phonon and tunnels from close to the Fermi energy in one electrode to an empty state near the Fermi energy in the other electrode, with the emission of a phonon of well-defined energy, $\hbar\omega_p$. Fig. 7.1(b) shows a colour map of $G\left(V_b, V_g\right)$ in which some of these step-like features are discernible as a series of faint vertical striped modulations in the colour map. Also visible is a dark blue, X-shaped region in which G is small. This corresponds to the passage of the chemical potential through the Dirac point of the two MLG electrodes as V_b and V_g are varied; here, the conductance is suppressed due to the small density of electronic states into which electrons can tunnel. Using an electrostatic model [7], which includes a small amount of doping in the bottom electrode (p-type, 2.5×10^{11} cm^{-2}) as a fitting parameter, we determine the condition for the intersection of the chemical potential with a Dirac point in each of the two graphene electrodes. The calculated loci of these intersections are shown by the yellow dashed line in Fig. 7.1(b); they correspond closely with the measured X-shaped low conductance region.

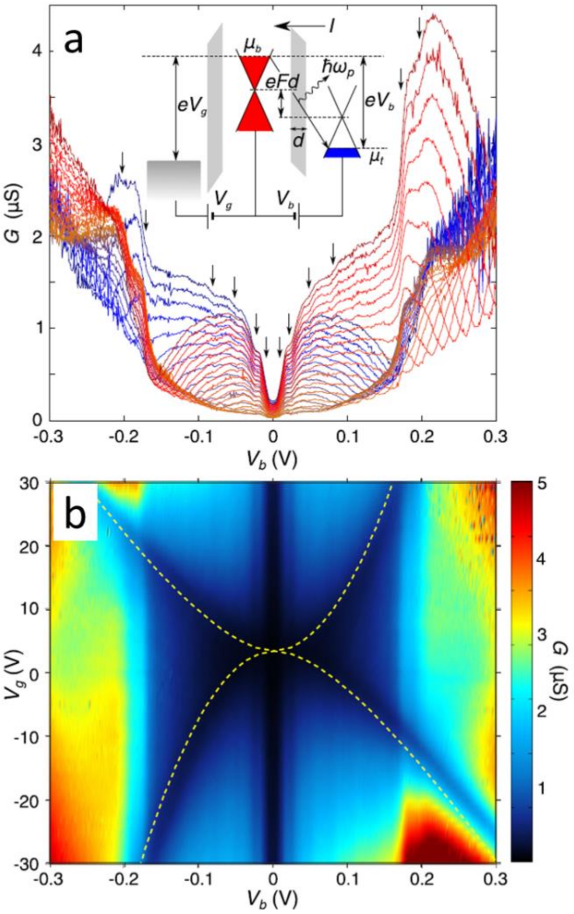

Fig. 7.1 Differential conductance of Device 1 at *T*= 4 K

(a) $G(V_b)$for $V_g = -30$ V (red) to 30 V (blue) and intervals ΔV_g=2 V. Inset: Schematic band diagram of Device 1 with bias V_b and gate V_g voltages applied to the MLG electrodes, which are separated by an hBN barrier of thickness d=0.9 nm. Here, $\mu_{b,t}$ are the chemical potentials of the bottom and top electrodes and F is the electric field across the barrier. A phonon-assisted tunnel process is shown schematically. **(b)** Colour map of dI/dV_b for a range of V_g and V_b.

The vertical stripes in the $G(V_b, V_g)$ map are faint because the step-like modulation in $G(V_b)$ is only a small fraction of the total conductance. Most of the monotonic increase of $G(V_b)$ with V_b can be partly eliminated by taking the second derivative dG/dV_b, which reveals the weak but sharp phonon-assisted resonances more clearly. Fig. 7.2(a) shows a gray-scale contour map of $\alpha dG/dV_b$, where $\alpha = |V_b|/V_b = \pm 1$. Here, the phonon-assisted tunnelling features appear as easily discernible bright vertical stripes, indicated by arrows, at well-defined values of V_b, at which $G(V_b)$ rapidly increases. These values are independent of gate voltage, but their amplitudes at low V_b are significantly stronger at large positive and negative values of V_g.

Interestingly, the vertical stripe features are not observed in the conductance maps of similar devices in which the graphene electrodes are closely aligned to within 2° (see Figs. 2 and 3 of ref. [9]). We can exclude the possibility that the features are plasmon related as the sheet density n in both graphene electrodes is strongly dependent on V_g: n varies from ~10^{12} cm^{-2} (holes) through zero to ~10^{12} cm^{-2} (electrons) between V_g=−30 V and 30 V. Even though the plasma frequency of carriers in graphene varies relatively weakly with n (~$n^{1/4}$) [28], plasmon related resonances would have a significant gate voltage dependence, which is not observed.

Since the bias voltage values$|V_b|$ of the weak resonant features are independent of gate voltage and are the same in both negative and positive biases, we can display them more clearly by averaging over all 60 of the measured $\alpha dG/dV_b$ plots in the range −30 V<V_g<30 V. This procedure significantly reduces the level of background noise. The result of this averaging procedure for Device 1 is shown in Fig. 7.3(a). It reveals the phonon-assisted resonances as a series of well-defined peaks. The corresponding plot for another device, Device 2, is also shown. The overall forms of the two curves are qualitatively similar, with the exception of some notable differences, e.g., the position of the strong peaks at high V_b>0.12 V.

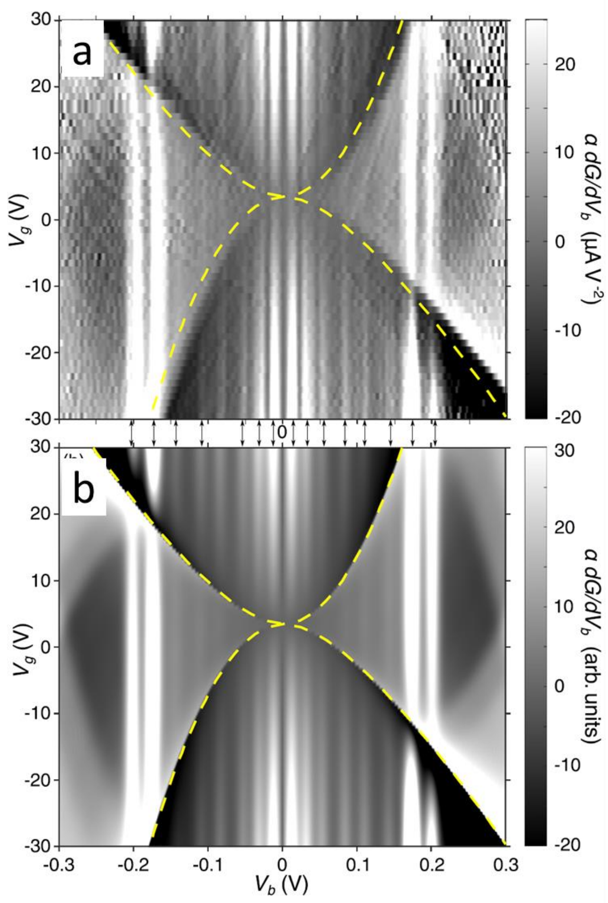

Fig. 7.2 Gray-scale contour maps of $\alpha dG/dV_b$ for Device 1

(a) Measured plots $\alpha dG/dV_b$ for Device 1. **(b)** Calculated gray-scale map of $\alpha dG/dV_b$ for T=4 K, best fit to data in Fig. 7.2(a) using the model described in the text and in Table 1. Yellow dashed curves show where the chemical potential in a graphene layer intersects with the Dirac point in that layer.

To understand the physical origin of the peaks in Fig. 7.3(a), we compare them to the one-phonon densities of states of MLG (red curve) and a graphene-hBN bilayer (green); the lower three curves show the partial density of states associated with the predominant motion of the carbon, boron, and nitrogen atoms in the bilayer; the solid and dashed curves show contributions by in- and out-of-plane phonons, respectively. The full phonon dispersion curves of the graphene-hBN bilayer [17] are shown in Fig. 7.3(b).

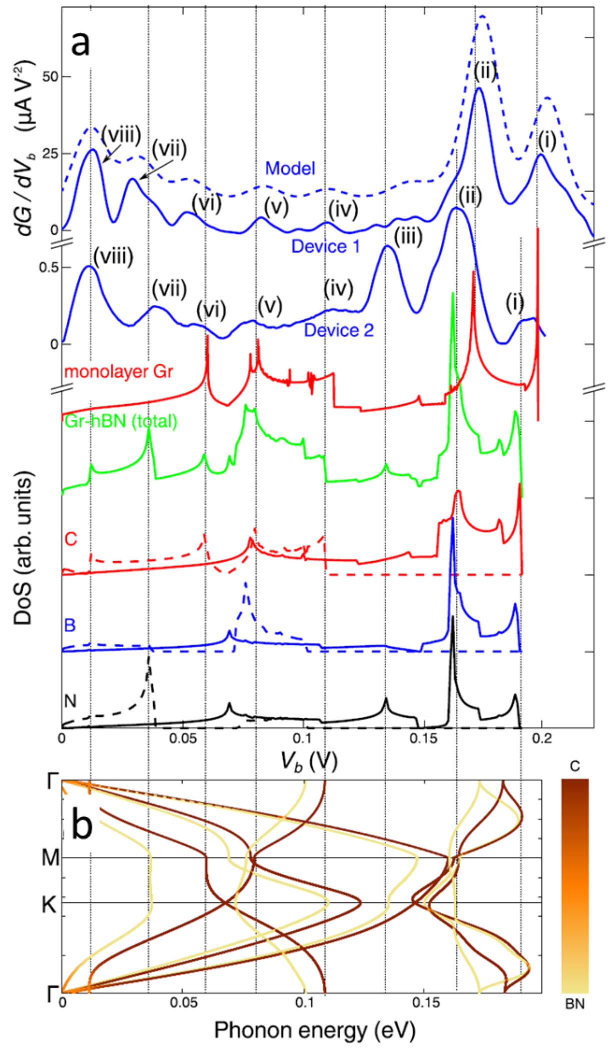

Fig. 7.3 Density of phonon states and phonon dispersion in graphene-hBN heterostructures

(a) The three top curves (blue): dG/dV_b averaged over all gate voltages for our model (dashed) and measured data for Devices 1 and 2 (both solid). Lower curves: Total density of phonon states for MLG (red, monolayer Gr) and a graphene-hBN heterostructure [green, Gr-hBN (total)]. Lower three curves: The partial density of states associated with the carbon (red, C), boron (blue, B), and nitrogen (black, N) atoms of a graphene-hBN heterostructure. Solid and dashed curves show contributions by in- and out-of-plane phonons, respectively. **(b)** Phonon dispersion of a graphene-hBN heterostructure [17]. Vertical dotted curves are guides to the eye, highlighting the alignments.

The phonon density of states and the phonon dispersion curves were determined by using the "phonopy" package [29] with the force constants obtained by the finite displacement method [30,31], using the Vienna *ab initio* simulation package (VASP) [32,33]. For the phonon density of states, a tetrahedron smearing was applied for higher accuracy. A detailed description of the computational methods can be found in ref.[17].

At high bias, the two peaks labelled (i) and (ii) are close to the energies of the large densities of states associated with the weakly dispersed, high-energy optic phonons of MLG (Device 1) and a bilayer of graphene and hBN (Device 2). Note that peak (iii) at 130 meV in Device 2 is absent in Device 1. This energy corresponds closely to the flat region of the dispersion curve of the graphene-hBN bilayer near the K point of the Brillouin zone, which arises predominantly from vibrations of the nitrogen atom. This difference, and the variation of the position of peaks (i) and (ii), between the two devices may arise from differences in the relative lattice orientation of the graphene and hBN layers in the device.

Both devices exhibit peaks around 110, 84, and 53 mV, labelled (iv), (v), and (vi), corresponding to prominent features in the calculated density-of-state plots and the flat regions of the dispersion curves. An interesting feature of the data for both devices is the strong peak (viii) at low bias, around 12 mV, which we attribute to the weakly dispersed low-energy phonons close to the Γ point of the graphene hBN bilayer. This low-energy "out-of-plane" mode was intensively studied in inelastic x-ray spectroscopy measurement of bulk graphite and hBN [18]. Note that the resonant peak (vii) observed at 32 mV can be associated with a peak in the phonon density of states of the graphene-hBN bilayer, which arises predominantly from the motion of the nitrogen atoms and corresponds to the flat region of the lowest-energy acoustic mode at ~30 meV in the vicinity of the M and K points of the Brillouin zone.

As shown in Fig. 7.4, the resonant peaks broaden and their amplitudes decrease with increasing temperature, disappearing completely at temperatures $T \geq 150$ K. This is consistent with the thermal broadening of the electron distribution functions around the Fermi energies of the two graphene electrodes so that Pauli blocking of electron tunnelling for $eV_b < \hbar\omega_p$ is diminished as more states become available with increasing thermal smearing around the Fermi energies. We fit the data in Fig. 7.2(a) using a model in which an inelastic tunnelling transition is allowed only when the difference between the chemical potentials μ_b and μ_t in the bottom (b) and top (t) graphene layers, respectively, exceeds $\hbar\omega_p^i$, which corresponds to the bias voltage of a particular phonon-assisted resonance peak i in the conductance. At low temperatures (4 K), $eV_b = \mu_b - \mu_t - eFd$ greatly exceeds the thermal smearing ~ $2k_BT$ of the Fermi seas of the two graphene electrodes. The emission of a phonon of energy, $\hbar\omega_p^i$, becomes possible when eV_b exceeds $\hbar\omega_p^i$, thus opening up an inelastic scattering channel and resulting in a step-like rise in the current and a resonant peak in dG/dV_b when $eV_b = \hbar\omega_p^i$. In our model the current is given by:

$$I = \sum_i T(i) \int dE_b \int dE_t D_b(E_b) D_t(E_t) \{ \Gamma(E_b - E_t - \hbar\omega_p^i) f_b(E_b)[1 - f_t(E_t)] - \Gamma(E_t - E_b - \hbar\omega_p^i) f_t(E_t)[1 - f_b(E_b)] \}, \tag{1}$$

where $E_{b,t}$ is the electron energy in the b and t layers, $D_{b,t}(E)$ is the density of electronic states in these layers (which are shifted energetically by eFd), $\Gamma(E) = \exp(-E^2/2\gamma^2)$ with energy broadening γ=5 meV, and $f_{b,t}$ is the Fermi function in the bottom and top electrodes. $T(i)$ is a relative weighting factor that depends on the electron-phonon coupling and phonon density of states for each inelastic transition. We show the values of $T(i)$ used in our model in Table 1, which provides a qualitative indication of the relative strengths of the phonon-assisted processes.

Table 1 Phonon energies $\hbar\omega_p^i$ and weighting factors $T(i)$ used in Eq. (1) to obtain the fit to the experimental data shown in Fig. 7.2(b).

i	1	2	3	4	5	6	7	8
$\hbar\omega_p^i$ (meV)	12	32	53	84	110	143	174	201
$T(i)$	1.0	0.58	0.30	0.26	0.24	0.23	3..53	1.81

Using this model, and including phonon emission processes at threshold energies corresponding to the values of V_b, we obtain the gray-scale plot in Fig. 7.2(b), which accurately simulates the measured data in Fig. 7.2(a). In particular, the relative intensities of the vertical stripes are in good agreement with the measured data. At high positive and negative V_g, the asymmetry in the measured intensities of the resonances for positive and negative V_b is replicated by the model. This confirms that the peaks arise from tunnelling of carriers, mediated by phonon emission, from filled states near the chemical potential in one electrode into the empty states just above the chemical potential in the other.

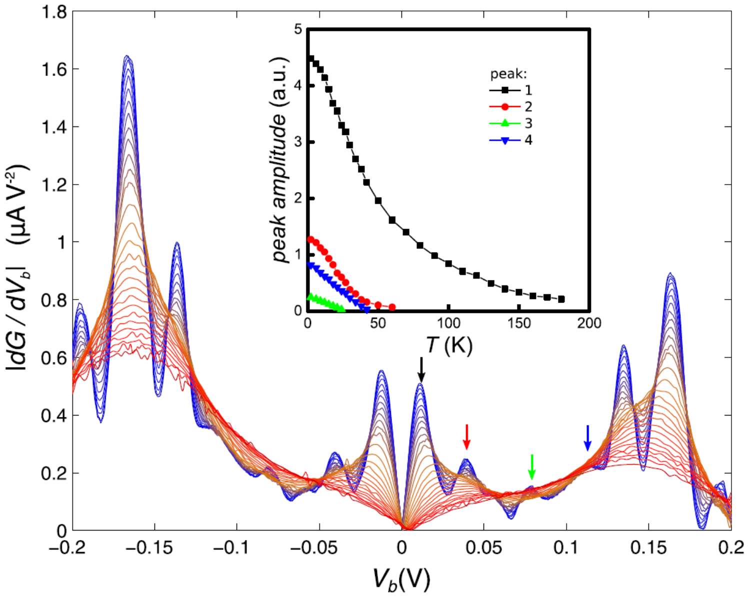

Fig. 7.4 Temperature dependence of phonon-assisted resonant tunnelling

Temperature dependence of $\left|d^2I/dV_b^2\right|$ *vs* V_b in Device 2 measured from *T*=2.3K to *T*=180K (blue to red) for V_b=40 V. Inset: Peak amplitude vs *T*. Curve colours match peaks marked by correspondingly coloured arrows in the main plot.

In conclusion, our measurements reveal a rich spectrum of inelastic phonon-assisted electron tunnelling peaks in the conductance of multilayer graphene-hBN tunnelling transistors. They allow us to probe electron-phonon interactions in this type of device and spectroscopically identify the energies and nature of the emitted phonons. Our results provide spectroscopic evidence that the tunnel current in van der Waals heterostructures is strongly suppressed by the large lateral momentum mismatch that arises when the crystalline lattices of the component electrodes are misaligned. Under these conditions, inelastic electron tunnelling with emission of phonons with well-defined energy plays a dominant role in carrying current perpendicular to the layers.

Acknowledgements

This work was supported by the EU FP7 Graphene Flagship Project 604391, ERC Synergy Grant, Hetero2D, EPSRC, the Royal Society, U.S. Army Research Office, U.S. Navy Research Office, and U.S. Airforce Research Office. M. T. G. acknowledges The Leverhulme Trust for support. S. V. M. and E. E. V. were supported by NUST MISiS (Grant No. K1-2015-046) and RFBR (Grants No. 15-02-01221 and No. 14-02-00792). G. J. S. and M. I. K. acknowledge financial support from the ERC Advanced Grant No. 338957 FEMTO/NANO. We are grateful to Gilles de Wijs and Annalisa Fasolino for useful discussions.

References

[1] K. S. Novoselov, A. K. Geim, S. V. Morozov, D. Jiang, Y. Zhang, S. V. Dubonos, I. V. Grigorieva, and A. A. Firsov, Science 306, 666 (2004).

[2] K. S. Novoselov, D. Jiang, F. Schedin, T. J. Booth, V. V. Khotkevich, S. V. Morozov, and A. K. Geim, Proc. Natl. Acad. Sci. USA 102, 10451 (2005).

[3] C. R. Dean et al., Nat. Nanotechnol. 5, 722 (2010)

[4] A. K. Geim and I. V. Grigorieva, Nature (London) 499, 419 (2013).

[5] A. C. Ferrari et al., Nanoscale 7, 4598 (2015).

[6] R. M. Feenstra, D. Jena, and G. Gu, J. Appl. Phys. 111, 043711 (2012).

[7] L. Britnell et al., Science 335, 947 (2012).

[8] L. Britnell, R. V. Gorbachev, A. K. Geim, L. A. Ponomarenko, A. Mishchenko, M. T. Greenaway, T. M. Fromhold, K. S. Novoselov, and L. Eaves, Nat. Commun. 4, 1794 (2013).

[9] A. Mishchenko et al., Nat. Nanotechnol. 9, 808 (2014).

[10] M. T. Greenaway et al., Nat. Phys. 11, 1057 (2015).

[11] A. G. Chynoweth, R. A. Logan, and D. E. Thomas, Phys. Rev. 125, 877 (1962).

[12] L. Eaves, P. S. S. Guimaranes, B. R. Snell, D. C. Taylor, and K. E. Singer, Phys. Rev. Lett. 55, 262 (1985).

[13] V. W. Brar, Y. Zhang, Y. Yayon, T. Ohta, J. L. McChesney, A. Bostwick, E. Rotenberg, K. Horn, and M. F. Crommie, Appl. Phys. Lett. 91, 122102 (2007).

[14] Y. Zhang, V. W. Brar, F. Wang, C. Girit, Y. Yayon, M. Panlasigui, A. Zettl, and M. F. Crommie, Nat. Phys. 4, 627 (2008).

[15] T. O. Wehling, I. Grigorenko, A. I. Lichtenstein, and A. V. Balatsky, Phys. Rev. Lett. 101, 216803 (2008).

[16] F. D. Natterer, Y. Zhao, J. Wyrick, Y.-H. Chan, W.-Y. Ruan, M.-Y. Chou, K. Watanabe, T. Taniguchi, N. B. Zhitenev, and J. A. Stroscio, Phys. Rev. Lett. 114, 245502 (2015).

[17] G. J. Slotman, G. A. de Wijs, A. Fasolino, and M. I. Katsnelson, Ann. Phys. (Berlin) 526, 381 (2014).

[18] J. Serrano, A. Bosak, R. Arenal, M. Krisch, K. Watanabe, T. Taniguchi, H. Kanda, A. Rubio, and L. Wirtz, Phys. Rev. Lett. 98, 095503 (2007).

[19] J. Maultzsch, S. Reich, C. Thomsen, H. Requardt, and P. Ordejón, Phys. Rev. Lett. 92, 075501 (2004).

[20] L. Wirtz and A. Rubio, Solid State Commun. 131, 141 (2004).

[21] A. C. Ferrari et al., Phys. Rev. Lett. 97, 187401 (2006).

[22] S. Jung, M. Park, J. Park, T.-Y. Jeong, H.-J. Kim, K. Watanabe, T. Taniguchi, D. H. Ha, C. Hwang, and Y.-S. Kim, Sci. Rep. 5, 16642 (2015).

[23] V. Perebeinos, J. Tersoff, and Ph. Avouris, Phys. Rev. Lett. 109, 236604 (2012).

[24] J. Chapman, Y. Su, C. A. Howard, D. Kundys, A. N. Grigorenko, F. Guinea, A. K. Geim, I. V. Grigorieva, and R. R. Nair, Sci. Rep. 6, 23254 (2016).

[25] M. Xue, G. Chen, H. Yang, Y. Zhu, D. Wang, J. He, and T. Cao, J. Am. Chem. Soc. 134, 6536 (2012).

[26] M. Petrović et al., Nat. Commun. 4, 2772 (2013).

[27] D. M. Guzman, H. M. Alyahyaei, and R. A. Jishi, 2D Mater. 1, 021005 (2014).

[28] E. H. Hwang and S. Das Sarma, Phys. Rev. B 75, 205418 (2007).

[29] A. Togo and I. Tanaka, Scr. Mater. 108, 1 (2015).

[30] G. Kresse, J. Furthmller, and J. Hafner, Europhys. Lett. 32, 729 (1995).

[31] K. Parlinski, Z.-Q. Li, and Y. Kawazoe, Phys. Rev. Lett. 78, 4063 (1997).

[32] G. Kresse and J. Furthmüller, Comput. Mater. Sci. 6, 15 (1996).

[33] G. Kresse and J. Furthmüller, Phys. Rev. B 54, 11169 (1996).

Chapter 8

Summary and outlook

8.1 Summary

In this thesis, several novel devices based on the graphene-hBN heterostructures have been fabricated and the underlying physics has been studied and discussed.

We fabricated graphene Josephson junctions with high carrier mobility and transparent G-S interfaces. Such high quality devices allowed us to study the new physics of ballistic graphene Josephson junctions. We observed clear Fabry-Pérot interference not only in the normal-state resistance but also in the critical current. Under high magnetic field up to 1000 flux quanta of the junction, the critical current appears and disappears randomly as function of carrier concentration and magnetic field. We attribute the high field Josephson effect to mesoscopic Andreev states that persist near the graphene edges.

By opening a gap in graphene, we found that the supercurrent at the CNP of graphene changes from uniform flow to propagation along the graphene edges. Our results show that the insulating state of gapped graphene is electrically shunted by the conducting edge channels, which explains a long-standing puzzle of why graphene transistors have a low ON/OFF ratio.

By studying the graphene tunnelling transistors and the Raman spectroscopy of twisted BLG before and after annealing, we probed a structural transition in bilayer graphene from incommensurate twisted stacking to commensurate AB stacking. We found that the low-energy electronic dispersion preserves linearity in twisted BLG, but changes to almost parabolic in BLG. The structural transition is achieved by macroscopic scale graphene self-rotation driven by the van der Waals energy.

We observed a series of gate independent kinks in the differential conductance of graphene-hBN tunnelling transistors, which are attributed to the phonon-assisted resonant tunnelling phenomenon. The phonon energies corresponding to the resonances are compared with the lattice dispersion curves of graphene-hBN heterostructures and are close to peaks in the single phonon density of states.

8.2 Outlook

8.2.1 Supercurrent in graphene quantum Hall regime

Superconductivity and quantized Hall states are both macroscopic quantum phenomena that allow electrical currents to flow without dissipation. The QHE occurs in two-dimensional electron gases subjected to perpendicular magnetic fields. In the quantum Hall regime, the current is fully carried by dissipationless edge states that travel in only one direction along the edge, known as chiral edge current. Studies of the integer and fractional QHE have yielded many fascinating physics. In addition, there has been great interest in understanding the emergent physics from the interplay between the QHE and other correlated states, for instance the Josephson supercurrent. However, this interplay has proven to be experimentally difficult. A small magnetic field will destroy the supercurrent and more fundamentally will break the time-reversal symmetry, which is essential for s-wave pairing of conventional superconductors.

It has been proven that graphene can be coupled to superconductors with transparent interfaces, and can sustain supercurrents. High quality graphene enters the quantum Hall regime in the presence of a relatively small magnetic field (few Tesla), while the electrodes still remain superconducting. Thus, graphene Josephson junction is an ideal platform to examine the coupling between supercurrents and the QHE.

Amet *et al*. recently demonstrated the interplay of superconductivity and the QHE in graphene-hBN heterostructures with superconducting MoRe contacts at 10mK. Magnetic fields of ~2 T ensured that the radius of the cyclotron orbit was smaller than both the junction length and the mean free path. At the same time, the opposite free edges were far enough apart to prevent edge coupling through conventional Andreev reflections. Remarkably, the behavior of the differential resistance unambiguously showed signatures of supercurrents.

The observation of superconductivity in the quantum Hall regime is an important step forward to the realisation of Majorana fermions. In addition, the fractional QHE in graphene can emerges in magnetic fields as small as 5T[110]. Thus, we can start to look forward the interplay between the fractional QHE and the proximity superconductivity in graphene Josephson junctions in the near future.

8.2.2 Supercurrent in quasi-one-dimensional graphene systems

Graphene nanoribbons (GNRs), narrow stripes of graphene, have emerged as promising building blocks for nanoelectronic devices because of the tunable properties by adjusting the width, length and the edge topology. GNRs with zigzag edges are particularly interesting because of spin-polarized edge states. Along each edge, the electrons all spin in the same direction; an effect which is referred to as ferromagnetic coupling. At the same time, the antiferromagnetic coupling ensures that the electrons on the other edge all spin in the opposite direction. The spin-polarized edge states are proposed to support ballistic transport. However, it has proven experimentally difficult to probe such edge currents due to disorders and scattering processes.

Recent advances in bottom-up synthesis have allowed the production of atomically precise zigzag GNRs[111]. Now, it is possible to create high quality Josephson junctions based on zigzag GNRs contacted by superconductors. By studying the Fraunhofer interference pattern of critical currents under a small magnetic field, it is possible to rebuild the spatial current distribution.

There is another approach to achieve quasi-one-dimensional ballistic transport in graphene by confining the Dirac fermions using split-gates technique. The fermi wavelength in high quality graphene can be tuned from few tens of nanometres to few hundreds of nanometres, which are comparable to the width of formed graphene QPC. The fundamental result of such confinement is the conductance quantization in multiple of the conductance quanta.

Quantization of the critical current in superconducting QPC has been observed two decades ago by studying a split-gates superconductor-2DEG-superconductor Josephson junction[112]. A recent work done by M. Kee *et. al.*[113] showed that conductance quantization in graphene QPC can be achieved by gate-defined carrier guiding which is identical to the conductance quantization in zigzag GNRs. Thus, it would be very interesting to investigate the Josephson effect and Andreev reflection in superconducting QPC based on graphene.

8.2.3 Graphene-hBN RTDs as high-frequency oscillators

RTDs operating above THz at room temperature have been demonstrated recently[114-116]. The first graphene RTD was achieved by controlling the twisted angle between two graphene electrodes[103,104], in which the resonant tunnelling and NDC arise from the energy and momentum conservation of Dirac fermions tunnelling through a thin hBN barrier. The first graphene RTD showed a peak-to-valley ratio of ~ 2 at room temperature suggesting potential applications in high frequency circuits[103,104]. Although the proof-of-principle devices only produced stable oscillations in the MHz range[104], mainly limited by the external parameters such as the parasitic capacitance between the contact pads and the Si back gate. Compared with conventional double-barrier RTDs, the time to transit the barrier of graphene RTDs is much shorter than the dwell time in the quantum well. Theoretical work suggested that current oscillations with frequency up to several hundred GHz is achievable by carefully optimizing the diode and circuit parameters including the graphene doping level, device geometry, alignment between two graphene electrodes, and the circuit impedances[117].

Bibliography

1 Novoselov, K. S., Geim, A. K., Morozov, S. V., Jiang, D., Zhang, Y., Dubonos, S. V., Grigorieva, I. V., Firsov, A. A. Electric field effect in atomically thin carbon films. *Science* **306**, 666-669 (2004).

2 Geim, A. K., Novoselov, K. S. The rise of graphene. *Nature materials* **6**, 183-191 (2007).

3 Castro Neto, A. H., Peres, N. M. R., Novoselov, K. S., Geim, A. K. The electronic properties of graphene. *Reviews of Modern Physics* **81**, 109-162 (2009).

4 Novoselov, K. S., Geim, A. K., Morozov, S. V., Jiang, D., Katsnelson, M. I., Grigorieva, I. V., Dubonos, S. V., Firsov, A. A. Two-dimensional gas of massless Dirac fermions in graphene. *Nature* **438**, 197-200 (2005).

5 Zhang, Y., Tan, Y. W., Stormer, H. L., Kim, P. Experimental observation of the quantum Hall effect and Berry's phase in graphene. *Nature* **438**, 201-204 (2005).

6 Katsnelson, M. I., Novoselov, K. S., Geim, A. K. Chiral tunnelling and the Klein paradox in graphene. *Nature Physics* **2**, 620-625 (2006).

7 Yang, A. F., Kim, P. Quantum interference and Klein tunnelling in graphene heterojunctions. *Nature Physics* **5**, 222-226 (2009).

8 Stander, N., Huard, B., Goldhaber-Gordon, D. Evidence for Klein tunneling in graphene p-n junctions. *Physical Review Letters* **102**, 026807 (2009).

9 Cheianov, V. V., Fal‘ko, V. I., Altshuler, B. L. The Focusing of Electron Flow and a Veselago Lens in Graphene p-n Junctions. *Science* **315**, 1252-1256 (2007).

10 Lee, G.-H., Park, G-H., Lee, H-J. Observation of negative refraction of Dirac fermions in graphene. *Nature Physics* **11**, 925-930 (2015).

11 Bolotin, K. I., Ghahari, F., Shulman, M. D., Stormer, H. L., Kim, P. Observation of the fractional quantum Hall effect in graphene. *Nature* **462**, 196-199 (2009).

12 Du, X., Skachko, I., Duerr, F., Luican, A., Andrei, E. Y. Fractional quantum Hall effect and insulating phase of Dirac electrons in graphene. *Nature* **462**, 192-195 (2009).

13 Hunt, B., Sanchez-Yamagishi, J. D., Young, A. F., Yankowitz,M., LeRoy,B. J., Watanabe, K., Taniguchi, T., Moon, P., Koshino, M., Jarillo-Herrero, P., Ashoori, R. C. Massive Dirac fermions and Hofstadter butterfly in a van der Waals heterostructure. *Science* **340**, 1427-1431 (2013).

14 Dean, C. R., Wang, L., Maher, P., Forsythe, C., Ghahari, F., Gao, Y., Katoch, J., Ishigami, M., Moon, P., Koshino, M., Taniguchi, T., Watanabe, K., Shepard, K. L., Hone, J., Kim, P. Hofstadter's butterfly and the fractal quantum Hall effect in moire superlattices. *Nature* **497**, 598-602 (2013).

15 Ponomarenko, L. A., Gorbachev, R. V., Yu, G. L., Elias, D. C., Jalil, R., Patel, A. A., Mishchenko, A., Mayorov, A. S., Woods, C. R., Wallbank, J. R., Mucha-Kruczynski, M., Piot, B. A., Potemski, M., Grigorieva, I. V., Novoselov, K. S., Guinea, F., Fal'ko, V. I., Geim, A. K. Cloning of Dirac fermions in graphene superlattices. *Nature* **497**, 594-597 (2013).

16 Profeta, G., Calandra, M., Mauri, F. Phonon-mediated superconductivity in graphene by lithium deposition. *Nature Physics* **8**, 131-134 (2012).

17 Nandkishore, R., Levitov, L. S., Chubukov, A. V. Chiral superconductivity from repulsive interactions in doped graphene. *Nature Physics* **8**, 158-163 (2012).

18 Efetov, D. K., Kim, P. Controlling electron-phonon interactions in graphene at ultrahigh carrier densities. *Physical Review Letters* **105**, 256805 (2010).

19 Andreev, A. F. Thermal conductivity of the intermediate state of superconductors. *Soviet Journal of Experimental and Theoretical Physics* **19**, 1228-1231 (1964).

20 Heersche, H. B., Jarillo-Herrero, P., Oostinga, J. B., Vandersypen, L. M. & Morpurgo, A. F. Bipolar supercurrent in graphene. *Nature* **446**, 56-59 (2007).

21 Miao, F., Wijeratne, S., Zhang, Y., Coskun, U. C., Bao, W., Lau, C. N. Phase-Coherent Transport in Graphene Quantum Billiards. *Science* **317**, 1530-1534 (2007).

22 Du, X., Skachko, I., Andrei, E. Y. Josephson current and multiple Andreev reflections in graphene SNS junctions. *Physical Review B* **77**, 184507 (2008).

23 Girit, C., Bouchiat, V., Naaman, O., Zhang, Y., Crommie, M. F., Zettl, A., Siddiqi, I. Tunable graphene dc superconducting quantum interference device. *Nano letters* **9**, 198-199 (2009).

24 Ojeda-Aristizabal, C., Ferrier, M., Guéron, S., Bouchiat, H. Tuning the proximity effect in a superconductor-graphene-superconductor junction. *Physical Review B* **79**, 165436 (2009).

25 Borzenets, I. V., Coskun, U. C., Jones, S. J., Finkelstein, G. Phase Diffusion in Graphene-Based Josephson Junctions. *Physical Review Letters* **107**, 137005 (2011).

26 Jeong, D., Choi, J-H., Lee, G-H., Jo, S., Doh, Y-J., Lee, H-J. Observation of supercurrent in PbIn-graphene-PbIn Josephson junction. *Physical Review B* **83**, 094503 (2011).

27 Lee, G.-H., Jeong, D., Choi, J-H., Doh, Y-J., Lee, H-J. Electrically Tunable Macroscopic Quantum Tunneling in a Graphene-Based Josephson Junction. *Physical Review Letters* **107**, 146605 (2011).

28 Coskun, U. C., Brenner, M., Hymel, T., Vakaryuk, V., Levchenko, A., Bezryadin, A. Distribution of Supercurrent Switching in Graphene under the Proximity Effect. *Physical Review Letters* **108**, 097003 (2012).

29 Komatsu, K., Li, C., Autier-Laurent, S., Bouchiat, H., Guéron, S. Superconducting proximity effect in long superconductor/graphene/superconductor junctions: From specular Andreev

reflection at zero field to the quantum Hall regime. *Physical Review B* **86**, 115412 (2012).

30 Choi, J.-H., Lee, G-H., Park, S., Jeon, D., Lee, J-O., Sim, H-S., Doh, Y-J., Lee, H-J. complete gate control of supercurrent in graphene p-n junctions. *Nature communications,* doi:10.1038/ncomms3525 (2013).

31 Deon, F., Sopic, S., Morpurgo, A. F. Tuning the influence of microscopic decoherence on the superconducting proximity effect in a graphene Andreev interferometer. *Physical Review Letters* **112**, 126803 (2014).

32 Mizuno, N., Nielsen, B., Du, X. Ballistic-like supercurrent in suspended graphene Josephson weak links. *Nature communications*, doi:10.1038/ncomms3716 (2013).

33 Calado, V. E., Goswami, S., Nanda, G., Diez, M., Akhmerov, A. R., Watanabe, K., Taniguchi, T., Klapwijk, T. M., Vandersypen, L. M. K. Ballistic Josephson junctions in edge-contacted graphene. *Nature nanotechnology* **10**, 761-765 (2015).

34 Ben Shalom, M., Zhu, M. J., Fal'ko, V. I., Mishchenko, A., Kretinin, A. V., Novoselov, K. S., Woods, C. R., Watanabe, K., Taniguchi, T., Geim, A. K., Prance, J. R. Quantum oscillations of the critical current and high-field superconducting proximity in ballistic graphene. *Nature Physics* **12**, 318-322 (2016).

35 Allen, M. T., Shtanko, O., Fulga, I. C. , ,Akhmerov, A. R., Watanabe, K., Taniguchi, T., Jarillo-Herrero, P., Levitov, L. S. , Yacoby, A. Spatially resolved edge currents and guided-wave electronic states in graphene. *Nature Physics* **12**, 128-133 (2016).

36 Amet, F., Ke, C. T., Borzenets, I. V., Wang, J., Watanabe, K., Taniguchi, T., Deacon, R. S., Yamamoto, M., Bomze, Y., Tarucha, S., Finkelstein, G. Supercurrent in the quantum Hall regime. *Science* **352**, 966-970 (2016).

37 Kumaravadivel, P., Du, X. Signatures of evanescent transport in ballistic suspended graphene-superconductor junctions. *Scientific reports* **6**, 24274 (2016).

38 Beenakker, C. W. J. Specular Andreev Reflection in Graphene. *Physical Review Letters* **97**, 067007 (2006).

39 Efetov, D. K., Wang, L., Handschin, C., Efetov, K. B., Shuang, J., Cava, R., Taniguchi, T., Watanabe, K., Hone, J., Dean, C. R., Kim, P. Specular interband Andreev reflections at van der Waals interfaces between graphene and NbSe2. *Nature Physics* **12**, 328-332 (2016).

40 Ma, M., Zyuzin, A. YU. Josephson Effect in the Quantum Hall Regime. *Europhysics Letters* **21**, 941-945 (1993).

41 Stone, M., Lin, Y. Josephson currents in quantum Hall devices. *Physical Review B* **83**, 224501 (2011).

42 Rickhaus, P., Weiss, M., Marot, L., Schonenberger, C. Quantum Hall effect in graphene with superconducting electrodes. *Nano letters* **12**, 1942-1945 (2012).

43 Katsnelson, M. I. *Graphene: carbon in two dimensions*. (Cambridge University Press, 2012).

44 McCann, E. Asymmetry gap in the electronic band structure of bilayer graphene. *Physical Review B* **74**, 161403 (2006).

45 Oostinga, J. B., Heersche, H. B., Liu, X., Morpurgo, A. F., Vandersypen, L. M. Gate-induced insulating state in bilayer graphene devices. *Nature materials* **7**, 151-157 (2008).

46 Zhang, Y., Tang, T. T., Girit, C., Hao, Z., Martin, M. C., Zettl, A., Crommie, M. F., Shen, Y. R., Wang, F. Direct observation of a widely tunable bandgap in bilayer graphene. *Nature* **459**, 820-823 (2009).

47 Schwierz, F. graphene transistors. *Nature nanotechnology* **5**, 487-496 (2010).

48 Han, M. Y., Ozyilmaz, B., Zhang, Y., Kim, P. Energy band-gap engineering of graphene nanoribbons. *Physical Review Letters* **98**, 206805 (2007).

49 Stampfer, C., Fringes, S., Güttinger, J., Molitor, F., Volk, C., Terrés, B., Dauber, J., Engels, S., Schnez, S. M., Jacobsen, A., Dröscher, S., Ihn, T.,

Ensslin, K. Transport in graphene nanostructures. *Frontiers of Physics* **6**, 271-293 (2011).

50 Elias, D. C., Nair, R. R., Mohiuddin, T. M. G., Morozov, S. V., Blake, P., Halsall, M. P., Ferrari, A. C., Boukhvalov, D. W., Katsnelson, M. I., Geim, A. K., Novoselov, K. S. Control of Graphene's Properties by Reversible Hydrogenation: Evidence for Graphane. *Science* **323**, 610-614 (2009).

51 Britnell, L., Gorbachev, R. V., Jalil, R., Belle, B. D., Schedin, F., Katsnelson, M. I., Eaves, L., Morozov, S. V., Mayorov, A. S., Peres, N. M., Neto, A. H., Leist, J., Geim, A. K., Ponomarenko, L. A., Novoselov, K. S. Field-effect tunneling transistor based on vertical graphene heterostructures. *Science* **335**, 947-950 (2012).

52 Li, J., Martin, I., Büttiker, M., Morpurgo, A. F. Topological origin of subgap conductance in insulating bilayer graphene. *Nature Physics* **7**, 38-42 (2011).

53 Dean, C. R., Young, A. F., Meric, I., Lee, C., Wang, L., Sorgenfrei, S., Watanabe, K., Taniguchi, T., Kim, P., Shepard, K. L., Hone, J. Boron nitride substrates for high-quality graphene electronics. *Nature nanotechnology* **5**, 722-726 (2010).

54 Britnell, L., Gorbachev, R. V., Jalil, R., Belle, B. D., Schedin, F., Katsnelson, M. I., Eaves, L., Morozov, S. V., Mayorov, A. S., Peres, N. M., Neto, A. H., Leist, J., Geim, A. K., Ponomarenko, L. A., Novoselov, K. S. Electron tunneling through ultrathin boron nitride crystalline barriers. *Nano letters* **12**, 1707-1710 (2012).

55 Sohn, L. L., Kouwenhoven, L. P. & Schön, G. *Mesoscopic electron transport*. Vol. 345 (Springer Science & Business Media, 2013).

56 Landauer, R. Spatial Variation of Currents and Fields Due to Localized Scatterers in Metallic Conduction. *IBM Journal of Research and Development* **1**, 223-231 (1957).

57 van Wees, B. J., van Houten, H., Beenakker, C. W., Williamson, J. G., Kouwenhoven, L. P., van der Marel, D., Foxon, C. T. Quantized conductance

of point contacts in a two-dimensional electron gas. *Physical Review Letters* **60**, 848-850 (1988).

58 Wharam, D. A., Thornton, T. J.,Newbury, R., Pepper, M., Ahmed, H., Frost, J. E. F., Hasko, D. G., Peacock, D. C., Ritchie, D. A., Jones, G. A. C. One-dimensional transport and the quantisation of the ballistic resistance. *Journal of Physics C* **21**, 209-214 (1988).

59 Sharvin, Y. V. On the possible method for studying fermi surfaces. *Soviet Journal of Experimental and Theoretical Physics* **21**, 655 (1965).

60 Ferry, D. K., Goodnick, S. M. & Bird, J. *Transport in nanostructures*. (Cambridge University Press, 2009).

61 Wallace, P. R. The Band Theory of Graphite. *Physical Review* **71**, 622-634 (1947).

62 Novoselov, K. S. M., E., Morozov, S. V., Fal'ko, V. I., Katsnelson, M. I., Zeitler, U., Jiang, D., Schedin, F., Geim, A. K. Unconventional quantum Hall effect and Berry's phase of 2π in bilayer graphene. *Nature Physics* **2**, 177-180 (2006).

63 McCann, E., Fal'ko, V.I. Landau-Level Degeneracy and Quantum Hall Effect in a Graphite Bilayer. *Physical Review Letters* **96**, 086805 (2006).

64 Mayorov, A. S., Elias, D. C., Mucha-Kruczynski,M., Gorbachev, R. V., Tudorovskiy, T., Zhukov, A., Morozov, S. V., Katsnelson, M. I., Fal'ko, V. I., Geim, A. K., Novoselov, K. S. Interaction-Driven Spectrum Reconstruction in Bilayer Graphene. *Science* **333**, 860-864 (2011).

65 Klitzing, K. v., Dorda, G., Pepper, M. New Method for High-Accuracy Determination of the Fine-Structure Constant Based on Quantized Hall Resistance. *Physical Review Letters* **45**, 494-497 (1980).

66 Novoselov, K. S., Jiang, Z., Zhang, Y., Morozov, S. V., Stormer, H. L., Zeitler, U., Maan, J. C., Boebinger, G. S., Kim, P., Geim, A. K. Room-temperature quantum Hall effect in graphene. *Science* **315**, 1379 (2007).

67 Williams, J. R., DiCarlo, L., Marcus, C. M. . Quantum Hall Effect in a Gate-Controlled p-n Junction of Graphene. *Science* **307**, 638-652 (2007).

68 Halperin, B. I. Quantized Hall conductance, current-carrying edge states, and the existence of extended states in a two-dimensional disordered potential. *Physical Review B* **25**, 2185-2190 (1982).

69 Eisenstein, J. P., Stormer, H. L. The Fractional Quantum Hall Effect. *Science* **248**, 1510-1516 (1990).

70 Gusynin, V. P., Sharapov, S. G. Unconventional integer quantum Hall effect in graphene. *Physical Review Letters* **95**, 146801 (2005).

71 Novoselov, K. S. J., D., Schedin, F., Booth, T. J., Khotkevich, V. V., Morozov, S. V., Geim, A. K. Two-dimensional atomic crystals. *Proc Natl Acad Sci U. S. A.* **102**, 10451-10453 (2005).

72 Yankowitz, M., Xue, J., LeRoy, B. J. Graphene on hexagonal boron nitride. *Journal of physics. Condensed matter* **26**, 303201 (2014).

73 Watanabe, K., Taniguchi, T., Kanda, H. Direct-bandgap properties and evidence for ultraviolet lasing of hexagonal boron nitride single crystal. *Nature materials* **3**, 404-409 (2004).

74 Xue, J., Sanchez-Yamagishi, J., Bulmash, D., Jacquod,P., Deshpande, A., Watanabe, K., Taniguchi, T., Jarillo-Herrero, P., LeRoy, B. J. Scanning tunnelling microscopy and spectroscopy of ultra-flat graphene on hexagonal boron nitride. *Nature materials* **10**, 282-285 (2011).

75 Mayorov, A. S., Gorbachev, R. V., Morozov, S. V., Britnell, L., Jalil, R., Ponomarenko, L. A., Blake, P., Novoselov, K. S., Watanabe, K., Taniguchi, T., Geim, A. K. Micrometer-scale ballistic transport in encapsulated graphene at room temperature. *Nano letters* **11**, 2396-2399 (2011).

76 Wang, L. M., I., Huang, P. Y., Gao, Q., Gao, Y.,Tran, H., Taniguchi, T., Watanabe, K., Campos, L. M., Muller, D. A., Guo, J., Kim, P., Hone, J., Shepard, K. L., Dean, C. R. One-Dimensional Electrical Contact to a Two-Dimensional Material. *Science* **342**, 614-617 (2013).

77 Giovannetti, G., Khomyakov, P. A., Brocks, G., Kelly, P. J., van den Brink, J. Substrate-induced band gap in graphene on hexagonal boron nitride:Ab initiodensity functional calculations. *Physical Review B* **76**, 073103 (2007).

78 Yankowitz, M., Xue, J., Cormode, D., Sanchez-Yamagishi, J. D., Watanabe, K., Taniguchi, T., Jarillo-Herrero, P., Jacquod, P., LeRoy, B. J. Emergence of superlattice Dirac points in graphene on hexagonal boron nitride. *Nature physics* **8**, 382-386 (2012).

79 Woods, C. R., Britnell, L., Eckmann, A., Ma, R. S., Lu, J. C., Guo, H. M., Lin, X., Yu,G. L., Cao, Y., Gorbachev, R. V., Kretinin, A. V., Park, J., Ponomarenko, L. A., Katsnelson, M. I., Gornostyrev, Yu. N., Watanabe, K., Taniguchi, T., Casiraghi, C., Gao, H-J., Geim, A. K., Novoselov, K. S. Commensurate–incommensurate transition in graphene on hexagonal boron nitride. *Nature Physics* **10**, 451-456 (2014).

80 Gorbachev, R. V., Song, J. C. W., Yu, G., Kretinin, A. V., Withers, F., Cao, Y., Mishchenko, A., Grigorieva, I. V., Novoselov, K. S., Levitov, L. S., Geim, A. K. Detecting topological currents in graphene superlattices. *Science* **346**, 448-452 (2014).

81 Tinkham, M. *Introduction to superconductivity: Second Edition*. (Dover Books on Physics, 2004).

82 London, F. & London, H. in *Proceedings of the Royal Society of London A: Mathematical, Physical and Engineering Sciences.* 71-88 (The Royal Society).

83 Maxwell, E. Isotope Effect in the Superconductivity of Mercury. *Physical Review* **78**, 477-477 (1950).

84 Reynolds, C. A., Serin, B., Nesbitt, L. B. The Isotope Effect in Superconductivity. I. Mercury. *Physical Review* **84**, 691-694 (1951).

85 Bardeen, J., Cooper, L. N., Schrieffer, J. R. Microscopic Theory of Superconductivity. *Physical Review* **106**, 162-164 (1957).

86 Bardeen, J., Cooper, L. N., Schrieffer, J. R. Theory of Superconductivity. *Physical Review* **108**, 1175-1204 (1957).

87 Blonder, G. E., Tinkham, M., Klapwijk, T. M. Transition from metallic to tunneling regimes in superconducting microconstrictions: Excess current, charge imbalance, and supercurrent conversion. *Physical Review B* **25**, 4515-4532 (1982).

88 Blonder, G. E., Tinkham, M. Metallic to tunneling transition in Cu-Nb point contacts. *Physical Review B* **27**, 112-118 (1983).

89 Josephson, B. D. Possible new effects in superconductive tunnelling. *Physics Letters* **1**, 251-253 (1962).

90 Ambegaokar, V., Baratoff, A. Tunneling Between Superconductors. *Physical Review Letters* **10**, 486-489 (1963).

91 Kulik, I. O., Omel'Yanchuk, A. N. Properties of superconducting microbridges in the pure limit. *Soviet Journal of Low Temperature Physics* **3** (1977).

92 Dubos, P., Courtois, H., Pannetier, B., Wilhelm, F. K., Zaikin, A. D., Schön, G. Josephson critical current in a long mesoscopic S-N-S junction. *Physical Review B* **63**, 064502 (2001).

93 Popinciuc, M., Calado, V. E., Liu, X. L., Akhmerov, A. R., Klapwijk, T. M., Vandersypen, L. M. K. Zero-bias conductance peak and Josephson effect in graphene-NbTiN junctions. *Physical Review B* **85**, 205404 (2012).

94 Borzenets, I. V., Coskun, U. C., Mebrahtu, H. T., Bomze, Yu V., Smirnov, A. I., Finkelstein, G. Phonon Bottleneck in Graphene-Based Josephson Junctions at Millikelvin Temperatures. *Physical Review Letters* **111**, 027001 (2013).

95 Lee, G. H., Kim, S., Jhi, S. H., Lee, H. J. Ultimately short ballistic vertical graphene Josephson junctions. *Nature communications*, doi:10.1038/ncomms7181 (2015).

96 Cuevas, J. C., Yeyati, A. L. Subharmonic gap structure in short ballistic graphene junctions. *Physical Review B* **74**, 180501 (2006).

97 Titov, M., Beenakker, C. W. J. Josephson effect in ballistic graphene. *Physical Review B* **74**, 041401 (2006).

98 Du, X., Skachko, I., Barker, A. & Andrei, E. Y. Approaching ballistic transport in suspended graphene. *Nature nanotechnology* **3**, 491-495 (2008).

99 Du, X., , Prober, D. E., Vora, H., McKitterick, C. B. Graphene-based Bolometers. *Graphene and 2D Materials* **1**, 1-22 (2014).

100 Haigh, S. J., Gholinia, A., Jalil, R., Romani, S., Britnell, L., Elias, D. C., Novoselov, K. S., Ponomarenko, L. A., Geim, A. K., Gorbachev, R. Cross-sectional imaging of individual layers and buried interfaces of graphene-based heterostructures and superlattices. *Nature materials* **11**, 764-767 (2012).

101 Kretinin, A. V., Cao, Y., Tu, J. S., Yu, G. L., Jalil, R., Novoselov, K. S., Haigh, S. J., Gholinia, A., Mishchenko, A., Lozada, M., Georgiou, T., Woods, C. R., Withers, F., Blake, P., Eda, G., Wirsig, A., Hucho, C., Watanabe, K., Taniguchi, T., Geim, A. K., Gorbachev, R. V. Electronic properties of graphene encapsulated with different two-dimensional atomic crystals. *Nano letters* **14**, 3270-3276 (2014).

102 Mizuta, H., Tanoue, T. *The physics and applications of resonant tunnelling diodes*. Vol. 2 (Cambridge University Press, 2006).

103 Britnell, L., Gorbachev, R. V., Geim, A. K., Ponomarenko, L. A., Mishchenko, A., Greenaway, M. T., Fromhold, T. M., Novoselov, K. S., Eaves, L. Resonant tunnelling and negative differential conductance in graphene transistors. *Nature communications*, doi:10.1038/ncomms2817 (2013).

104 Mishchenko, A., Tu, J. S., Cao, Y., Gorbachev, R. V., Wallbank, J. R., Greenaway, M. T., Morozov, V. E., Morozov, S. V., Zhu, M. J., Wong, S. L., Withers, F., Woods, C. R., Kim, Y. J., Watanabe, K., Taniguchi, T., Vdovin, E. E., Makarovsky, O., Fromhold, T. M., Fal'Ko, V. I., Geim, A. K., Eaves, L., Novoselov, K. S. Twist-controlled resonant tunnelling in graphene/boron nitride/graphene heterostructures. *Nature nanotechnology* **9**, 808-813 (2014).

105 Roblin, P., Rohdin, Hans. *High-speed heterostructure devices: from device concepts to circuit modeling*. (Cambridge University Press, 2002).

106 Ferrari, A. C., Meyer, J. C., Scardaci, V., Casiraghi, C., Lazzeri, M., Mauri, F., Piscanec, S., Jiang, D., Novoselov, K. S., Roth, S., Geim, A. K. Raman spectrum of graphene and graphene layers. *Physical Review Letters* **97**, 187401 (2006).

107 Gorbachev, R. V., Riaz, I., Nair, R. R., Jalil, R., Britnell, L., Belle, B. D., Hill, E. W., Novoselov, K. S., Watanabe, K., Taniguchi, T., Geim, A. K., Blake, P. Hunting for monolayer boron nitride: optical and Raman signatures. *Small* **7**, 465-468 (2011).

108 Geim, A. K., Grigorieva, I. V. Van der Waals heterostructures. *Nature* **499**, 419-425 (2013).

109 Novoselov, K. S., Mishchenko, A., Carvalho, A., Castro Neto, A. H. 2D materials and van der Waals heterostructures. *Science* **353**, 461-463 (2016).

110 Amet, F., Bestwick, A. J., Williams, J. R., Balicas, L., Watanabe, K., Taniguchi, T., Goldhaber-Gordon, D. Composite fermions and broken symmetries in graphene. *Nature communications* **6**, 5838, doi:10.1038/ncomms6838 (2015).

111 Ruffieux, P., Wang, Shi, Yang, B., Sánchez-Sánchez, C., Liu, J., Dienel, T., Talirz, L., Shinde, P., Pignedoli, C. A. Passerone, D. Dumslaff, T., Feng, X., Müllen, K., Fasel, R. On-surface synthesis of graphene nanoribbons with zigzag edge topology. *Nature* **531**, 489-492 (2016).

112 Takayanagi, H., Akazaki, T., Nitta, J. Observation of maximum supercurrent quantization in a superconducting quantum point contact. *Physical Review Letters* **75**, 3533-3536 (1995).

113 Kim, M., Choi, J-H., Lee, S-H., Watanabe, K., Taniguchi, T., Jhi, S-H., Lee, H-J. Valley-symmetry-preserved transport in ballistic graphene with gate-defined carrier guiding. *Nature Physics* **Advanced online publication**, doi:10.1038/nphys3804 (2016).

114 Suzuki, S., Asada, M., Teranishi, A.,, Sugiyama, H., Yokoyama, H. Fundamental oscillation of resonant tunneling diodes above 1 THz at room temperature. *Applied Physics Letters* **97**, 242102 (2010).

115 Koyama, Y., Sekiguchi, R., Ouchi, T. Oscillations up to 1.40 THz from Resonant-Tunneling-Diode-Based Oscillators with Integrated Patch Antennas. *Applied Physics Express* **6**, 064102 (2013).

116 Feiginov, M., Kanaya, H., Suzuki, S., Asada, M. Operation of resonant-tunneling diodes with strong back injection from the collector at frequencies up to 1.46 THz. *Applied Physics Letters* **104**, 243509 (2014).

117 Gaskell, J., Eaves, L., Novoselov, K. S., Mishchenko, A., Geim, A. K., Fromhold, T. M., Greenaway, M. T. Graphene-hexagonal boron nitride resonant tunneling diodes as high-frequency oscillators. *Applied Physics Letters* **107**, 103105 (2015).